FULL-SCALE MEASUREMENTS AND SYSTEM IDENTIFICATION: A TIME-FREQUENCY PERSPECTIVE

VOLUME I

A Dissertation

Submitted to the Graduate School

of the University of Notre Dame

in Partial Fulfillment of the Requirements

for the Degree of

Doctor of Philosophy

by

Tracy Lynn Kijewski-Correa, B.S.C.E., M.S.C.E.

_____

Ahsan Kareem, Director

Department of Civil Engineering and Geological Sciences

Notre Dame, Indiana

April 2003

FULL-SCALE MEASUREMENTS AND SYSTEM IDENTIFICATION: A TIME-FREQUENCY PERSPECTIVE

Abstract

by

Tracy Lynn Kijewski-Correa

The rapid development of the global, urban landscape propels structures to new heights and spans, enhancing the role of structural engineers in assuring a safe and habitable built environment. In this new era of high-rise buildings and long-span bridges, design challenges continually arise, motivating the need to better understand the dynamic behavior of these structures through full-scale monitoring. In the context of such programs, the role of inherent damping, which proves critical for this flexible class of structures, must be quantified with accuracy – a challenging endeavor considering that narrowbanded response must be analyzed often without the benefit of measured input. More significantly, due to the presence of nonlinear and nonstationary characteristics in the measured data, traditional analysis tools may be incapable of capturing some of the salient features. This dissertation addresses these very issues by discussing the estimation of inherent damping from ambient data and evaluating its uncertainty via bootstrap resampling; by introducing a comprehensive wavelet-based analysis framework tailored to accommodate nonlinear and nonstationary features of Civil Engineering signals; and finally by introducing an on-going tall building monitoring program in Chicago, which

includes the configuration, calibration and application of Global Positioning Systems for the dynamic monitoring of displacements.

In particular, the wavelet framework introduced in this research, predicated on the properties of the Morlet Wavelet, provides flexible criteria for the separation of closely-spaced modal contributions, discretization of the time-frequency plane, and identification and melioration of end effects through a reflective padding scheme. Within this framework, wavelets are demonstrated to be capable of revealing hidden characteristics in simulated and measured wind, wave and earthquake data. In these discussions, the wavelet instantaneous bandwidth is introduced as a means to track subcyclic nonlinear behavior in a manner comparable to the Hilbert Spectra. Other wavelet applications in this study include its adaptation for identification of correlation in time and frequency and its enhancement through smart thresholding schemes. This framework also provides the backdrop for the extension of wavelets to the identification of frequency and damping in Civil Engineering structures, for which a number of processing concerns become paramount.

For My Family,

who have shown me that
with love, faith and family
nothing is impossible…

CONTENTS

VOLUME I

TABLES

VOLUME I

VOLUME II

FIGURES

VOLUME I

VOLUME II

ACKNOWLEDGEMENTS

This dissertation serves as a testament to the quality of a Notre Dame education and all it has inspired in me. I am especially fortunate to have been given the opportunity to attend this university for each of my degrees, during which I have been surrounded by some of my dearest friends and most respected colleagues. As much as the faculty of Notre Dame has been instrumental in my training and fostering, they are but a part of a larger Catholic community — the "Notre Dame family" — that has supported me during the most difficult times of my life. This family includes the many dedicated faculty who have served as my educators, my committee of Drs. Kareem, Chang, Kirkner and Kurama who took great time and care to read and critique this research, and the department's support staff over the years: Tammy, Judy, Mollie, Chris, Carrie and Denise, who kept me on track and kept this whole operation running. However, I realize that none of this would have been possible without the vision of my advisor and friend, Ahsan Kareem, who saw the potential of a junior in his Structural Analysis course and opened the world of research and academia to her. Thank you, "bossman," for never losing faith in me and in what I could become one day. Only two men have affected me in such a profound way, and I hope you know that you are one of them. Thank you for challenging me, mentoring me, inspiring me and ultimately guiding me toward a future that is brighter than any I could have imagined.

During my time at Notre Dame, I had opportunities I would never have found anywhere else — none more apparent than the full-scale monitoring program introduced in this work. I am grateful first and foremost to the engineers, owners and managers of these buildings for their continued support and cooperation with this research program. I would also like to thank the management of the Old Republic Building in Chicago for serving as the reference station for our GPS monitoring program. Particularly, in the development of this GPS framework, I must recognize a number of individuals: my mother and her staff for coordinating the installation and maintenance of the GPS reference station, John Berkebile of the St. Joseph County Parks Department for allowing us access to the Anderson Road site, Derrik Miles and James Stowell of Leica Geosystems for their advice in configuring the sensor, Brent Bach for helping to assemble the mounts and cabinetry, and Dr. Kwon, Tiphaine and Lijuan for helping to calibrate the system and post-process the GPS data. However, in the larger scope of my research, I have collaborated with a number of individuals and organizations who have greatly enriched my work, and therefore I would also like to thank at this time: my colleagues at Skidmore Owings and Merrill in Chicago and the Boundary Layer Wind Tunnel Laboratory at the University of Western Ontario, Dr. Yukio Tamura of the Tokyo Institute of Polytechnics, Mr. Frank Durgin formerly of MIT, Dr. Yin Zhou of Malouf Engineering, and Dr. Kurtis Gurley of the University of Florida at Gainesville.

Over the last six years at Notre Dame, I have been surrounded by so many amazing friends that I am truly privileged to know: Tim, Laura, Dan, my roommates over the years: Gale, Kate, Rachel, Lisa, Joy and Katy, Enos, the Dessanyakes, Shelley, Greg, the Sims, the Van Dykes, the Ohtoris, Bill, Nathan, Pete, the Morgens, Nelson, Andrea,

Ethan, Katie, Clara, Tony, Dana, Naru, Erica, Sara, Brad, Kelly, George, my office mates: Kara, Karrie-Ann and Ann, and everyone else that has been a part of our CE/GEOS family. Thank you all for helping me to create Notre Dame moments of laughter and love. In particular, I would like to thank Amy and Kenny for blessing me with the sister and brother I never had. And I would be remiss if I forgot to recognize my other family at Notre Dame — "Team Kareem" — for providing intellectual stimulus, support and ultimately friendship: Kurt, Mike, Fred, Luigi, Gang, Swaroop, Dr. Ohdo, Dr. Kanda, Tiphaine, Devin, Lijuan, Dr. Chen, Dr. Zhou and Dr. Kwon.

Of course, none of these experiences and relationships would have ever materialized had I not come to Notre Dame, and I attribute that great achievement to my family, beginning with my mother who gave me life and had the courage and strength to raise me on her own. Thank you, Mommy, for showing everyone that we could manage just fine. But thankfully, we were not truly alone, and my life was so much richer for the grace, love and guidance of my late grandparents and my aunts and uncles. Over the years, our family has grown with the addition of my cousins, my stepfather and my in-laws, who have continued to provide me with a supportive, nurturing environment grounded deeply in faith and family that empowered us all throughout the stressful years of my graduate education and my grandparents' illnesses. My one pillar through all these trials and challenges has been my husband Marco, who always was my biggest cheerleader, my strongest ally, my deepest confidant, and my best friend. Marco, I am so fortunate to have you in my life. I also cannot forget my little fuzzy friend who relaxes me every night after a long day at work: Bob the cat.

Finally, I would like to gratefully acknowledge support from National Science Foundation Grant CMS 00-85109, the National Science Foundation Graduate Research Trainee program, the National Defense Science and Engineering Graduate Fellowship through the Department of Defense, the NASA Indiana Space Grant, the Center for Applied Mathematics at the University of Notre Dame and the additional resources and support of the Department of Civil Engineering and Geological Sciences.

Note: PDF versions of this dissertation are available, in color, at the following website: www.nd.edu/~nathaz.

CHAPTER 1

OVERVIEW

The rapid development of the global, urban landscape continues to propel structures to new heights and spans, enhancing the role of structural engineers in assuring a safe and habitable built environment. In this new era of high-rise buildings and long-span bridges, the advancements in the state-of-the-art have presented new design challenges and unveiled dynamic behaviors that were not previously considered, but prove critical for this new breed of structure. Just as the limits of engineering design are tested in these ambitious projects, so too must the limits of the research which supports them, in the form of interactive design tools to better quantify the response of tall buildings in both sway and torsion (Zhou et al., 2003), in full-scale monitoring projects to better understand the in-situ dynamic response of these structures in real wind environments, and in innovative time-frequency analysis tools to investigate nonlinear and nonstationary characteristics in both their response and environmental loading. The following study primarily explores these latter two areas to demonstrate that the new challenges facing Civil Engineering can only be addressed by pushing the envelope, and in doing so, laying the foundation for the next generation of advancements.

1.1 Civil Engineering's Enigma

The challenges that face Civil Engineering practice begin and end with the basic equation of motion:

$$M\ddot{X} + C\dot{X} + KX = F \tag{1.1}$$

where M is the mass, K is the stiffness and C is the damping coefficient. X is the displacement response of the structure to some external force F, where the dots above the displacement variable are indicative of the derivative order. A great concern of Civil Engineering comes from the right side of this equation, in the search for accurate quantification of the forces or demand on the structure, often complicated by the stochastic nature of naturally occurring loads such as earthquakes, waves and wind. Meanwhile, the evolving complexity of the left hand side of this equation, corresponding to structural capacity, will continue to challenge Civil Engineers, in the face of nonlinearities, modal coupling and self-excited forces arising from modern and futuristic structures. However, before even moving on to more complicated versions of this expression and absent any external load, there is still great uncertainty in even this most basic equation. That uncertainty lies in damping, a true enigma in structural dynamics (Gurley & Kareem, 1996; Kijewski & Kareem, 2000). The second chapter of this study will explore the sources of uncertainty surrounding structural damping, the challenges associated with its estimation, and the viability of existing techniques for its extraction from full-scale, ambient vibration data, invoking a bootstrap resampling scheme detailed in the Appendix of this study to investigate the variance of damping estimates.

1.2 Moving into a New Analysis Domain

The discussions of structural damping and its estimation challenges in Chapter 2 highlight an important observation: many physical processes of interest to Civil Engineers manifest nonlinear and nonstationary features. As a result, their complete characterization may not be accomplished via Fourier Transforms, necessitating a new analysis framework. Chapter 3 chronicles the evolution from the Fourier domain to a time-frequency domain home to the multi-resolution Wavelet Transform. As motivated in Chapter 3, the dual nature of wavelet transforms, being a simultaneous transform in both time and frequency, justifies its recent extension to the analysis of stochastic processes of interest to Civil Engineering, adapting the transform to a number of situations where Fourier transforms were traditionally used to define quantities of interest. However, when considering the time and frequency information concurrently, wavelets can be used to determine the times and frequencies at which signal energy content is strongest, through examination of scalograms and coscalograms, e.g. Gurley & Kareem (1999). More specific insights into the linear and quadratic interplay between two signals in both time and frequency can be gained utilizing wavelet coherence and bicoherence measures (Gurley et al., 2003), as discussed in Chapter 6.

By exploiting the dual potential of wavelets, other analyses based primarily in either the time or frequency domain can also be performed. For example, the evolution of frequency content in time can be examined using wavelet scalograms and wavelet instantaneous frequency spectra, as demonstrated in Chapter 5 for measured time histories of earthquakes, wind velocity and wave elevation, known to possess nonlinear

and nonstationary features. Similarly, the distribution of wavelet coefficients with frequency at a window in time provides a familiar spectral representation whose evolutionary properties can be monitored to provide insights into nonlinear and nonstationary behavior, as demonstrated with a number of measured and simulated time histories in Chapter 7, which evaluates the performance of Wavelet Transforms and Hilbert Spectral Analysis. Further, tracking the variation of wavelet coefficients in the time domain permits complete system identification, a process that has particular challenges for long-period, flexible structures, as discussed in Chapter 8.

Of course, the introduction of new analysis frameworks brings with it a number of computational and processing challenges that must be fully reconciled to provide physically meaningful results. A large component of this study is dedicated to exploring and rectifying a number of these computational challenges, providing practical processing tools and guidelines for the implementation of wavelet transforms, particularly in the analysis of long-period systems. Although challenges did not surface in prior applications concerned with mechanical systems, who are generally characterized by higher frequency, broader-band signals, the transition to the time-frequency domain for the analysis of Civil Engineering structures highlighted the need to understand more fully various processing concerns, particularly for the popular Morlet wavelet. Specifically, as these systems may possess longer period motions and thus require finer frequency resolutions, the particular impacts of end effects become increasingly apparent. The discussion of these issues begins in Chapter 3 with an overview of Wavelet Transform theory and its relationships to the analytic signal. Chapter 4 then delves more fully into the various processing concerns in the context of the wavelet's multi-resolution

character and includes guidelines for selection of wavelet central frequencies, highlights their role in complete modal separation, and quantifies their contributions to end effects errors, which may be minimized through a reflective padding scheme. Other topics addressed include the discretization of the time-frequency plane and ridge extraction techniques. Further, these processing issues and analysis guidelines are articulated throughout Chapters 5-8 in the analyses and examples that follow. For example, the presence of statistical noise due to a lack of ensemble averaging in wavelet coherence maps is discussed and rectified in Chapter 6 through a variety of thresholding techniques and variable integration schemes. Though the application of wavelet transforms in Civil Engineering is in its infancy, the examples provided in this study demonstrate its promise as a tool to redefine the probabilistic and statistical analysis of processes in Civil Engineering and beyond.

1.3 The Call to Full-Scale

As discussed in Chapter 2, constructed facilities provide the most viable venue for study of inherent damping, motivating the need to develop extensive monitoring programs for a diverse suite of buildings of varying height and structural form. The high-rise community would particularly benefit from this enhanced understanding. The designers in this community limit the drifts of a structure through an increase in stiffness provided by an efficient choice of lateral system to satisfy serviceability criteria, all the while recognizing that such modifications may not always significantly reduce the levels of acceleration, of particular importance for occupant comfort concerns. In this latter case, it is the structure’s damping that becomes the integral component in satisfying the crucial

habitability criteria for tall buildings, implying that a better understanding of the inherent damping levels in common construction is necessary to insure that modern designs are capable of providing the required provisions for energy dissipation. In fact, the high-rise community's need for a firm and reliable understanding of in-situ damping levels is underscored by the plethora of auxiliary damping devices that have been installed in recent decades (Kareem et al., 1999).

However, an enhanced understanding of inherent damping levels is not the sole benefit of full-scale monitoring. Consider the fact that tall buildings are actually one of the few constructed facilities whose design relies solely upon analytical and scaled wind tunnel models that have yet to be systematically validated in full-scale. Therefore, if full-scale data could be compared against design predictions, tall building designers and wind engineers would have a firmer understanding of the deficiencies and strengths of the current design practice. Thus, to address these ranging needs, three tall buildings in Chicago, representing structural systems most common to high-rise construction, are being continuously monitored by the University of Notre Dame, in collaboration with the Boundary Layer Wind Tunnel Laboratory at the University of Western Ontario and Skidmore Owings and Merrill in Chicago (Abdelrazaq et al., 2000). The subsequent analysis of the data collected through these efforts will provide valuable insight into a variety of response characteristics for tall buildings, including the inherent damping, and permit the systematic validation and enhancement of existing design practice through comparisons with analytical and wind tunnel response estimates.

Traditional monitoring devices, including anemometers and accelerometers, whose selection, assembly, and installation are discussed in Chapter 9, are supplemented by high-precision Global Positioning Systems (GPS) to monitor structural displacements that were previously difficult to recover, particularly the static components of wind–induced response and thermal effects. The systems, with real time kinematic (RTK) potential, allow for complete dynamic monitoring of displacements at up to 10 samples/second. Chapter 10 introduces the concept of Global Positioning Systems for monitoring structural displacements in Civil Engineering and the anticipated sources of error, while Chapter 11 details the configuration and analysis parameters for the GPS components used in this research. Chapter 12 discusses a series of calibration tests investigating the influence of satellite position on system performance and verifying the ability of the GPS instrumentation to track complex waveforms and realistic long-period structural response to random excitations for motions at the sub-centimeter level and for frequencies up to 2 Hz. Chapter 13 then presents an analysis of some of the preliminary data from this on-going full-scale monitoring program.

Although the tools developed in this study draw heavily from a multi-disciplinary foundation, they are developed with the intent of improving the Civil Engineer's ability to completely characterize all the components of Equation 1.1, from the nonlinear and nonstationary loads impacting the structure, to the nonlinear dynamic features in the structure itself, none more illusive than inherent damping. As Chapter 14 summarizes, this often requires excursions into new research areas, borrowing from other disciplines in order to establish foundations for future advancements in Civil Engineering.

CHAPTER 2

DAMPING IDENTIFICATION AND ASSOCIATED UNCERTAINTY

2.1 Introduction

Despite the advancements that have been made in structural engineering in the last century, one critical parameter remains an enigma: damping. The complexity of this parameter is in part due to the diversity of sources contributing to the overall energy dissipation capability. These sources include: 1) damping inherent to the bulk material of which the system is formed, 2) boundary damping due to the dissipation between interfaces or joints in the structure, and 3) dissipation associated with the structure's contact with soil or a fluid field, in the case of aerodynamic or hydrodynamic damping. In particular, the boundary damping is difficult to quantify and represents significant non-linear losses. It is unclear which variables affect the damping forces and the appropriate models to represent these effects. As the choice of model relies on the mechanisms of damping, the fact that there are numerous mechanisms, which are more varied and less understood than the physical mechanisms governing mass and inertia, makes the appropriate choice of model increasingly difficult (Woodhouse, 1999; Kijewski & Kareem, 2000). As damping cannot be related to building materials and member configurations in a direct manner like mass and stiffness, a universal model for structural

damping is not possible and damping levels are simply assigned in the design process based on limited apocryphal data.

Consider this generalized form of the aforementioned equation of motion, for a single-degree-of-freedom (SDOF) mechanical oscillator, given by

$$M\ddot{X} + f_D + KX = F \ . \tag{2.1}$$

The linearity of this expression is achieved by replacing the damping force f_D with a viscous damping model:

$$f_d(\dot{x}) = C\dot{X} \ , \tag{2.2}$$

where C is the viscous damping coefficient. The result is the following equation of motion

$$\ddot{X} + 2\xi\omega_n\dot{X} + \omega_n{}^2 X = F/M \tag{2.3}$$

where ω_n is the natural angular frequency ($\omega_n = 2\pi f_n$) and ξ is the damping ratio, the ratio of the assigned viscous damping to the critical damping value. Under this accepted practice, any source of nonlinearity is obscured, as the linear viscous damping ratio is inherently independent of amplitude, in contrast to other damping models, e.g. Coulomb or quadratic (Kareem & Kijewski, 2000).

The shortcomings of assuming viscous damping levels became apparent with the transition to light and flexible structures, as assumed levels of damping, on the order of 1% critical damping for steel structures and 2% for concrete, were often not realized in the constructed building. For this class of tall, wind-sensitive structures, the diminished

levels of damping realized in practice led to a host of serviceability and especially habitability problems that were not anticipated in design. The resounding difficulty in engineering known levels of damping in design was partly responsible for the flurry of auxiliary damping devices in recent years, which were found to provide measurable and controllable levels of this critical parameter (Kareem et al., 1999).

Since an exact model for damping cannot be constructed on an element level, a viable alternative was to develop empirical expressions for modal damping based upon the levels observed in existing structures. Of course, this requires an extensive and reliable survey of constructed facilities. Only recently have such databases become available in the form of the Japanese Damping Data Base (JDDB) (Tamura et al., 1996) featuring dynamic properties of 278 structures, and an international database featuring dynamic properties of 185 buildings in Asia, Europe and North America (Lagomarsino & Pagnini, 1995). From these and other databases, a variety of expressions have been developed, including those by Engineering Sciences Data Unit (1990), based upon the natural frequency and dimension of the building, and those fit to the JDDB dependent upon the natural frequency of reinforced concrete structures (Tamura, 1997). Despite the efforts to fit these existing databases with empirical functions, which correlate damping with parameters such as natural frequency, it appears that the levels of damping to be expected in the structure are a function of numerous other variables including the material and foundation type. The situation is compounded by the fact that additional levels of damping may be provided by non-structural elements and cladding components. As these characteristics vary from structure to structure, the identification of an “expected level of damping” for a given design becomes a daunting task.

The situation is further complicated by the fact that the full-scale damping data currently cataloged manifests considerable scatter, indicating that significant errors may be introduced. Haviland (1976) reported a wide range of data for different levels of response amplitudes in a variety of structural systems and building heights and showed that log-normal and gamma distributions provided the best fit to the damping variations. The coefficient of variation (CoV) of the damping estimates, defined as the ratio of the standard deviation σ to the mean μ, based on this data set, varied from 42% to 87%. Davenport & Hill-Carroll (1986) reexamined the database and noted that the CoV ranged from 33% to 78% and suggested a value of 40%. Thus the use of empirical expressions based upon data with this degree of scatter could lead to the design of a building that on paper may meet serviceability and occupant comfort criteria, but in practice, does not. The limited success of these efforts may be due to a lack of structural diversity in the full-scale observations, the damping parameter's observed amplitude dependence, and difficulty in its estimation from measured ambient vibration data. This latter issue will be addressed in greater detail throughout this chapter.

2.2 Traditional Approaches to Damping Identification from Wind-Induced Response

As the analysis of measured response currently provides the only viable means to quantify the levels of damping in structures, methodologies for structural testing, monitoring and system identification have received considerable attention in recent decades. Through these efforts, a host of methodologies for system identification have surfaced, each tailored to specific applications. In the case where the system inputs are

measured or known, (e.g. forced vibrations using shaker, impact testing, earthquake response), a variety of attractive system identification tools are available, e.g. Ghanem & Shinozuka (1995). However, in the case of wind loading, due to spatio-temporal variations in surface pressure, there is no direct relationship between the wind speed and associated wind loads on the various faces of the structure (Simiu & Scanlan, 1996). Thus, for the analysis of most full-scale data from wind-induced response, system identification approaches requiring measured input are not viable. As a result, the assumptions of Gaussian, stationary, white noise input are invoked to permit meaningful analysis of wind-induced response by limited system identification approaches, e.g. Desforges et al. (1995), Littler (1995), Wang & Haldar (1997). Among these approaches, spectral analysis (SA) and the time-domain-based, Random Decrement Technique (RDT) are the most common, with the spectral approach being the more traditional of the two.

2.2.1 Spectral Analysis and Inherent Errors

With the advent of the Fast Fourier Transform in the 1960's, Fourier spectral analysis became the primary means by which to analyze signals in Civil Engineering, as the superposition of harmonic components in Fourier Analysis is intuitively appealing for mechanical oscillators, providing a global energy distribution at each frequency *f* contained in the signal *x(t),* i.e. producing a "stationary spectrum" $\hat{X}(f)$ called the Fourier spectrum:

$$\hat{X}(f) = \int_{-\infty}^{\infty} x(t) e^{-i2\pi ft} dt \,. \tag{2.4}$$

Particularly in the case of wind-excited structures, the assumption of white noise input yields an attractive representation of the unknown input as a constant power spectrum, an assumption particularly valid in the narrow bandwidth of structural response. For this reason, spectral analysis became the popular choice for system identification for of wind-induced response.

As discussed, for example, in Bendat & Piersol (1986), the spectral estimate can be simply generated by segmenting the measured response time history into blocks of sufficient length T to provide the desired spectral resolution Δf_{FFT}, defined as the difference between adjacent discrete frequencies, given by:

$$f_k = \frac{k}{T} = \frac{k}{N\Delta t} \quad k = 0, 1, \ldots, N-1 \tag{2.5}$$

where N is the actual number of discrete data points x_n in the block of length T, sampled at the time step Δt. Commonly, N is selected to the nearest power of 2 to permit use of the Fast Fourier Transform (FFT), a convention used in this chapter, according to

$$\hat{X}(f_k) = \Delta t \sum_{n=0}^{N-1} x_n \exp\left[-i\frac{2\pi kn}{N}\right] \quad k = 0, 1, \ldots, N-1. \tag{2.6}$$

The FFT is applied to each block of data to produce the Fourier coefficients according to Equation 2.6. The squared magnitudes of each set of Fourier coefficients produces a single raw spectrum. The spectra produced by this method are then averaged, under standard ergodic assumptions, to obtain an estimate of the power spectral density (PSD), $\hat{S}xx(f)$ evaluated at discrete frequencies, f_k:

$$\hat{S}_{xx}(f_k) = \frac{1}{T}\left(\frac{1}{N_s} \sum_{nn=1}^{N_s} \left| \hat{X}_{nn}(f_k) \right|^2 \right) \quad k = 0, 1, \ldots, N\text{-}1. \tag{2.7}$$

where N_s is the number of spectra being averaged.

The use of Fourier Transforms in this and other applications have highlighted additional concerns such as side lobe leakage, often requiring additional windowing measures that can increase the effective bandwidth of the spectra. As a result, an understanding of spectral leakage and aliasing is requisite when applying the Fourier Transform. These processing issues are discussed in more detail in (Bendat & Piersol, 1986).

The normalized bias error of the resulting power spectrum in the vicinity of the resonance frequency f_r reflects the importance of the frequency resolution achieved in this process (Bendat & Piersol, 1986):

$$\varepsilon_b \left[\hat{S}_{xx}(f_r) \right] \approx -\frac{1}{3}\left(\frac{\Delta f_{FFT}}{B_r} \right)^2 \tag{2.8}$$

where B_r is the half-power bandwidth of the Fourier power spectrum, approximated by

$$B_r = 2\xi f_n. \tag{2.9}$$

Note the introduction of the half-power bandwidth (HPBW) in Equation 2.9 is an approximation valid only for lightly damped systems, i.e. $\xi < 0.1$, for which the resonant frequency may be taken as the natural frequency of the system (Bendat & Piersol, 1986). Conveniently, this relationship permits a very simple and direct means of system identification from the response PSD, given that the input spectrum is constant. Again,

this assumption is typically acceptable when the ambient excitations of the system can be approximated as white noise, at least in the vicinity of the spectral peak. Figure 2.1 illustrates that the half-power bandwidth may be determined by identifying, via interpolation between the discrete frequencies, the two frequencies f_2 and f_1 that correspond to half the maximum amplitude of the PSD. Assuming symmetry of the spectral peak, the HPBW is then defined as the difference between these two frequencies: $B_r = f_2 - f_1$, with the frequency corresponding to the spectral peak taken as the natural frequency of the system. This permits the system damping to be identified readily from Equation 2.9. On the other hand, more sophisticated curve fitting the response spectra may also be conducted in lieu of relying on the HPBW e.g. Littler (1995) or when limited data is available, e.g. the maximum likelihood method (Montpellier, 1996) with parameter averaging (Montpellier et al., 1998) and autoregressive (AR) modeling of response spectra (Cao et al., 1997; Kijewski & Kareem, 1999).

These alternative schemes are useful in situations where limited amounts of data render the generation of a smooth spectrum difficult, since it is governed by the limitation of the normalized variance given in Bendat & Piersol (1986) as

$$\mathrm{var}\left[\hat{S}_{xx}(f)\right] \approx \frac{1}{N_s}. \tag{2.10}$$

Note that this expression assumes that the raw spectra were determined from independent, disjoint blocks of data of length T without the inclusion of windowing. Overlapped processing of spectral estimates may be invoked when limited data are available, as discussed in Bendat & Piersol (1986).

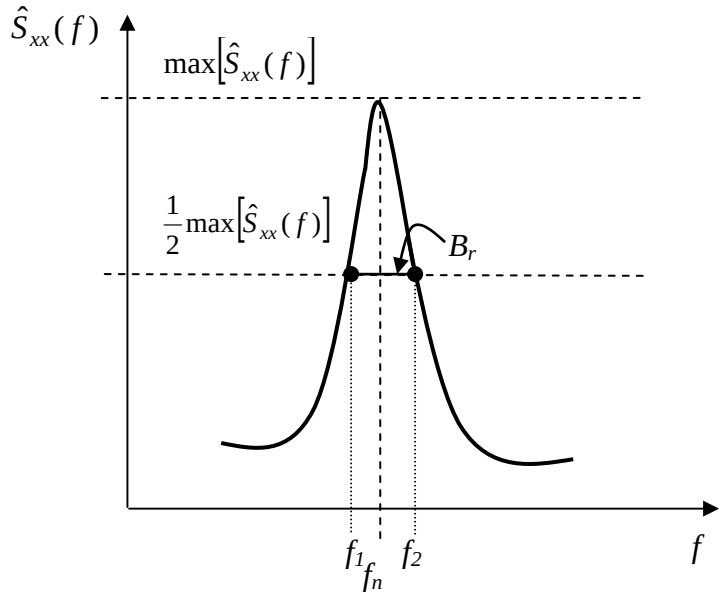

FIGURE 2.1. Schematic of half-power bandwidth method of spectral system identification

For the narrowband processes common to Civil Engineering, small spectral bandwidths place restrictions on the frequency resolution of the transformed data, as the spectral resolution must be fine enough to resolve the sharp spectral peak, dictated by the aforementioned bias error in Equation 2.8. In addition, to minimize the variance of the spectral estimate in Equation 2.10, a sufficient number (N_s) of sample spectra must be averaged. This introduces the infamous paradox in spectral analysis: considering that only limited data are available for analysis, increasing the length of each ensemble to reduce bias errors directly implies that there will be fewer ensembles available for minimizing the variance. On the other hand, increasing the number of ensembles restricts the length of each ensemble, increasing bias. The negative bias error implies that the amplitude of the peak of the spectrum is always underestimated, leading to an overestimation of damping. In the case of stationary data analysis, increasing the time

interval *T* over which the analysis is conducted will decrease the random errors in the estimates of statistical properties; however in the case of nonstationary signals, an increase in this interval *T* will result in a smoothing of the actual time variations in the statistical properties of the signal, reiterating the importance of stationarity assumptions in Fourier analysis. Thus the primary challenge in spectral analysis is obtaining a sufficient amount of stationary data to minimize both competing sources of error. Note that selective ensemble averaging and parameter averaging have been proposed to relax the stringent stationarity requirements (Littler, 1995; Isyumov & Morrish, 1997).

2.2.2 Random Decrement Technique

One way to avoid entirely the resolution issues associated with Fourier Transform techniques is to restrict analysis to the time domain. Though system identification in the time domain is often difficult without explicit knowledge of the input, under the same general assumptions made in spectral analysis for wind-induced response data, alternative analysis tools are available. One popular approach is the Random Decrement Technique (Gurley & Kareem, 1996), due to its ability to overcome the strict requirements for lengthy stationary data imposed by traditional spectral approaches.

The decrement is generated by capturing a sample of prescribed length from the time history upon the satisfaction of a threshold condition (Cole, 1973). This triggering condition, in its strictest sense, will specify both amplitude and slope criteria, though applications of the RDT in the literature have adopted varying trigger conditions, as discussed in later in Section 2.2.2.4. Note also that the duration of segments captured is

subjective, but typically is on the order of a several cycles of oscillation. The segments meeting these conditions are averaged to in essence remove the random component of the response, assumed to be zero mean, leaving Random Decrement Signature (RDS). Mathematically this operation is represented by an expectation

$$D(\tau) \equiv E\left[X(t_2) \middle| X(t_1) = X_o \cap \dot{X}(t_1) = \dot{X}_o\right] \tag{2.11}$$

where the assumption of stationarity allows the introduction of a time variable $\tau = t_2 - t_1$.

The RDS was shown by Vandiver et al. (1982) to be proportional to the autocorrelation signature ($R_{xx}(\tau)$) for the system, assuming in the derivation a more relaxed trigger condition in that only an amplitude trigger X_o is specified:

$$D(\tau) \equiv E\left[X(t_2) \middle| X(t_1) = X_o\right] = X_o R_{xx}(\tau) / R_{xx}(0). \tag{2.12}$$

Though the RDT essentially provides an estimate of the autocorrelation function, it is able to produce this estimate without the same strict requirements for lengthy stationary data, as discussed by Jeary (1992).

The expectation in Equation 2.11, assuming ergodicity, can be replaced by an average of N_r triggered segments $X_{tt}(t)$ over a single time history

$$D(\tau) = \frac{1}{N_r} \sum_{tt=1}^{N_r} \left(X_{tt}(\tau) \middle| X_{tt}(0) = X_o \cap \dot{X}_{tt}(0) = \dot{X}_o\right). \tag{2.13}$$

A conceptualization of the process of generating the RDS, shown in Figure 2.2, reflects a common representation of the RDT, in which the total response is viewed as the superposition of the forced vibration response with the homogeneous component or free

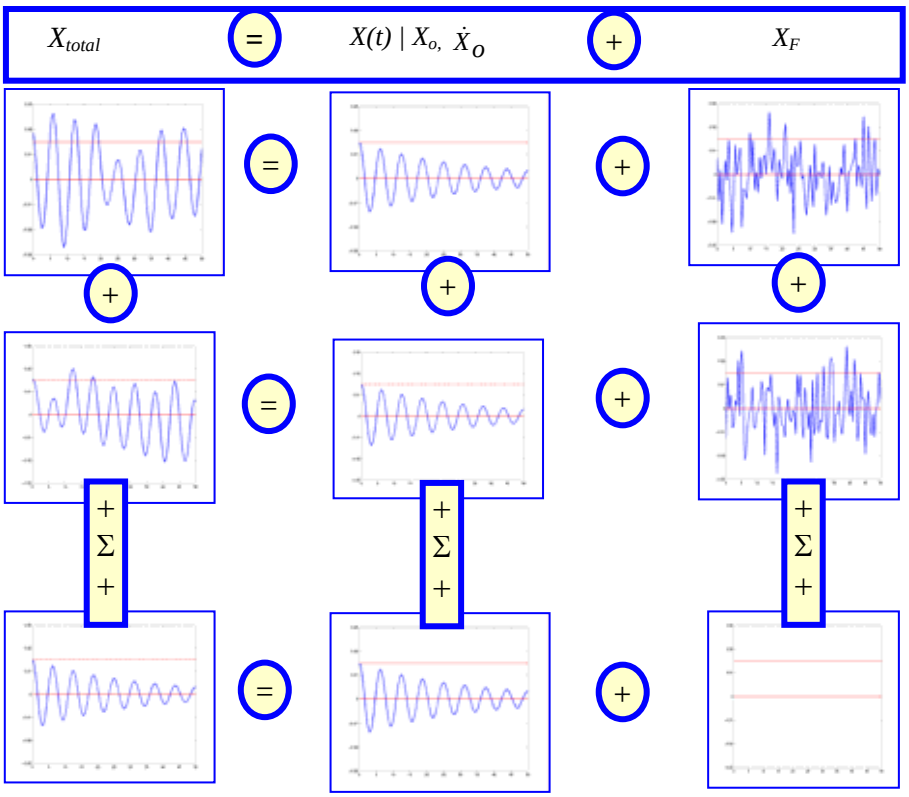

FIGURE 2.2. Conceptualization of the Random Decrement Technique for local extrema triggering condition

vibration decay from given initial conditions, i.e. the triggering condition. Successive averaging of segments of this response will tend to cancel out the random component of the response, assumed to be zero mean. This leads to the perception that the Random Decrement Technique yields the free vibration response of the system. However, this is only the case for a linear oscillator excited by Gaussian, zero-mean, white noise, for which the autocorrelation function, normalized by a constant `C,` takes the following form:

$$R_{xx}(\tau) = Ce^{-\xi\omega_n\tau}\cos(\omega_D\tau) \ , \tag{2.14}$$

which is analogous to the free vibration response of an oscillator with damped natural frequency ω_D, assumed equivalent to its undamped counterpart for a lightly damped system. As long as the white noise assumption remains valid (implications of this are discussed in Kareem & Gurley (1996) and Spanos & Zeldin (1998)), the analogs between Equations 2.11 and 2.14 may be exploited for system identification by a number of strategies, e.g. via least squares minimization to obtain best-fit estimates of damping ξ and natural frequency f_n, letting $C = X_o/R_{xx}(0)$.

Alternatively, the damping can easily be identified from the peaks in the decay curve via the logarithmic decrement. Let $D_p(n)$ and $D_p(n+1)$ define two consecutive peaks in the RDS decay curve. The logarithmic decrement (LogDec) is then defined from these two peaks:

$$\delta \equiv \ln \frac{D_p(n)}{D_p(n+1)} = \frac{2\pi\xi}{\sqrt{1-\xi^2}}, \tag{2.15}$$

implying that for lightly damped systems, $\delta \approx 2\pi\xi$. It has been observed (Clough & Penzien, 1993), that a more accurate estimate of the damping using logarithmic decrement is obtained by considering peaks separated by m (multiple) cycles, yielding the following expression for estimating the damping of lightly damped systems by logarithmic decrement

$$\xi \approx \frac{D_p(n) - D_p(n+m)}{2m\pi D_p(n+m)}. \tag{2.16}$$

to directly identify the damping from the peaks in the decay curve.

Under the aforementioned theoretical assumptions, the RDS will be unbiased with variance that can be expressed by (Vandiver et al., 1982):

$$\text{var}[D(\tau)] = E[D^2(\tau)] - E[D(\tau)]^2 = R_{xx}(0)/N_r[1 - R_{xx}^2(\tau)/R_{xx}^2(0)]. \qquad (2.17)$$

The presence of noise was ignored in this idealized derivation, as was the potential correlation between the captured segments. Thus, to satisfy these theoretical constraints, captured segments are often not allowed to overlap. Note also that, as indicated by Equation 2.17, the amplitude level selected for the triggering condition is theorized to have no direct effect on the variance, though it will dictate the number of segments averaged. Clearly, this number of segments should be increased as much as possible to minimize variance; however, in application, the amplitude of the trigger has been observed to influence the accuracy of the resulting damping estimates, as discussed in Section 2.2.2.2.4, and in the case of systems with amplitude-dependent damping, the damping estimated from the resulting random decrement signature corresponds to the viscous damping ration at the amplitude level associated with that trigger (Tamura & Suganuma, 1996).

The preceding discussion assumed that the response was comprised of a single mode. Conventionally, the incorporation of bandpass filtering (Kijewski & Kareem, 1999; Tamura & Suganuma, 1996) prior to the application of the RDT is required to insure this condition for measured data. However, the Random Decrement Technique can also be applied directly to a time history that may have multiple modes present. In this case, the resulting RDS will be proportional to a multi-degree-of-freedom (MDOF) autocorrelation function, or under the assumed conditions discussed previously, a

superposition free vibration decays for several modes. The identification of the MDOF signature can then be conducted by an appropriate technique, e.g. Ibrahim Time Domain Method (Ibrahim, 1977; Mahmoud et al., 2001) or, as discussed in Chapter 8, wavelet transforms can be used to decouple the signature's individual components.

2.2.2.1 Types of Triggering Conditions

The use of RDT in the literature has highlighted a differing opinion on the number of segments required to successfully average out the random component of the response. As demonstrated later in this chapter, this may significantly depend on the level of randomness in the excitation itself. However, the differing opinions may be more directly attributed to the triggering condition employed. As shown in Equation 2.11, trigger conditions can strictly specify either an amplitude or slope level or both, leading to a variety of trigger conditions in the literature. Ibrahim (2001) discusses the four most common triggers:

level crossing: $$\left\{X_{tt}(0) = X_o\right\} \tag{2.18}$$

positive point: $$\left\{X_{low} < X_n(0) < X_{high}\right\} \tag{2.19}$$

zero up-crossing: $$\left\{X_{tt}(0) = 0 \cap \dot{X}_{tt}(0) > 0\right\} \tag{2.20}$$

local extrema: $$\left\{X_{low} < X_{tt}(0) < X_{high} \cap \dot{X}_{tt}(0) = 0\right\}. \tag{2.21}$$

The level crossing condition is arguably the most fundamental triggering condition and is assumed in the theoretical derivations in Vandiver et al. (1982) resulting in Equations 2.12 and 2.17. The positive point condition, which specifies a range of values in order to generate more eligible samples, is a potentially more realistic version of the level

crossing criteria, as it is rare to encounter values within the time history that identically equal some arbitrary trigger amplitude. The positive point condition, in order to more strictly approach the level crossing condition, may assume its range based on some percentage of the desired amplitude level, e.g. on the order of a few percent. On the other hand, more robust ranges can be selected in Equation 2.19 to include a wide variety of amplitude levels, akin to the procedure in Tamura & Suganuma (1996). The ranges were selected in that study to guarantee that each had a pre-determined number of eligible segments. The zero up crossing condition identifies zero crossing points within the signal, though this condition again may require some relaxation to include a range of values within a few percent, as it again is rare to encounter identically zero values in a sampled time history. Note that this trigger condition has no potential to reference the signature to a specific amplitude level and therefore lacks physical significance for the applications in this study. The final condition, which is formally presented in Tamura & Suganuma (1996), captures only peaks falling within a specified amplitude range. This triggering condition is the most strict, as it firmly specifies both an amplitude and slope. This range can be made very narrow to stringently reference a particular amplitude for tracking amplitude-dependent dynamic properties, as advocated herein, or again relaxed for a more robust range of amplitudes. Tamura & Suganuma (1996) utilized this relaxed trigger to track amplitude-dependent damping in full-scale data. Note the trigger condition more completely supported by the mathematical theory developed in Vandiver et al. (1982) is the level crossing condition or positive point trigger with narrow range. The local extrema approach merely becomes a special case of the level crossing

condition, reducing the number of eligible segments by enforcing the zero slope condition.

To this suite of triggering conditions, one may also supplement the level crossing by a positive slope. The best rationale for this trigger comes from the fact that, as the signal ascends toward a local extremum, it may pass through the specified amplitude level, and it may be assumed that, following this peak in the time history, the signal will descend toward the zero level, again crossing the specified amplitude but with a negative slope. As these events are usually within a limited time frame, segments captured at both of these crossings will likely have a high degree of correlation. As the segments are assumed independent in theory, the selection of a positive slope becomes a simple way to prevent the capture of highly correlated segments. However, if other measures are being taken to enforce the condition of nonoverlapping segments, this added slope condition is truly not necessary.

2.2.2.2 Investigations of Factors Influencing RDT Quality

The sensitivity of RDS to the violation of various assumptions in its theory will be explored in the subsequent sections. Authors have discussed the implications of violating the white noise assumption in the RDT (Kareem & Gurley, 1996; Spanos & Zeldin, 1998), illustrating that the RDS cannot be equal to the free vibration curve if the excitation is not truly white. However, there has been no treatment of the implications of correlation between samples. Similarly, the influence of trigger condition and nonstationarity, also not explored systematically in the literature, will be investigated in

the subsequent sections. For demonstrative purposes, analyses of a SDOF oscillator excited by Gaussian, zero-mean, white noise are utilized. The response of this 0.2 Hz system with 1% critical damping ratio was simulated for 12 hours, sampled at 2 Hz. Unless stated otherwise, the strictest trigger condition of local extrema was utilized, specifying an amplitude range of +/- 3% of the desired trigger amplitude.

One of critical parameters to be explored is the variance of the RDS. Though the variance of the signature may be obtained directly from the N_r segments used in the averaging process, this is merely a sample variance. However, resampling schemes such as bootstrapping can be exercised as an alternative means by which to estimate the true variance of the signatures (Efron & Tibshirani, 1993). A bootstrap resampling scheme will be utilized to gauge the variance of the random decrement signature, so as to obtain a better estimate of the true variance. The Appendix of this study contains more information on the bootstrap methodology for estimating the variance of random decrement signatures and the simulation of variance envelopes, which highlight the areas of greatest variance in the random decrement signature. It is hoped that the introduction of such a scheme will provide practitioners with a simple means by which to estimate the variance of their RDS and provide a measure of the reliability when theoretical assumptions are not entirely met and closed form expressions for variance cannot be used due to violations of the assumptions made in their derivation. All bootstrapped estimates discussed in the subsequent sections are based on $B=50$ replicates.

2.2.2.2.1 Suggested Expression for Random Decrement Signature Variance

Before analyzing the various factors contributing to the performance of the Random Decrement Technique, the bootstrap variance estimate will validated against the closed form expression for variance in Equation 2.17. The examination of the simulated data shown in Figure 2.3 agrees in trend with the closed form expression. As the initial conditions are indeed enforced at $\tau=0$, the RDS is theoretically most reliable at this point. Subsequently, the signature increasingly breaks down further from this point, as the deviations between the theoretical decay curve and the RDS demonstrate. The bootstrapped replicates of the decrement signature form a variance envelope, shown as the second of a sequence of plots in Figure 2.3. This provides some appreciation of the variance in estimates, propagating with time.

Note also that the closed form expression for variance in Equation 2.17 is based upon the autocorrelation function in Equation 2.14 and yields results that are counter-intuitive to the actual behavior. In theory, the variance will oscillate as a squared cosine function, indicating that it will reach maximum every half cycle. With time, these oscillations diminish and the variance will approach a near constant value of the signal variance divided by N_r. However, this variance estimate would indicate that within a half cycle of the trigger threshold the error has already reached its maximum value. This would indicate that in its present form, the error estimate is not a true representation of the behavior of the decrement, as the bootstrapped estimates and intuitive arguments presented in Vandiver et al. (1982) also confirm. This work offers a more practical, limiting case for the error

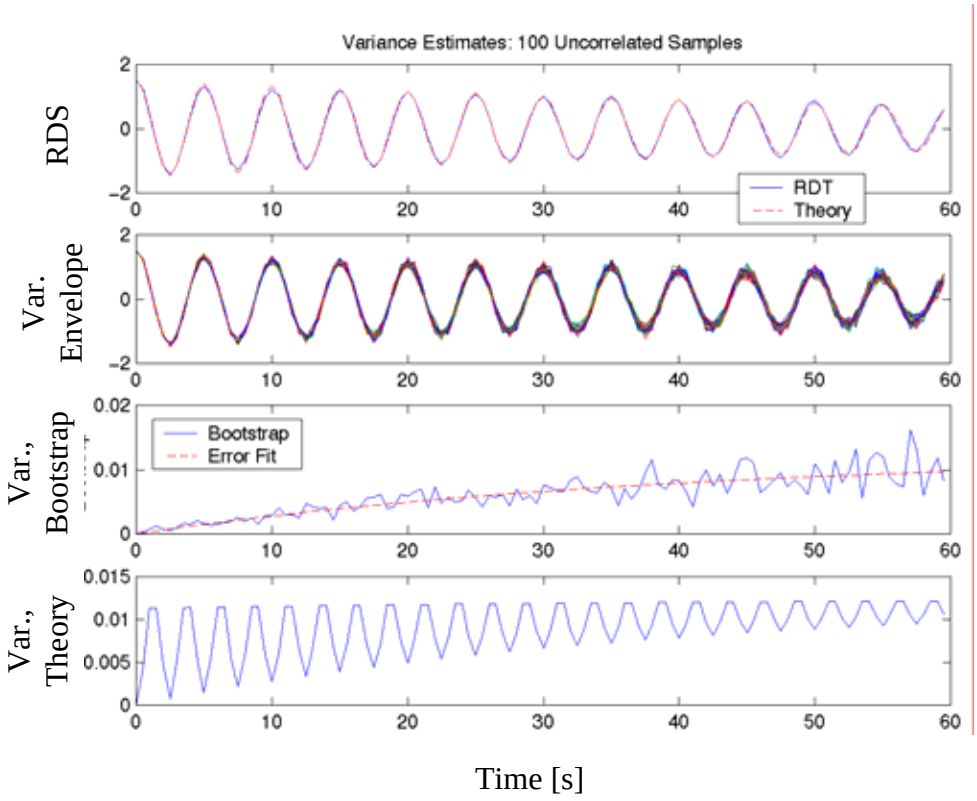

FIGURE 2.3. (top to bottom) RDT against theoretical autocorrelation, bootstrap variance envelope, bootstrapped variance estimate against Equation 2.17, theoretical variance in Equation 2.13, uncorrelated segments

$$\varepsilon_{RDS}(\tau) = R_{XX}(0)/N_r\left(1-e^{-2\xi\omega_D\tau}\right). \tag{2.22}$$

As shown by the dashed line in Figure 2.3, this limiting error forms the lower bound in theory, providing a more reasonable approximation of RDS variance. The bootstrap, in providing a realistic estimate of variance also fits well against Equation 2.22. As the bootstrap variance is consistent with the theoretical variance, it is deemed appropriate for variance estimation in this chapter.

2.2.2.2.2 Significance of Overlap Between Captured Segments

In the development of the random decrement variance in Equation 2.17, it was assumed that the segments captured for averaging are independent, i.e. they do not share any part of the time history. This restriction limits the amount of segments available for averaging, an especially concerning issue since the number of segments averaged is a critical parameter in reducing the variance of random decrement signatures, as will be shown in the subsequent section. Therefore, the ability to allow overlap in captured segments would be beneficial. To explore the implications of violating this assumption, bootstrapping is used to estimate the variance of the random decrement signatures when overlapping of segments is permitted.

By comparing Figure 2.3 and 2.4, the effects of correlation on the quality of the estimates appears not to be considerable, in comparison to the same analysis for uncorrelated segments in Figure 2.3. In fact, aside from some random fluctuations in the bootstrapped variance estimate, the correlated case produces the same limiting variance as the uncorrelated case, fit by Equation 2.22. Further, by examining Figure 2.5, one can see that there is no increase in the bootstrapped estimate of cyclic variance (averaged bootstrap variance in the RDS over one cycle of oscillation) as a result of permitting some correlation between samples. By allowing some overlap between adjacent samples, the user is now afforded additional samples for averaging, a critical requirement for the use of RDT.

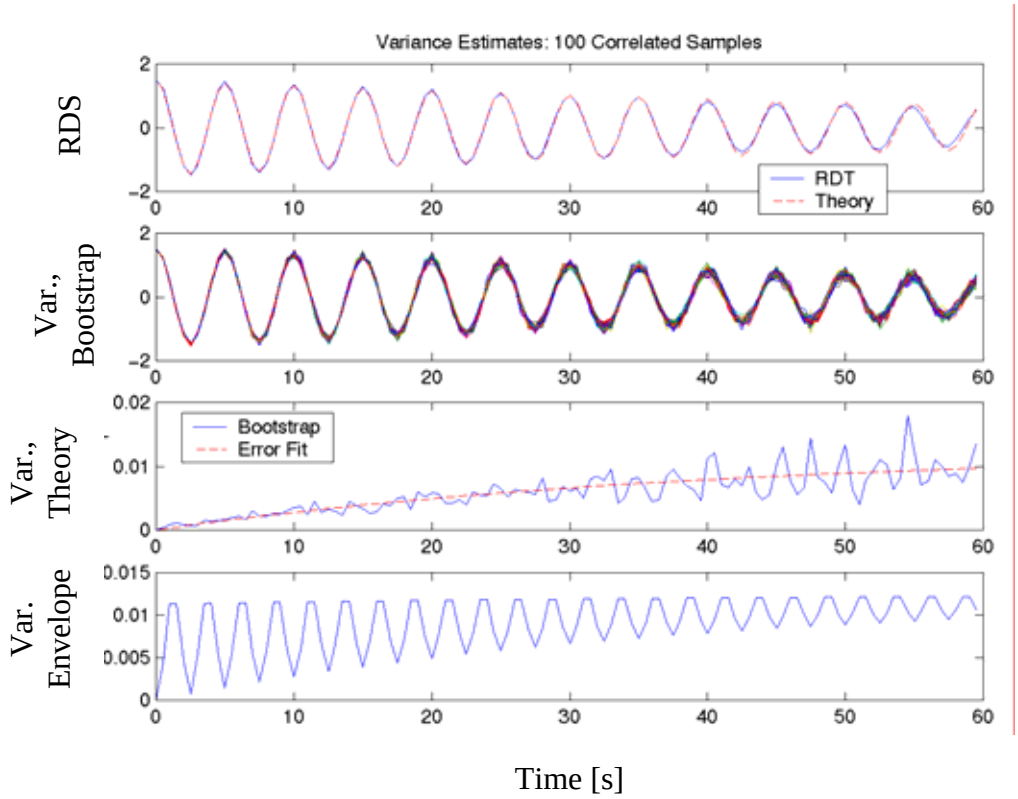

FIGURE 2.4. (top to bottom) RDT against theoretical autocorrelation, bootstrap variance envelope, bootstrapped variance estimate against Equation 2.12, theoretical variance in Equation 2.13, correlated segments

2.2.2.2.3 Required Number of Captured Segments

Despite the widespread use of the RDT, there still is much debate surrounding the amount of data required to yield reliable estimates. In order to accomplish the averaging required to completely remove the random component of the response, some researchers recommend 400 to 500 segments (Yang et al., 1983), while others recommend at least 2000 (Tamura et al., 1992). As shown by Figure 2.5, by averaging the bootstrap variances over each cycle of the RDT signature, one can monitor the increase in variance as more cycles are considered in the estimate. Clearly, as the number of segments

averaged increases, this variance decreases. However, it is interesting to note whether or not the RDS variance is a good indication of the accuracy of a given damping estimate. The error of logarithmic decrement estimates averaged over a number of cycles is also shown in Figure 2.5. The reliability of single cycle damping estimates is poor even though this is where the variance in the RDT estimate is minimum. Thus, a more accurate means of damping estimation is required to permit estimates using only the first few cycles of the RDS, which are more stable. In fact, only by considering 3 or more cycles do estimates approach an accuracy of 10%; however, there is a trade-off in that the variance in the estimates also increases with the number of cycles. Thus the estimates of damping by logarithmic decrement are best when performed within the first 4 cycles with more than N_r=200 averages, when the local extrema triggering condition is utilized, for which errors in damping estimation by logarithmic decrement are between 10-20%. Later examples will further demonstrate the accuracy of damping estimation including the influence of trigger condition on the required number of averages. Finally, to enhance the quality of damping estimate over the early cycles of the RDS, the use of a least squares curve-fitting approach may be advocated, as discussed later in this chapter.

2.2.2.2.4 Significance of Triggering Condition on Damping Estimation

The last section reflected that, for a given amplitude, an increase in the number of segments averaged in the decrement will reduce the signature variance, as predicted by the expression in Equation 2.17, though the performance in terms of damping estimation can be quite variable. Certainly, the variance of the RDS signifies the potential variability in the signature. As the damping is identified solely from the peaks of the function

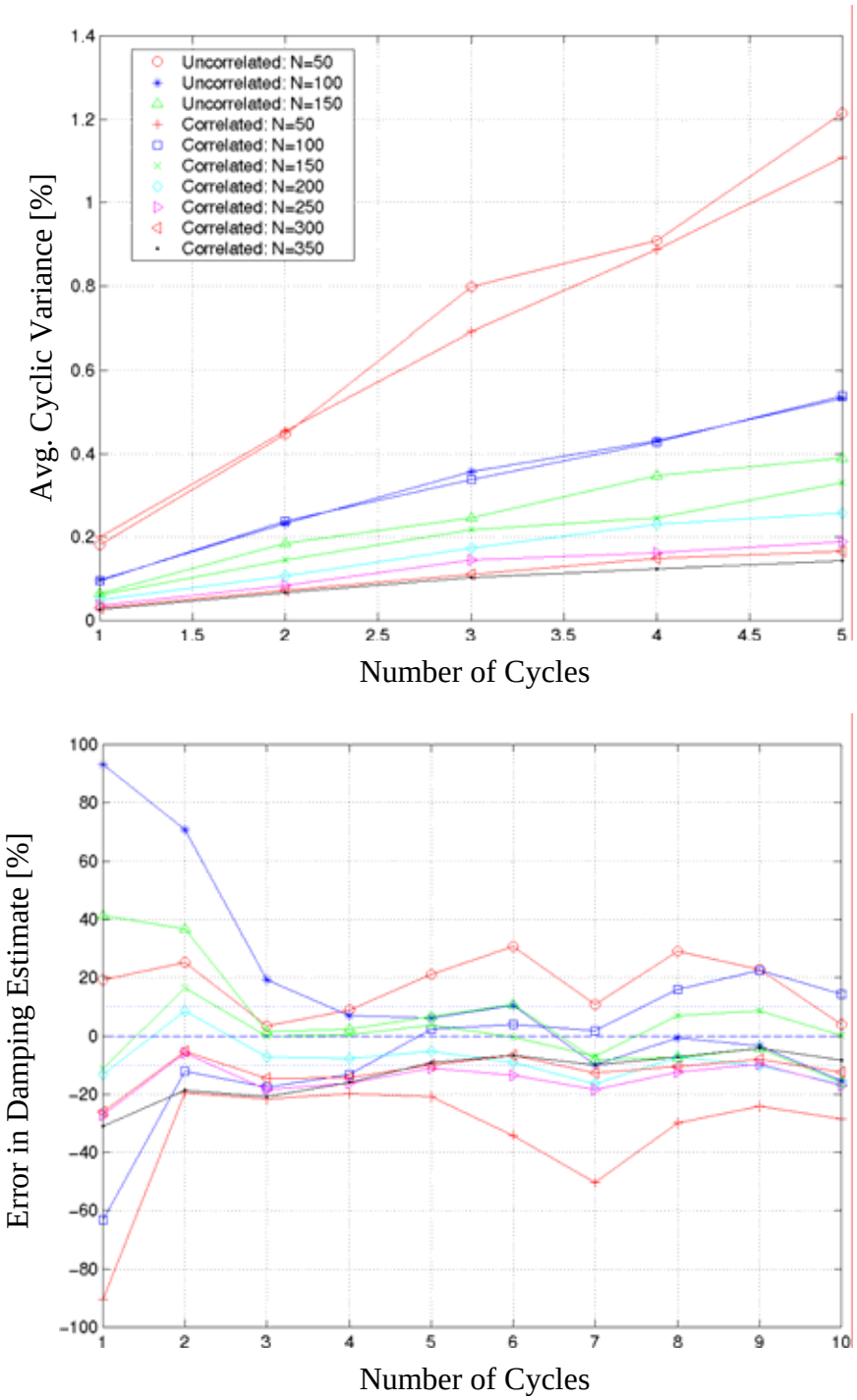

FIGURE 2.5. RDT cyclic variance (top) and resulting damping estimation error

marking the decay curve of the RDS, although variance of the signature on the whole may be small, damping values can still have some scatter if these peaks are the least reliable components of the RDS, justifying the findings in Figure 2.5. Further, the peaks in the decay curve may be less than or greater than the amplitudes expected in theory, leading to damping values that can be over or underestimates. For spectral analysis, the spectral bandwidth is always wider than theory, leading to a consistently overestimated and biased damping estimate. Thus the behavior of estimated damping values, as shown in Figure 2.5, must be investigated, along with the influence of trigger condition, trigger amplitude and overlap between the decrement segments. Such an investigation follows herein.

The only unique trigger condition that allows some amplitude referencing is the level crossing or positive point condition, with the local extrema being a special case of this condition. These latter two triggers are explored for a host of amplitude levels, with a range of +/-3% of the specified amplitude level. Recall that the theoretical developments of the RDT in Equations 2.12 and 2.17 assume the captured segments don't overlap. Thus three correlation cases are considered by varying the length (T_{RDS}) of the captured segments to investigate the influence of this assumption. These correlation conditions are T_{RDS} = 50 seconds (10 cycles of oscillation), implying that segments 50 seconds long will be captured and no portion of the time history within those 50 seconds is eligible to trigger the capture of a new segment. A second case lengthens this requirement to $T_{RDS} = 100$ seconds (20 cycles of oscillation), reducing further the potential for correlation between segments. A third case places no restriction on overlapping segments, thus T_{RDS} = 0 s, allowing correlation freely.

The random response of the system discussed in Section 2.2.2.2 was simulated four times (referred to as Runs I, II, III, IV) using different seeds in the random number generator to demonstrate the variability of response histories (shown in Figure 2.6) with the same spectral and probabilistic description, shown in Figure 2.7, distributing Gaussian about a zero mean with standard deviations listed in Table 2.1. The power spectral densities of the response all identify the frequency of the oscillator and all appear to have the same distribution of energy in the low frequencies. While Runs II and IV have higher energy levels in the high frequencies, this characteristic has no obvious influence on results.

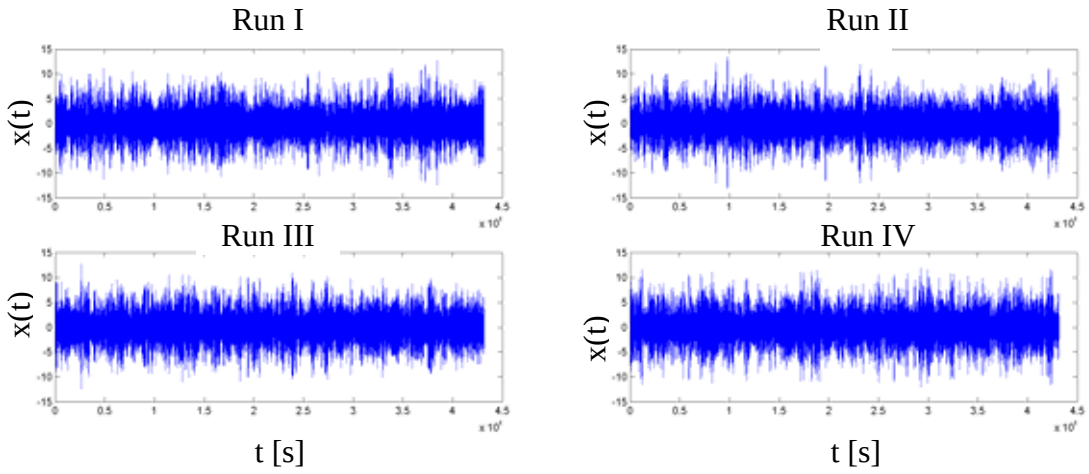

FIGURE 2.6. Time histories of SDOF response for Runs I-IV

TABLE 2.1

STANDARD DEVIATIONS OF SIMULATED TIME HISTORIES

Run I	Run II	Run III	Run IV
3.11	3.00	2.99	3.17

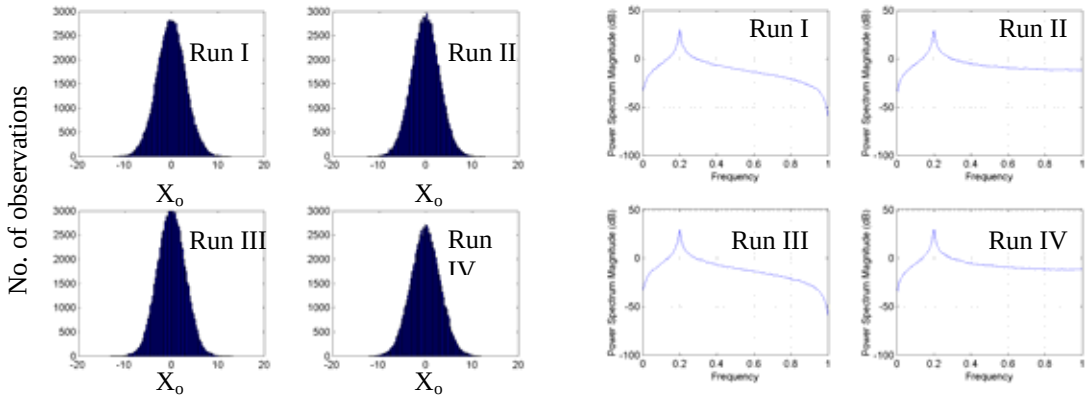

FIGURE 2.7. Histograms (left) and power spectra for simulated response in Runs I-IV

The Random Decrement Technique is applied to each simulated time history, using varying trigger conditions and the three correlation conditions described above. A damping estimate is then obtained from two full cycles of the resulting signatures using the logarithmic decrement. To verify the inherent error in the LogDec approach, damping was estimated from the first two cycles of impulse response functions, generated directly from the system equation of motion. It was found that the LogDec overestimated the damping of this system as 0.0107. As a result, the quality of LogDec damping estimates from the RDS should be appropriately weighted for this inherent bias. The tabulated results provided in this chapter therefore shade the values of damping which fall within 10% of the LogDec bias, i.e. 0.0096-0.0117, in darker hues. Results corresponding to 11-20% error relative to the biased LogDec estimate, i.e. damping values of 0.0085-0.0095 and 0.0118-0.0128, are shaded with a lighter hue.

Table 2.2 lists the results for the positive point trigger, specifying the target amplitude as a multiple M of the standard deviation of the response. N_r^{tot} is the total number of segments satisfying the trigger condition, while N_r is the number of segments actually averaged to form the RDS, after the enforcement of correlation restrictions. A visual comparison seems to reflect that Run II shows the poorest performance, demonstrating that the randomness inherent in some records may require relatively a larger number of segments to fully average out, as will be discussed further in Section 2.3. For the positive point trigger, allowing correlation understandably increases the number of samples in the average, yielding more reliable damping estimates. Therefore, the influence of correlation does not appear negative. A fact also affirmed in Section 2.2.2.2.2. The damping appears to be consistently estimated in Runs I, III and IV, when a the trigger satisfies the following condition: $3\sigma > X_o > 1\sigma$.

Low triggers, though having a large number of samples in the average, yield inconsistent performance. This is an interesting result, as the variance of the decrement signature is shown to minimize with the number of averages and lower trigger amplitudes certainly afford more potential averages in the Gaussian distribution of amplitude values. Although variance of decrement signatures is theorized not to depend upon the trigger level, the performance is inconsistent for $X_o < \sigma$, though at times the estimates are quite accurate. Intuitively, one may argue that the trigger condition bears some influence on the performance of the decrement. As noted by Vandiver et al. (1982), triggers below or on the order of the root mean square (RMS) of the process will occur frequently within the time history, increasing the potential for correlation that may lead to larger variance in cases where $T_{RDS} = 0$ s. However, simulations show that the greater number of averages

TABLE 2.2

ESTIMATED LOGDEC DAMPING VALUES USING POSITIVE POINT TRIGGERS

Run I							
		T_{RDS} = 0 s		T_{RDS} = 50 s		T_{RDS} = 100 s	
M	X_o	N_r/N_r^{tot}	ξ	N_r/N_r^{tot}	ξ	N_r/N_r^{tot}	ξ
0.5	1.55	902/903	0.0099	432/903	0.0123	291/903	0.0145
0.75	2.33	1198/1202	0.0146	489/1202	0.0162	313/1202	0.0191
1.0	3.10	1251/1251	0.0094	497/1251	0.0133	317/1251	0.0091
1.5	4.66	966/968	0.0100	966/968	0.0100	256/968	0.0123
2.0	6.21	552/555	0.0096	212/555	0.0089	157/555	0.0086
2.5	7.76	250/252	0.0101	99/252	0.0103	81/252	0.0107
3.0	9.32	64/64	0.0106	30/64	0.0107	27/64	0.0120
3.5	10.8	16/16	0.0079	5/16	0.0029	5/16	0.0029
4.0	12.4	3/3	0.0074	1/3	0.0028	1/3	0.0028
Run II							
		T_{RDS} = 0 s		T_{RDS} = 50 s		T_{RDS} = 100 s	
M	X_o	N_r/N_r^{tot}	ξ	N_r/N_r^{tot}	ξ	N_r/N_r^{tot}	ξ
0.5	1.50	882/885	0.0094	426/885	0.0086	280/885	0.0072
0.75	2.25	1223/1224	0.0182	510/1224	0.0168	322/1224	0.0195
1.0	3.00	1216/1216	0.0148	489/1216	0.0113	312/1216	0.0113
1.5	4.50	1008/1008	0.0118	385/1008	0.0124	268/1008	0.0135
2.0	6.00	539/539	0.0103	225/539	0.0100	168/539	0.0146
2.5	7.50	248/248	0.0126	98/248	0.0141	78/248	0.0144
3.0	9.00	77/77	0.0126	31/77	0.0119	28/77	0.0111
3.5	10.5	12/12	0.0108	7/12	0.0145	7/12	0.0145
4.0	12.0	2/2	0.0042	1/2	0.0055	1/2	0.0055
Run III							
		T_{RDS} = 0 s		T_{RDS} = 50 s		T_{RDS} = 100 s	
M	X_o	N_r/N_r^{tot}	ξ	N_r/N_r^{tot}	ξ	N_r/N_r^{tot}	ξ
0.5	1.49	897/899	0.0106	428/899	0.0083	287/899	0.0126
0.75	2.24	1141/1142	0.0105	480/1142	0.0116	313/1142	0.0144
1.0	2.99	1232/1232	0.0077	488/1232	0.0046	312/1232	0.0045
1.5	4.49	992/992	0.0104	385/992	0.0128	253/992	0.0097
2.0	5.98	542/542	0.0115	222/542	0.0116	168/542	0.0113
2.5	7.48	183/183	0.0101	80/183	0.0120	66/183	0.0125
3.0	8.98	76/76	0.0108	32/76	0.0087	27/76	0.0088
3.5	10.5	21/21	0.0050	8/21	0.0057	8/21	0.0057
4.0	**11.9**	**6/6**	**0.0128**	**4/6**	**0.0136**	**4/6**	**0.0136**
Run IV							
		T_{RDS} = 0 s		T_{RDS} = 50 s		T_{RDS} = 100 s	
M	X_0	N_r/N_r^{tot}	ξ	N_r/N_r^{tot}	ξ	N_r/N_r^{tot}	ξ
0.5	1.59	922/923	0.0131	432/923	0.0137	283/923	0.0175
0.75	2.38	1108/1110	0.0110	469/1110	0.0093	300/1110	0.0097
1.0	3.17	1239/1239	0.0088	473/1239	0.0106	304/1239	0.0175
1.5	4.76	1043/1043	0.0104	386/1043	0.0112	272/1043	0.0103
2.0	6.34	553/553	0.0100	211/553	0.0106	160/553	0.0099
2.5	7.93	220/220	0.0094	93/220	0.0089	76/220	0.0096
3.0	9.52	95/95	0.0101	38/95	0.0111	33/95	0.0096
3.5	11.1	24/24	0.0141	11/24	0.0162	11/24	0.0162
4.0	12.7	0/0	N/A	0/0	N/A	0/0	N/A

afforded offsets any increase in variance due to correlation, though it may be theorized that the lower amplitude segments within the time history have a greater level of correlation than the segments with higher amplitude, though this is yet to be proven. Conversely, the large amplitude triggers may be assumed to be particularly unreliable due to the limited number of averages.

The range of behavior in Table 2.2 further emphasizes that specific features within a given time history may impact performance, even when all the very idealized theoretical conditions are satisfied, as typified by the poor performance of Run II. Realizing that full-scale data is far less ideal, Jeary (1992) proposed some guidelines for removing portions of time histories that may cause break down in decrement signatures, "eliminating the type of data which produce spurious results." As certain characteristics in the time series can make the averaging process more difficult, Jeary recommends that following types of sequences be omitted from the time histories:

- "sequences in which "drop-outs are present"
- "sequences in which sudden changes in [root mean square] rms occur"
- "sequences in which beating between two modes of vibration occurs"

The customary practice of filtering about one mode of vibration aids particularly in enforcing this last condition. However, Jeary advocates repeatability of results as well, since spurious findings tend to distribute themselves randomly, in accordance with the nature of the process. In this work, it is suggested that such repeatability may be achieved by selecting several trigger amplitudes close to one another, identifying the damping

from each resulting decrement signature, and then examining the variability in damping estimates. The variability is assumedly small due to the proximity in amplitude level and the fact that the number of averaged segments should be similar. Outlier samples may then be distinguished or more appropriately, an average of the identified properties over this range can be taken as the damping estimate referenced to the average trigger, as shown in Table 2.3.

TABLE 2.3

REPEATABILITY AND LOCAL AVERAGING FOR RUN I, LOCAL EXTREMA TRIGGER, $T_{RDS} = 0$

X_o	N_r	ξ	$\mu[X_o]$	$\mu[\xi]$
9.0	68	0.0088		
9.1	60	0.0101		
9.2	52	0.0117	9.25	0.0102
9.3	46	0.0110		
9.4	47	0.0096		
9.5	39	0.0103		

Table 2.4 shows the results for the application of the RDT using the local extrema trigger, where the same amplitude levels used in the positive point triggers in Table 2.2 are used as the amplitude levels in the local extrema trigger condition in Table 2.4. In addition, as the mean peak value is often chosen as a potential trigger, since it will afford a large number of averages, the analysis is conducted for this trigger as well. Looking at the results for the four cases in Table 2.4, there is not much loss of samples due to the enforcement of any correlation conditions, in part because the additional criteria on the slope reduces the potential proximity of captured segments that would introduce

TABLE 2.4

ESTIMATED DAMPING VALUES USING LOCAL EXTREMA TRIGGER

Run I						
	T_{RDS} = 0 s		T_{RDS} = 50 s		T_{RDS} = 100 s	
X_o	N_r/N_r^{tot}	ξ	N_r/N_r^{tot}	ξ	N_r/N_r^{tot}	ξ
1.55	137/137	0.0226	137/137	0.0226	137/137	0.0226
2.33	223/223	0.0197	223/223	0.0197	223/223	0.0197
3.1	345/345	0.0131	345/345	0.0131	345/345	0.0131
4.66	344/344	0.0118	343/344	0.0117	343/344	0.0117
6.21	265/266	0.0124	265/266	0.0124	265/266	0.0124
7.76	147/148	0.0093	147/148	0.0093	144/148	0.0098
9.32	48/47	0.0098	45/47	0.0097	44/47	0.0100
10.8	14/14	0.0086	9/14	0.0081	9/14	0.0081
12.4	1/1	0.0028	1/1	0.0028	1/1	0.0028
3.74*	379/379	0.0112	377/379	0.0113	376/379	0.0115
Run II						
	T_{RDS} = 0 s		T_{RDS} = 50 s		T_{RDS} = 100 s	
X_o	N_r/N_r^{tot}	ξ	N_r/N_r^{tot}	ξ	N_r/N_r^{tot}	ξ
1.50	130/130	0.0358	130/130	0.0358	130/130	0.0358
2.25	270/270	0.0314	270/270	0.0314	270/270	0.0314
3.00	345/345	0.0217	345/345	0.0217	345/345	0.0217
4.50	409/409	0.0145	409/409	0.0145	409/409	0.0145
6.00	272/272	0.0107	272/272	0.0107	272/272	0.0107
7.50	153/153	0.0129	153/153	0.0129	153/153	0.0129
9.00	52/52	0.0144	49/52	0.0144	48/52	0.0145
10.5	9/9	0.0122	7/9	0.0145	7/9	0.0145
12.0	2/2	0.0042	1/2	0.0055	1/2	0.0055
3.51*	363/364	0.0162	362/364	0.0164	359/364	0.0164

*mean of peak values.

correlation. However, as the peak condition removes many segments that were eligible in the positive point condition, the number of segments is minimized. Interestingly, when capturing only segments initiating with peaks, adding more samples does not improve performance dramatically and may even deteriorate the RDS. This is due to the fact that over the three correlation conditions the number of samples being averaged does not vary significantly enough to make dramatic impact on performance. As shown in Figure 2.4,

TABLE 2.4 (CON'T)

Run III						
	T_{RDS} = 0 s		T_{RDS} = 50 s		T_{RDS} = 100 s	
X_o	N_r/N_r^{tot}	ξ	N_r/N_r^{tot}	ξ	N_r/N_r^{tot}	ξ
1.49	131/131	0.0420	47/131	0.0200	129/131	0.0428
2.24	235/235	0.0172	235/235	0.0172	235/235	0.0172
2.99	309/309	0.0069	309/309	0.0069	309/309	0.0069
4.49	358/358	0.0092	358/358	0.0092	358/358	0.0092
5.98	281/281	0.0140	279/281	0.0138	278/281	0.0138
7.48	105/105	0.0125	102/105	0.0118	102/105	0.0118
8.98	46/46	0.0114	44/46	0.0111	43/46	0.0116
10.5	12/12	0.0025	11/12	0.0034	11/12	0.0034
11.9	**3/3**	**0.0123**	**2/3**	**0.0085**	**2/3**	**0.0085**
3.53*	348/348	0.0129	348/348	0.0129	347/348	0.0131
Run IV						
	T_{RDS} = 0 s		T_{RDS} = 50 s		T_{RDS} = 100 s	
X_o	N_r/N_r^{tot}	ξ	N_r/N_r^{tot}	ξ	N_r/N_r^{tot}	ξ
1.59	132/132	0.0541	132/132	0.0541	132/132	0.0541
2.38	230/231	0.0242	230/231	0.0242	230/231	0.0242
3.17	323/323	0.0139	323/323	0.0139	323/323	0.0139
4.76	395/395	0.0122	394/395	0.0122	394/395	0.0122
6.34	273/273	0.0128	273/273	0.0128	272/273	0.0130
7.93	126/126	0.0100	124/126	0.0100	123/126	0.0100
9.52	63/63	0.0100	58/63	0.0096	57/63	0.0098
11.1	20/20	0.0136	12/20	0.0149	12/20	0.0149
12.7	0/0	N/A	0/0	N/A	0/0	N/A
3.44*	327/327	0.0131	327/327	0.0131	327/327	0.0131

*mean of peak values.

despite general trends, the variance estimates can still have fluctuations, and this is reflected in the results in Table 2.4 in the absence of significant increases in N_r. The performance of the local extrema RDS tends to stabilize as more samples are added, as shown later in Section 2.4.2. Thus if only limited data is available, the positive point method may be better. Interestingly, the amplitude levels that again performed the best were the same trigger levels that performed well in the positive point method. This finding is again surprising. While a trigger in the vicinity of the peak distribution's

median yields a large number of averages, higher amplitude trigger levels associated with the 1.5-3σ amplitude often outperform them. This may again indicate that contrary to Expression 2.17, the trigger amplitude has some influence on performance, in conjunction with number of averages. It is arguable that the segments associated with triggers in the amplitude range of 1-3σ may have correlation behaviors different from its counterparts producing equal number of eligible segments at lower amplitudes.

In a final series of simulations, the trigger condition is relaxed to allow consideration absolute values of a specified amplitude in Equations 2.18, 2.19 or 2.2.1. This modified implementation of the decrement is given by

$$D(\tau) = \frac{1}{N_r}\sum_{tt=1}^{N_r}\left(\text{sgn}(X_{tt}(0))X_{tt}(\tau)\middle\| X_{tt}(0)\right| = X_o \cap \dot{X}_{tt}(0) = \dot{X}_o\Big) \tag{2.23}$$

which should afford additional segments for averaging, though potentially raising correlation concerns. The results from this investigation are shown in Table 2.5 and only Runs I and II are considered for brevity. By allowing the potential for full correlation (T_{RDS} = 0) and using the positive point trigger, there is a marked increase in the number of averages in comparison to Table 2.2, but with no significant improvement in performance. Thus, at some point, segments may overlap so much that they do not help to further reduce variance, though apparently causing little determent. In this case, enforcing T_{RDS} = 50 s seems to improve results for the low amplitude triggers, perhaps minimizing the effects of correlation, but detracts from the performance of higher amplitude triggers by reducing N_r. However, in the local extrema trigger simulations, the use of an absolute value amplitude did appear to improve performance in the fully correlated and T_{RDS} =

TABLE 2.5

INFLUENCE OF ABSOLUTE VALUE TRIGGER CONDITIONS

Abs. Value Amplitude Trigger							
Run I							
		T_{RDS} = 0 s		T_{RDS} = 50 s		T_{RDS} = 100 s	
M	X_0	N_r/N_r^{tot}	ξ	N_r/N_r^{tot}	ξ	N_r/N_r^{tot}	ξ
0.5	1.55	1835/1838	0.0090	568/1838	0.0107	344/1838	0.0046
0.75	2.33	2355/2361	0.0140	612/2361	0.0114	357/2361	0.0125
1.0	3.10	2492/2492	0.0095	602/2494	0.0115	348/2494	0.0089
1.5	4.66	1902/1907	0.0096	432/1907	0.0107	282/1907	0.0098
2.0	6.21	1143/1149	0.0098	253/1149	0.0087	183/1149	0.0085
2.5	7.76	502/505	0.0101	119/505	0.0078	91/505	0.0078
3.0	9.32	128/128	0.0110	40/128	0.0098	33/128	0.0105
3.5	10.8	38/38	0.0057	8/38	0.0077	8/38	0.0077
4.0	12.4	5/5	0.0089	1/5	0.0028	1/5	0.0028
Run II							
		T_{RDS} = 0 s		T_{RDS} = 50 s		T_{RDS} = 100 s	
M	X_0	N_r/N_r^{tot}	ξ	N_r/N_r^{tot}	ξ	N_r/N_r^{tot}	ξ
0.5	1.50	1816/1820	0.0101	562/1820	0.0070	343/1820	0.0090
0.75	2.25	2402/2404	0.0155	621/2404	0.0112	365/2404	0.0129
1.0	3.00	2497/2500	0.0141	614/2500	0.0135	363/2500	0.0187
1.5	4.50	2003/2003	0.0117	463/2003	0.0124	299/2003	0.0117
2.0	6.00	1109/1109	0.0113	278/1109	0.0115	198/1109	0.0125
2.5	7.50	481/481	0.0123	124/481	0.0128	96/481	0.0134
3.0	9.00	144/144	0.0134	40/144	0.0148	34/144	0.0146
3.5	10.5	22/22	0.0124	9/22	0.0136	9/22	0.0136
4.0	12.0	6/6	0.0084	1/6	0.0037	1/6	0.0037

*mean of peak values.

50 s cases by again generating more averages. Excessive overlap was not a consideration for the local extrema condition, unlike its positive point counterpart, as this stricter triggering condition using only peaks already minimizes the potential for overlap.

One final interesting observation can be made for the high amplitude triggers. At high amplitudes, the limited number of averages prohibits consistent performance. However, even with so few averages, these triggers may produce more reasonable

TABLE 2.5 (CON'T)

Abs. Value Peak Trigger						
Run I						
	T_{RDS} = 0 s		T_{RDS} = 50 s		T_{RDS} = 100 s	
X_0	N_r/N_r^{tot}	ξ	N_r/N_r^{tot}	ξ	N_r/N_r^{tot}	ξ
1.55	268/268	0.0206	162/268	0.0140	139/268	0.0043
2.33	449/449	0.0160	262/449	0.0151	196/449	0.0153
3.10	660/660	0.0103	330/660	0.0123	236/660	0.0132
4.66	670/670	0.0111	312/670	0.0122	220/670	0.0119
6.21	547/549	0.0112	211/549	0.0114	165/549	0.0126
7.76	295/297	0.0105	108/297	0.0085	86/297	0.0079
9.32	99/99	0.0103	38/99	0.0086	32/99	0.0089
10.8	26/26	0.0084	8/26	0.0096	8/26	0.0096
12.4	2/2	0.0064	½	0.0028	1/2	0.0028
3.74*	744/744	0.0108	273/744	0.0096	236/744	0.0085
Run II						
	T_{RDS} = 0 s		T_{RDS} = 50 s		T_{RDS} = 100 s	
X_0	N_r/N_r^{tot}	ξ	N_r/N_r^{tot}	ξ	N_r/N_r^{tot}	ξ
1.50	280/280	0.0315	181/280	0.0315	154/280	0.0353
2.25	519/519	0.0306	283/519	0.0349	208/519	0.0309
3.00	702/702	0.0197	350/703	0.0182	247/703	0.0182
4.50	790/790	0.0157	344/790	0.0162	249/790	0.0153
6.00	546/546	0.0119	241/546	0.0128	179/546	0.0133
7.50	300/300	0.0121	118/300	0.0115	93/300	0.0124
9.00	102/102	0.0148	39/102	0.0153	33/102	0.0142
10.5	20/20	0.0109	8/20	0.0120	8/20	0.0120
12.0	5/5	0.0046	1/5	0.0037	1/5	0.0037
3.51*	740/742	0.0140	346/742	0.0129	245/742	0.0165

*mean of peak values.

damping estimates than the same number of averages would at a lesser amplitude levels. Stability is achieved when a high number of averages are present, though this will never be the case for the amplitude values which lying in the tails of the distribution.

Intuitively, at high amplitudes the points satisfying the trigger condition are closely associated with maximum values within the signal. They may represent a pulse or high amplitude burst within the signal. However, following this pulse, before the arrival

of the next significant excitation, the amplitude will naturally tend to diminish, leading to a lull of the time history. As a result, the very decay characteristic, which is being isolated in the RDT, surfaces more likely at these higher amplitudes than at their lower counterparts. This may help to explain why higher amplitude triggers from 1-3 σ outperform other triggers that may afford more averages.

To illustrate, consider Run III for the trigger condition of X_o=11.9 (4σ), shown in bold in Tables 2.2 and 2.4. The six captured segments meeting the positive point condition for T_{RDS} = 0, and later averaged to form the RDS, are shown in Figure 2.8. The dotted line is the theoretical free vibration for this case. If the other two correlation conditions (T_{RDS} = 50 and 100 s) were to be enforced, two of theses segments, $X_3(t)$ and $X_4(t)$, would be negated. On the other hand, the even stricter conditions imposed by the local extrema condition would select only $X_3(t)$, $X_4(t)$ and $X_5(t)$ for T_{RDS} = 0 and if no overlap between captured segments is permitted, only $X_3(t)$ and $X_5(t)$ would be retained. It should be noted that indeed, at this high amplitude, some of the segments already closely resemble the decay curve for the system, implying that fewer averages are required for meaningful results. As opposed to the segments captured at smaller amplitudes, such as those shown by the top two images at the left of Figure 2.2, where the captured segments in no way resemble a decay. Unfortunately, there are few segments at these higher amplitude levels and typically not enough to average the RDS into a fully stable signature.

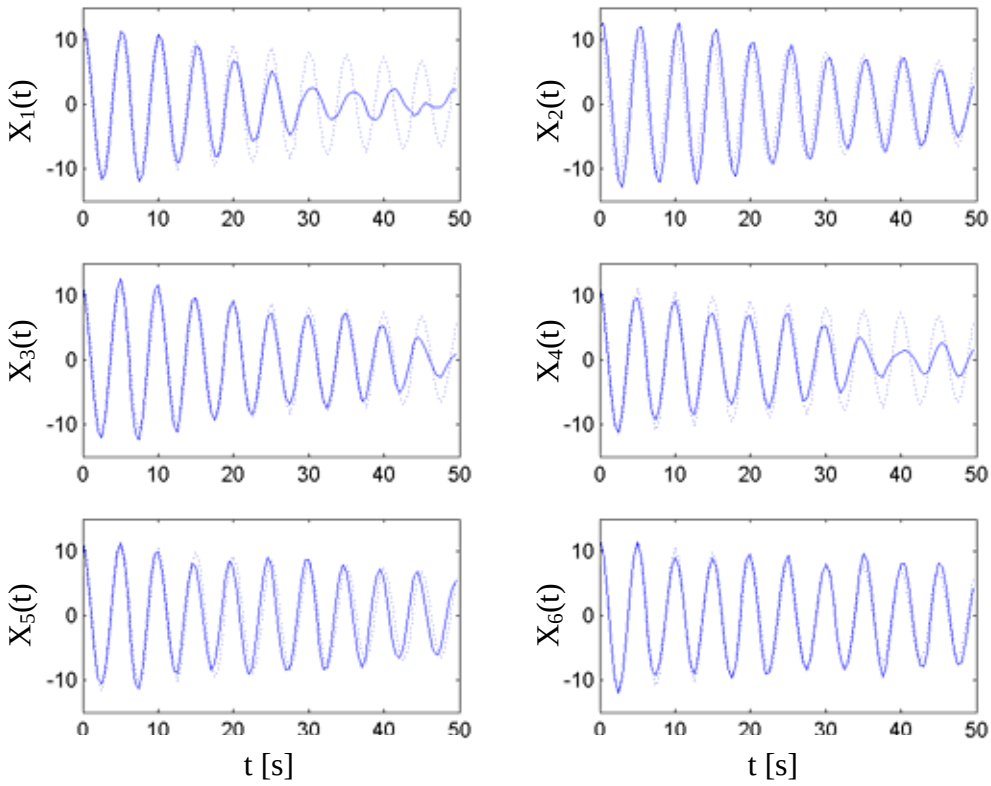

FIGURE 2.8. Captured random decrement segments for Run III, X_o=11.9. Dotted line indicates theoretical free vibration decay at this amplitude level

2.2.2.2.5 Influence of Nonstationarity on Random Decrement Signatures

As the requirements of lengthy stationary data sets had often precluded the use of traditional spectral and autocorrelation techniques, the RDT was proposed as a way to circumvent this problem by permitting analysis on shorter lengths of stationary data. Though it is often assumed that wind-induced response of structures is stationary, examination of full-scale data has often demonstrated otherwise. Even so, there has been little treatment of the ability of RDT to perform under nonstationary conditions (Jeary,

1992). To illustrate the implications of stationarity on the RDT, two signals were studied using the same oscillator defined in Section 2.2.2.2. In signal 1, the random input is comprised of two, 4-hour blocks of standard Gaussian white noise (termed segments 1 & 3) separated by a 4-hour block of zero mean, white noise drawn from a uniform distribution (termed segment 2). The definitions of stationarity require that all statistical properties be invariant with time, strictly implying that all the data be drawn from the same distribution. A sudden pocket of nonstationarity is introduced to violate this assumption.

Figure 2.9 illustrates the implications of the violation of stationarity in signal 1 by examining the bootstrapped variance for several triggering thresholds. Note that in each of these cases, the same number of segments ($N_r=200$) was averaged. Although the variance is theoretically independent of triggering level, as evidenced by Equation 2.17, this figure displays an increase in variance with triggering level when compared to the limiting variance function of Equation 2.22. These findings may be rationalized by in light of the histograms of the peaks within each block of data, which were omitted for brevity. Over ninety percent of the high amplitude peaks are located in segments 1 & 3. As a result, when using these higher amplitude trigger conditions, shown in blue, there may be only a few isolated samples drawn from segment 2. The Gaussian samples by themselves are incapable of averaging out the variance introduced by the isolated samples captured from segment 2, thus leading to corrupted results for these higher trigger levels. Conversely, low amplitude trigger conditions shown in shades of red have a sufficient number of samples drawn from segment 2 to cancel out the variance from the uniformly distributed response component. The presence of such localized pockets of

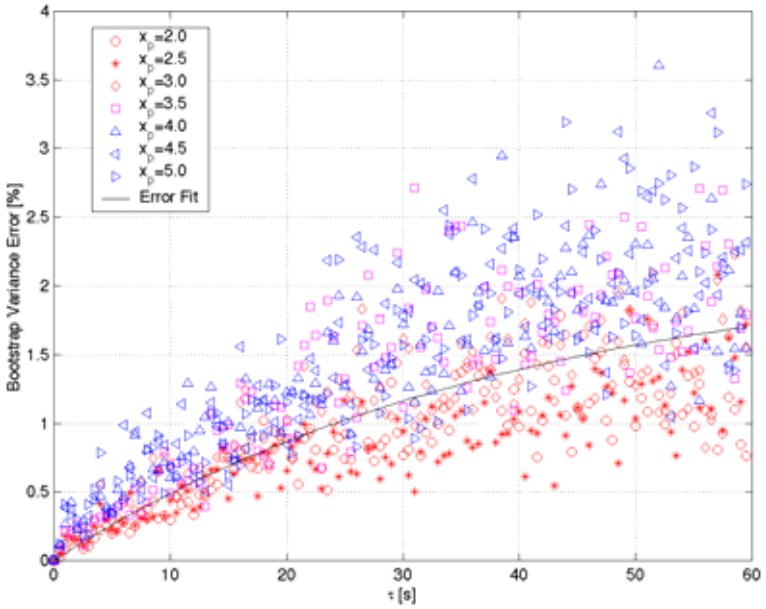

FIGURE 2.9. Bootstrap variance estimates for non-stationary signal 1 with error expression in Equation 2.22 shown by solid line (N_r=200)

nonstationarity appears to be the culprit Jeary (1992) hoped to negate by establishing the conditions for feature removal bulleted in the previous section. Through the use of such pre-treating in the time history, these local nonstationary features can be removed to improve the overall reliability of the RDS.

A second nonstationary signal was investigated by enveloping the excitation by a sinusoidal function. As opposed to the previous instance, this case simulates a global phenomenon, with a sinusoid of 2-hour period modulating the Gaussian, white noise excitation. As shown by Figure 2.10, in this case the dependence upon triggering amplitude is of course not present, as all levels of triggering reflect the same poor performance when compared to variance estimate in Equation 2.22, although higher trigger levels seem to scatter toward higher variances. This reflects the power of global

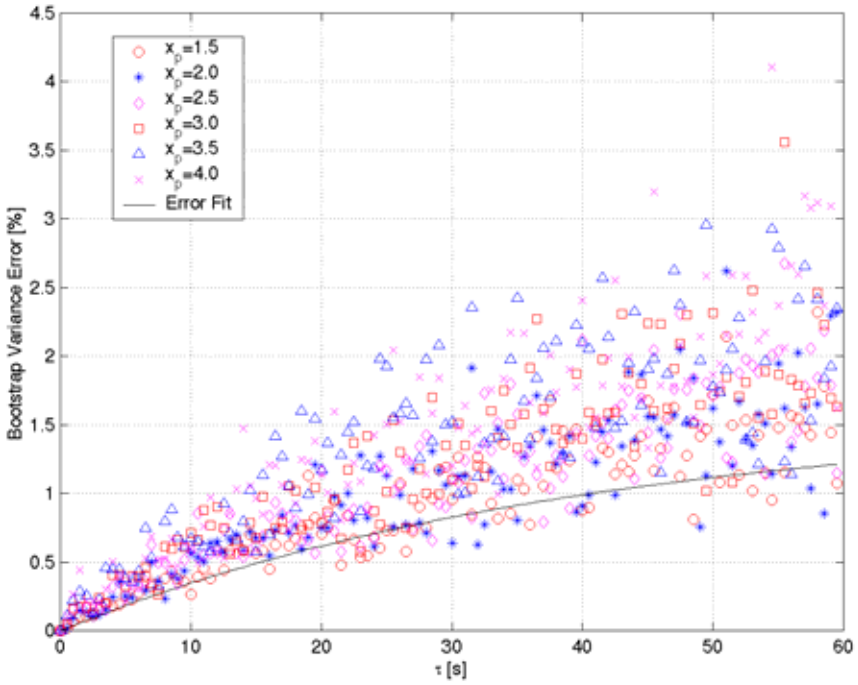

FIGURE 2.10. Bootstrap variance estimates for nonstationary signal 2

nonstationary features in the data, as the variance of estimates will be far greater than idealized theory would predict.

2.3 Uncertainty in System Identification and Damping Estimation

System identification by any approach represents the process through which optimal values of system parameters are obtained, though this is complicated without the benefit of measured input. In this process, the variability in the PSD and RDS is of concern. While some understanding of uncertainty is available, through Equations 2.10 and 2.17, specific measures of variance in frequency or damping estimates are in general not known. As the exercises in Section 2.2.2.2.4 and Figure 2.5 demonstrate, damping values

can fluctuate, even when the variance is supposedly minimized. Seybert (1981) recognized this concern and derived approximate expressions for the bias and random errors in the damping estimation using the half-power bandwidth of power spectra. Even though these depend on the very quantity being estimated, they have proven insightful and indicate that the normalized bias in the damping estimate is approximately 1.5 times the normalized bias of the power spectrum. This derivation was made realizing that the bias of the PSD itself in the vicinity of the HPBW points will directly affect the estimates of damping. Seybert (1981) also derived an approximate expression for the normalized variance of the damping estimate, again confirming that the damping variance is proportional to the number of raw spectra considered. However, the expression has limited utility in this case, as the measure of the coherence function between the input and output processes at the HPBW points is required. Another option is empirical expressions for the coefficient of variation, such as those determined by Montpellier (1996). Though useful, these expressions are again approximate and idealized, an issue that will be addressed in the following section.

To explore the variability in system identification by SA and RDT, frequency and damping are estimated from the response of ambiently-excited SDOF oscillators sampled at 10 Hz. In accordance with common practice, the minimum required spectral resolution is determined by limiting the normalized spectral bias error in Equation 2.8 to less than -2% and determining the required number of FFT points (N) conservatively to the nearest power of two. To minimize normalized variance errors to 10%, enough data is generated to yield 100 sufficiently resolved raw spectra. These time histories are generated by exciting a SDOF system with a band limited Gaussian, zero mean white noise process.

This random input was simulated from a target band-limited spectrum, with unit magnitude from 0 Hz to a specified cutoff frequency f_c (Li & Kareem, 1993a). The resulting simulation parameters are documented in Table 2.6 for three cases: Cases A, B and C.

Though often not obtainable in practice, significant amounts of stationary data are considered for illustrative purposes. The first case represents a lightly damped 1 Hz oscillator. The latter two cases involve more narrowband systems, requiring significantly more data to achieve the same spectral bias and variance errors. In Case C, though the same amount of data is generated, the length of segments captured in the RDT is shortened from T_{RDS} = 60 s to T_{RDS} = 30 s in order to increase the number of segments being averaged, with assumedly minimal influence due to correlation. To demonstrate the worst-case performance of the RDT, the local extrema trigger condition is enforced, selecting a value of 3% the median peak value to generate most possible segments. Individual time histories generated by this approach were retained for the subsequent resampling analysis presented in Sections 2.4.1 and 2.4.2.

Armed with this data, the normalized bias is assumed to be less than -2% and the normalized variance to be 10%, but the exact error in the frequency and damping identified from the PSD is still not known. To illustrate the variability possible, the systems in Table 2.6 are each simulated 50 times. In each case, the same amount of data is used so that the normalized bias and random errors on paper are the same, and the system is then identified by both the spectral analysis and Random Decrement Technique discussed previously. Further, since the variance in the RDS increases with each cycle of

oscillation, system identification is applied over only the first two cycles of the RDS. Since the logarithmic decrement was shown in Figure 2.5 to manifest variability in this range, a least squares fit of Equation 2.14 is utilized for damping identification.

TABLE 2.6

PROPERTIES OF SIMULATED CASES

CASE	f_c (Hz)	f_n (Hz)	ξ	N	N_s	N_r[a]	Length of Data (Hr)
A	5	1.0	0.01	4096	100	~600-700	11.4
B	1	0.2	0.01	16384	100	~700-800	45.5
C	1	0.2	0.01	16384	100	~1100-1200	45.5

[a]Actual N_r will very in each run dependent upon the number of peaks forming non-overlapping segments.

Even in the presence of a favorable amount of data, the variability inherent in this random process can cause considerable scatter in the identified parameters, as shown by Table 2.7, summarizing the statistics of the simulations, including the mean, standard deviation, and coefficient of variation. From Table 2.7 and Figure 2.11, which graphically displays the data for Case B, it is not surprising to confirm that the frequency is relatively simple to identify with accuracy. The damping, on the other hand, is much more difficult. As expected, SA produces a biased overestimation of the damping present, as the smoothing of the spectrum results in an underestimation of the spectral peak and thus an overestimation of the damping. The fact that the SA bias is consistent should not be surprising since the goal was to maintain the same level of bias. Though the normalized bias in the power spectrum is less than –2%, the normalized bias in the

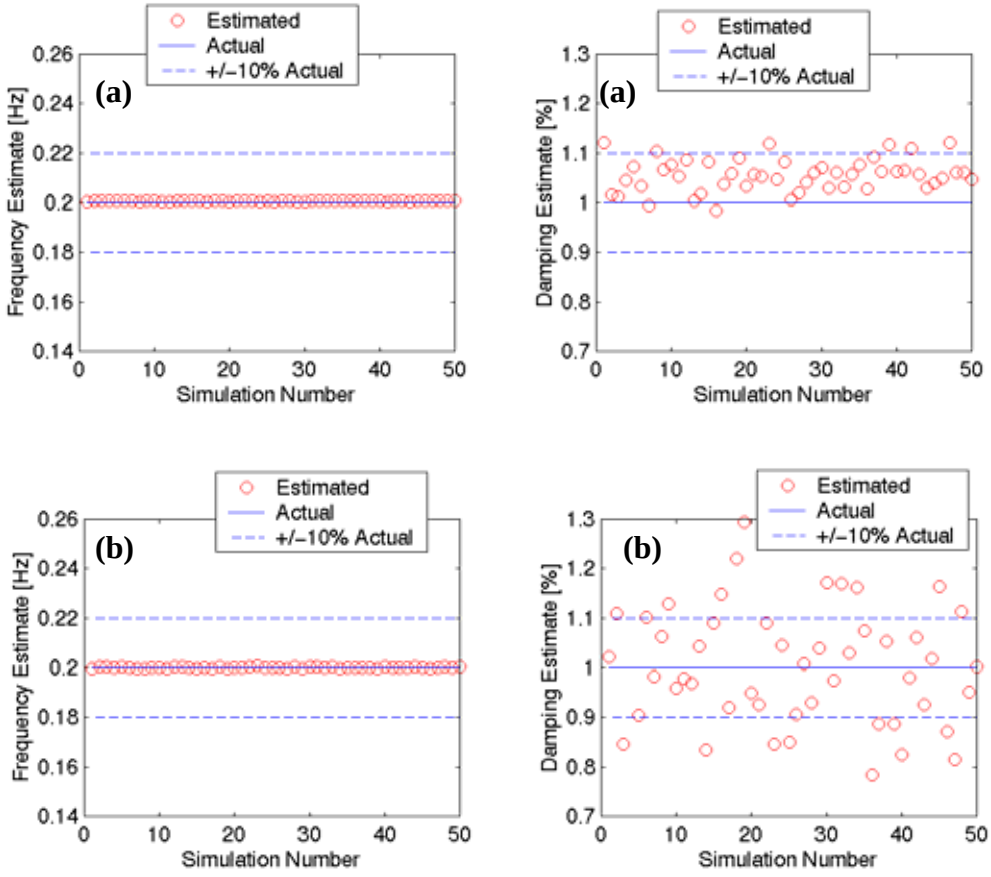

FIGURE 2.11. Identified dynamic properties of simulated data: identification of Case B by (a) spectral analysis and (b) Random Decrement Technique

TABLE 2.7

STATISTICS OF MONTE CARLO SIMULATIONS

	$\mu[f_n]$ (Hz)	$\sigma[f_n]$ (Hz)	bias $[f_n]$ (Hz)	CoV $[f_n]$	$\mu[\xi]$	$\sigma[\xi]$	bias$[\xi]$	CoV$[\xi]$
				CASE A				
SA	1.0023	0.0012	0.0023	0.12%	0.01041	0.00029	0.00041	2.76%
RDT	1.0003	0.0014	0.0003	0.14%	0.00921	0.00124	-0.00079	13.50%
				CASE B				
SA	0.2007	0.00026	0.0007	0.13%	0.01056	0.00033	0.00056	3.12%
RDT	0.2001	0.000256	0.0001	0.13%	0.00995	0.00126	-0.00005	12.67%
				CASE C				
SA	0.2006	0.00027	0.00060	0.13%	0.01052	0.00032	0.00052	3.01%
RDT	0.2000	0.00025	-0.00002	0.12%	0.01011	0.00109	0.00011	10.79%

damping estimated from it is several times that amount. Recall that Seybert's (1981) expression underestimated this over prediction as only 1.5 times the normalized PSD bias. As expected, the bias does become a bigger problem in the narrowband system. For Case C, this narrowband system was resimulated, with the same amount of data as in Case B. As a result, the marginal changes in the statistics associated with the SA are only the result of the new random excitation generated in simulation. The variance is largely unchanged with standard error changing only by 4% between the two cases. The CoV for the SA in all cases is between 2.75 and 3.15%. It should be relatively constant for all cases as the length of data was selected to maintain the same bias and random errors in the PSD. Note that the variance estimates in Table 2.7 are still about one-half the estimates provided in Montpellier (1996).

Though both approaches have near identical performance with respect to frequency identification, there is, unfortunately, a considerable amount of scatter in the RDT damping result, leading to a CoV that is an order of magnitude greater than SA result. This CoV is nearly half that observed by Montpellier (1996), as expected due to the large amount of data considered. The level of bias in the RDT result is more significant in the relatively broader band system, perhaps due to the limited number of segments being averaged. However, when large amounts of segments are available, the estimate of damping is nearly unbiased, as expected. Note that since the least squares fit is used, the biased observed in LogDec damping estimates in Section 2.2.2.2.4 is negated. This is advantageous since narrowband systems are increasingly difficult to identify by spectral analysis. The larger number of RDS averaged in Case C helps to further reduce the deviation of damping estimates by RDT. Increasing N_r by a few hundred samples has

led to a nearly a 15% decrease in the standard deviation and as shown in Section 2.2.2.2.4, the negative impacts of correlation are often offset by this increase in the number of averages.

It is important to note that due to the random nature of the process identical amounts of data subjected to the same SA can produce an estimate of damping which has no error or as much as 10% error. Though 10% error may be reasonable, this situation also illustrates a very favorable and perhaps unrealistic amount of stationary data. Under these ideal conditions, the damping estimated by independent simulations has inherent variability, which is no doubt enhanced under less ideal conditions. On the other hand, the RDT identification of the system from any one of these simulations can produce estimates of damping that are near exact or in error by up to 20-30%. Though Table 2.7 illustrates that if one has the luxury of repeating an experiment 50 times under identical conditions, acceptable results are obtainable in the average, it is beneficial to be able to assess the accuracy of identified parameters from a given time history. The accuracy of any identification by one of these two approaches is contingent upon the level of randomness in the measured data and the degree to which it has been eliminated in the averaging process.

2.4 Variance of Damping Estimates via Bootstrapping

Typically, without the advantage of repeated experiments or measured input, the dynamic analyst is forced to make the best of only limited observations to perform system identification and determine the reliability of that estimate. Non-parametric resampling

schemes such as the bootstrapping technique introduced in this chapter and discussed further in the Appendix can be useful in such cases. These approaches amount to treating the observed samples as if they are representative of the larger population, then resampling this limited data to approximate variance. Using this computationally simple scheme, the analyst can take the time history that would normally result in a single estimate of damping with no variance measure and effectively "extend" that data through resampling in order to approximate the variance of that estimate. Such approaches further allow the assignment of confidence intervals without necessitating knowledge of the parameter distribution. This practical tool is introduced here to quantify random errors of damping estimates garnered from these two common system identification approaches.

It should be noted that other system identification techniques have also considered the issue of statistical reliability of the identification process. For example, Autoregressive Moving Average (ARMA) schemes (e.g. Spanos & Zeldin, 1996; Li & Kareem, 1993b) or simplified Autoregressive (AR) models utilizing the Maximum Entropy Method, e.g. Cao et al. (1997) implicitly provide performance measures in terms of prediction errors, which indirectly reflect the quality of the AR or ARMA identification. More recently, a Bayesian spectral density approach was introduced by Katafygiotis & Yuen (2001) to update the PDF of modal parameters for ambiently-excited data. The resulting PDF obtained in the minimization scheme was found to be well approximated by a Gaussian distribution, whose mean is indicative of the optimal parameter estimates and covariance yields a direct measure of uncertainty. Approaches like these provide a variance estimate of the damping parameter as a byproduct of the minimization operation or "goodness of fit" to an assumed model. The associated errors

then indicate how well the estimated damping parameter value fits the available data, providing one form of reliability measure.

On the other hand, the intent of this work is not to propose an altogether new SI technique with error estimates to quantify a "goodness of fit." Rather, this study provides a practical computational tool to generate the statistical reliability measures for frequency and damping parameters estimated using traditional approaches like SA and RDT, for which no statistical confidence measures are implicitly provided. It is the inherent randomness in the data that influences the quality of the PSD and RDS and thereby the damping estimates garnered from them. As these schemes must average out the effects of randomness, their performance becomes dependent upon sufficient amounts of available data. The intent of this work is to mimic this random characteristic to provide a supplementary tool to gauge the potential variance in the resulting damping estimate from a given spectral or random decrement analysis.

For each case in Table 2.6, the bootstrapping scheme outlined in the Appendix is applied to selected time histories simulated by Monte Carlo in Section 2.3. To illustrate the information that can be gained, particularly when limited data is available, increments of the total time history are analyzed so that the influence of the number of raw spectra (N_s) and the number of segments in RDT (N_r) can be determined. As the frequency is estimated with near certainty every time, it shall not be discussed here for brevity. The tables that follow contain the bootstrap estimate of the parameter, in this case damping, ξ_{boot}, defined as the mean of the parameter identified from B=1000 bootstrap replicates (see Appendix Equation A.2). The traditional estimate of the parameter, without any

resampling, is commonly termed the plug-in estimate, ξ_{plugin}. The standard deviation of the bootstrap replicates σ_B, as defined by Equation A.1, and the CoV, defined as the ratio of the standard error to the bootstrap mean in Equation A.2, are also provided. The bootstrap bias in the estimate is then defined as the difference, $\xi_{boot} - \xi_{plugin}$. This measure is important, as a small bootstrap bias, relative to the standard error, confirms that the bootstrap is a good estimate of the parameter, e.g. $bias/\sigma < 0.25$. As this measure becomes larger, the bootstrap estimates may no longer be accurate and require bias correction, which is discussed further in Efron & Tibshirani (1993). Additionally, by virtue of the bootstrapping scheme, histograms depicting the distribution of the damping estimate from a given time history can be obtained. These are useful tools for identifying the underlying distribution of damping estimates and its associated characteristics. An example of such a histogram for the damping estimates from a single time history (Case B) is given in Figure 2.12. While viewing these results, please be reminded that the simulated system had a critical damping ratio of 0.01.

Additionally, confidence intervals are defined for the damping estimate. By traditional analysis, only a single estimate of damping is available from each simulated time history. However, through the bootstrapping scheme, this estimate is enhanced by a family of associated estimates, which can give valuable insight into the reliability of a given damping estimate. In the most elementary formulation, a level of confidence can be selected, and then the replicates that correspond to this level can be identified from the resampled distribution (Efron & Tibshirani, 1993). By virtue of the non-parametric nature of this approach, there is no need to make any assumptions about the Normality of the

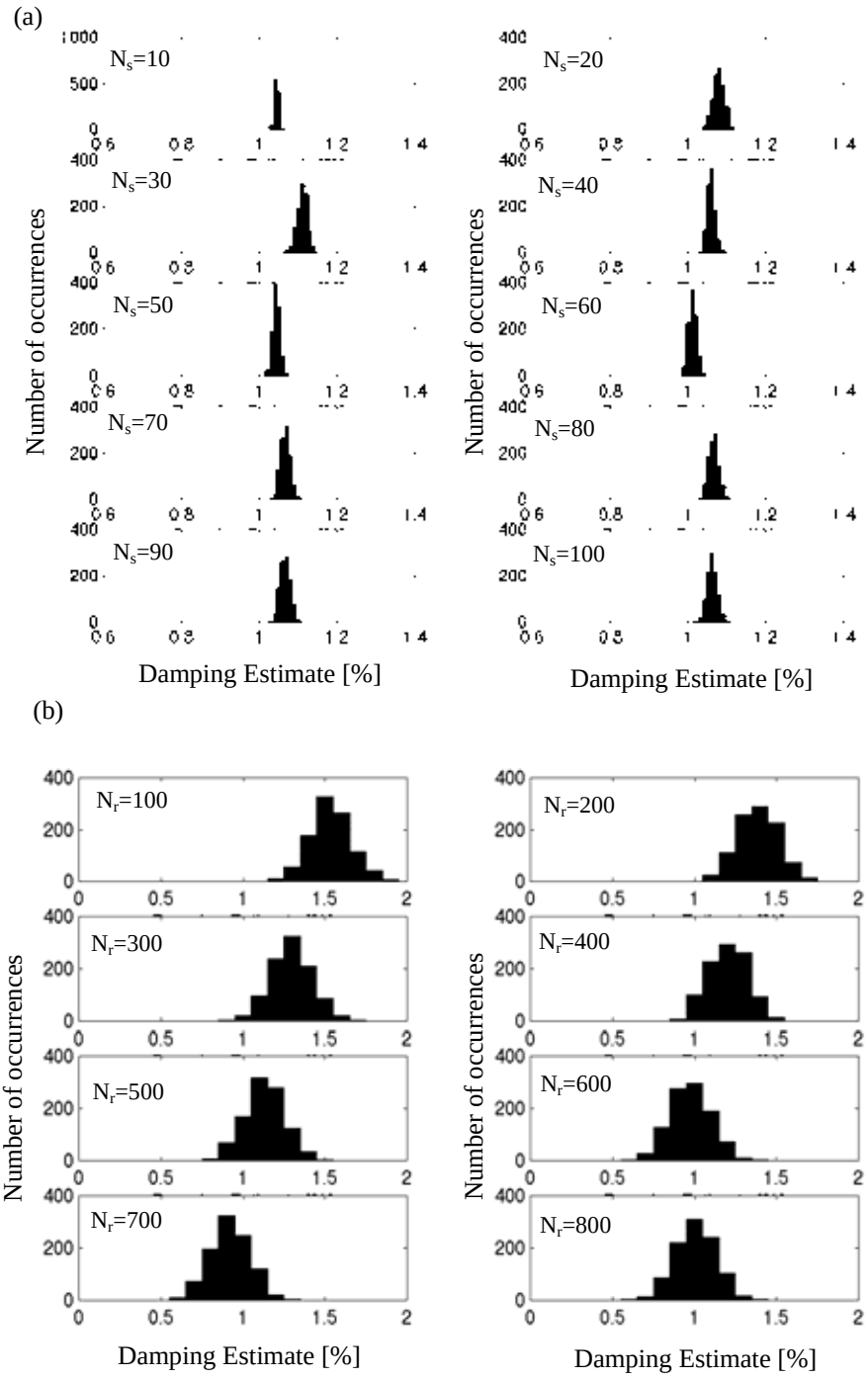

FIGURE 2.12. Histogram of bootstrap simulations on (a) PSD and (b) RDS for Case B

damping estimates. This is especially useful in cases where the PSD or RDS is generated from a limited number of samples. However, when the CoV of the bootstrapped replicates is small, e.g. less than 20% and the bootstrap biases are negligible, a Gaussian PSD may be assumed to describe the distribution of the bootstrapped damping parameter. The 95% confidence bands are then approximated to lie within 2 standard deviations of the bootstrap mean (Efron & Tibshirani, 1993). These bands are provided in the last column of the following tables for comparison.

2.4.1 Discussion: Bootstrapping Damping Estimates for Spectral Analysis

As shown in Table 2.8, the bootstrap investigations conducted on a single record from the Monte Carlo simulations in Section 2.3 predict significantly smaller values of standard errors than anticipated for spectral analysis. However, the relative changes are consistent with Monte Carlo predictions, when examining the full data set (N_s=100), shaded in gray. Case A has smallest variance, thus one would expect the Case A bootstraps to reflect that smaller variance in comparison to Cases B and C. Likewise, Case C produced a slightly smaller value of standard error than Case B, a trend reflected in the bootstrap errors. From the sample histogram in Figure 2.12, it is evident that in cases of limited data there are shifts in the damping estimate distribution about various mean values. It is only for $N_s>50$ that the behavior stabilizes and the damping estimates distribute about a relatively constant mean, indicating that the variance is sufficiently minimal.

It is interesting to note that, even with modest amounts of data (e.g. N_s=10), a relatively good estimate of the damping is obtainable, while the addition of further

TABLE 2.8

STATISTICS OF BOOTSTRAP REPLICATIONS OF CRITICAL DAMPING RATIO: ESTIMATES BY SPECTRAL ANALYSIS

CASE A							
N_s	ξ_{boot}	ξ_{plugin}	bias[ξ]	σ[ξ]	CoV	95% bootstrap	95% normal
10	0.010299	0.01030	-0.000011	0.000084	0.82%	(0.01016, 0.01044)	(0.01013, 0.01047)
20	0.010478	0.010481	-0.000029	0.000082	0.78%	(0.01034, 0.01060)	(0.01031, 0.01064)
30	0.010571	0.010564	0.000064	0.000081	0.77%	(0.01044, 0.01071)	(0.01041, 0.01073)
40	0.010167	0.010165	0.000016	0.000079	0.78%	(0.01004, 0.01030)	(0.01001, 0.01032)
50	0.010099	0.010096	0.000032	0.000078	0.77%	(0.00997, 0.01023)	(0.00994, 0.01025)
60	0.009940	0.009940	0.000041	0.000080	0.80%	(0.00981, 0.01007)	(0.00978, 0.01010)
70	0.010127	0.010131	-0.000037	0.000082	0.81%	(0.00999, 0.01025)	(0.00996, 0.01029)
80	0.010075	0.010079	-0.000044	0.000079	0.78%	(0.00995, 0.01020)	(0.00993, 0.01023)
90	0.010043	0.010041	0.000019	0.000076	0.76%	(0.00991, 0.01017)	(0.00989, 0.01019)
100	0.010029	0.010027	0.000013	0.000083	0.83%	(0.00989, 0.01016)	(0.00986, 0.01019)
CASE B							
N_s	ξ_{boot}	ξ_{plugin}	bias[ξ]	σ[ξ]	CoV	95% bootstrap	95% normal
10	0.01044	0.01044	-0.000001	0.000049	0.47%	(0.01036, 0.01052)	(0.01034, 0.01054)
20	0.01077	0.01080	-0.000031	0.000143	1.33%	(0.01053, 0.01101)	(0.01049, 0.01106)
30	0.01110	0.01110	-0.000005	0.000130	1.17%	(0.01088, 0.01130)	(0.01084, 0.01136)
40	0.01058	0.01061	-0.000033	0.000105	0.99%	(0.01041, 0.01077)	(0.01037, 0.01079)
50	0.01043	0.01044	-0.000015	0.000095	0.91%	(0.01027, 0.01059)	(0.01024, 0.01062)
60	0.01012	0.01012	0.000002	0.000104	1.03%	(0.00996, 0.01029)	(0.00991, 0.01033)
70	0.01067	0.01075	-0.000081	0.000121	1.13%	(0.01048, 0.01088)	(0.01043, 0.01091)
80	0.01064	0.01065	-0.000009	0.000134	1.26%	(0.01043, 0.01086)	(0.01038, 0.01091)
90	0.01067	0.01069	-0.000024	0.000130	1.22%	(0.01043, 0.01089)	(0.01041, 0.01093)
100	0.01061	0.01065	-0.000045	0.000132	1.24%	(0.01039, 0.01083)	(0.01035, 0.01087)

TABLE 2.8 (CON'T)

CASE C							
N_s	ξ_{boot}	ξ_{plugin}	bias[ξ]	$\sigma[\xi]$	CoV	95% bootstrap	95% normal
10	0.010637	0.010637	-0.000001	0.000065	0.61%	(0.01053, 0.01075)	(0.01051, 0.01077)
20	0.010104	0.010104	0.000000	0.000117	1.16%	(0.00992, 0.01030)	(0.00987, 0.01034)
30	0.010187	0.010193	-0.000007	0.000113	1.11%	(0.01001, 0.01038)	(0.00996, 0.01041)
40	0.010453	0.010464	-0.000010	0.000107	1.02%	(0.01026, 0.01062)	(0.01024, 0.01067)
50	0.010516	0.010522	-0.000006	0.000103	0.98%	(0.01032, 0.01068)	(0.01031, 0.01072)
60	0.010346	0.010348	-0.000002	0.000122	1.18%	(0.01015, 0.01052)	(0.01010, 0.01059)
70	0.010089	0.010094	-0.000005	0.000109	1.08%	(0.00991, 0.01026)	(0.00987, 0.01031)
80	0.009837	0.009840	-0.000003	0.000123	1.25%	(0.00963, 0.01005)	(0.00959, 0.01008)
90	0.009922	0.009917	0.000005	0.000121	1.22%	(0.00973, 0.01012)	(0.00968, 0.01016)
100	0.009993	0.009991	0.000002	0.000116	1.16%	(0.00980, 0.01020)	(0.00976, 0.01022)

recorded data may lead to poorer estimates. This may seem counterintuitive, as the variance of the PSD has been shown to reduce with the number of raw spectra being averaged. However, the inherent randomness of the process must be considered. The first few hours of data may not have significant randomness in comparison to later components of the overall time history, luckily leading to a reasonable estimate of damping. Likewise the variance is also dependent on the magnitude of the PSD itself, which also fluctuates in each case considered. These random fluctuations can and should be expected when limited data is used, as the variance is high (Vandermeulen et al., 2000). It is only in the limit that a more stable and reliable PSD results – one without

marked fluctuations as more data is considered in the average. As evidenced by Figure 2.12 and Table 2.8, it would indicate that this is achieved for $N_s>60$ for the narrowband system, but achieved much sooner, $N_s>40$ for Case A.

As evident from Figure 2.11, there is a discernable amount of bias in the spectral estimate of the narrowband system, shifting the mean critical damping ratios to approximately 0.0105. The inherent bias in the estimate cannot be overcome by the bootstrapping approach, as also noted in Vandermeulen et al. (2000). Spectra with an outright bias cannot be enhanced by this approach, as they are not truly representative of the system to be identified, but rather a biased representation of that system. As the bootstrap cannot repair sampled data, but can merely make inferences about its various statistics, the confidence intervals and all relevant statistical distributions will be clustered about this biased mean, as illustrated by the histograms shown in Figure 2.12. In this case, even placing 95% confidence intervals on the estimate will not capture the true damping value. Note that Seybert's (1981) derivation can provide a normalized bias estimate for ξ. Knowing that the SA consistently overestimates damping, the rough normalized bias formula may be offered as a correction to the estimates and used to refine the confidence bands.

2.4.2 Discussion: Bootstrapping Damping Estimates for Random Decrement Technique

As shown in Figure 2.11, the distribution of RDT damping estimates on the same data manifest considerably more scatter than SA estimates, consistent with the findings of the Monte Carlo simulation. The sensitivity of RDT damping estimates was fully discussed

in 2.2.2.2.4. It should be noted that an enhancement in performance may be achieved using the more relaxed positive point trigger or by using the averaging of damping estimates of adjacent amplitude trigger levels as shown in Table 2.3 to mitigate the influence of outlier segments. Once again, the distributions in Figure 2.12 shift as more samples are considered. As shown by Table 2.9, as N_r increases, their behavior tends to stabilize about a consistent mean value, similar to what was found in SA approach. Even in this stable range, there is still some fluctuation in the estimate, consistent with the findings in Section 2.2.2.2.4 requiring the aforementioned local averaging over adjacent triggers.

However, unlike SA results, the behavior of RDT estimate using local extrema trigger clearly indicates that limited amounts of data offer little hope of an accurate result, as many eligible triggers are eliminated by this strict condition. In such cases, the positive point trigger with $T_{RDS} = 0$ should be used, as advocated in Section 2.2.2.2.4. Rather, the results steadily improve with the number of samples being considered: for $N_r>500$, the damping estimates are consistently within 10% of the actual value. The level of variance in the RDT estimate, as shown by Monte Carlo simulation, is markedly greater than the SA, due again to the sensitivity of trigger amplitude. It can be implied that the SA approach is more of an averaged approach that does not allow referencing to a trigger level. Likewise, by selecting a local range of trigger amplitudes in the RDT, as opposed to just the median peak value used here, the average damping value should be comparable to those determined by SA, while still preserving the ability to amplitude reference a damping estimate.

TABLE 2.9

STATISTICS OF BOOTSTRAP REPLICATIONS OF CRITICAL DAMPING RATIO: ESTIMATES BY RDT

CASE A							
N_r	ξ_{boot}	ξ_{plugin}	bias[ξ]	$\sigma[\xi]$	CoV	95% bootstrap	95% normal
100	0.010636	0.010586	0.000051	0.001105	10.39%	(0.00876, 0.01244)	(0.00843, 0.01285)
200	0.012293	0.012320	-0.000023	0.001144	9.31%	(0.01041, 0.01417)	(0.01001, 0.01458)
300	0.012927	0.012932	-0.000006	0.001207	9.34%	(0.01088, 0.01495)	(0.01051, 0.01534)
400	0.011308	0.011340	-0.000032	0.001225	10.83%	(0.00934, 0.01339)	(0.00886, 0.01376)
500	0.011149	0.011163	-0.000013	0.001264	11.34%	(0.00901, 0.01323)	(0.00862, 0.01368)
600	0.010915	0.010971	-0.000056	0.001237	11.33%	(0.00881, 0.01295)	(0.00844, 0.01339)
CASE B							
N_r	ξ_{boot}	ξ_{plugin}	bias[ξ]	$\sigma[\xi]$	CoV	95% bootstrap	95% normal
100	0.01533	0.01532	0.000004	0.001239	8.08%	(0.01334, 0.01747)	(0.01285, 0.01781)
200	0.01386	0.01381	0.000054	0.001223	8.82%	(0.01181, 0.01591)	(0.01142, 0.01631)
300	0.01296	0.01296	0.000002	0.001259	9.72%	(0.01089, 0.01500)	(0.01044, 0.01548)
400	0.01203	0.01188	0.000159	0.001174	9.76%	(0.01010, 0.01397)	(0.00969, 0.01438)
500	0.01132	0.01126	0.000056	0.001231	10.88%	(0.00921, 0.01333)	(0.00886, 0.01378)
600	0.00974	0.00976	-0.000013	0.001243	12.76%	(0.00772, 0.01093)	(0.00726, 0.01223)
700	0.00917	0.00917	0.000005	0.001220	13.30%	(0.00717, 0.01203)	(0.00673, 0.01161)
800	0.01005	0.01000	0.000048	0.001218	12.13%	(0.00808, 0.01201)	(0.00761, 0.01248)

TABLE 2.9 (CON'T)

CASE C							
N_r	ξ_{boot}	ξ_{plugin}	bias[ξ]	σ[ξ]	CoV	95% bootstrap	95% normal
100	0.004597	0.004578	0.000019	0.001132	24.61%	(0.00281, 0.00644)	(0.00233, 0.00686)
200	0.006960	0.007009	-0.000049	0.001151	16.53%	(0.00510, 0.00889)	(0.00466, 0.00926)
300	0.008277	0.008304	-0.000027	0.001175	14.20%	(0.00635, 0.01014)	(0.00593, 0.01063)
400	0.008907	0.008922	-0.000015	0.001118	12.55%	(0.00709, 0.01070)	(0.00667, 0.01114)
500	0.008850	0.008850	0.000000	0.001128	12.74%	(0.00701, 0.01067)	(0.00659, 0.01110)
600	0.009955	0.009860	0.000095	0.001152	11.57%	(0.00812, 0.01196)	(0.00765, 0.01226)
700	0.010079	0.010108	-0.000029	0.001189	11.80%	(0.00810, 0.01204)	(0.00770, 0.01246)
800	0.009909	0.009971	-0.000062	0.001204	12.15%	(0.00808, 0.01198)	(0.00750, 0.01232)
900	0.010256	0.010229	0.000027	0.001162	11.33%	(0.00834, 0.01219)	(0.00793, 0.01258)

This large standard deviation is accurately represented by the bootstrap analysis, in part due to the fact that the RDT is an unbiased estimator. This was not possible in the biased SA where the predicted variance was much less than the observed Monte Carlo result. As the RDT tends to stabilize after a significant number of averages, the changes in standard deviation are quite small when additional samples are added. Between Cases A and B, the Monte Carlo standard deviation changes only marginally, by about 2%, explaining why the bootstrapped estimates for these two cases show only slight difference. In the same way, the standard deviation takes on consistently smaller values in Case C than in Case B, reflecting the reduction in variance due to the inclusion of additional segments in the average. Unlike the biased SA approach, the broad confidence intervals predicted by bootstrapping RDT results will encase the predicted result at

minimum for $N_r>400$. It is important to emphasize that traditional RDT damping estimates lack any type of interval estimate. Thus such tools can offer insight where previously there was none.

Interestingly, a cursory examination of the ratio of bias to standard deviation for both RDT and SA data confirms that SA generally produces relatively large biases in the bootstrap data, whose ratios to the standard error exceed 0.25. On the other hand, RDT produces very small biases in the bootstrap analysis. Large biases often indicate that the bootstrap analysis of the data may not be accurate, as it was shown that the bootstrap approach could not capture the variance predicted by Monte Carlo for SA. Bias corrected data may be resampled, but is should be noted that this is risky practice and is thus not advocated in this study as it often leads to an increase in standard error. More details may be found in Efron & Tibshirani (1993).

2.5 The Challenges of Nonlinearity and Nonstationarity

Spectral analysis is marred by the unavoidable presence of nonstationarity concerns that are inherent in long records. As a result, curve fitting has been advocated to smooth spectral estimates garnered from shorter but assuredly stationary blocks of data. For example, Breukelman et al. (1993), Montpellier et al. (1998), and Jones & Spartz (1990) fit the spectral estimates to a transfer function of a SDOF system by employing a maximum likelihood estimator or in the latter case, a least squares approach. By selecting a sample length that is long enough to ensure sufficient frequency resolution, while avoiding nonstationarity problems, and ensemble averaging records obtained under

similar conditions to reduce the variance of spectral estimates, smooth spectra can be obtained for linear systems. However, the characteristic features of nonlinear systems that have transfer functions that depart from linear behavior and the response of systems to nonlinear loading may be obscured in such a curve fitting approach. Though this spectral representation can provide an "averaged" sense of the structural properties, the inability to track specific features and properties of a system in time limits the information which can be gained from the data. The transform's inability to capture any local features of the signal results form the fact that it decomposes the signal into a linear combination of infinite trigonometric functions, which are incapable of recognizing time-varying system characteristics.

These nonlinearities in either the loading or structural system induce an amplitude-dependence in the frequency and damping parameters, which further complicates estimation. In particular, the level of equivalent viscous damping has been shown to increase considerably with the level of response in the structure (e.g. Jeary & Ellis, 1981; Ellis, 1996; Fukuwa et al., 1996). This can be explained when considering again that viscous damping is generally proposed in the equation of motion to represent all of the various damping mechanisms, resulting in a model that is non-ideal over a wide range of amplitudes for non-linear systems. As a result, real structures with nonlinear characteristics, whose damping is identified assuming such a model, will manifest non-linearity or a damping that changes with amplitude (Ellis, 1998), implying that the system is then assumed equivalently linear at a given amplitude level.

Based on such full-scale observations, it was proposed that damping in structures be classified into three distinct plateaus (Jeary, 1986) as illustrated by Figure 2.13. Considering that the boundary damping attributed to the frictional losses between interfaces of materials contributes significantly to the energy dissipation in structures, the relative displacement of these interfaces will dictate the amount of friction losses that occur. The intuitive arguments for this model are as follows: at low levels of motion, most cracks and joints within the structure are not significantly slipping. Once a sufficient number of these interfaces are activated, they will dissipate energy in proportion to their relative displacements, accounting for the linearly increasing portion of Figure 2.13. At the high amplitude plateau, all interfaces have been activated, thus defining the maximum level of damping that should not be exceeded unless damage were to occur within the structure. Note that the slippage of these interfaces can also be assumed to diminish stiffness, thereby explaining the reduction in natural frequency with increasing amplitude

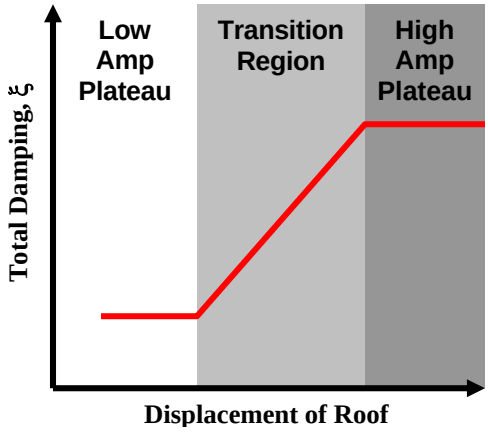

FIGURE 2.13. Amplitude-dependent damping model

observed in full-scale data.

An empirical model for this type of behavior was proposed by Jeary (1986) based upon full-scale data generated using controlled sinusoidal excitations. This model for the total damping is given by

$$\xi = \xi_o + \xi_I \frac{|X_H|}{H} \tag{2.24}$$

for a given mode in the structure. ξ_o is the low amplitude level of damping, ξ_I is the incremental damping in the transition region, H is the height of the structure, and X_H is the displacement at the top of the structure. Specific expressions for each variable can be found in Jeary (1986). Other amplitude-dependent damping expressions were proposed by ESDU (1983), Lagomarsino (1993) and Tamura et al. (1995). In light of this amplitude dependence, any system identification approach should be capable of accounting for these characteristics, as observed levels of damping must be referenced to the amplitude of motion.

As a result, the favorable performance of spectral analysis in comparison to the Random Decrement Technique with local extrema trigger shown in the idealized demonstrations in Section 2.4 are often negated in real-world applications where nonlinearities and nonstationarities are present, as the Random Decrement Technique is capable of detecting amplitude-dependent damping (Jeary, 1992; Tamura & Suganuma, 1996). As shown in Kareem & Gurley (1996) through the use of a nonlinear softening oscillator, the damping associated with the trigger condition amplitude is estimated accurately within the first few cycles of the RDS decay, as they are closest to the

enforcement of the initial conditions. As a result of the nonlinearity, the damping values will begin to deviate in later cycles moving further from the trigger condition. As similarly observed by Tamura & Suganuma (1996), by treating the non-linear system as locally linear at the triggering condition, the RDS in the first cycle are consistent with the free-vibration curve of the linear system for the level of damping and natural frequency associated with the amplitude level specified by the triggering condition. Thus, the use of RDT for these types of systems should restrict amplitude-referenced frequency and damping estimates to the values obtained from the first few cycles of oscillation, where the system is locally linear. Further, when using a selective pre-treatment and processing of the time history introduced in Section 2.2.2.2.4, time histories with certain localized non-stationary features can still be processed by the Random Decrement Technique, as discussed in Jeary (1992).

2.6 Conclusions

This chapter introduced the significance of damping for minimizing wind-induced response and the challenges associated with its estimation from ambient vibration data. Two common approaches for system identification were then presented: the Random Decrement Technique and traditional spectral analysis. The uncertainty associated with the two approaches was investigated via Monte Carlo simulation, and bootstrapping was proposed to provide a practical tool for assessing the uncertainty associated with an estimate of damping by either technique. It was shown that the bootstrap standard deviation of the RDT damping estimate was consistent the variance of the damping estimates determined from repeated simulation of the system by Monte Carlo. On the

other hand, the bootstrapped standard deviation of the damping estimate derived from spectral analysis was considerably less than its Monte Carlo counterpart, attributed to the fact that it was tainted by the bias inherent in the sample population.

The chapter also went into a detailed analysis of the factors contributing to the performance of the Random Decrement Technique. Although other studies had considered the ramifications of violating the white noise assumption or the nonlinearity of the oscillator, none had systematically addressed other issues governing the performance of the technique. This chapter responded to this deficiency by investigating the influence of potential correlation between captured segments, the required number of captured segments to generate a stable signature, the significance of the selected triggering condition, and the influence of nonstationarity. For the positive point trigger, it was found that the increased number of segments averaged in the RDS offsets any negative consequence resulting from allowing more potential correlation. The damping under these conditions appears to be consistently estimated in most cases when the trigger amplitude satisfies the following condition: $3\sigma > X_o > 1\sigma$. Further, when using the local extrema trigger, it was similarly found that the trigger amplitude corresponding to this range performed best, as opposed to low amplitude triggers that afforded more segments for averaging. Regardless, the performance of the RDT stabilizes under any trigger condition as considerably more segments are averaged, implying that when limited amounts of data are available, the restrictiveness of the trigger should be relaxed via the positive point condition. Finally, though the Random Decrement Technique was found to accommodate mild nonlinearity and localized nonstationarity, the prevalence of these features requires a modified analysis framework.

2.7 Moving into the Time-Frequency Domain

As nonlinearity and nonstationarity, more often that not, characterize the processes of interest in Civil engineering, there was a pressing need to develop analysis tools that could accommodate these features. Although the Fourier Transform revolutionized signal processing and its applications to various disciplines perhaps like no other development, its inability to adequately handle nonstationary and nonlinear phenomenon has proven problematic. Even the Random Decrement Technique's ability to provide nonlinear analysis and accommodate nonstationarity to some degree is a limited victory in light of the amount of data required to successfully obtain the decrement signature. The inadequacy of such techniques rooted in stationary assumptions becomes even more apparent when signals with significant nonlinearities or localized frequency characteristics are present. Recognizing the shortcomings of these more traditional approaches, a thrust towards new analysis frameworks such as time-frequency analysis is unfolding, as discussed in Chapter 3.

CHAPTER 3

TRANSITION TO THE TIME-FREQUENCY DOMAIN

3.1 The Departure from Fourier Analysis

While the contributions of the Fourier Transform to signal processing cannot be denied, the fact that actual data is often characterized by localized features obscured by the infinite bases of the Fourier Transform prompted a departure from this classical approach. To demonstrate, consider the waveform in Figure 3.1. The softening of frequency over an isolated time interval is not reflected in the resulting power spectrum. Even if the Fourier spectrum had detected this contribution and represented it as a secondary peak, there would be no indication of the duration of this component within the signal, as all time information is discarded in the transform.

In these cases, it becomes necessary to move to another analysis domain governed by transforms that produce a time-frequency distribution (TFD) of energy. The introduction of these transforms can be traced back to the mid-1940's, based upon the work of Wigner (1939) in quantum mechanics. The applications of these concepts in signal processing is largely credited to the work by Ville (1948) and Gabor (1946) and

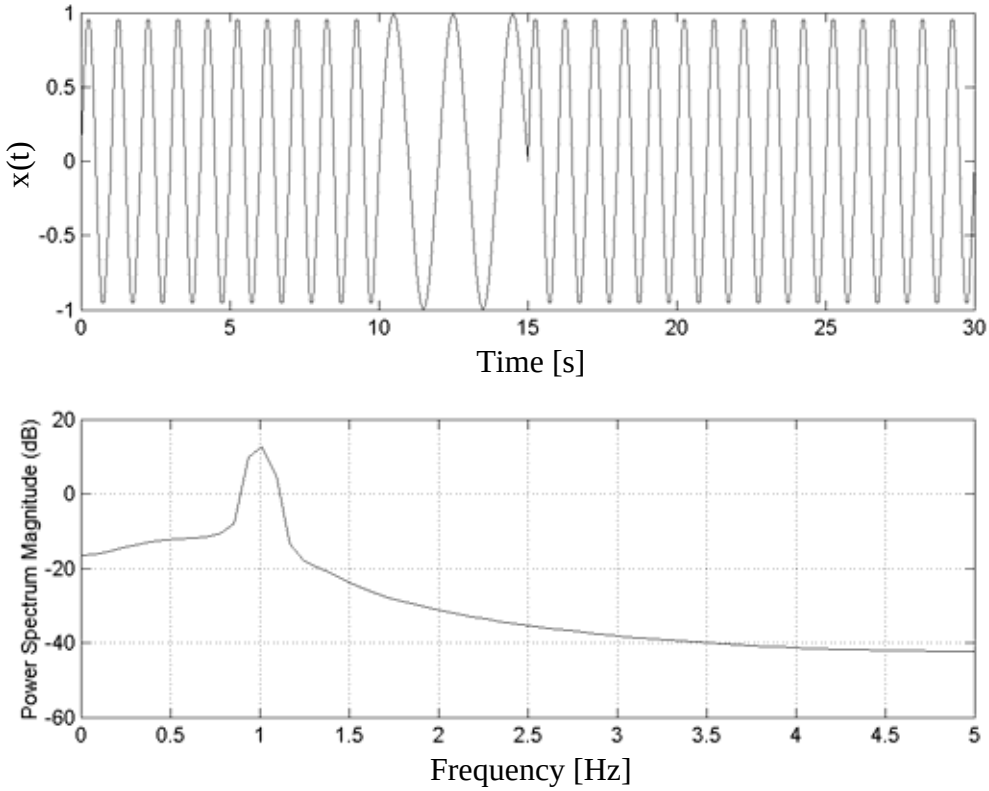

FIGURE 3.1. Sine wave with local frequency change (top) and traditional power spectral magnitude

are discussed in further detail in Carmona et al. (1998) and Mallat (1998). In this chapter, the theory developed by various sources are unified and organized, and the details relevant to Civil Engineering are highlighted. As the essential components of wavelet and time-frequency analysis theory are introduced, anecdotes and subsequent discussions are provided to assimilate the various components of the theory, largely grounded in mathematics and signal processing, and recast it in the unique perspective of Civil Engineering applications.

3.2 Short-Time Fourier Transform

To overcome the limitations of Fourier Transforms, a Short-Time Fourier Transform (STFT) was developed by Gabor (1946). Since the harmonic waves used in traditional Fourier analysis are continuous, it is impossible for this representation to have a local spectral density suitable for uncovering transient information. Thus, the Fourier Transform was modified by a short-duration window *w(t)* centered at time, *τ*. The spectral coefficients could then be determined over this short length of data, which is assumed to be stationary, yielding the STFT

$$STFT(\tau, f) = \int_{-\infty}^{\infty} x(t) w^*(t-\tau) e^{-i2\pi ft}\, dt \tag{3.1}$$

where * denotes complex conjugate and *i* is the imaginary number. This new breed of transform was one of the first time-frequency distributions, named for their ability to depict energy densities as a dual function of frequency and time. The transform, appropriately nicknamed the *Gabor Transform*, became quite popular due to its intuitive appeal in light of the widely used Fourier Transform, conserving energy between the time and frequency domain in a similar manner.

The performance of this transform is greatly dependent upon the choice of window function, which can simply be the traditional boxcar, i.e. rectangular, window. Proper windows are those with good localization in both the time and frequency domains and are chosen subjectively based on the application. Other popular choices include the Hanning and Hamming windows and the Gaussian function discussed in Section 3.2.2 (Carmona et al., 1998). An energy representation, commonly known as the *spectrogram*,

can then be obtained by plotting the squared modulus of the transform to highlight the time-frequency distributions of energy in the signal. While the notion of a moving Fourier Transform is attractive for uncovering localized signal features, it still is plagued by the same issues facing the traditional Fourier Transform.

3.2.1 Heisenberg Uncertainty Principle

As discussed in Chapter 2, spectral analysis is limited by the fact that high resolution cannot be obtained in both the time and frequency domains as a result of their inverse relationship. Contracting a function in time to improve its localization will dilate it in the frequency domain. The measure of time duration, T_x, and frequency bandwidth, B_x, of a signal has been defined in many ways, but the most common definition was proposed by Gabor (1946):

$$T_x^2 = \frac{\int_{-\infty}^{\infty} t^2 |x(t)|^2 dt}{\int_{-\infty}^{\infty} |x(t)|^2 dt} \tag{3.2}$$

$$B_x^2 = \frac{\int_{-\infty}^{\infty} f^2 |\hat{X}(f)|^2 df}{\int_{-\infty}^{\infty} |\hat{X}(f)|^2 df} \tag{3.3}$$

where *x(t)* is a zero mean signal and $\hat{X}(f)$ is its Fourier Transform. These in essence serve as a measure of the mean square value of the signal in both time and frequency normalized by the variance or total energy content. The product of this bandwidth and time duration, often termed *BT product*, is constant, with its minimum value possible obtained for a Gaussian signal,

$$B_x T_x \geq \frac{1}{4\pi}. \tag{3.4}$$

This relation is commonly termed the *Heisenberg Inequality* or *Heisenberg Uncertainty Principle.* This important development defines the primary constraint on time-dependent spectra, as one cannot obtain a high degree of resolution in both the time and frequency domains simultaneously. A rigorous proof of this principle may be found in Chui (1992).

Similarly, this definition may be used to define the resolution of a particular zero mean window function:

$$\Delta t_w^{\,2} = \frac{\int_{-\infty}^{\infty} t^2 \left|w(t)\right|^2 dt}{\int_{-\infty}^{\infty} \left|w(t)\right|^2 dt} \tag{3.5}$$

$$\Delta f_w^{\,2} = \frac{\int_{-\infty}^{\infty} f^2 \left|\hat{W}(f)\right|^2 df}{\int_{-\infty}^{\infty} \left|\hat{W}(f)\right|^2 df} \tag{3.6}$$

where *w(t)* is the window function and $\hat{W}(f)$ is its Fourier Transform. The relation in Equation 3.4 still applies and the product of these two resolutions must be greater than or equal to 1/4π. As the Gaussian functions establish the lower bound in Equation 3.4, they are typically chosen as the window function *w(t)* in the STFT. Note that analogs to Equations 3.3-3.6 for windows or signals that are not zero mean are provided in Carmona et al. (1998).

3.2.2 Resolutions of the STFT: The Heisenberg Box

Based on the frequency and time resolutions in Equations 3.5 and 3.6, the STFT at time *t* and frequency *f* represents the signal content in a distinct area of the time-frequency plane defined by the *Heisenberg box* with the following dimensions

$$\left[t - \Delta t_w, t + \Delta t_w\right] \times \left[f - \Delta f_w, f + \Delta f_w\right]. \tag{3.7}$$

The dimensions of the box do not change with the frequency being analyzed but remain fixed: the box having a width of $2\Delta f_w$ along the frequency axis and $2\Delta t_w$ along the time axis. As argued by Chui (1992), since frequency is directly proportional to number of cycles in a specific interval of time, a narrow time window is required to locate high-frequency phenomena and a wide time-window is necessary for more thorough investigation of low-frequency phenomena. As a result, this transform is not well suited for analysis of signals that may have both low and high frequency components. This is demonstrated schematically in Figure 3.2, as fewer cycles of the low frequency component of the signal are considered in the fixed Heisenberg box of the STFT. Similarly, the time resolution does not become finer at high frequencies, where it is required to separate rapidly varying high frequency components. To demonstrate, consider the sum of two hyperbolic chirps shown in Figure 3.3. The STFT's spectrogram cannot track the rapidly varying frequencies of the two chirps due to its non-optimal resolutions, resulting in a blurring of their energy in the high frequency range.

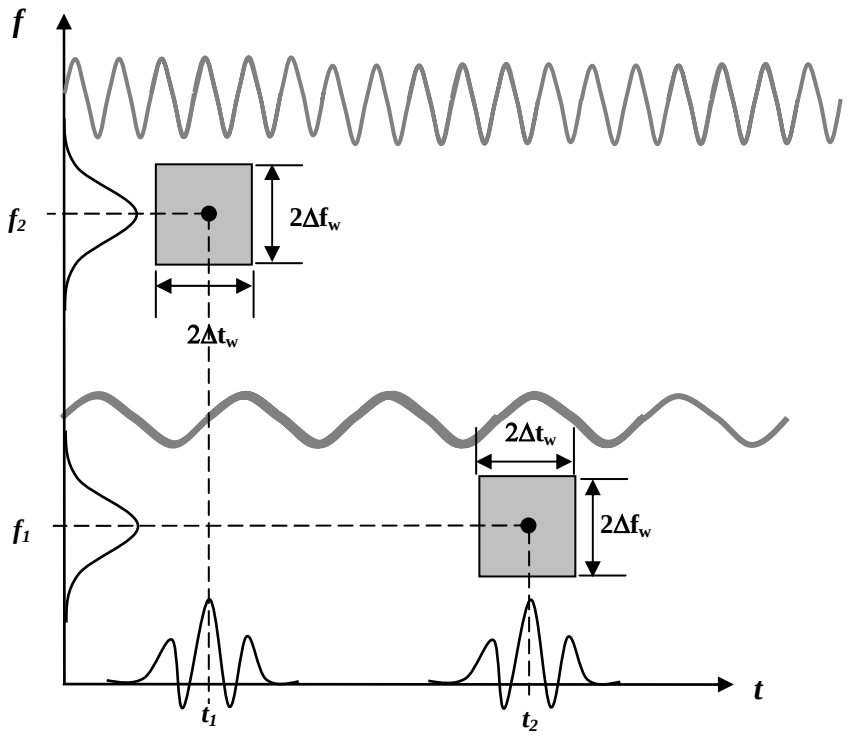

FIGURE 3.2. Concept of Heisenberg box for short-time Fourier Transforms

3.3 Moving Toward the Wavelet Domain

It becomes evident that by breaking the signal down into a series of basis functions of finite length, one can overcome some of the limitation of stationarity. As Fourier basis functions are localized in frequency but not in time, an alternative was introduced in the previous section to localize the Fourier Transform through the addition of a window function. However, constraints of the Heisenberg Uncertainty Principle limit the obtainable resolutions and render them non-optimal over a range of frequencies. An alternative approach would be to design basis functions that are local in both frequency and in time and then scaled via dilations to optimally adjust their resolutions based on the frequency being analyzed, yielding a multi-resolution analysis.

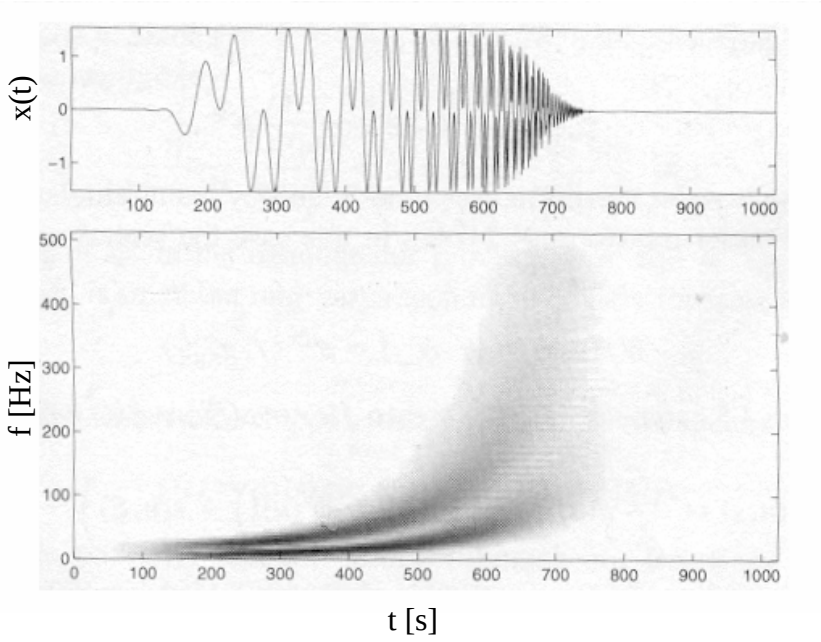

FIGURE 3.3. Sum of two hyperbolic chirps and resulting spectrogram (Mallat, 1998)

The Wavelet Transform (WT) was engineered with this in mind. Through an adaptation to the Heisenberg Uncertainty Principle, the Wavelet Transform concedes that arbitrarily good resolution in both time and frequency is not possible. Thus the transform optimizes its resolutions as needed. It provides good resolution at high dilations or low frequencies, sacrificing its time resolution in this regime to satisfy the Heisenberg Uncertainty Principle. As the variations of low frequency components with time are typically gradual, this loss is not of consequence. In the time domain, the transform has good resolution at high frequencies in order to identify transient signal features. The fundamental differences between the Fourier Transform, the Short Time Fourier Transform and the Wavelet Transform are shown in Figure 3.4. The advantages of the Wavelet Transform approach are evident upon revisiting the two hyperbolic chirps in Figure 3.3. A plot of the energy distribution from the Wavelet Transform of the signal is

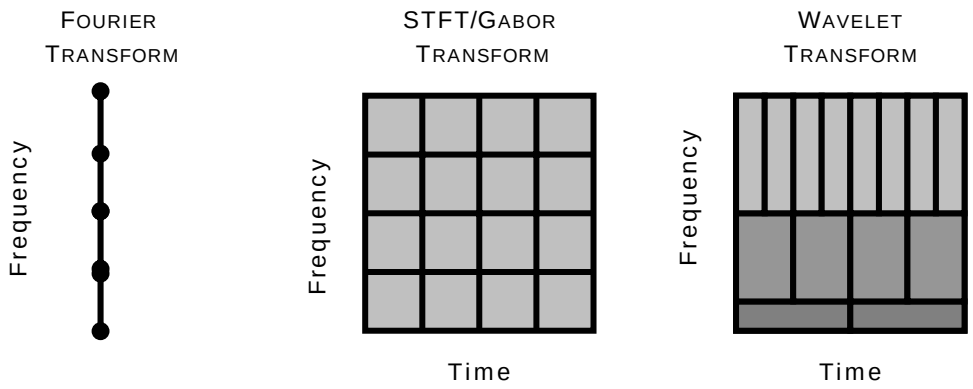

FIGURE 3.4. Evolution of time-frequency analysis

provided in Figure 3.5 and demonstrates that the multi-resolution time-frequency analysis can identify the two components.

3.4 The Transform

The relations governing Wavelet Transforms have been articulated and proven in a number of texts, e.g. Chui (1992), Mallat (1998) and Carmona et al. (1998). Therefore, only relevant details are presented herein for brevity. The continuous Wavelet Transform (CWT) is a linear transform that decomposes a signal *x(t)* via basis functions that are simply dilations and translations of the parent wavelet *g(t)* through the convolution with the signal according to

$$W(a,t) = \frac{1}{\sqrt{a}} \int_{-\infty}^{\infty} x(\tau) g^{*}\left(\frac{\tau - t}{a}\right) dt \tag{3.8}$$

where * denotes complex conjugate. Dilation by the scale, *a*, inversely proportional to frequency, represents the periodic or harmonic nature of the signal. The resulting wavelet coefficients, *W(a,t)*, represent a measure of the similitude between the dilated/shifted

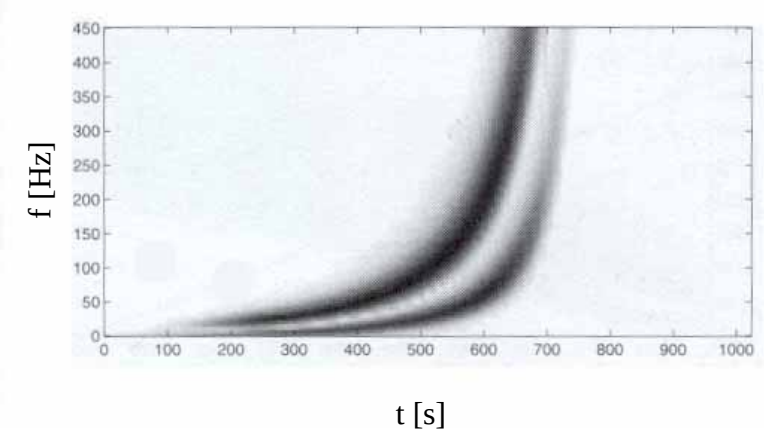

FIGURE 3.5. Wavelet transform of two hyperbolic chirps shown in Figure 3.3 (Mallat, 1998)

parent wavelet and the signal at time *t* and scale (frequency) *a*. The normalization by the root of scale insures that the integral energy given by the wavelet is independent of the dilation.

Calculation of the Wavelet Transform can be expedited in the frequency domain through the use of Fourier Transforms. Thus, the convolution in Equation 3.8 can equivalently be represented as a product in the Fourier domain with Fourier frequency *f*

$$W(a,t) = \sqrt{a}\int_{-\infty}^{\infty} \hat{X}(f)\hat{G}^{*}(af)e^{i2\pi ft}df \ . \tag{3.9}$$

where $\hat{X}$ and $\hat{G}$ denote the Fourier Transforms of the signal and the parent wavelet.

3.4.1 Completeness

For well-defined parent wavelets (the conditions surrounding this will be discussed in Section 3.4.2), the inverse transform is given by

$$x(t) = \frac{1}{C_g} \int_{-\infty}^{\infty} \int_{-\infty}^{\infty} W(a,t) \frac{1}{\sqrt{a}} g^* \left(\frac{t-\tau}{a} \right) \frac{da}{a^2} d\tau \tag{3.10}$$

where C_g is defined as

$$C_g = \int_{-\infty}^{\infty} \frac{|G(f)|^2}{f} df \, . \tag{3.11}$$

From the Wavelet Transform, an energy distribution plot called a *scalogram* can be generated by plotting the squared modulus of the transform. This representation, analogous to the spectrogram, represents the energy content of the signal at distinct time and frequency (scale) pairs

$$SG(a,t) = |W(a,t)|^2 \quad \text{or} \quad SG(f,t) = \left| W\left(\frac{f_o}{f}, t \right) \right|^2 . \tag{3.12 a, b}$$

Unlike its STFT counterpart, the energy distribution in the scalogram is multi-resolution.

As demonstrated by proof in Chui (1992) and Mallat (1998), the Wavelet Transform conserves mean square energy for real signals

$$E_x = \int |x(t)|^2 dt = \frac{1}{C_g} \int_{-\infty}^{\infty} \int_{-\infty}^{\infty} SG(a,t) \frac{da}{a^2} dt \tag{3.13}$$

or equivalently

$$E_x = \int |x(t)|^2 dt = -\frac{1}{C_g} \int_{-\infty}^{\infty} \int_{-\infty}^{\infty} SG\left(f \big/ f_o, t \right) df dt \tag{3.14}$$

providing an analog to Plancherel's Theorem. Thus the wavelet can be viewed either as measure of time-scale or time-frequency energy density.

3.4.2 Conditions on Parent Wavelets

The transform offers great flexibility, in that, any number of functions satisfying some basic constraints can serve as the parent wavelet in Equation 3.8. This flexibility has permitted authors to tailor the shapes and time-frequency features of wavelets to match the characteristics of signals they wish to detect, e.g., Wang (2001). The first condition on a candidate parent wavelet *g(t)* is that the function $g \in L^2(\Re)$ satisfy an *admissibility condition*

$$C_g < +\infty . \tag{3.15}$$

This admissibility condition is necessary to guarantee that the inverse transform in Equation 3.10 is valid. To guarantee this, the parent wavelet should be a zero mean function such that

$$\int_{-\infty}^{\infty} g(t)dt = 0 \tag{3.16}$$

and thereby $\hat{G}(0) = 0$. By requiring that $\hat{G}(0) = 0$ and that $\hat{G}(f)$ be continuously differentiable, the admissibility condition is automatically satisfied. The condition of continuous differentiability can readily be established for signals with sufficient time decay

$$\int_{-\infty}^{\infty} (1+|t|)|g(t)|dt < +\infty . \tag{3.17}$$

In essence, this chain of properties helps to guarantee that the transform has finite support in both the time and frequency domains, forming the “little waves” that gave rise to the

transform's name. Note that, in some cases, the parent wavelet may also be normalized so that $\|g(t)\| = 1$.

Parent wavelets satisfying these conditions may be subdivided into two classes: real and analytic (or progressive), as discussed by Mallat (1998); however, only the former class are presented herein, as they are the focus of the wavelet analyses in this work. In general, an analytic signal is defined as a function that does not have energy content at negative frequencies, i.e. has Fourier coefficients of zero at these frequencies. Though complex in nature, analytic wavelets can be entirely characterized by their real component. By definition, the lower limits of integration with respect to frequency and scale in Equations 3.13 and 3.14 can be set to zero for this class of parent wavelets. The suppression of negative frequencies also introduces a factor of two to these integral relations, as shown in Mallat (1998).

3.5 Wavelet Resolutions: The Heisenberg Box

The scalogram in Equation 3.12 represents the level of energy within a box in the time-frequency domain, called a *Heisenberg box*. This box is centered at time *t* and frequency *f* and has dimensions that are scaled versions of the time (Δt_g) and frequency (Δf_g) resolutions of the parent wavelet

$$\Delta t = a\Delta t_g \qquad \text{and} \qquad \Delta f = \Delta f_g / a . \tag{3.18 a, b}$$

The box dimensions are then given by

$$\left[t - a\Delta t_g, t + a\Delta t_g\right] \times \left[f - \Delta f_g / a, f + \Delta f_g / a\right] \tag{3.19}$$

giving the box a span of $2\Delta t$ in the time domain and $2\Delta f$ in the frequency domain. Note that the area of this box remains constant, $4\Delta t\Delta f$, though the resolutions are a function of scale. Thus, the Wavelet Transform gives local information about the function *x(t)* over the time interval $\left[t - a\Delta t_g, t + a\Delta t_g\right]$ and over the frequency interval $\left[f - \Delta f_g / a, f + \Delta f_g / a\right]$.

These basic relations demonstrate that the Heisenberg box of the wavelet shrinks in the frequency domain at low frequencies (large scales) and shrinks in the time domain at high frequencies (small scales). As shown in Figure 3.6, this makes the transform better suited to capture the details of signal content at those frequencies. Though a host of time-frequency transformations are available, only the Wavelet Transform is uniquely capable of adaptively adjusting to the Heisenberg Uncertainty Principle. In essence, the Wavelet Transform concedes that arbitrarily good resolution in both time and frequency is not possible. Thus the transform optimizes its resolutions as needed. It provides good resolution at high dilations or low frequencies, ideal for Civil Engineering applications, while sacrificing its time resolution in this regime to satisfy the Uncertainty Principle. In the time domain, the transform has good resolution at high frequencies in order to identify signal singularities or discontinuities, a feature often exploited in health monitoring applications, e.g. Corbin et al. (2000).

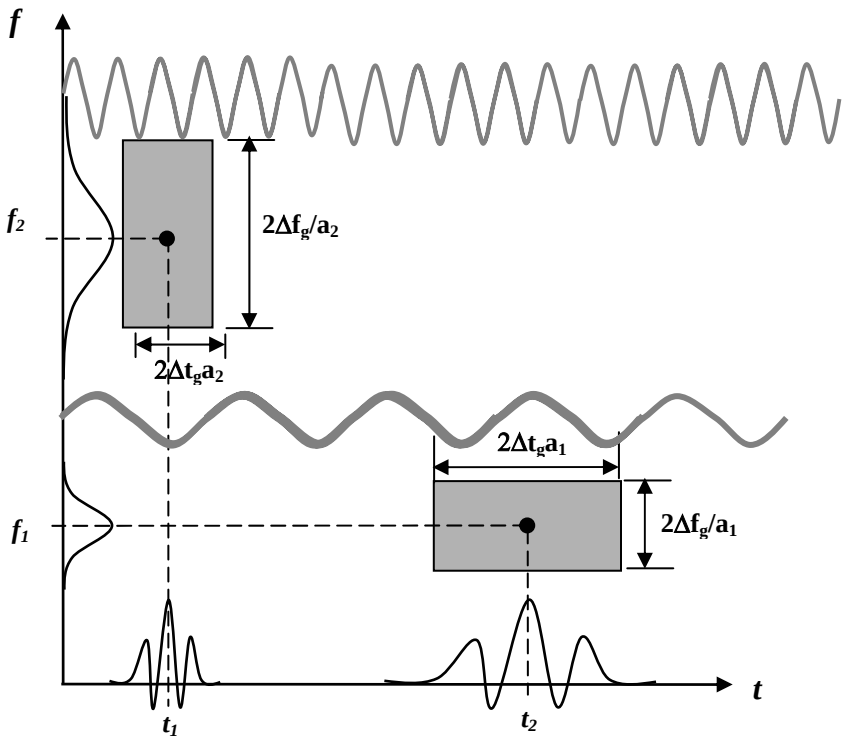

FIGURE 3.6. Concept of Heisenberg box for Wavelet Transforms

Physically, the measure provided in Equation 3.18a,b indicates that two pulses in time cannot be identified unless they are more than Δt apart. Similarly, two distinct frequency components cannot be discerned unless they are more than Δf apart.

3.6 Discretization and Orthogonality

Frame theory establishes the completeness, stability and redundancy of linear discrete signal representations, providing conditions for discretizing windowed Fourier Transforms and Wavelet Transforms to retain a complete and stable, though potentially redundant, representation (Carmona et al., 1998; Mallat, 1998). A complete representation can be obtained only if the Heisenberg boxes of the transform fully cover

the time-frequency plane. Thus the sampling of the time-frequency space is based on the time-frequency spread of the window *w(t)* in windowed Fourier Transforms or of the parent wavelet *g(t)* in Wavelet Transforms. As long as the entire time-frequency plane is covered by the Heisenberg boxes tied to each time and frequency/scale, the representation is complete, though it still may be redundant and unstable in reconstruction.

In moving toward a stable representation, the scales are often sampled along an exponential sequence due to inverse relationship with frequency, according to the bandwidth of the parent wavelet, while the time translations are sampled uniformly at intervals proportional to the discretized scales. However, conditions introduced in Mallat (1998) provide for a complete and stable translation-invariant representation, a capability crucial in pattern recognition by discretizing only the frequency (scale). These common dyadic Wavelet Transforms sample at *v* intermediate scales, or voices, over each octave $\left[2^j, 2^{j+1}\right]$ and leave the time variable untouched. This leads to a dyadic scale sequence $\left\{a^j\right\}_{j<0}$ for $a = 2^{\frac{1}{v}}$. The dyadic discrete Wavelet Transform (DWT) is then defined for a signal *x[n]* of length *N* as

$$W[a^j, n] = \frac{1}{\sqrt{a^j}} \sum_{m=0}^{N-1} x[m] g^* \left[\frac{m-n}{a^j} \right]. \tag{3.20}$$

This expression of the discrete Wavelet Transform enables calculation by fast filter bank algorithms. More importantly, when satisfying specific conditions of *tight frames*, entire classes of orthogonal wavelets can be developed, as discussed in Carmona et al. (1998)

and Mallat (1998). Common orthogonal wavelets include Haar, Meyer and Daubechies class. While beyond the scope of this work, these wavelets are tailored for image/signal compression and reconstruction, though their time translation variance limits their usage for pattern recognition (Wang, 2001), in which case the same transient information at a different time may manifest different patterns in the time-frequency domain (Zheng et al., 2002), motivating the use of the above mentioned dyadic transform. The use of the DWT is furthermore not feasible for many of these investigations due to the limitations in frequency and time resolution due to the sparse sampling of time-frequency space to create tight frames. For this reason, Continuous Wavelet Transforms are advocated in this work and the proper conditions for their discretization are provided in Chapter 4.

3.7 Wavelet-Transforms and Analytic Signals

Although the notions of TFDs have been utilized in signal processing for decades to examine the variations in signal frequency with time, their extension to the identification of the dynamic properties of mechanical and civil structures has evolved only recently. The foundations for these analyses are deeply rooted in analytic signal theory and the properties of phase and amplitude in complex signals, which are briefly overviewed herein.

3.7.1 Instantaneous Frequency

A real signal $x(t)$ may be represented as an amplitude $A(t)$ modulated with a time-varying phase $\phi(t)$

$$x(t) = A(t)\cos\phi(t)\,. \tag{3.21}$$

The *instantaneous frequency* (IF) is defined as the positive derivative of the phase

$$IF(t) = \frac{1}{2\pi}\frac{d}{dt}\phi(t)\,. \tag{3.22}$$

While the notion of frequency at an instant may seem paradoxical, the simplest way to conceptualize the notion of an "instantaneous" frequency is as the frequency of a sine wave that locally fits the signal under consideration.

There are indefinitely many amplitude/phase pairs that can represent the signal in the form of Equation 3.21. For example, the signal could be represented as a frequency-modulated signal with constant amplitude or an amplitude-modulated signal with constant frequency. Amongst these pairs, there is one amplitude and phase pair that has many desirable properties. This pair is determined by defining an *analytic signal*, *z(t),* through a linear filtering operation that suppresses all negative frequencies. It was proposed by Gabor (1946) to generate this complex analytic signal using a filter that simply shifts the phases all frequency components by $-\pi/2$

$$z(t) = x(t) + iH[x(t)]\,. \tag{3.23}$$

The operator $H[\cdot]$ denotes the Hilbert Transform, defined mathematically as

$$H[s(t)] = \int_{-\infty}^{\infty}\frac{x(t-\tau)}{\pi\tau}\,. \tag{3.24}$$

The operation denoted in Equation 3.24 is merely the convolution of *x(t)* with *1/t*, or it can be thought of as a phase shift of the signal by 90^o. As a result, *x(t)* and *H[x(t)]* are said to be in *quadrature*. This complex signal can then be completely characterized by

$$z(t) = A_z(t)e^{i\phi_z(t)} \tag{3.25}$$

with nonnegative amplitude A_z and phase ϕ_z with values in the interval $[0,2\pi)$, forming the so-called *canonical pair*.

Since $\mathrm{Re}[z(t)] = x(t)$

$$x(t) = A_z(t)\cos\phi_z(t) \tag{3.26}$$

yielding the *canonical representation* of *x(t).* Based on this representation, Ville (1948) proposed to calculate the instantaneous frequency of the signal *x(t)* using the analytic signal *z(t)*

$$IF(t) = \frac{1}{2\pi}\frac{d}{dt}\phi_z(t) = \frac{1}{2\pi}\frac{d}{dt}[\angle z(t)]. \tag{3.27}$$

Note that the work in this field by Ville (1948) then led to his definition of an instantaneous spectrum describing the spread of frequencies about this mean frequency, known as the Wigner-Ville Distribution (WVD). However, for real signals, WVD produces "ghost terms" as a consequence of the interference between positive and negative frequencies (Carmona et al., 1998). It has also been observed that the WVD can even exhibit negative bandwidth spectra (Jones & Boashash, 1990). Such lack of physical significance to measures derived from the WVD led to some concerns for its practical application. The measure in Equation 3.25 has physical significance only when $\phi_z(t)$ and $A_z(t)$ meet some basic conditions associated with *asymptotic signals*, discussed in the following section.

3.7.2 Theory of Asymptotic Signals

The class of asymptotic signals can be represented by the amplitude and phase of their analytic counterparts. To identify if such a representation can be made, the following condition is stated in Carmona et al. (1998)

$$z(t) = A(t)e^{i\lambda\phi(t)} + O\left(\lambda^{-3/2}\right) \quad \text{as} \quad \lambda \to \infty \tag{3.28}$$

where λ is a positive number. This statement infers that the analytic signal approximation becomes increasingly valid as the phase variations increase relative to the amplitude variations. This characteristic distinguishes asymptotic signals and permits the analytic signal approximation

$$z(t) \approx A(t)e^{i\lambda\phi(t)}. \tag{3.29}$$

In practical applications, the term λ is not known; however, Equation 3.28 nevertheless places a very loose condition that the oscillations coming from the phase term should be much faster than those coming from the amplitude term. This criterion may be best imagined by viewing the amplitude and phase components of the signal in the Fourier domain. The Fourier spectra of the amplitude ($S_A(f)$) and phase ($S_\phi(f)$) must be well separated to satisfy this condition, as shown schematically in Figure 3.7.

Satisfaction of the asymptotic signal assumption has special benefits for analytic Wavelet Transforms. As proven in Carmona et al. (1998), for the class of asymptotic signals, the analytic Wavelet Transform coefficients at the *stationary points* are directly proportional to the analytic signal *z(t)* plus an error term again on the order of $\lambda^{-3/2}$. The

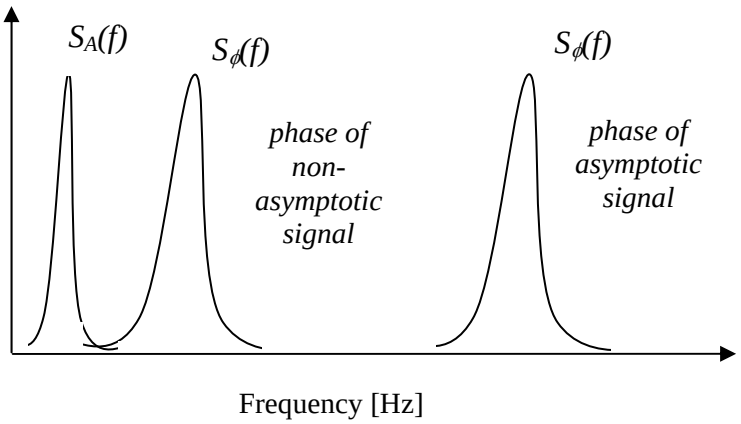

FIGURE 3.7. Schematic representation of asymptotic signal conditions

stationary points are time-scale ordinates at which the frequency of the scaled wavelet coincides with the local frequency of the signal. These findings indicate that as a signal more strictly meets the asymptotic signal assumption, as $\lambda \to \infty$, i.e. as the oscillations of the phase term increase relative to the amplitude term, the better the wavelet coefficients in the vicinity of the stationary points approximate the analytic signal. This finding then allows analytic wavelet coefficients at these stationary points to be used directly to estimate the analytic signal in Equation 3.25 instead of the Hilbert Transform as in Equation 3.23. The merits of this development will be highlighted in a later section.

3.7.3 Theory of Wavelet Ridges

In cases for which these asymptotic signal assumptions are met, the Wavelet Transform coefficients have some attractive characteristics in the vicinity of the aforementioned stationary points. At these locations, the frequency of the scaled wavelet coincides with the local frequency of the signal at that time. This similitude yields very large wavelet

coefficients at the scales associated with these frequencies, reflecting the property of analytic wavelets to "concentrate" at the dominant frequencies within an asymptotic signal. This pronounced localization is the hallmark of asymptotic signals in the time-frequency domain. The scales at which these concentrations occur forms a *ridge* in the time-frequency plane described mathematically by

$$a_r(t) = \frac{\omega_o}{\phi'(t)} = \frac{2\pi f_o}{IF(t)} \tag{3.30}$$

where $\phi'(t)$ is the derivative of the phase and ω_o (or f_o) is the *central frequency* of the parent wavelet, i.e. the frequency at which the Fourier Transform of the parent wavelet focuses. This relationship indicates that once the scales associated with ridges are identified, they can be used to define the analytic signal directly since

$$W(a_r(t), t) \propto z(t) \tag{3.31}$$

and extract the instantaneous frequency of the signal, provided that there are no significant noise components corrupting the signal (Carmona et al., 1998). Wavelet coefficients along these ridges form the *wavelet skeleton*. The precise methodologies for the extraction of wavelet ridges will be overviewed in Chapter 4.

3.7.4 Asymptotic Signals and Mechanical Oscillators

In the simplest structural identification problem of free vibration or impulse response, the system has a distinguishable enveloped sinusoidal behavior given by

$$h(t) = A_o e^{-\xi\omega_n t} \cos(\omega_n \sqrt{1-\xi^2}\, t) = A_o e^{-\xi\omega_n t} \cos(\omega_D t) \tag{3.32}$$

where A_o is the initial displacement condition and θ is a phase shift. The analytic signal is then

$$z(t) = A_o e^{-\xi\omega_n t + i\omega_D t}. \tag{3.33}$$

The amplitude function is given by

$$A(t) = |z(t)| = A_o e^{-\xi\omega_n t} \tag{3.34}$$

with phase described by

$$\phi(t) = \angle z(t) = \omega_D t. \tag{3.35}$$

Thus the damped natural frequency can be determined from the derivative of the phase, equivalently viewed as the instantaneous frequency in Equation 3.27. Assuming a lightly damped system, where $\omega_D \approx \omega_n$, the damping can be determined from Equation 3.34.

The above relations are of course contingent upon the asymptotic signal assumption being met, with the phase variations occurring more rapidly than those of the amplitude. Later in Chapter 7, a specific example demonstrates the implications of violating this condition for mechanical oscillators. If the frequency and damping terms in the above relations are time-varying, the identification of instantaneous frequency and damping values for a nonlinear system can similarly be accomplished using Equations 3.34 and 3.35. Feldman (1994a,b) advocated this more traditional approach using Hilbert Transforms to generate the analytic signal in Equation 3.33. However, this transform has inherent limitations, explored in the following section.

3.7.5 Alternative Methods to Generate Analytic Signals for Multi-Component Data

Despite its wide usage, the Hilbert Transform is especially sensitive to the asymptotic signal restrictions. The extent to which this condition is satisfied dictates whether the

transform truly yields the quadrature component. Breakdowns were demonstrated in the free vibration of mechanical oscillators with low natural frequencies as damping was increased (Ruzzene et al., 1997). To circumvent this, other transforms were proposed that would directly yield a complex representation without the approximation in Equation 3.23. Transforms such as the Wigner-Ville Distribution (Feldman & Braun, 1995) were employed; however they were limited by the restriction of monocomponent signals, much like the Hilbert Transform.

There is considerable debate surrounding how to quantify the conditions under which the Hilbert Transform can be used to obtain the analytic signal in Equation 3.25 and allow Equation 3.27 to yield a physically meaningful instantaneous frequency. The leakage of signal energy into negative frequencies of the Fourier spectrum constitutes one condition under which the Hilbert Transform will not yield the quadrature component (Boashash, 1992a), as analytic signals suppress negative frequencies; however, a more concerning issue surrounds its inability to handle signals with multiple frequency components. To demonstrate, consider a signal with several distinct harmonic components, e.g. a summation of several sine waves of varying frequency. Despite the presence of several distinct frequencies, the direct application of the Hilbert Transform to extract the instantaneous frequency in the aforementioned strategy will yield a single estimate of instantaneous frequency at each instant of time that is an average or composite of all the individual frequency components present. This inability to directly distinguish multiple components leads to this "monocomponent" restriction, necessitating that there be only a single frequency component present in the signal at each time.

Therefore, prior to the application of the Hilbert Transform, "multi-component" signals must undergo some type of bandpass filtering operation.

Understandably, this “monocomponent” or “multi-component” terminology arises from a Fourier perspective, appealing to those familiar with modal structural analysis backgrounds. Unfortunately, there is no clear criteria to determine if a given signal is truly multi-component or monocomponent, despite efforts by Boashash (1992a) defining multi-component signals as those that may be comprised by a weighted sum of monocomponent signals. Cohen & Lee (1989) used this same premise to propose similar methods to identify multi-component signals. However, the lack of a precise means to distinguish multi-component signals led to the adoption of a "narrowband" condition (Schwartz et al., 1966). Even with this definition, the manner in which narrowbandedness is determined is subjective, leaving the possibility that signals meeting a specified narrowband condition may still contain multiple frequency components at a given instant in time, as the example in Section 7.5.5 will later demonstrate. Thus, while the debate over correctness of terminology still ensues, the signal processing community in general concurs that the more closely a signal approaches a strictly narrowband condition, the better the Hilbert Transform approximates the quadrature signal and thereby the instantaneous frequency (Boashash, 1992a). For the purposes of this work, the terminology of monocomponent and multi-component signals will be retained to respectively describe signals that have one or multiple distinct frequencies at each instant in time.

The bandpassing process required for multi-component signals can be difficult for closely spaced modes and must be addressed when using the Hilbert Transform (Lee & Park, 1994) or the Wigner-Ville Distribution (Feldman & Braun, 1995). A viable multi-component decoupling approach, Empirical Mode Decomposition, used in conjunction with the Hilbert Transform, was proposed by Huang et al. (1998) and will be discussed in further detail in Chapter 7. The use of this approach has permitted system identification of large structures using the Hilbert Transform analytic signal approach (Yang et al., 2000). However, the Wavelet Transform provides an alternative analysis framework that directly produces a complex analytical signal and separates multiple components, circumventing the need for bandpass filtering. Recognizing the ability of wavelet transforms to decouple multi-component signals, a number of researchers began applying this technique in various forms for analysis of impulse (Huang et al,. 1994; Robertson et al., 1998a,b) and free vibration response (Hans et al., 2000; Lamarque et al., 2000; Ruzzene et al., 1997; Staszewski, 1997). The three latter studies drew upon the unique characteristics of Morlet wavelets and the relationships adapted Equations 3.34 and 3.35 for wavelet system identification in linear and nonlinear systems, with wavelet amplitude and phase being proportional to their counterparts in the analytic signal along wavelet ridges.

3.8 Benefits of the Wavelet Transform for Civil Engineering Applications

This chapter chronicled the evolution of time-frequency analysis and overviewed the mathematical theory governing Wavelet Transforms and their relationship to asymptotic signals. The wavelet's ability to uncover local and transient features, while implicitly

decoupling multiple frequency components, makes it a system identification and analysis tool well suited to a variety of problems in Civil Engineering, including the study of earthquake, wind and wave-induced response (Gurley & Kareem, 1999). For example, in the case of earthquakes, the onset of damage can be identified in time by the lengthening of the structural period, or shortening of natural frequency in the wavelet map, and related to the characteristics of the ground motion at that instant. Clearly such insights could not be gained through traditional Fourier techniques, as subsequent chapters will demonstrate in the analysis of a variety of simulated and measured signals. However, before such analyses can be conducted, a number of processing issues must be addressed to insure the proper application of the transform and meaningful interpretation of results. The wavelet analysis framework in Chapter 4 addresses these issues.

CHAPTER 4

FRAMEWORK FOR WAVELET-BASED ANALYSIS

4.1 Necessity for Unified Analysis Framework

The use of wavelet-based analysis in a variety of fields previously focused largely on qualitative measures of time-varying frequency content, during which signal processing concerns were not previously raised. However, the adaptation of the transform to more quantitative analyses, including system identification, necessitates that these processing concerns be explored and remedied. Just as years of Fourier Transform applications have uncovered issues associated with leakage, aliasing and frequency resolution, investigation into such phenomenon for wavelet-based analysis is lacking. One component of this research effort was to develop a complete framework for wavelet analysis to address these concerns and insure the most accurate wavelet coefficients possible. This chapter first presents the parent wavelet that is used throughout this research and then introduces each of the processing considerations associated with this wavelet and, based upon the properties of this parent wavelet, provides some appropriate remedies. This framework provides the backdrop for this research, creating a single framework in which this class of wavelet can be extended to Civil Engineering applications.

4.2 Morlet Wavelets

The great flexibility in the transform leads to a variety of parent wavelets, each providing a different scalogram representation for a given signal. This dependence on the choice of parent wavelet has been criticized by some, e.g., Huang et al. (1998). However, others counter that the parent wavelet should be selected based upon shape and form of the signal in question or a particular feature to be extracted, making this flexibility an asset. Wang (2001) demonstrates the significance of selecting parent wavelets that resemble assorted transients in mechanical systems and using this ability to zoom in on a specific signal feature. While there is a wide array of mother wavelets available for analysis, a particular class of wavelet is best suited for the purposes of this study. The Morlet wavelet, an approximately analytic wavelet, is merely the frequency modulation of a real and symmetric window function — the Gaussian window. The Morlet Wavelet (Grossman and Morlet, 1984) can be viewed as a Gaussian-windowed Fourier Transform

$$g(t) = e^{-|t|^2/2} e^{j2\pi f_o t} = e^{-|t|^2/2}(\cos(2\pi f_o t) + j\sin(2\pi f_o t)). \tag{4.1}$$

whose sine and cosine basis functions oscillate at the central frequency f_o. For this reason, this wavelet is sometimes called the *Gabor* wavelet. Dilations of this temporally localized parent wavelet then allow the "effective frequency" of this sine-cosine pair to change in order to match harmonic components within the signal. Its basic analogs to the Fourier Transform, shown in Figure 4.1, make it well suited to for harmonic analysis in the time-frequency domain. This wavelet approximately satisfies the conditions placed on parent wavelets in Section 3.4.2 for sufficiently large values of f_o., e.g. greater than $5/(2\pi)$ or 0.8 (Carmona et al., 1998).

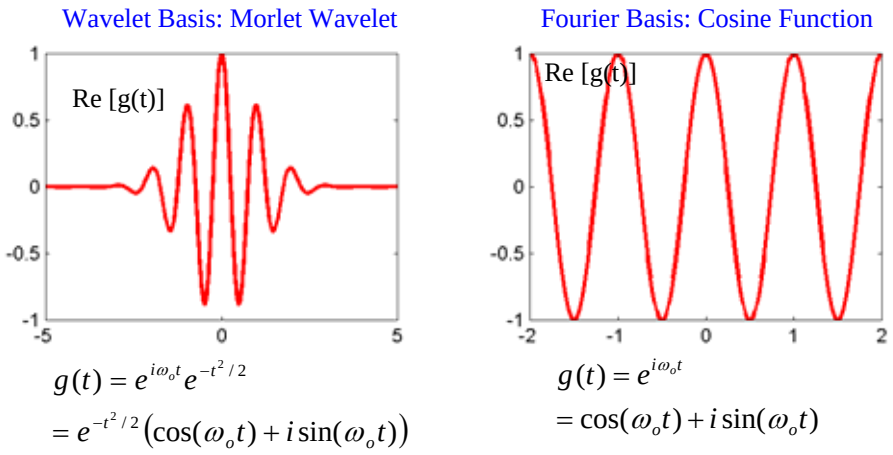

FIGURE 4.1. Comparison of basis functions for Fourier and Morlet Wavelet Transforms

The Morlet wavelet is equivalently localized in the frequency domain, as evidenced by the Fourier Transform of the dilated Morlet wavelet

$$G(af) = \sqrt{2}\sqrt{\pi}e^{-2\pi^2(af - f_o)^2}. \tag{4.2}$$

In the case of the Morlet Wavelet, there is a unique relationship between the dilation parameter of the transform, the scale *a*, and the Fourier frequency *f* at which the wavelet is focused. This relationship is evident by maximizing Equation 4.2 to yield:

$$a = f_o / f. \tag{4.3}$$

The direct relationship to Fourier frequency and analogs to the Fourier Transform itself makes the Morlet wavelet analysis quite natural for interpretation by engineers already versed in Fourier analysis. Note that the relation between Fourier frequency and scale can be approximately estimated for some other parent wavelets, as discussed in Meyers et al. (1993), though few can deliver as direct a relation as that shown in Equation 4.3.

4.2.1 Frequency Resolutions: Tuning the Central Frequency

While the relationship for wavelet frequency resolution in Equation 3.18b may seem straightforward, for the Morlet wavelet the issue of resolution is complicated by the fact that it is a Gaussian-windowed Fourier Transform. Unfortunately, this window lacks measurable duration. An "effective duration" can be defined by drawing on the common use of the Gaussian window in both the Short-Time Fourier Transform and the Morlet wavelet. Thus the mean-square definition for frequency duration given by Equation 3.6 can similarly be used to yield (Chui, 1992)

$$\Delta f_g = \frac{1}{2\pi\sqrt{2}}. \tag{4.4}$$

Combining this with Equations 3.18b and 4.3, the resolution of the Morlet wavelet at a given frequency f_i is given by

$$\Delta f_i = \frac{f_i}{2\pi\sqrt{2}\, f_o}. \tag{4.5}$$

This not only dictates that the frequency resolution will improve for longer period signals, but also implies that the resolution capabilities can be appropriately adjusted for the analysis through careful selection of the central frequency of the Morlet wavelet, a fact emphasized throughout this research and by Wooh & Veroy (2001). As pointed out by Cohen (1999), this is a delicate matter that can lead to significant distortion of the signal if the trade offs between time and frequency resolution are not properly balanced. Intuitively, as this central frequency increases, the frequency resolution is enhanced as more cycles are condensed within the localized window, as shown in Figure 4.2. The analyses throughout this study exploit this flexibility to "tune" the wavelet analysis to

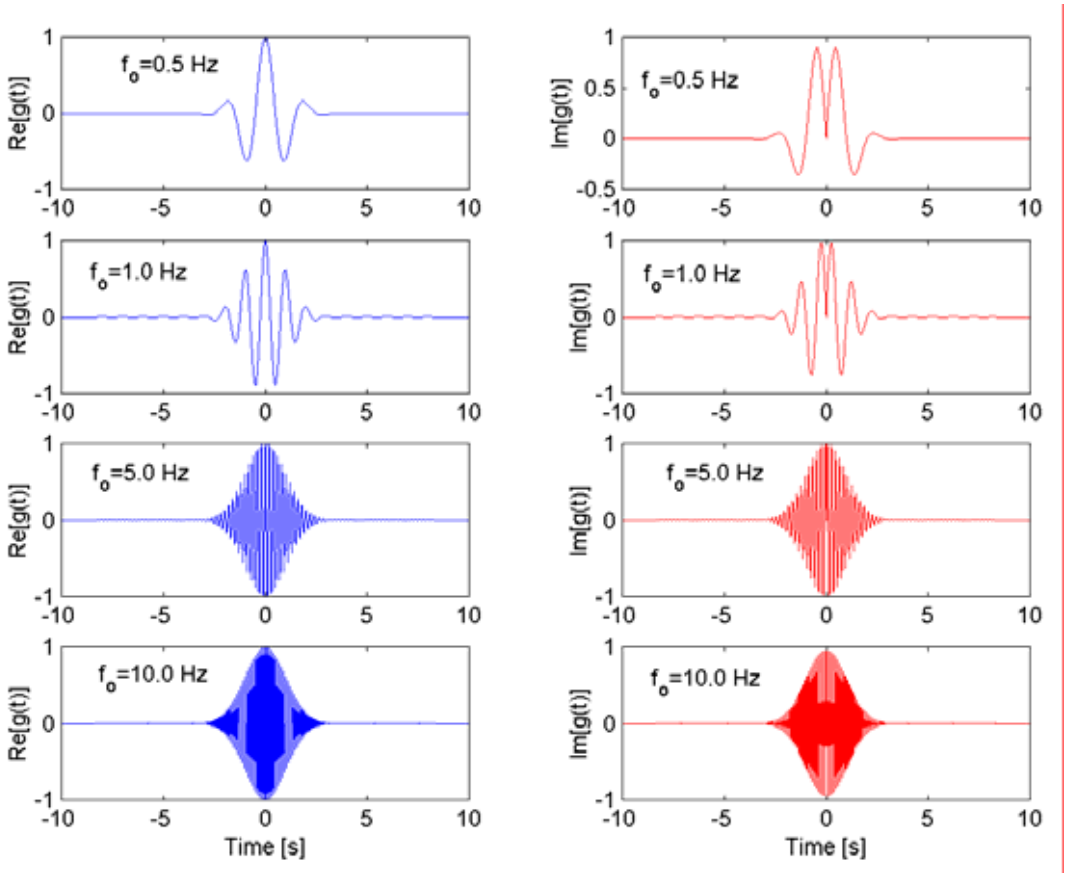

FIGURE 4.2. Real and imaginary components of Morlet wavelet for various central frequencies

extract the desired characteristics of the signal under consideration, conducting analyses in tiers to progressively refine the frequency resolution. In Chapters 5 and 7, examples demonstrate the notions of primary and secondary wavelet analyses with increasing central frequency. The central frequency can also be varied over an entire suite of values by treating f_o as a third variable in the Wavelet Transform, in essence creating a four-dimensional view of wavelet coefficients varying with time, scale and central frequency, as proposed in Wang (2001); however, such a rigorous analysis is not required if the required value of the parameter can be determined a priori using a simple inspection of the time series.

In particular, this research has explored the issue of closely spaced frequency components and the importance of central frequency tuning, as shown later in Section 7.5.5, making the following observations. To achieve complete separation, it should be first noted that the bandwidth (or width of the Heisenberg box) associated with a given frequency in a Wavelet Transform is $2\Delta f_i$. However, by basing the bandwidth measure on Gabor's mean square estimate for the Gaussian window (see Equation 4.4), only about 68% of the frequency window is accounted for. This measure essentially defines one standard deviation (σ) of the window mean, yielding a frequency window with a total bandwidth $2\Delta_f$ or 2σ, as shown in Figure 4.3. However, the duration of this frequency window is misleadingly narrow, assuming a better frequency resolution than is truly present. To more strictly define the bandwidth, one should note that roughly 95% of the window lies within 2 standard deviations of the mean, as also noted in Figure 4.3, for which the effective bandwidth is $4\Delta_f$ or 4σ. An even stricter condition would extend the definition to 3 standard deviations, also shown in Figure 4.3, encompassing 99% of the window. These considerations become important when confronted with the need to separate closely spaced modes, as demonstrated in the analyses in Chapter 8.

Therefore, Equation 4.5 may be generalized, given the need to separate two closely spaced frequency components f_1 and f_2, where the minimum central frequency for an analysis can be determined by

$$f_o = (2\alpha)\frac{f_{1,2}}{2\pi\sqrt{2}\Delta f_{1,2}} \tag{4.6}$$

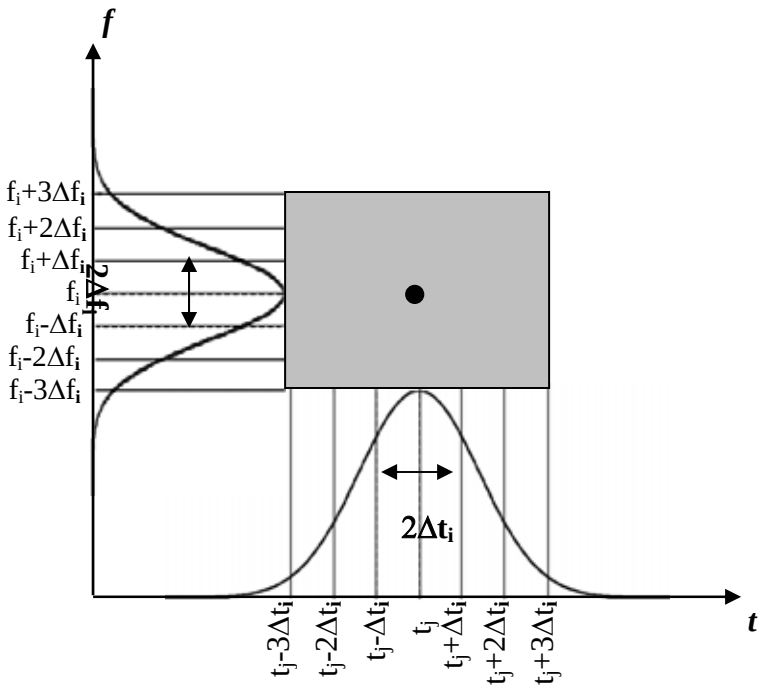

FIGURE 4.3. Effective frequency and time resolutions of Morlet wavelet and associated Heisenberg box

$f_{1,2}$ can be taken as either f_1 or f_2 or an average of the two, as the choice has little impact for small values of $\Delta f_{1,2}$, the separation between the two frequency components. α is the parameter defining how much overlap between the Gaussian analysis windows at adjacent frequencies is permitted. As shown in Figure 4.4, using the traditional mean square definition for the bandwidth of the Gaussian window amounts to $\alpha = 1$. As determined by Equation 4.6, the wavelet analysis windows centered at the two frequencies will overlap significantly. However, increasing α to 2 and applying Equation 4.6, a larger central frequency is adopted, yielding analysis windows that are narrower, and though centered at the same two frequencies, now has reduced overlap. Note that α can be increased to 3, insuring complete modal separation. As will be shown later in

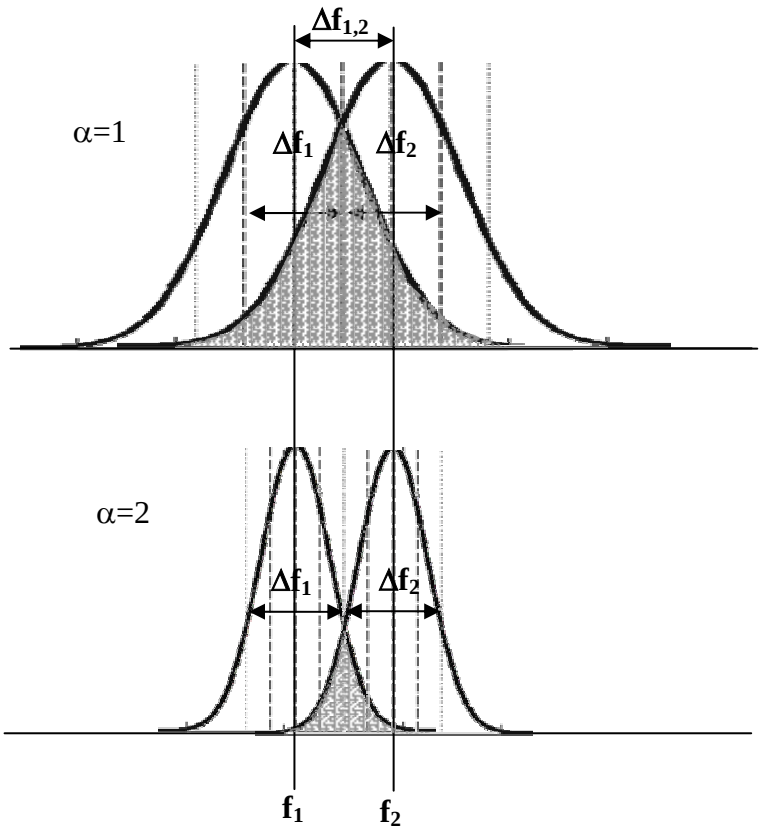

FIGURE 4.4. Schematic demonstration the implication of parameter selection for modal separation

Chapter 8, retaining $\alpha = 2$ is typically sufficient to insure adequate modal separation for system identification in most linear systems, though total modal separation via $\alpha = 3$ may be necessary for closely spaced modes when nonlinear system identification is performed.

4.2.2 Temporal Resolution: A Physical Understanding of End Effects

Similarly, the temporal resolution of the Morlet wavelet is dictated by the Gaussian window, defined using the aforementioned mean square definition (Chui, 1992)

$$\Delta t_g = \frac{1}{\sqrt{2}} \ . \tag{4.7}$$

As mentioned in the discussion of the STFT in Chapter 3, the uncertainty principle dictates that the minimum value of the time and frequency resolution product is $1/4\pi$, giving the Morlet wavelet the best possible time and frequency resolutions.

The temporal resolutions of a wavelet analysis have direct bearing on the significance of end effects in Wavelet-Transformed data, which have been noted in a number of applications, e.g. Staszewski (1998). The presence of end effects in wavelet analyses was previously credited to many familiar numerical by-products of Fourier Transforms, as they are used to calculate Wavelet Transforms according to Equation 3.9. As the Fourier Transform assumes periodicity of the time series, Torrence & Compo (1998) proposed the familiar tactic of zero padding the beginning and end of the time series, lengthening the time series to the nearest power of two to speed calculations by FFT. However, the discontinuity potentially created at the signal ends by the sudden transition to zero values in padded regions manifests itself as a smearing of energy in the wavelet time-frequency plane. While Torrence & Compo (1998) quantify the *cone of influence* to define the region where end effects are prevalent, they proposed no formal solution. An alternative remedy is to create a smoother transition to zero end values, time series tapering using windowing functions has also been proposed (Meyers et al., 1993), though the modification of signal energy as a result of the windowing function is unattractive. However, the Gaussian window on the Fourier basis of the Morlet Wavelet Transform already eliminates the more classical problem that discontinuities and a lack of

periodicity present for Fourier-based numerical implementations, implying that the persistent end effects in Morlet Wavelet-Transformed data have another source.

Though the cone of influence allows the quantification of *end effects regions,* it offers no remedy, leading to the corruption of considerable amounts of wavelet coefficients. This issue is addressed in this work through the following developments and the introduction of a reflective padding scheme. To revisit this issue, examine the convolution operation in Equation 3.8 and the parent wavelet in Equation 4.1. It is evident that, although the wavelet is focused at a given time and represents the temporal content in this vicinity, the window extends into both the past and future (see Figure 4.3), by an extent dependent on the scale being analyzed. The scaled time resolution of the wavelet is given by

$$\Delta t_i = \frac{f_o}{f_i \sqrt{2}} . \tag{4.8}$$

As illustrated by Figure 4.5, the temporal window is elongated at the lower frequency, f_1. As the analysis time t_j lies within Δt_1 of the ends of the signal, the analysis window extends into a region with no available data, yielding wavelet coefficients based on an "incomplete" signal. Intuitively, it is reasonable to then question the accuracy of wavelet-transformed data within Δt_i of the beginning and end of the signal.

Once again, this resolution in Equation 4.8 is based on the classical mean square definition in Equation 3.5, approximating the effective temporal duration as a single standard deviation of the Gaussian window. Examining Figure 4.6, in light of the previous discussion with respect to frequency resolution, it is evident that the expression

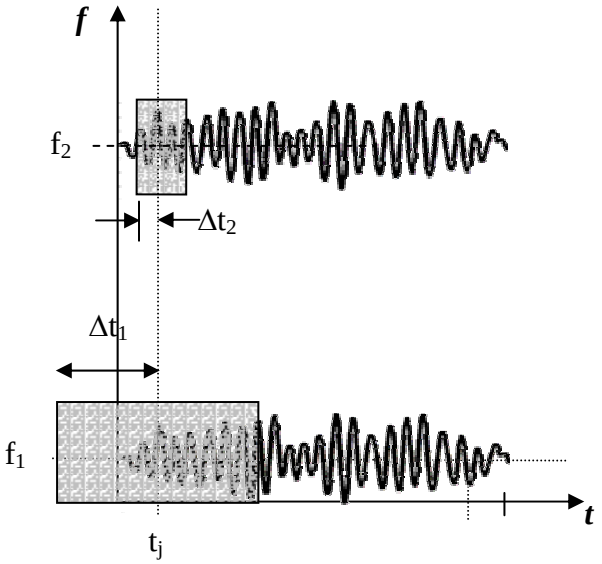

FIGURE 4.5. Illustration of region susceptible to end effects

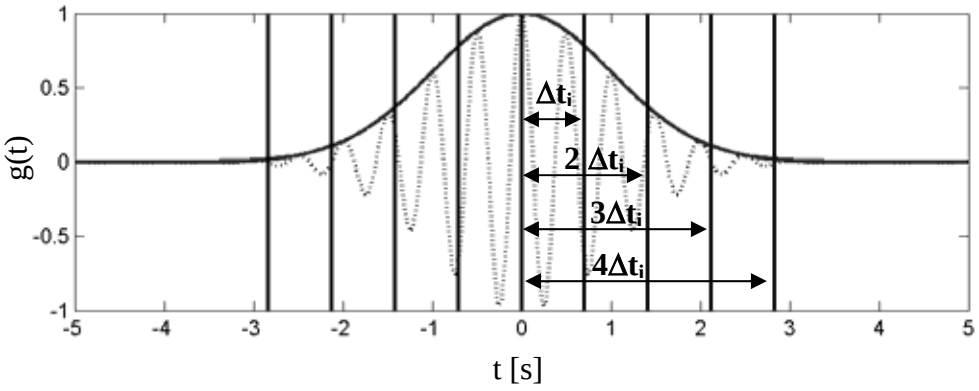

FIGURE 4.6. Real component of Morlet wavelet with Gaussian window emphasized

in Equation 4.8 accounts only for 68% of the total window area. A more stringent condition may be obtained by defining the effective temporal resolution of the Morlet wavelet as 2σ or $2\Delta t_i$, in order to account for about 95% of the Gaussian window. Defining a $3\Delta t_i$ as the temporal resolution can impose an even more stringent condition.

Dependent on the desired level of accuracy, either of these conditions can be imposed to quantify the regions potentially at risk to end effects. The general expression

$$\beta\Delta t_i \le t_j \le T - \beta\Delta t_i \,, \tag{4.9}$$

where β can be set to any positive, nonzero value, provides a practical limit on the translations *t* that can be considered in a wavelet analysis of a signal of length *T*. Thus, only wavelet coefficients satisfying Equation 4.9 can be reliably analyzed. Equation 4.8 dictates that meaningful analyses at low frequencies require larger amounts of data, so that several cycles of the low frequency phenomena can be retained.

4.2.2.1 End Effects: Influence of End Effects on Spectral Amplitude

For a simple illustration of the implications of end effects on spectral amplitude, consider a sine wave with frequency f_n (taken as 1 Hz). In theory, the Morlet Wavelet Transform of this signal yields a scalogram that is constant with time

$$\left|W(a,t)\right|^2 = 2\pi^3 a e^{-4\pi^2 (af_n - f_o)^2} \,. \tag{4.10}$$

The values of the wavelet scalogram, at a given time, can be plotted to yield an *instantaneous power spectrum*. Equation 4.10 equivalently provides this for the simple sinusoidal signal.

Performing the Morlet Wavelet Transform (f_o = 2 Hz) on the sinusoid yields a time-varying scalogram, in contrast to the anticipated result. The evolution of the scalogram with time can be examined by plotting the scalogram values along the wavelet ridge. This result, shown in Figure 4.7, displays a rounding of what should be a constant scalogram coefficient. The degree of deviation from the theoretical result, shown as the dotted line, becomes less marked in the interior of the signal. The vertical bars denote the end effects regions defined in Equation 4.9 for various values of β and indicate that the calculated Wavelet Transform will more accurately approach the theoretical result for $\beta > 2$.

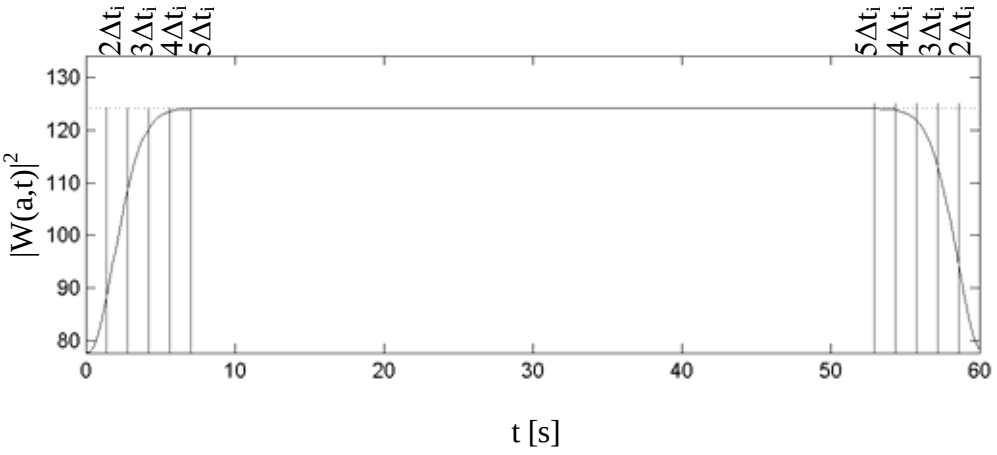

FIGURE 4.7. Scalogram of sine wave along ridge. Dotted line denotes theory and solid line is calculated result. Vertical bars demarcate end effects regions, $\beta\Delta t_i$, for β=1-5

Figure 4.8 further illustrates the ramifications of analyzing instantaneous power spectra taken from end effects regions. The calculated instantaneous spectra at each time are plotted one atop the other in gray, essentially collapsing the scalogram in time. According to Equation 4.10, there should be no variation among them. However, by

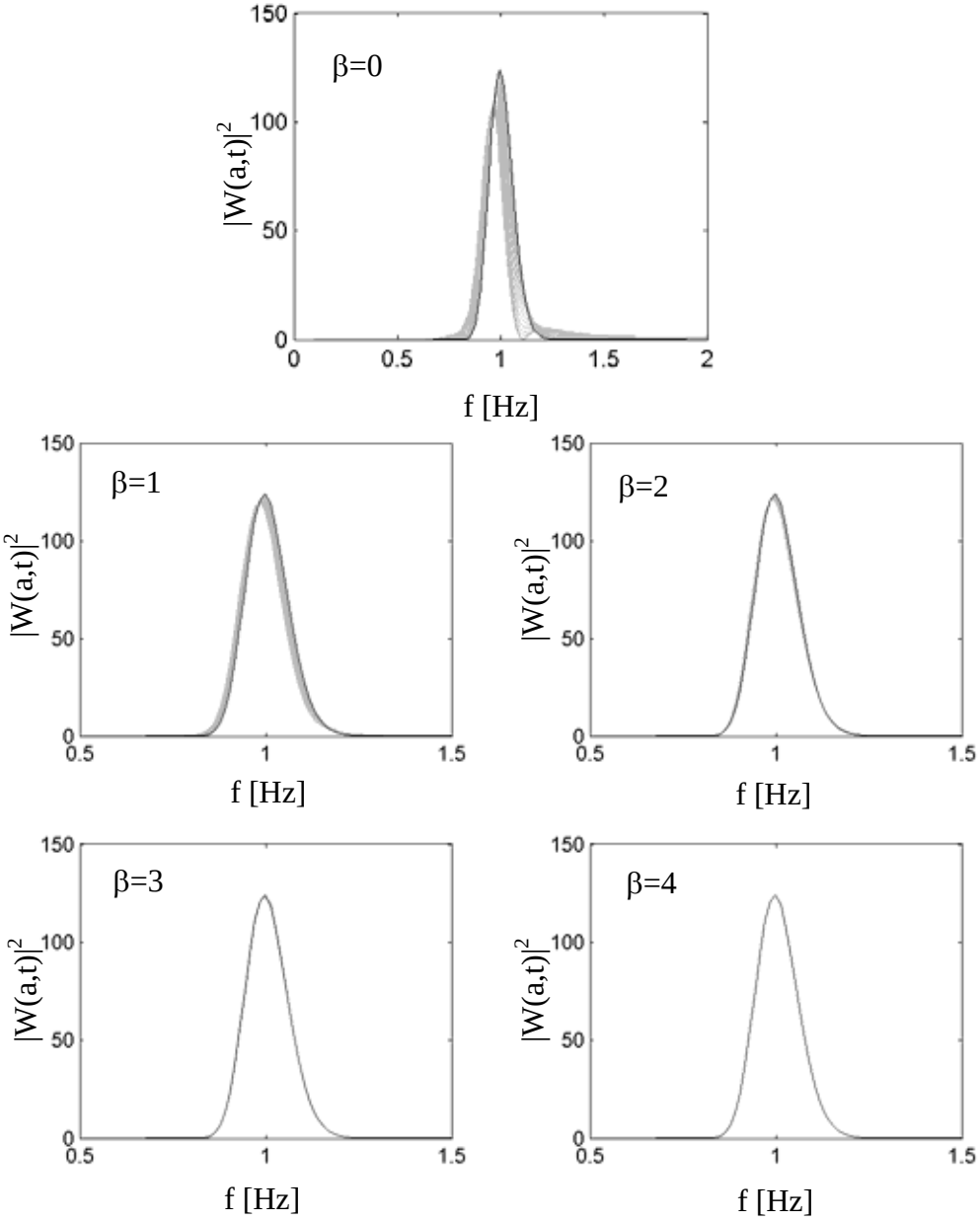

FIGURE 4.8. Deviations of simulated instantaneous spectra (gray) from theoretical result (black) as end-effects regions are progressively neglected

including the spectra from end effects regions ($\beta = 0$), there is considerable variance in the plot, as the spectra show notable deviations from Equation 4.10 shown in black. Note that the deviations are more marked on the high frequency side of the spectrum, a result of the lessened frequency resolution at lower scales. Through a more stringent condition, increasing β in Equation 4.9, the neglected regions lengthen, the variance among the spectra is reduced, and the deviations from the theoretical expression are minimized. Note that even the commonly used definition of wavelet temporal duration ($\beta = 1$) is an insufficient measure of the end effects region producing these deviant spectra. Unfortunately, the use of larger β values reduces the amount of useable transformed data. Thus, while $\beta = 4$ produces a sufficiently accurate means to quantify end effects regions and separate deviant spectra, $\beta = 3$ is shown in Chapter 8 to be sufficient for most analyses in terms of capturing accurately the spectral amplitude.

4.2.2.2 End Effects: Influence on Spectral Bandwidth Estimation

As a consequence of the windowing applied by the Gaussian function in the Morlet wavelet, the bandwidth of the resulting wavelet instantaneous spectra are larger than their Fourier equivalent. This gives the appearance of a larger value of effective damping in the signal, the extent of which depends on the scale analyzed. Consider the Morlet wavelet expression in the Fourier domain, given by Equation 4.2. The half-power bandwidth introduced in Chapter 2 can be used to provide a simple measure of the bandwidth of wavelet spectra. The HPBW is defined in this case as the two frequencies that coincide to half the amplitude of the wavelet's instantaneous spectral peak, shown as f_1 and f_2 in Figure 4.9.

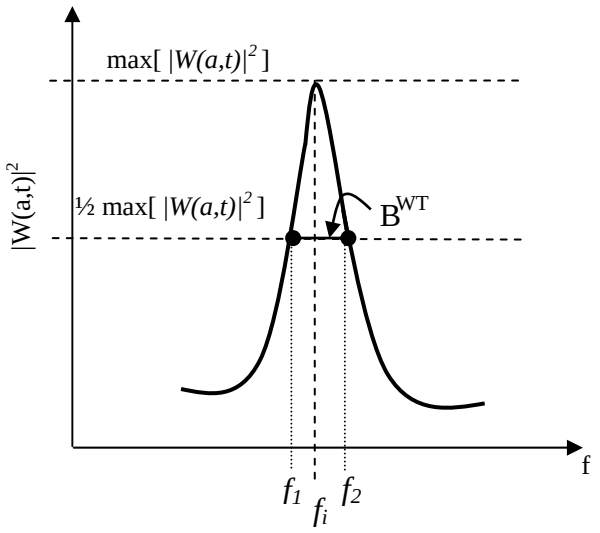

FIGURE 4.9. Schematic representation of half-power bandwidth estimation

The HPBW is defined the difference between these two frequencies

$$B_{WT} = f_2 - f_1 . \tag{4.11}$$

The two frequencies corresponding to the half-power level of the Morlet spectra are given by

$$f = f_o \pm \frac{\sqrt{\ln(2)}}{2\pi} \tag{4.12}$$

yielding a half-power bandwidth of

$$B_{morl} = \frac{\sqrt{\ln(2)}}{\pi} . \tag{4.13}$$

This is the half-power bandwidth of the Morlet wavelet. For a simple sine wave, the Morlet Wavelet Transform will localize at the frequency of the sine wave, though the bandwidth of the wavelet spectrum will be completely dictated by the parent wavelet, as

a sine in theory has no bandwidth. Recalling that the resolutions of the Wavelet Transform are merely scaled versions of the parent wavelet, this half-power bandwidth measure in Equation 4.13 can be similarly scaled by dividing by a. Note that in the definition of the half-power bandwidth, the spectra is assumed symmetrical. Due to the multi-resolution nature of wavelets, wavelet spectra broaden toward the higher frequencies, but for a narrowbanded spectrum, the assumption of symmetry can be retained. Therefore, the scale at which this half-power bandwidth is evaluated should be the scale defining the ridge of the transform, at which the signal energy is focused. Understandably, this scale corresponds to the instantaneous frequency of the system, or in this case, the frequency of a simple sine wave, f_n. Thus the half-power bandwidth of a wavelet-transformed sine wave is given by

$$B_{WT} = \frac{\sqrt{\ln(2)}}{\pi}\frac{f_n}{f_o}. \tag{4.14}$$

As discussed in the previous example, deviations in terms of amplitude of the instantaneous spectra were sufficiently mitigated by neglecting those spectra which were generated in the end effects regions, defined by assuming $\beta = 4$. As shown in Figure 4.7, the characteristic rounded amplitude deviations of end effects regions seem to diminish after $4\Delta t$. However, the influence of end effects on more sensitive spectral measures such as the half-power bandwidth is not completely remedied by neglecting this end region. The implications of not neglecting spectra drawn from end effects regions is shown in the first image in Figure 4.10, revisiting the same signal from Section 4.2.2.1 for a more refined wavelet analysis with f_o=5 Hz. The calculated half-power bandwidth deviates significantly at the ends of the signal from the theoretical result shown by the dashed line.

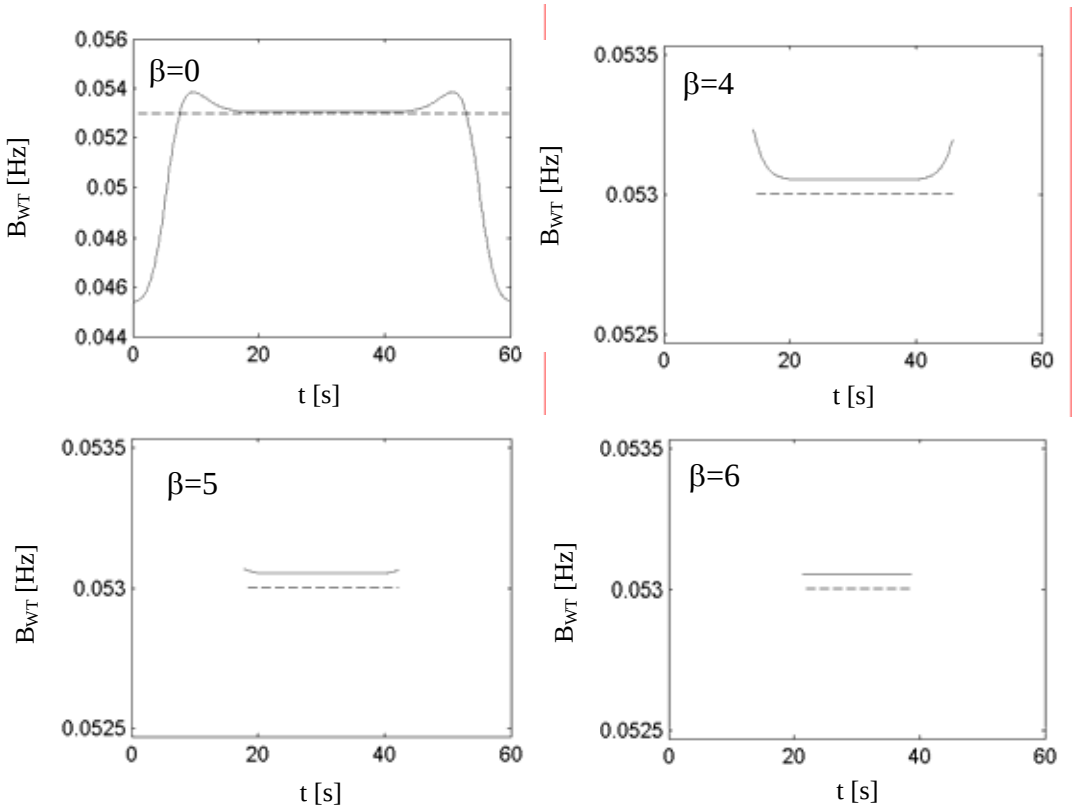

FIGURE 4.10. Improvements made in half-power bandwidth estimates by successively neglecting larger end effects regions. Theoretical prediction (dashed) and calculated result

Using the criteria of $\beta = 4$ to neglect regions defined by Equation 4.9 improves the result, though the deviations from theory are still quite evident in the tails. By selecting more stringent conditions on β, the deviations from theory are minimized and the bandwidth estimated in the simulation takes on a constant value. For $\beta = 6$, the deviation between theory ($B_{WT} = 0.053$) and simulation ($B_{WT} = 0.053$) are essentially identical. Though the deviations in Figure 4.10 are easily explained by the end effects phenomenon, simply neglecting these regions in analysis yields to a considerable loss of data, especially in the case of bandwidth estimation, where for $\beta = 6$, only one-third of the transformed signal is deemed reliable.

4.2.2.3 End Effects: Melioration via Reflective Padding

The loss of considerable regions of a signal is the unfortunate consequence of end effects. Particularly for more sensitive measures like bandwidth, the loss of useable transformed signal can be quite significant: approximately 10 times the effective duration of the lowest frequency component of interest. Meyers et al. (1993) noted the presence of these effects and compiled a number of strategies for their minimization. However, in these discussions, the authors largely attributed the problem to one associated with the use of Fourier transforms in calculating the wavelet transform. As a result, the authors presented strategies directly from Fourier processing annals. The first remedy, the introduction of a cosine window to preprocess the time history, essentially led to a loss of meaningful data. The authors then proposed detrending the data and removing the mean to enhance performance of the Fourier transform and found the technique to have no benefit in mitigating wavelet end effects. Though these are common methods for Fourier processing, they did not provide great utility for wavelets since they did not address the aforementioned root cause: the wavelet's assimilation of past, present and future information in each analysis window. However, their final remedy to pad the data with a short tail gradually approaching zero did focus inadvertently on this root cause. Though never motivated in their work as such, the padding of the beginning and end of the signal with surrogate values to place the true signal of interest at the center of the transformed vector has promise. In so doing, the "dummy" values at the tails were allowed to be corrupted by the end effects phenomenon, preserving the true data in question. Meyers et al. (1993) chose this technique to force periodicity upon nonperiodic data, again reflecting the authors' theory that Fourier transforms were ultimately to blame. Though

this was a positive first step, the rather arbitrary tails of empirically defined length did not preserve signal characteristics at the ends, nor provided recommendations on the length of tails required to mitigate end effects corruption. In a later study, Torrence & Compo (1998) attempted a similar elongation of a signal at its ends using zero padding; however, it should be reiterated that the wavelet considers both past and present information at each time step, so the addition of zero values still provides wavelet coefficients at the ends that are derived in part from a "zero-value" signal. Though the greatest contribution to a wavelet coefficient at that point in time comes from the signal immediately surrounding that point, data displaced further in time are also considered to an extent. Therefore the signal cannot be padded with zero values or arbitrary non-zero values as suggested by Meyers et al. (1993), as analysis of the true signal near the beginning and end of the original signal will certainly dip into these padded regions. Thus, the regions should locally preserve the frequency and bandwidth characteristics of the signal.

This local preservation can be achieved by merely reflecting the signal about its beginning and end, appropriately based on the odd or even character of the signal. If continuity of the signal is not preserved in the transition to the padded region, the wavelet will rightfully detect a discontinuity. Thus improper padding can equally introduce further errors to Wavelet Transforms. To illustrate, consider a simple sine and cosine pair shown Figure 4.11. To preserve continuity at the ends, even functions must be directly reflected and odd functions must be reflected negatively. This same notion can be extended to more complicated signals. Figure 4.12 illustrates an arbitrary signal and the shaded regions that will potentially be useless following the Wavelet Transform.

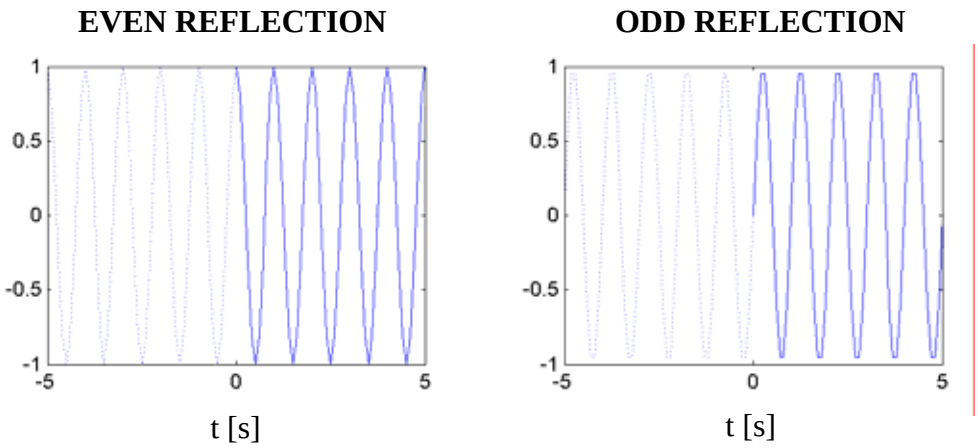

FIGURE 4.11. Even and odd signals and their respective reflections (dotted line)

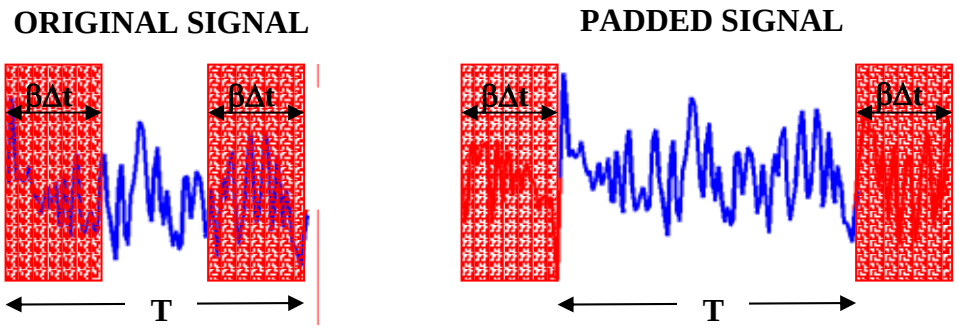

FIGURE 4.12. Concept of signal padding for arbitrary function

Depending on the level of β and f_o selected, these regions can consume two-thirds or more of the signal. In the padding operation, the signal is elongated by $2\beta\Delta t$ as the signal is continuously reflected about the start and end of the signal. Now the two shaded regions envelop the dummy reflections of the signal, while entire duration of the true signal is conserved and can be analyzed with little contamination from end effects.

Mathematically, this operation may be conducted by considering a signal x described by

$$x = \begin{bmatrix} x_1 & x_2 & \dots & x_N \end{bmatrix} \tag{4.15}$$

with sampled time vector

$$t = \begin{bmatrix} t_1 & \dots & t_N \end{bmatrix}. \tag{4.16}$$

The temporal duration of the analyzing wavelet is then determined using Equation 4.8 based on the lowest frequency being considered in the analysis (f_1), as this frequency will yield the longest duration Δt_1 and thereby dictates the maximum end effects anticipated. β is then selected based on the desired accuracy of the resulting spectra, and the time ordinates closest to the termination of the end effects regions are then identified by

$$t_0 = \min\left[t > \beta\Delta t_1\right] \text{ and } t_m = \max\left[t < (t_N - \beta\Delta t_1)\right]. \tag{4.17}$$

The modified signal x_{MOD} is constructed by reflecting the signal x (for even functions) or its negative (for odd functions) for the duration of $\beta\Delta t_1$ about t_1 and t_N, according to

$$x_{MOD} = \begin{bmatrix} \pm x_n & \pm x_{n-1} & \dots & x_1 & \dots & x_N & \pm x_{N-1} & \dots & \pm x_0 \end{bmatrix} \tag{4.18}$$

where x_n and x_0 are the values of the sampled signal x at time t_0 and t_m. x_{MOD} is then Wavelet Transformed and the coefficients calculated from the padded regions are simply neglected, retaining only the coefficients of the true signal for meaningful analysis. This pre-processing technique will be referred to herein as *reflective padding*.

4.2.2.4 End Effects: Efficacy of Reflective Padding Scheme

As sine waves are represented by wavelets in a very simplistic form, they are now used to illustrate the efficacy of the proposed padding scheme. Recall that the wavelet instantaneous spectrum of a simple sine wave does not vary in time. As shown by Figure 4.7, the scalogram of a simple sine, when viewed purely as a function of time, is a constant. Deviations from that constant were shown to be the hallmark of end effects in the Wavelet Transform. Thus any signal composed of a series of *M* sine waves, will yield a scalogram containing *M* constant ridges in the time-frequency domain. The values of the scalogram along each ridge can be individually examined for deviations from the theoretical result. Fortunately, though this summation of sines is capable of generating complicated time series, they are simply analyzed in the wavelet domain by virtue of its inherent bandpass filtering. Therefore, the efficacy of the reflective padding scheme on a complicated time series can be demonstrated by examining the simple behavior of the component sines in the wavelet domain.

The following signal is generated for this example

$$x(t) = \sum_i \sin(\omega_i t) \tag{4.19}$$

where $\omega_i = 2\pi$ [0.28 Hz, 0.5 Hz, 0.7 Hz, 1.0 Hz, 1.4 Hz, 1.65 Hz, 1.9 Hz, 2.25 Hz, 2.7 Hz, 3.25 Hz]. The signal was simulated for 10 minutes, sampled at 10 Hz. Snapshots of the first 100 s of the signal are shown in Figure 4.13. As a consequence of the multi-resolution character of wavelets, at higher frequencies, the frequency resolution is reduced. Thus, the last 6 harmonics may overlap one another considerably if a low

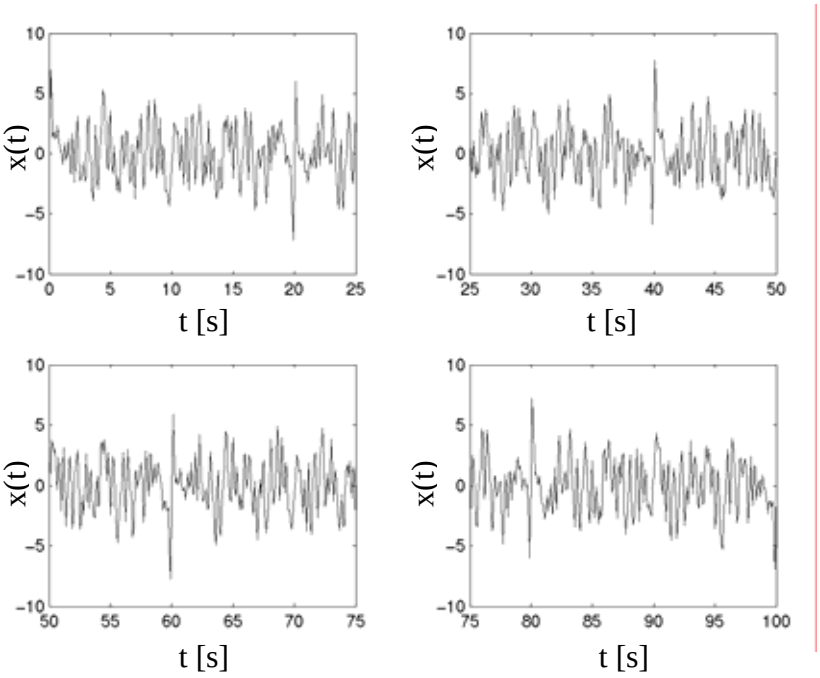

FIGURE 4.13. Simulated time series for validation of padding scheme

frequency Morlet wavelet is chosen. Therefore, to enhance the frequency resolution and separate closer-spaced, high frequency content, a central frequency of 10 Hz is chosen for the analysis.

Following the calculation of the Wavelet Transform, the ten ridges are extracted from the resulting scalogram. Though omitted for brevity, these plots display a characteristic rounding as previously observed in Figure 4.7. It is evident that the end effects regions, even for such a large central frequency, decrease significantly with increasing frequency, as indicated by Equation 4.8. This may be the reason that previous studies did not encounter significant manifestations of end effects, as most wavelet analyses have been concerned with higher frequency mechanical systems. However, in

the study of low frequency Civil Engineering structures, the presence of end effects should be anticipated and remedied, making the proposed padding procedure of essence.

The overlaying of the instantaneous spectra in time to collapse the scalogram along that axis demonstrates the deviations that occur in these end regions, as shown in Figure 4.14. The calculated wavelet spectra are shown in gray, with the theoretical prediction in black. First note that the spectra again have a variable bandwidth that decreases with frequency, as discussed previously. This is a consequence of the enhanced frequency resolution of the wavelet for large scales. For the low frequency components, the deviations are not as evident, due to the scaling of the plot. However, the deviations are more marked for the high frequency components due to the lack of frequency resolution. Although the end effects regions for the higher frequency modes are not as lengthy, the deviations of the few spectra taken from these regions are considerable, especially in the case of the 10^{th} component. It is evident that the 10 Hz Morlet wavelet was capable of separating the modes of the system. Note that the quality of Figure 4.14 could have been enhanced by simply neglecting the spectra that were derived from end effects regions, however that results in a loss of a significant amount of data.

The lowest harmonic component produced the largest end effects region in the wavelet skeleton, approximately 100 seconds of corrupted coefficients. Thus, this value, at minimum, must be used to pad the signal, as discussed previously. The success of the padding operation is first gauged by looking at Figure 4.15, an overlay of the instantaneous spectra, as was shown for the unpadded case in Figure 4.14. In this case, the spectra generated from the Wavelet Transform of the modified signal in Equation

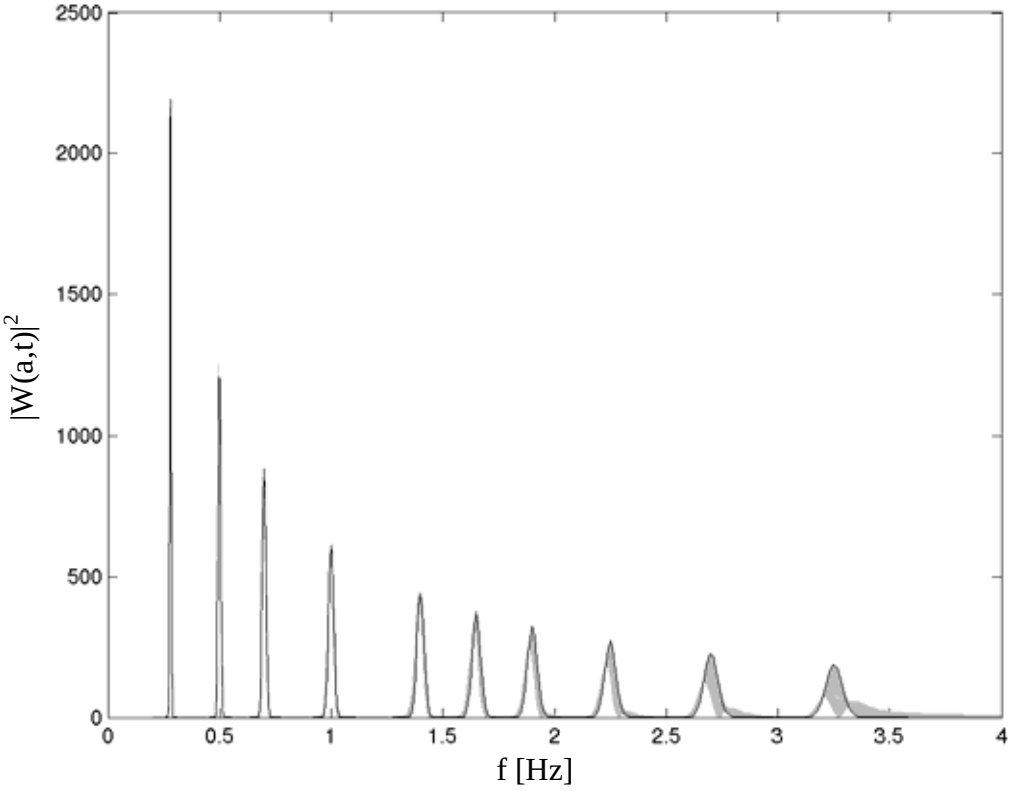

FIGURE 4.14. Superposition of instantaneous spectra over all time for calculated Wavelet Transform (gray) with theoretical prediction (black)

4.18 are plotted. Only spectra obtained from the true signal are plotted and all those determined from the virtual values of the padded signal are discarded. Note that there is no discernable difference between the predicted and calculated results when assuming $\beta = 4$.

In terms of bandwidth estimates, the half-power bandwidth's accuracy is enhanced in these end regions when the padding scheme is employed. For brevity, a demonstration is provided using only three of the modes. Figure 4.16 displays the unpadded bandwidth measures, demonstrating the characteristic trademark of end effects. Note again that the portions of the signal lost due to end effects is more marked at lower

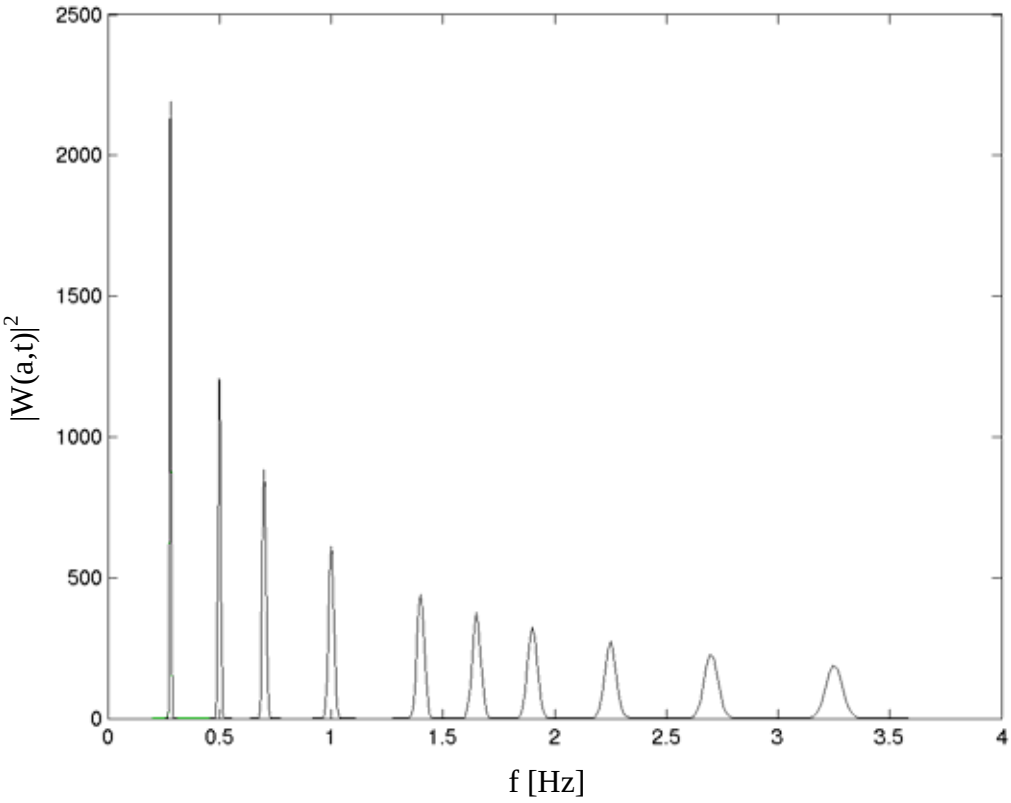

FIGURE 4.15. Superposition of instantaneous spectra over all time for calculated Wavelet Transform (gray) with theoretical prediction (black) with padding operation

frequencies, where nearly one-third of the values have been compromised. As demonstrated in Figure 4.16, $\beta = 6$ is a necessary condition to remove all traces of end effects in the bandwidth measure. Using this condition in conjunction with the padding operation, a precise definition of the half-power bandwidth is maintained over the entire duration of the signal, as shown in Figure 4.16d-f. The simulated bandwidth measure is less than 0.2% of the theoretical prediction for all of the modes in this example.

Although padding the signal with itself insures that the spectral content of surrogate regions locally matches that of the true signal, this should not be viewed as a

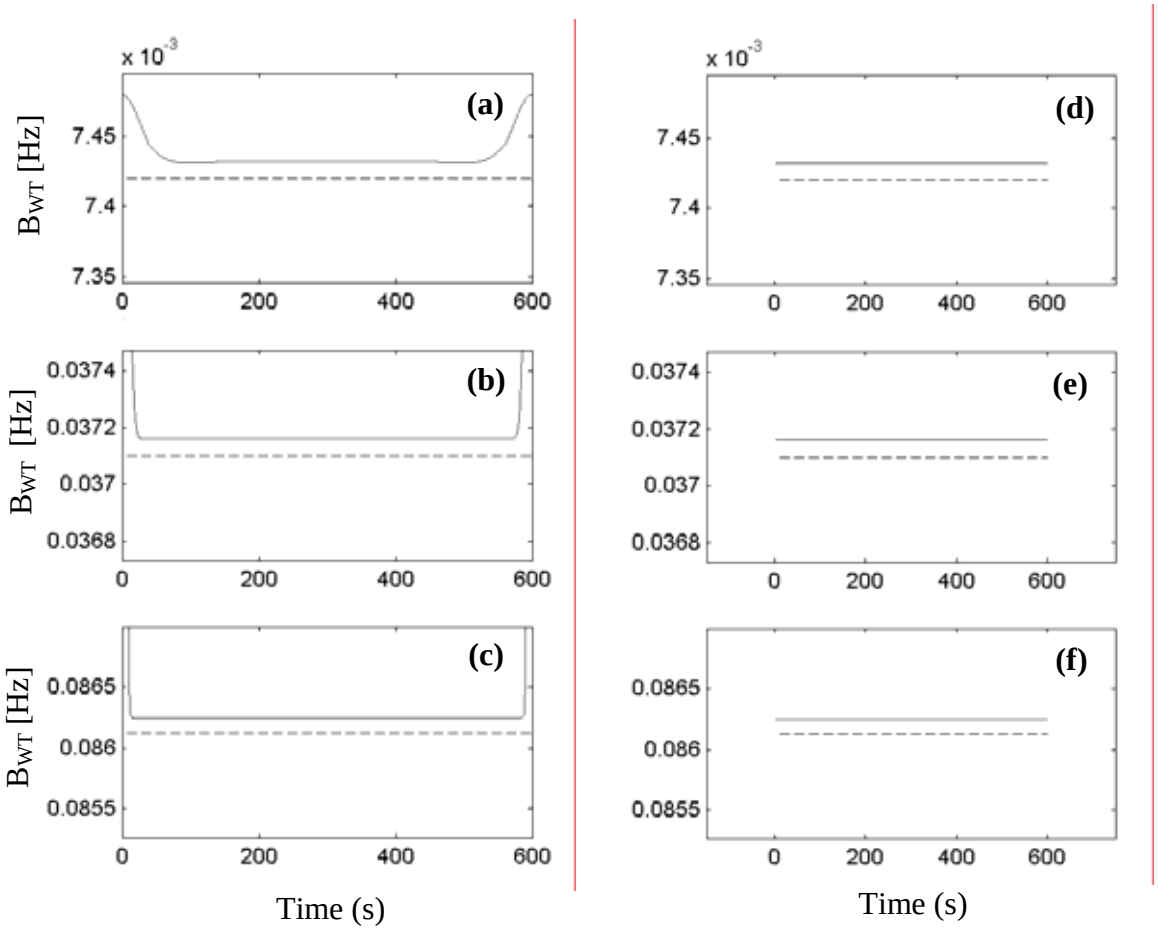

FIGURE 4.16. Efficiacy of padding operation to reduce end effects in wavelet bandwidth measures, theoretical prediction (dashed) and simulation (solid): (a) first mode half-power bandwidth without padding, (b) fifth mode half-power bandwidth without padding, (c) tenth mode half-power bandwidth without padding, (d) first mode half-power bandwidth with padding and $\beta = 6$, (e) fifth mode half-power bandwidth with padding and $\beta = 6$, (f) tenth mode half-power bandwidth with padding and $\beta = 6$

way to defeat the Heisenberg Uncertainty Principle. It should be reiterated that the end effects are merely a physical manifestation of the wavelet's inherent analysis windows, which lengthen as f_o is increased. Although the end effects can be repaired, the larger temporal analysis windows imply that changes in the system that occur in shorter time intervals than this window may be completely obscured. Thus, the central frequency should be kept to the smallest value possible to provide the needed frequency resolution without compromising the ability of the wavelet to detect nonlinear and nonstationary phenomenon.

4.2.2.5 End Effects: Comparison of Zero Padding and Reflective Padding

A comparison of the proposed reflected padding technique and the zero padding solution in Torrence & Compo (1998) is shown in Figure 4.17, zooming in at only one end, since the effects manifest themselves identically at both ends of the signal. The example shown in Figure 4.17a is the magnitude of the wavelet skeleton for a 2 Hz cosine wave. In this case the signal begins and terminates with a value of 1. Again, in theory this skeleton should be a constant value over all time. Without any padding, the skeleton magnitude gradually approaches the anticipated constant value. Padding with zeros actually amplifies the characteristic rounding within the cone of influence. On the other hand, using the padding scheme proposed herein, the wavelet skeleton magnitude achieves a constant value immediately, mitigating the presence of end effects. The theoretical magnitude of the wavelet skeleton is shown by a dotted line, which is actually right on top of the reflective padded result. Figure 4.17b shows the same analysis for a sine wave. In this case, the skeleton magnitudes without padding are not as dramatically diminished,

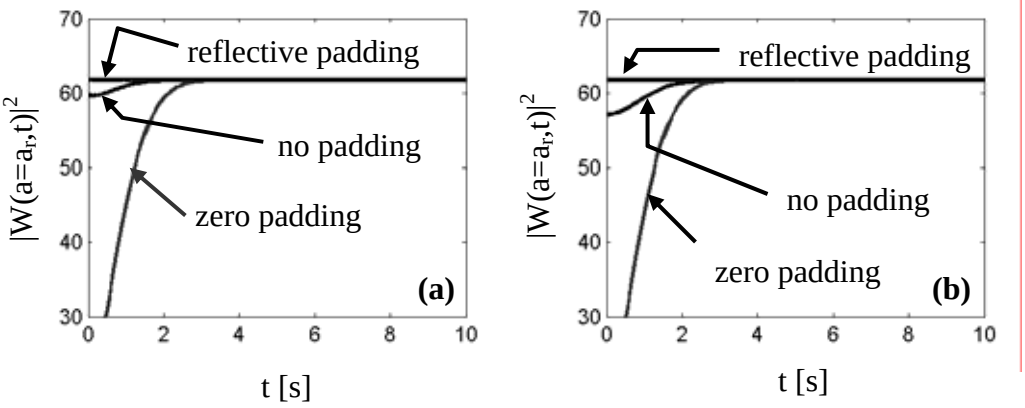

FIGURE 4.17. (a) 2 Hz cosine; (b) 2 Hz sine – influence of padding on wavelet skeleton magnitude

due to the fact that the signal already begins and ends with zero values, providing some periodicity of the signal from a Fourier perspective. Using the odd function, reflective padding scheme recommended here, the end effects are effectively mitigated. While the use of zero padding to the nearest power of two may increase the efficiency of calculations when Wavelet Transforms are calculated via Fourier Transforms, this measure does nothing to mitigate end effects arising from incomplete information and may even enhance them. Subsequent examples throughout this study will demonstrate the improvements in wavelet-based system identification as a result of this padding operation, as well as the lingering limitations.

4.2.2.6 Tuning Temporal Separation

It should be noted that temporal resolutions of wavelets not only dictates the end effects phenomenon, but also governs the ability to separate events in close temporal proximity. Equation 4.8 may be used to determine the central frequency necessary to separate two

closely spaced events in time. The actual duration of signal characteristics from inspection of the time series, e.g. the time duration of a single peak or pulse in the signal, gives some indication of the time resolution that would be required. When deciding what central frequency is appropriate for a given analysis, the compromise between time and frequency resolution must always be carefully considered. The recommendation of this work is to approach analysis in tiers, particularly for complex systems or for those with more wideband characteristics. Such tiered analyses are presented in Chapters 5 and 7, with the examples in Chapter 7 providing more discussion on how to identify the necessary time resolution from characteristics of a time series. Just like zoom transforms in Fourier analysis (Bendat & Piersol, 1986), a fine frequency resolution wavelet analysis can be performed to accurately identify the various components in the signal. Then over each identified range of frequencies, a more temporally refined Wavelet Transform may be conducted to unveil time-varying properties, as illustrated later in Chapter 7.

4.3 Discretization of Time-Frequency Plane

The use of this continuous Wavelet Transform is attractive not only for its analogs to Fourier Transforms, but more importantly since it is not constrained in terms of resolution by the rigid discretization of Discrete Wavelet Transforms. The use of continuous Wavelet Transforms permits finer frequency resolution necessary for the nature of the analysis of the narrowband signals encountered in this research. As discussed in Chapter 3, frame theory governs the discretization of the time-frequency plane for windowed Fourier Transforms and Wavelet Transforms. In the case of the Morlet wavelet introduced in this chapter, its intimate relationship to the Fourier

Transform implies that it shares many aspects of the frame theory associated with windowed Fourier Transforms. Work by Daubechies (1990), discussed in Carmona et al. (1997) and Mallat (1998), identified a critical sampling density called the *Nyquist density*. In this framework, given that the time axis is sampled at increments of δt and the frequency axis at δf, a complete representation is obtained when

$$\delta t \delta f = 1. \tag{4.20}$$

According to the *Balian-Low Theorem*, this would require the window function on a Fourier basis to be either non-smooth or have slow time decay. This violates the basic conditions placed on the parent wavelets in Chapter 3 and excludes many windows with desirable properties used in Short-Time Fourier Transforms. As a result, an orthogonal Fourier basis with a differentiable window of compact support, either through Morlet wavelets or Short-Time Fourier Transforms, is not possible. (Note this fact motivated largely the popularity of many Discrete Wavelet Transforms.) The choice of a discontinuous window, e.g rectangular (boxcar), yields an orthogonal windowed Fourier bases according to the condition in Equation 4.20. Though this window is commonly used in Fourier analysis, its utility in Short-Time Fourier Transforms is limited due to its bad frequency localization. In general, all windows satisfying the expression in Equation 4.20 will be poorly localized or have poor regularity (Carmona et al., 1998).

One alternative would be to undersample the space by having $\delta f \delta t > 1$, yielding a representation that is not complete. Or conversely, sampling at less that 1 to yield a representation that may be overcomplete (Carmona et al., 1998). In the development of a

disccretization of scheme in this work for the Morlet wavelet, the following observations become relevant:

- The representation can still be complete as long as the full time-frequency domain is covered by the Heisenberg boxes of the sampled times and scales, forcing the sampling at less than the Nyquist density.
- In reconstruction, there are stability concerns associated with Wavelet Transforms in such cases, though that is not an issue, given that reconstruction is not within the scope of this work.
- A complete but oversampled representation may be redundant and thus strategies to minimize redundancy must be formulated.

Unfortunately, few authors give much thought to the appropriateness of discretizations used in conjunction with Morlet wavelets. At minimum, the discretization of the time-frequency domain must be less than the Nyquist density to avoid the loss of information, without resorting to a resolution that is so fine that it results in a prohibitive redundancy of information. Torrence & Compo (1998) simply proposed the use of fractional powers of two to discretize the scale (frequency) variable. However, this does not account in any way for the bandwidth of the parent wavelet, potentially providing redundant information in the frequency domain, even if the Nyqusit density condition is satisfied. Other applications may arbitrarily or uniformly discretize the analysis scales, with no regard for frame theory and the frequency resolution of the parent wavelet. Therefore, this study will address this issue by exploiting the flexibility this continuous

transform affords through an adjustable discretization framework that is considerate of the wavelet bandwidth.

The duration of the Morlet wavelet in the frequency domain based on the mean-square definition of Gabor in Equation 3.6 can be used as a guideline for the specification for the discrete frequencies at which to evaluate the transform to minimize the redundancy and gain meaningful information. Assuming the retention of all sampled time domain data forces δt in Equation 4.20 to the inverse of the signal sampling rate f_s. Thus the discretization of scales to insure sampling at less than the Nyquist density requires only that $\delta f < f_s$.

For the Morlet wavelet, the basic frequency bandwidth δf is given by $2\Delta f_i$, where Δf_i is defined in Equation 4.5. This requires that

$$\frac{2\Delta f_g f_i}{f_o} < f_s \tag{4.21}$$

The maximum frequency f_i that can be considered in an analysis is the Nyquist frequency, or one-half the sampling rate. As a result

$$\Delta f_g < f_o \tag{4.22}$$

where Δf_g, given in Equation 4.4, takes on a value of approximately 0.113 Hz. Recall that to satisfy admissibility conditions, f_o must take on values greater than 0.8, thus satisfying this condition. Therefore, for all practical applications, as long as the scales are discretized so that adjacent frequencies are separated by one bandwidth of the analyzing

wavelet, the sampling will be less than the Nyquist density and will adequately represent the signal's time-frequency domain.

The above discussion demonstrates that the wavelet representations meeting these minimum requirements are complete, however, the issue of overresolution must still be addressed. Figure 4.18 demonstrates this concern. The figure shows four slices of wavelet scalograms at a given time, yielding wavelet instantaneous frequency spectra. The signal analyzed is a sine wave at 1 Hz. The scales of the Wavelet Transform are discretized by an arbitrary spacing, inconsiderate of the bandwidth. As the discretization of scales becomes finer and finer, the bandwidth of the wavelet analysis windows at adjacent frequencies begins to overlap. By allowing significant overlap between wavelet analysis windows at neighboring frequencies, significant overresolution is apparent, particularly in the last spectrum. Also note that the use of arbitrary discretization that does not vary with frequency causes the lower frequencies to be overresolved more significantly than higher frequencies.

To avoid this, a framework for the discretization of scales is presented here, attentive to the frequency-dependent bandwidth of the Morlet wavelet. The frequencies to be evaluated in the wavelet analysis are specified by

$$\tilde{f} = \left[f_1 \equiv f_{\max}, f_2 = f_1 - OF\Delta f_1, \ldots, f_i = f_{i-1} + OF\Delta f_{i-1}, \ldots, f_{\min} \right] \qquad (4.23)$$

where $f_{max} \leq f_s/2$ is the maximum frequency of interest, f_{min} is the minimum frequency of interest that can be no smaller than $1/T$ where T is the duration of the analyzed signal, and OF is introduced as an overlap factor to permit flexibility. Beginning at the highest desired frequency and working downward insures that the discretization is conservative,

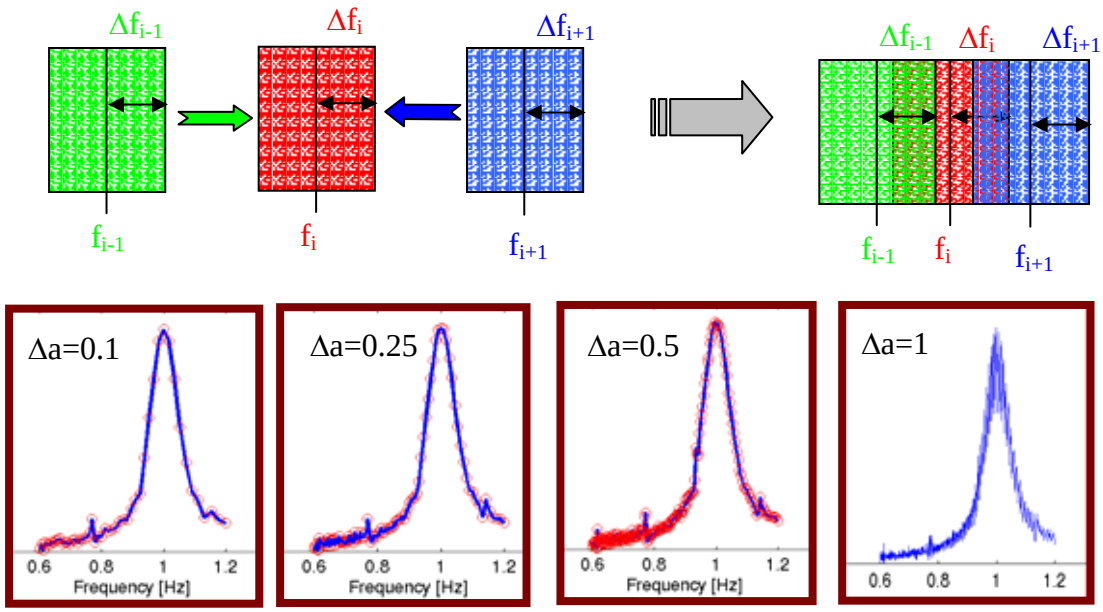

FIGURE 4.18. Implications of overlapping analyzing frequencies

as the bandwidth at higher frequencies is larger. The vector of frequencies is then transformed, according to Equation 4.3, to scales for analysis. The overlap factor, when set to 2, discretizes at the bandwidth of the Morlet wavelet, in a mean-square sense, satisfying the Nyquist density condition as long as the central frequency satisfies Equation 4.22. Increasing the overlap factor beyond 2, provides a more conservative and potentially incomplete representation if

$$\frac{OF\Delta f_g}{2} < f_o \tag{4.24}$$

is not satisfied. Thus overlap factors of 2 and under are used in this study to provide a smooth description of frequencies in the wavelet analyses and insure that Equation 4.24 is satisfied.

4.4 Ridge Extraction Techniques

When the Fourier Transform of the parent wavelet is sharply concentrated at a fixed value of frequency, as is the case of the Morlet wavelet in Equation 4.2, the continuous Wavelet Transform will have the tendency to "concentrate" at the frequency values associated with dominant harmonics in the signal, defining a series of curves called ridges that evolve with time. These ridges, discussed in Section 3.7.3, are locations where the frequency of the scaled wavelet coincides with the local frequency of the signal, as shown in Equation 3.30. Note that this equation illustrates that the scales corresponding to these ridges can be directly used to identify the instantaneous frequency, as shown in Figure 4.19. The ridge in the time-frequency domain is shown, as well as a slice of the scalogram at a specific time to yield an instantaneous spectrum focused at the instantaneous frequency of the system and with measurable bandwidth indicative of the richness of frequency content about this mean frequency component. While this avoids the need for the differentiation in Equation 3.35, the wavelet phase can still be used, often more precisely, to determine the instantaneous frequency for the class of asymptotic signals, using wavelet skeletons introduced in Chapter 3. The extracted skeletons are also shown in Figure 4.19.

The extraction of the ridges and their associated skeletons can be accomplished by a number of techniques. The *differential methods* are perhaps the most basic way to detect the ridge. In the case where the signal possesses a single ridge, it is sufficient to seek the maxima of the wavelet modulus over the scale variable at every time instant. This global maxima search is defined as

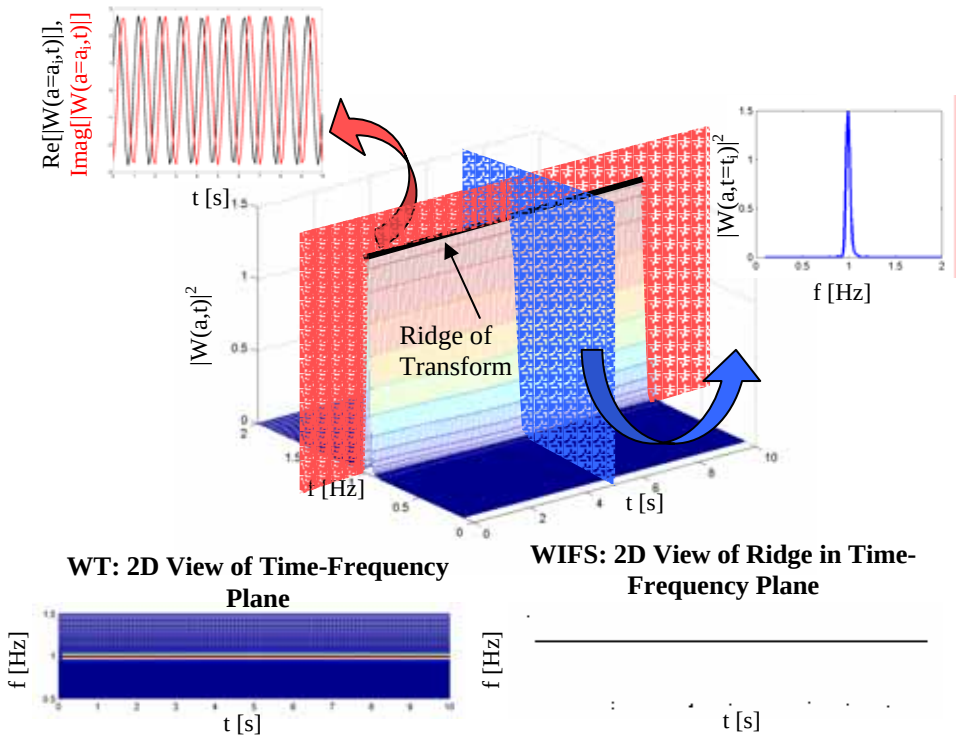

FIGURE 4.19. Schematic of various time-frequency characteristics of Wavelet Transforms

$$\left|W(a_r,t)\right| = \max_a \left|W(a,t)\right| . \tag{4.25}$$

The ridge is then given by a graph of the function $a_r(t)$ (Carmona et al., 1998). While this will yield a ridge estimate for the most rudimentary applications, it becomes evident that this approach will only be capable of capturing one ridge and must be modified to identify multiple local maxima for multicomponent signals. This modification is achieved, for example, by identifying peaks in the wavelet modulus corresponding to the location of ridges

$$\partial\left|W(a,t)\right| \Big/ \partial a \Big|_{a=a_r(t)} = 0 . \tag{4.26}$$

Unfortunately, this technique is less robust in the presence of noise, which introduces additional local maxima (Carmona et al., 1998). More precision can be achieved using the *Marseille Method* based on the wavelet phase. These methods identify the locations where the wavelet modulus shows a high degree of similitude with frequency components within a signal.

The ridge extraction approach can be an even more powerful tool when it is manipulated to extract an asymptotic signal from noise. Unlike the differential approaches, this more sophisticated class of techniques exploits the fact that the asymptotic signal has a ridge that is a smooth function of time, unlike the ridges associated with noise or other intermittent signal components that may appear as scattered fragments of a curve throughout the time-frequency plane. In addition to using the smoothness of the ridge to aid in the extraction scheme, information on the characteristics of the noise may also be integrated into the search algorithm to enhance performance.

Using the fact that the wavelets localize their energy near ridges and that the ridges of the asymptotic signals are smooth and slowly varying functions, a penalty function can be formulated

$$\varepsilon(a_r) = -\int SG(a_r(t),t)dt + \lambda\int \left|a_r'(t)\right|^2 dt + \mu\int \left|a_r''(t)\right|^2 dt \qquad (4.27)$$

and the ridge detection problem is recast as a minimization problem on this function, as discussed in Carmona et al. (1998). A Bayesian approach as well as other techniques can be used to propose penalty functions for seeking out smooth ridges. Since the numerical algorithms used to solve for the ridge in this manner can be unstable, alternative

approaches are provided in Carmona et al. (1998), including the “Corona” Method and the Iterated Conditional Modes (ICM) technique. These approaches are very attractive for separating a single asymptotic signal ridge from a bed of noise, but if there are multiple asymptotic ridges, more robust algorithms are required. This approach does not use any type of penalty function minimization, but rather introduces a stochastic system to generate occupation densities that draw the ridges through the *Crazy Climber Algorithm* (Carmona et al., 1998).

It should also be noted that the phase of the WT could also be used to isolate the ridges. As will be demonstrated in subsequent examples, the instantaneous frequency identified by the ridge is often more precise, but also more sensitive to noise (Carmona et al., 1997). Feldman & Braun (1995) noted that the estimate of the instantaneous frequency from phase information may be high in variance and concluded that a lower variance estimate can be obtained directly from the maxima of time-frequency distributions, an observation previously confirmed by Boashash (1992b). This is an important consideration for techniques based on Hilbert Transforms, which rely entirely on phase information to define the instantaneous frequency. Thus, the flexibility of dual venues for the instantaneous frequency estimation is a valuable asset for the Wavelet Transform.

Though the extraction techniques geared specifically to separate asymptotic signals are powerful and attractive, smooth ridges are often not present in the case of arbitrary natural signals or random processes. Therefore, for the more general analyses of signals throughout this study, the more traditional differential extraction methods

(Equation 4.26) are employed so that ridges from a variety of signal types and sources can be isolated. Further, the ridges identified in this manner are plotted as colored contours in the time-frequency plane, preserving the magnitude of the various ridge components. This perspective is termed by the author as a *wavelet instantaneous frequency spectrum* (WIFS)

$$WIFS(a,t) = \begin{cases} SG(a,t)\big|_{a=a_r(t)} \\ 0\big|_{a\neq a_r(t)} \end{cases}. \tag{4.28}$$

In this way, the dominant ridges can be differentiated from fainter ridge components that are often artifacts of noise variations or "shadows" of the dominant ridge, created by the side lobes of parent wavelet, $G(\omega)$. An example of the WIFS is also shown in Figure 4.19.

4.5 Conclusions

The multi-resolution capability of Wavelet Transforms makes it a powerful tool for time-frequency analysis, optimally adjusting to the Heisenberg Uncertainty Principle at each analysis frequency. However, in order to provide meaningful results, the transform must be applied with a proper understanding of its time-frequency resolutions. As these issues are rarely discussed within the literature, in part due to the infancy of Wavelet Transforms, a unified analysis framework is presented herein for the Morlet wavelet. This wavelet is advocated for use in this study by virtue of its analogs to Fourier Transforms and Fourier frequencies, making it well-suited for modal analysis familiar to most practicing engineers. A discussion of the resulting wavelet resolutions reiterated the importance of optimally adjusting the central frequency of the parent wavelet to achieve

the desired resolutions, e.g. to separate closely spaced modes. This discussion also provided a theoretical basis for the presence of end effects and offered a practical remedy in the form of reflective padding to extend the length of the time series to mitigate the influence of end effects. The chapter concluded by establishing a flexible framework for discretizing the time-frequency plane, cognizant of the bandwidth of the Morlet wavelet, and summarized strategies for ridge extraction, introducing the notion of wavelet instantaneous frequency spectra representative of the dominant frequency components within the signal. This processing framework provides the basis for all wavelet analyses that follow in the next four chapters.

CHAPTER 5

WAVELETS FOR SYSTEM IDENTIFICATION, PART I:

APPLICATIONS TO WIND, WAVE AND SEISMIC ANALYSIS

5.1 Introduction

Civil Engineering structures assume a wide array of structural forms and dynamical properties, as shown in Figure 5.1, subjecting the various classes of bridges, towers, buildings and ocean platforms to the threats of wind, wave and earthquake loads. These diverse natural loadings present further challenges in that they cannot be completely captured in a stationary analysis framework such as that provided by Fourier Transforms. As motivated earlier in Chapter 3 and in work by Gurley and Kareem (1999), wavelets provide a new venue for the detection of nonstationary features in natural loading and the resultant response previously obscured by traditional spectral representations. This potential is more fully explored in this chapter by applying a continuous wavelet analysis to measured wind, wave and seismic signals serving as input to Civil Engineering structures. The analyses also consider measured full-scale response of buildings and experimental investigations of offshore platforms under wind and wave action, representing the characteristics of each through wavelet scalograms, wavelet

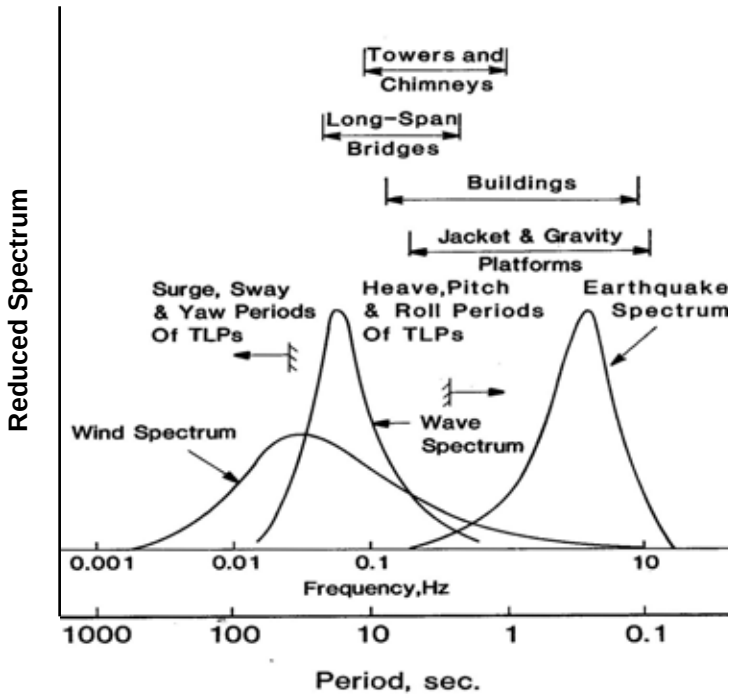

FIGURE 5.1. Spectra of environmental loads acting on Civil Engineering structures (taken from Kareem, 1987)

instantaneous frequency spectra and wavelet instantaneous spectra to reveal the distribution of signal energy with respect to both time and frequency. A comparison of wavelet marginal spectra and Fourier spectra is also provided to demonstrate the influence of wavelet multi-resolution characteristics on traditional spectral perspectives. Before these examples are introduced, however, this chapter will first introduce some additional wavelet theory and wavelet representations that will be employed herein, whose physical significance is demonstrated using a simple simulated signal.

5.2 Preliminaries

As discussed in Chapter 3, the wavelet *scalogram*, denoted as *SG(a,t)* by letting $b \equiv t$, was simply defined as the squared modulus of the wavelet coefficients. However, as

discussed in Chapter 4 in the context of the wavelet transformed harmonic components, the coefficients associated with a particular harmonic are actually weighted by the square root of the scale. Therefore, the amplitude of high frequency components in the scalogram will always be reduced by a factor of a and be smaller relative to the low frequency components. This convention arose from the definition of the wavelet transform according to Mallat (1998), who adopted this $\mathbf{L}^2$ normalization in the development of expressions to fully recover the signal energy in wavelet reconstructions. Besides its relevance to the conservation of energy and signal reconstruction, the weighting of the scalogram values by a essentially normalizes them relative to the size of the frequency window. Recall in Chapter 3 that the duration of the wavelet analysis window at a given frequency is inversely proportional to scale, implying that a wavelet coefficient associated with a high frequency was formed from data over a larger frequency range than its low frequency counterpart. The energy density of the scalogram can then be viewed as energy divided by the length of the frequency domain window. While this normalization is sensible considering the multi-resolution character of wavelets, it implies that a direct comparison of wavelet magnitudes cannot always be used to distinguish the relative contributions of a frequency component at a given instant in time, i.e. through instantaneous spectra or WIFS. Instead, the scalogram and WIFS can be used to identify the presence of particular frequency components in time and the frequencies with the highest energy densities relative to their respective frequency resolutions. To uncover the relative contributions of frequency components energy measures associated with the wavelet scalogram must be consulted.

The *marginal wavelet power spectrum*, also referred to as the *mean wavelet spectrum* (Lewalle, 1998), can be estimated by integration over the time variable as discussed in Perrier et al. (1995), which when implemented for a signal of finite duration *T*, may be expressed as

$$S_{WT}(a) = \frac{2}{C_g}\left[\frac{1}{T}\int_0^T SG(a,t)dt\right] \tag{5.1}$$

where C_g is the *admissibility factor* or norm of the parent wavelet, introduced in Chapter 3, and the factor of two is necessary since the analytic wavelets, such as the Morlet, suppress all negative frequencies. Note that the Fourier frequency corresponding to each scale in Equation 5.1 can be determined through the inverse relationship, making S_{WT} equivalently a function of frequency that can be readily compared to traditional Fourier spectra. In the case of the Morlet Wavelet, the admissibility factor is a function of the central frequency and can be determined by the numerical integration of the following expression

$$C_g = \int_{T_1}^{T_2} \frac{\left|G(\omega)\right|^2}{\omega} d\omega = \int_{T_1}^{T_2} \frac{2\pi e^{-(\omega-\omega_o)^2}}{\omega} d\omega\,. \tag{5.2}$$

Note that the definition of the admissibility condition in Chapter 3 specified limits of integration from zero to infinity. For this analytic wavelet, however, the localization of the Morlet wavelet in the frequency domain allows the numerical evaluation of Equation 5.2 to be conducted over a finite range of frequencies. Recall that the mean-square definition of the Morlet's frequency resolution, introduced in Chapter 3, spans one standard deviation of the Gaussian window. Extending this notion, 99.7% of the Gaussian window density lies within 3 standard deviations of the mean value, which in this case is

the central frequency. Thus, the infinite limits of integration can be reduced to just beyond the effective duration of the Gaussian window itself, to ease computation. Therefore, let T_1 and T_2 be defined as

$$T_1 = \omega_o - 5(\Delta\omega) = \omega_o - 5\left(1/\sqrt{2}\right) \text{ and } T_2 = \omega_o + 5(\Delta\omega) = \omega_o + 5\left(1/\sqrt{2}\right). \quad (5.3)$$

Note that a parametric investigation affirmed that assuming five standard deviations was sufficient to accurately compute the admissibility factor, as visualized when plotting the function $G(\omega)/\omega$ in Figure 5.2 for the case of a ω_o=4π rad/s Morlet wavelet.

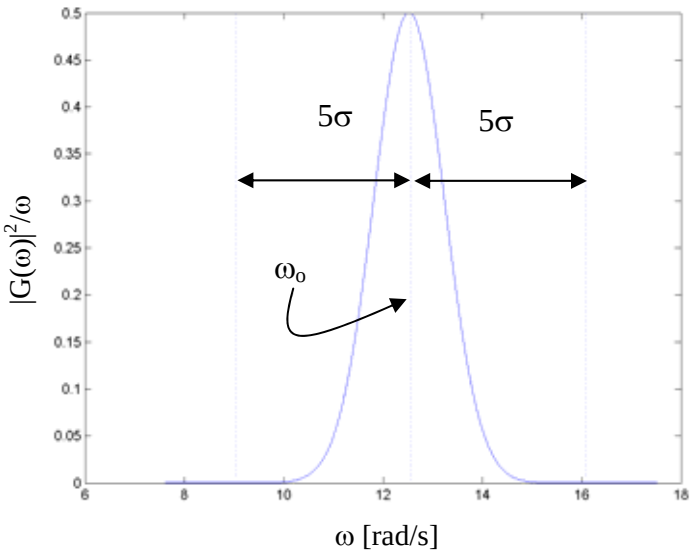

FIGURE 5.2. Admissibility function for 2 Hz Morlet wavelet

The mean square value or variance of the assumed zero mean signal can be then determined from the wavelet marginal power spectrum by integrating over the range of scales

$$\sigma_{WT}{}^2 = \int_{a_1}^{a_n} S_{WT}(a)\frac{da}{a^2}. \tag{5.4}$$

Note that the limits of integration are defined in terms of the finite range of scales considered in the analysis and will identically capture the signal variance as $a_1 \rightarrow 0$ and $a_2 \rightarrow \infty$, equivalent to the theoretical expression in Mallat (1998). Similarly, integrating over the range of Fourier frequencies can also provide an estimate of signal variance, as discussed in Mallat (1998),

$$\sigma_{WT}{}^2 = -\frac{1}{f_o}\int_{f_1}^{f_n} S_{WT}\left(f_o \middle/ f\right)df \tag{5.5}$$

where $S_{WT}(f_o/f) \equiv S_{WT}(a)$, $f_1 = f_o/a_1$ and $f_n = f_o/a_n$. The factor f_o emerges from the change of variables between Equation 5.4 and 5.5, and the negative sign arises from the inverse relationship between scale and frequency, essentially inverting the limits of integration. Either expression can be used to obtain a wavelet-based estimate of the signal variance that is equivalent to the true variance, provided that the limits of integration approach [0, ∞].

The wavelet marginal spectrum will be compared to the traditional Fourier spectrum in this chapter to highlight the added low-frequency insights afforded by wavelets. Ideally the Fourier spectra computed via the Fast Fourier Transform and marginal wavelet spectrum should be calculated using similar frequency resolutions, for a

fair comparison. However, due to the multi-resolution character of wavelets, this is not possible. Instead, the resolution of the Fourier analysis is kept close to a wavelet mean frequency resolution. The wavelet transform is calculated for a range of scales, associated with Fourier frequencies ranging from zero up to the Nyquist frequency, i.e. $f_s/2$. Therefore, the wavelet mean frequency resolution, $\overline{\Delta f}$ is defined as

$$\overline{\Delta f} = \frac{\bar{f}_{WT}}{f_o 2\pi\sqrt{2}} \tag{5.6}$$

where $\bar{f}_{WT}$ is the mean of the Fourier frequencies considered in the wavelet analysis. A mean temporal resolution can be defined in a similar manner

$$\overline{\Delta t} = \frac{f_o}{\sqrt{2}\,\bar{f}_{WT}}. \tag{5.7}$$

These two measures will be referenced in some examples within this chapter to indicate the relative accuracy of the wavelet analysis. The frequency resolution of the Fourier analysis Δf_{FFT} is then determined by selecting the number of FFT points (N_{FFT}), to the nearest power of two, that, when inverted and multiplied by the sampling rate f_s, is comparable to the mean wavelet mean frequency resolution. Fourier spectra are then calculated by breaking the signal into N_s blocks of length N_{FFT}, spanning $T = N_{FFT} / f_s$ seconds. The Fourier coefficients are calculated over that block of discretely sampled points x_n, via fast Fourier transforms (Bendat & Piersol, 1986), according to

$$X_k = \frac{1}{f_s} \sum_{n=0}^{N_{FFT}-1} x_n \exp\left[-i \frac{2\pi k n}{N_{FFT}} \right] \tag{5.8}$$

where k is the index corresponding to the discrete frequencies of the Fourier spectrum

$$f_k = \frac{k}{T} \qquad k = 0, 1, 2, \ldots, N/2. \tag{5.9}$$

An estimate of the power spectrum is then made by averaging the squared magnitude of the Fourier coefficients from each block, according to (Bendat & Piersol, 1986)

$$S_{FFT}(f_k) = \frac{2}{N_s T} \sum_{i=1}^{N_s} \left| X_k \right|^2 . \tag{5.10}$$

Note the averaging here replaces the expected value operation, and the factor of 2 is introduced to compensate for the fact that this is a one-sided spectral density, as indicated in Equation 5.9. The signal variance associated with the Fourier power spectrum is then estimated by the following expression

$$\sigma_{FFT}{}^2 = \int_{f_0}^{f_{N/2}} S_{FFT}(f_k) df \tag{5.11}$$

In addition to comparisons of the wavelet marginal spectrum and its Fourier counterpart, wavelet measures of *energy accumulation* are also presented throughout this chapter. The energy accumulations in the frequency domain, denoted *E(f),* are determined by an integral operation at each frequency of the wavelet marginal spectrum, according to

$$E(f_i) = \int_{f_1}^{f_i} S_{WT}\left(f_o \diagup f \right) df \qquad \text{for } i=1, 2, .. n \tag{5.12}$$

for each of the *n* Fourier frequencies considered in the wavelet analysis. Similarly, a time analog to the marginal spectrum may be defined as

$$S_{WT}(t) = -\int_{f_1}^{f_n} SG\left(f_o / f, t\right) df \ . \qquad (5.13)$$

Energy accumulations in the time domain, denoted *E(t),* are then appropriately determined by

$$E(t_j) = \int_{t_1}^{t_j} S_{WT}(t) dt \qquad \text{for } j=1, 2, .. m \qquad (5.14)$$

for each of the *j* discretely sampled time ordinates considered in the wavelet analysis. Rates of change or derivatives of each of these accumulation measures, with respect to frequency or time, denoted respectively as *dE(f)/df* or *dE(t)/dt*, and the maximum values of these accumulation rates will be of particular interest in subsequent discussions as they identify the arrival of significant events in time and frequency.

As mentioned previously, the assessment of the relative strength of a frequency component at a given instant in time should not be based on the amplitude of wavelet coefficients, but rather by the energy associated with that scale and can be determined by integrating the area under an instantaneous spectral peak. For this reason, a relative energy measure is provided by this work. Instantaneous spectra are merely scalogram coefficients associated with a particular instant in time that peak at each instantaneous frequency component denoted by IF_i. Therefore, the relative contribution to the *instantaneous signal energy* at that time t_j from that frequency component is defined here as the ratio of the area under that particular spectral peak to the overall area under the instantaneous spectrum

$$\hat{E}_i(t=t_j)=\frac{\int_{f_{1,i}}^{f_{2,i}} SG\left(f_o/f, t=t_i\right)df}{\int_{f_1}^{f_n} SG\left(f_o/f, t=t_i\right)df}. \quad (5.15)$$

In this case, the limits of integration in the numerator are the frequencies associated with the initiation and termination of an individual spectral component. Note each of the integrations specified in Equations 5.1, 5.2, 5.4, 5.5 and 5.11-5.15 are achieved numerically in this chapter using trapezoidal integration.

The following simulated example will demonstrate the utility of these additional wavelet spectral representations and energy measures, noting their ability to identify the arrival and participation of different frequency components. Armed with an understanding of these measures and wavelet visualizations, the analysis approach introduced here will then be extended to a number of measured earthquake ground motions and structural responses to earthquakes, winds and waves.

5.3 Example

The physical significance of the preceding measures is demonstrated by a simplified example. Consider a 100 second signal sampled at 10 Hz. For the first 50 s of the signal, a lone cosine described by $5\cos(8\pi t)$ is present. In the last 50 s of the signal, this is supplemented by an additional cosine of the same amplitude and half the frequency. A Morlet wavelet analysis with f_o = 3 Hz is conducted. This produces a wavelet mean frequency resolution of 0.103 Hz and mean temporal resolution of 0.771 s. Accordingly, 128 FFT points were selected to produce Fourier spectra with a resolution of 0.078 Hz.

The wavelet padding scheme discussed in Chapter 4 was implemented for $\beta = 3$ and an overlap factor, *OF* =1 was selected to produce the smooth wavelet spectra with minimal computational effort. As noted by Gurley & Kareem (1999), discretization of scales can be critical in insuring that a wavelet analysis accurately captures signal energy and spectral shape, often limiting the utility of the DWT in these arenas. The flexibility provided by the overlap factor, allows finer discretizations at the expense of computational effort. As shown in Table 5.1, the *OF* = 2 provides the most proper discretization of scales in terms of bandwidth definitions discussed in Chapter 4 and marks the maximum allowable *OF* providing reasonable estimates of signal variance. By increasing *OF* and essentially over resolving the space, there is no marked improvement in results despite greater computational expense. Thus the ability of the wavelet transformed data to replicate the actual RMS of the signal serves as a metric to assess the quality of the analysis parameters chosen.

TABLE 5.1

INFLUENCE OF OVERLAP FACTOR ON WAVELET ENERGY ESTIMATES

OF	Error in Energy Estimate
4	-13.4%
3	11.2%
2	0.345%
1	-0.140%
0.5	-0.162%

The resulting scalogram and wavelet instantaneous frequency spectrum are provided in Figure 5.3. Note that both the scalogram and the wavelet instantaneous

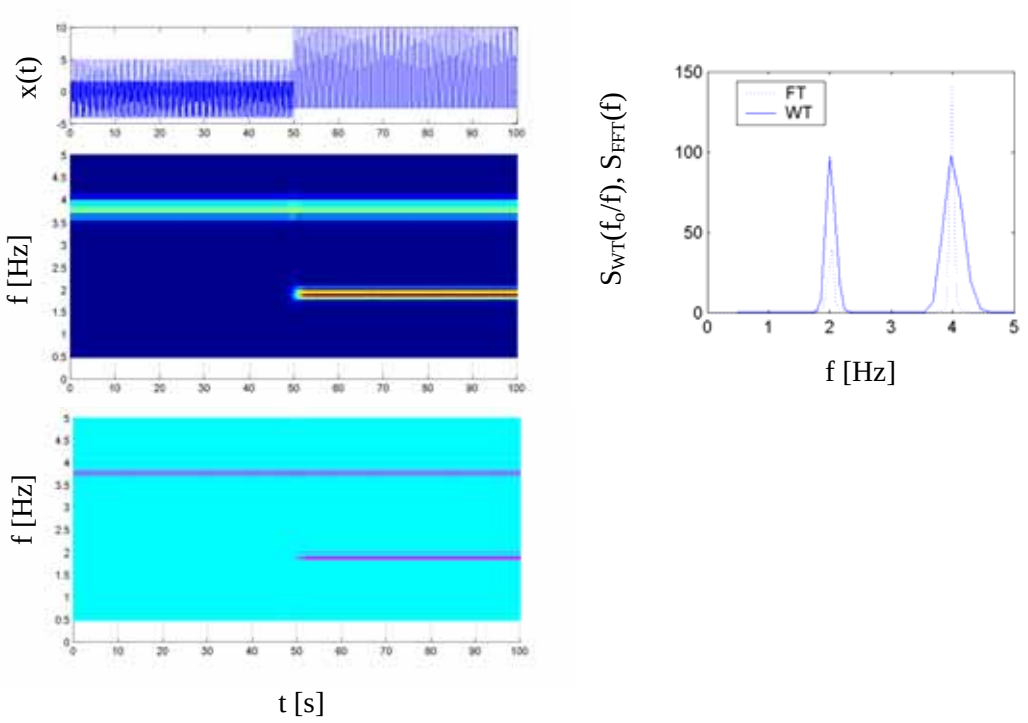

FIGURE 5.3. Example signal, wavelet scalogram and WIFS (left, top to bottom) and marginal spectral comparison with Fourier power spectrum (right)

frequency spectrum isolate the involved frequency bands as well as the time at which the second frequency contribution appears, albeit more precisely in the form of ridges in the WIFS. The relative magnitude of the peaks in the Fourier spectrum identify the higher frequency component as the more dominant in the signal, but this does not give any indication of how long each component was present. The Fourier spectrum could be interpreted as two frequency components of equal amplitude, but with the low frequency component only present a fraction of the time (as is the case here) or as two frequency components both present for the same amount of time, but the higher frequency component having a larger magnitude. The wavelet marginal spectral amplitudes are much less than their Fourier counterpart, due to the increased bandwidth from the

Gaussian window. In order for energy to be conserved by the wavelet, these amplitudes must be smaller. The relative magnitude of the wavelet peaks, if interpreted in the same manner as the Fourier spectrum, would indicate that the low frequency component slightly dominates. Recall however that the bandwidth of the high frequency component is larger than the low frequency component, as a result of the frequency dilation of the wavelet analysis window. The larger bandwidth implies that a lower spectral amplitude is necessary to insure that the area under the spectral peak corresponds to the true energy contribution from that particular frequency. This emphasizes the need to consider the area under the wavelet spectrum rather than its spectral amplitude when assessing the relative contributions of two well-separated components. Still, the overall signal energy is well captured by the wavelet. The RMS value of the signal is 4.34, while the area under the wavelet marginal spectrum produces a value of 4.33, and the area under the Fourier spectrum is 4.25. This proves that the measure in Equation 5.5 does compensate appropriately for the multi-resolution character of wavelets, which results in the modified spectral amplitudes.

The energy accumulation plots are provided in Figure 5.4 and are useful in determining critical events within the course of a signal. As the frequency energy accumulation plot at the left demonstrates, when read from right to left, the signal has no energy until 4 Hz, where it receives approximately two thirds of the total signal energy. The plateau between 4 Hz and 2 Hz further indicates that there are no additional energy contributions in this range. The increase to 100% energy at 2 Hz affirms that the remainder of the signal energy resides at this frequency. In time, it is similarly affirmed that one third of the signal energy is present at 50 s, when the second cosine is

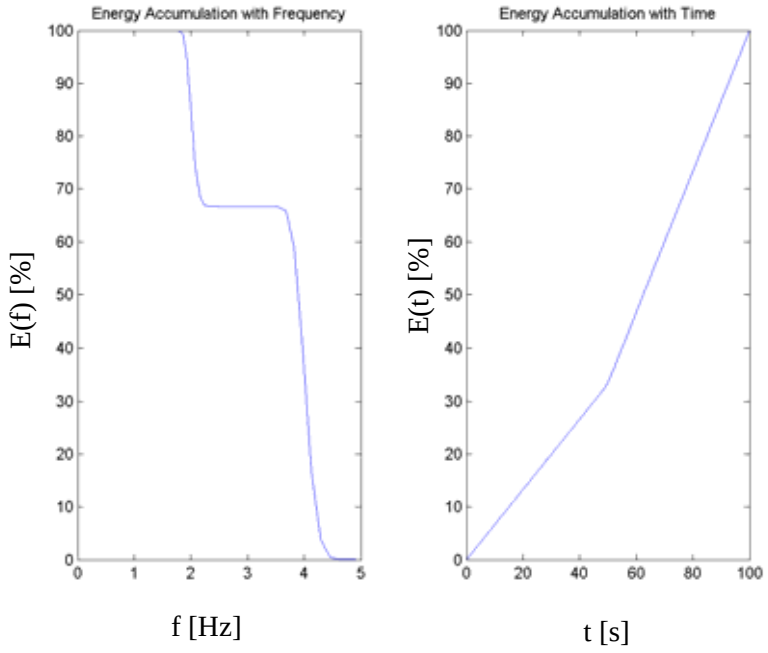

FIGURE 5.4. Energy accumulation in frequency domain (left) and time domain

introduced, changing the slope of the energy accumulation. The rates of change of the accumulation plots, presented in Figure 5.5, identify the arrival of specific events in time and frequency. The maximum change in energy in the frequency domain occurs at 4.05 Hz, corresponding to the dominant frequency component in the signal. The dramatic shift in the rate of energy accumulation in time is evident in the left image, with the maximum energy in the time domain being fully realized at 53 s and sustaining itself for the duration of the signal. Understandably, the major changes in energy accumulation with frequency occur at the two harmonics of the signal. Though for this simple example, the plots in Figure 5.5 don't seem to provide any significant additional information, these measures have greater utility in the case of more complex signals with a richer distribution of frequencies and nonstationary characteristics, which will be considered

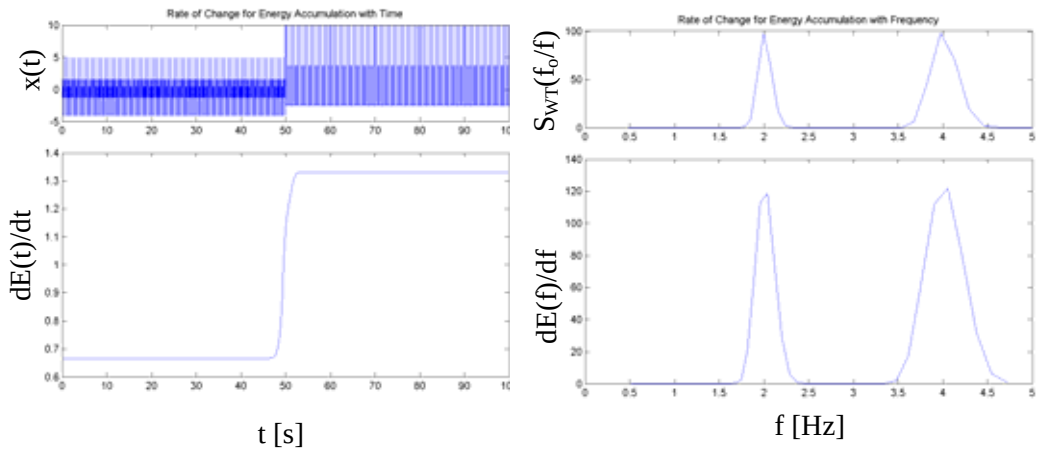

FIGURE 5.5. Signal and rate of change of energy accumulation in time domain (left) and marginal spectrum and rate of change of energy accumulation in frequency domain for example cosine signal

subsequently. Note again that these energy accumulations, being based on the area under the wavelet spectra, again compensate for the amplitude distortions that result from the multi-resolution analysis and therefore provide a true representation of the energy contributed by each frequency component.

The final series of plots in Figure 5.6 demonstrates the instantaneous spectra at 4 distinct time intervals in the course of the signal. The first plot is taken from the signal when only the 4 Hz component is present. The subsequent pair of plots show the appearance of the second component in the vicinity of 50 s, as the energy associated with that component gradually phases in to the scalogram. Once both components are fully present in the last plot, it is evident that the magnitudes of the instantaneous spectral peaks are not equal, despite the two cosines having the same amplitude. Again, this is to insure energy conservation, since the higher frequency peak is associated with a larger frequency range and thereby greater bandwidth, accounted for by the scaling of wavelet

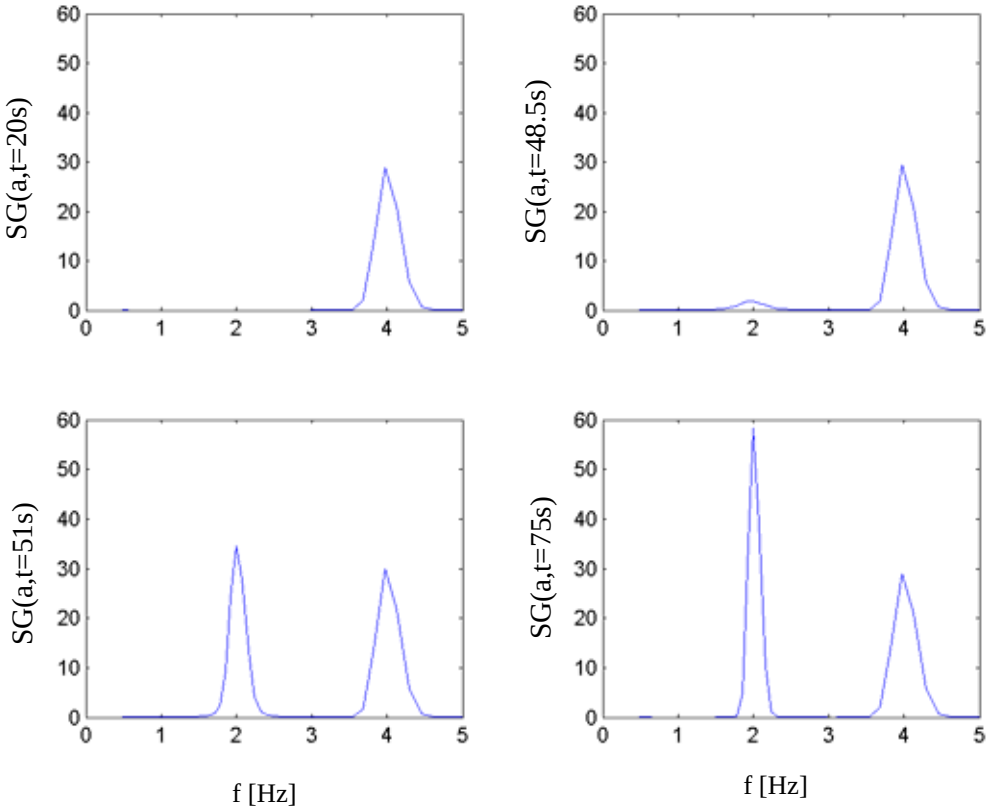

FIGURE 5.6. Wavelet instantaneous spectra taken at critical time steps in the example signal evolution: t=20 s, 48.5 s, 51 s, 75 s

scalogram values by *a*. However, by integrating the areas under the spectral peaks in each plot of Figure 5.6 and dividing by the total area under the curve as described in Equation 5.15, the relative strength of each component at that instant in time is assessed. The results are tabulated in Table 5.2 and indicate that the individual frequency components were identified with sufficient accuracy and their relative contributions, outside of the transitory period, were accurately identified, again affirming that by considering spectral energy and not amplitude, the effects of a multi-resolution analysis can be adequately compensated for. Note that the transitory period exists since the wavelet considers information to the past and future of a given time instant. Therefore, the occurrence of the

TABLE 5.2

RELATIVE CONTRIBUTIONS OF EACH COMPONENT TO INSTANTANEOUS SPECTRA FOR EXAMPLE

t_j	IF_1	$\hat{E}_1(t_j)$	IF_2	$\hat{E}_1(t = t_j)$
20 s	n/a	n/a	3.98	100%
49 s	1.98	7.4%	3.98	92.3%
51 s	1.98	45%	3.98	54.7%
75 s	1.98	50%	3.98	50%

second cosine is not pinpointed at an instant, but its occurrence is sufficiently localized in time. The scalograms, wavelet instantaneous frequency spectra and wavelet marginal spectra are considered throughout the subsequent discussions to permit a general identification of frequency components in time and to isolate meaningful events. The other wavelet energy measures based on wavelet instantaneous spectra are then consulted to determine the relative contributions of each frequency component or event in the signal.

5.4 Earthquakes

The birth of wavelets can actually be traced back to its applications in seismology. It was Morlet's work in reflection seismology that led him to propose sending shorter waveforms at high frequencies obtained by scaling a single function called a wavelet. At the same time, Grossman was working on coherent quantum states and realized the applicability of Morlet's idea to his field. The collaboration between these two led to the formalization of the continuous wavelet transform, known in French as *Ondelettes*

(Grossman & Morlet, 1984). Though these ideas were not new to mathematicians working in harmonic analysis and researchers in multi-scale image processing, the work of Grossman and Morlet, as well as the mathematician Meyer, brought together researchers from a variety of fields to unify the theory of wavelets. Therefore it is only fitting to return to the seismic problem as the first example of wavelet applications in Civil Engineering. As the discussions in Gurley & Kareem (1999) suggest, there is considerable promise in the applications of wavelet transforms in the analysis of not only seismic ground motions, but also the resulting response. The following sections apply the aforementioned wavelet measures in the analysis of nearfield records from five seismic events: El Centro (1940), Mexico City (1985), Loma Prieta (1989), Northridge (1994) and Kobe (1995). For these events, only the ground motions associated with the larger of the two horizontal directions are analyzed – the vertical components are not considered at this time. For each of these events, due to the short duration characteristics, a f_o = 1 Hz Morlet wavelet was first applied, and a more detailed examination of the frequency content was achieved using f_o = 3 Hz, with overlap factor (*OF*) of 1. These two analyses are referred to throughout the examples in this section as the primary and secondary analyses, respectively. Each signal is analyzed at scales corresponding to Fourier frequencies from 0.05 Hz to the Nyquist frequency. Dependent on the length of the record and the central frequency chosen, padding was provided wherever possible using β = 2 or 3. Subsequently, the analysis of a low-rise structure's response to the Northridge quake will also be investigated. It should be cautioned when viewing the following results that each of these earthquake records and their associated time and frequency characteristics depend strongly on local soil conditions and topography and should not be

considered representative of the complete suite of seismic motions associated with the event.

Finally, it should be again noted that all wavelet scalograms, marginal spectra, and instantaneous spectra do not correct for reduced spectral amplitude or enhanced spectral bandwidth that results from the multi-resolution analysis, though the area under each spectral peak does appropriately reflect the energy contributions of each component. For this reason, all energy accumulations and energy measures defined in this chapter and calculated from the data presented herein are based upon the area under the wavelet spectra, as discussed previously, and thus directly account for the consequences of multi-resolution analyses, providing a true energy measure and gauge of the relative contributions of each component, which cannot be ascertained directly from wavelet spectral amplitudes. Therefore, only the plots of energy accumulation and rates of change of energy accumulation appropriately account for this multi-resolution effect.

5.4.1 El Centro (1940)

The El Centro earthquake struck southern California on May 18, 1940 at 20:37 local time. The recorded time history of the event, sampled at 50 Hz, is subjected to two aforementioned wavelet analyses. The mean wavelet resolutions are given for each analysis in Table 5.3.

Figure 5.7 shows the wavelet scalograms for these two analyses and their accompanying wavelet instantaneous frequency spectra. The impact of wavelet resolutions is immediately obvious, as the coarser frequency resolution of the primary

TABLE 5.3

RESOLUTIONS OF FOURIER AND WAVELET ANALYSES

		f_o = 1 Hz		f_o = 3 Hz	
	Δf_{FFT}	$\overline{\Delta} f$	$\overline{\Delta} t$	$\overline{\Delta} f$	$\overline{\Delta} t$
El Centro	0.19 Hz	1.41 Hz	0.05 s	0.47 Hz	0.17 s
Guerrero MC	0.31 Hz	1.13 Hz	0.07 s	0.38 Hz	0.21 s
Loma Prieta	0.19 Hz	0.71 Hz	0.11 s	0.23 Hz	0.34 s
Northridge	0.19 Hz	0.71 Hz	0.11 s	0.23 Hz	0.34 s
Kobe	0.10 Hz	0.71 Hz	0.11 s	0.23 Hz	0.34 s

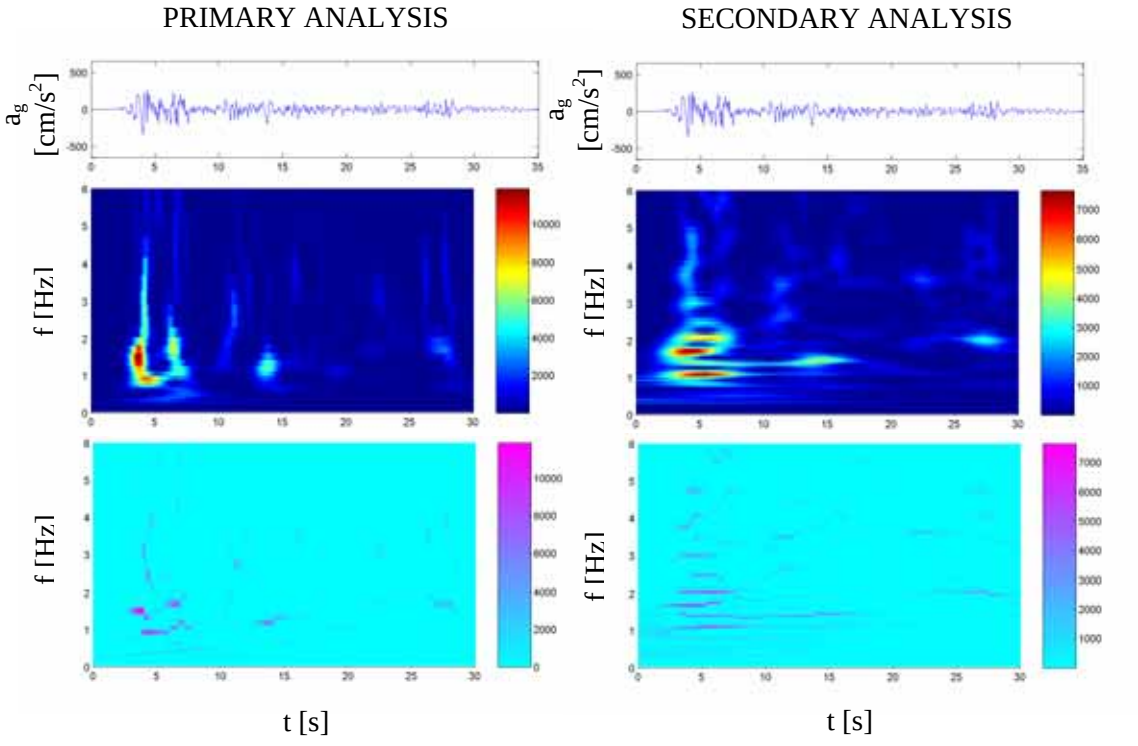

FIGURE 5.7. El Centro ground motion, wavelet scalogram and WIFS (top to bottom) for primary (left) and secondary analyses

analysis leads to long vertical bands and the coarser temporal resolution of the secondary analysis produces horizontal energy bands. However, viewing the two analyses in tandem can be beneficial. The primary analysis provides better temporal information and affirms that the energy lies dominantly between 4 and 7 s, though mostly near the former. In fact, three distinct events are detected in the vicinity of 3.6, 6.5 and 13.8 s. The first event has a broadband energy range the sweeps from 1 to 4 Hz, though focused between 1-2 Hz until the fifth second, when it narrows to the 1 Hz range. The second event also clusters in the 1-2 Hz range, while the third event is decidedly in the 1 Hz vicinity. Despite the presence of low frequency components in the wake of the first event, their contributions appear from the scalogram to be minor, as are the trace high frequency components. The WIFS affirms the richness of frequencies particularly associated with the first major pulse of the quake and to some extent, the secondary pulse, while isolating the persistent 1 Hz component. A wealth of intermittent high frequency and low frequency contributions is apparent, specifically in the vicinity of the first event near 4 s.

The secondary analysis separates distinct bands of energy near 1, 1.5, 1.7 and 2 Hz, though clearly concentrated near 1.5 Hz. In agreement with the primary analysis, the broadband features and dominant energy are localized near 5 s, which extends into the higher frequencies. The additional burst of energy at 27 s is more clearly associated with 2 Hz. The enhanced resolution of the WIFS in the secondary analysis affirms the richness of energy at 2.3 Hz and even down to 0.4 Hz. While the presence of contributions beneath 1 Hz were noted for this record by Huang et al. (1998), their contributions to the overall signal energy, relative to the other participating frequencies will be addressed

subsequently. Note also the variation in the ridges that indicate subtle shifts to higher and lower frequencies, only evident due to the enhanced frequency resolution.

A comparison of the Fourier power spectrum and the marginal wavelet spectrum for each analysis is provided in Figure 5.8. Table 5.3 lists the frequency resolution of the Fourier analysis and the mean frequency and time resolutions of the wavelet analysis. The traditional Fourier spectrum indicates that there is noteworthy energy below 1 Hz in this quake, though the vast majority of the signal's energy concentrates between 1 and 2.2 Hz, with peaks at 1.4 and 2.0 Hz and an additional peak near 4 Hz. Beyond 5 Hz, there is little energy content within the record. The low frequency energy rapidly falls off beneath 0.84 Hz. As expected the marginal wavelet spectrum in the primary analysis identifies the same general frequency content and dominance of the 1-2 Hz content, but with less of the details, due to the lower frequency resolution. The enhanced resolution of wavelets at the lower frequencies more clearly identifies the distinct presence of a low frequency contributor between 0.3 and 0.6 Hz, but lacking sufficient energy. The more refined resolutions in the secondary analysis provide greater detail on the robust distribution of energy between 0.82 and 2.5 Hz. The energy falls of quickly beyond this range. While a low frequency component is noted down to 0.4 Hz, it relative contributions again seem to pale in comparison to the energetic components in the vicinity of 1-2 Hz. While the general trends in the secondary wavelet marginal spectrum are consistent with that of the Fourier spectrum, there is a difference in amplitude, which is merely the function of the finer bandwidth in the secondary wavelet analysis, directly accounted for in the scaling by a. Still the energy is completely conserved in the wavelet representation, as evidenced by Table 5.4 when compared to the signal standard deviation σ.

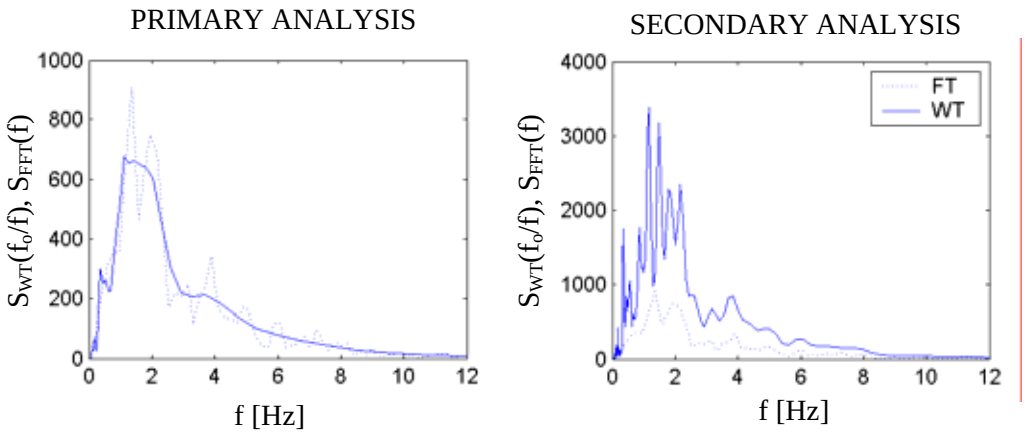

FIGURE 5.8. Wavelet marginal spectra with Fourier power spectrum for primary (left) and secondary analyses for El Centro quake

TABLE 5.4

SIGNAL STANDARD DEVIATION AS ESTIMATED FROM FOURIER AND WAVELET MARGINAL SPECTRA

	σ [cm/s^2]	σ_{FFT} [cm/s^2]	σ_{WT} [cm/s^2]	
			f_o = 1 Hz	f_o = 3 Hz
El Centro	44.06	44.15	44.10	44.07
Guerrero MC	24.20	24.81	24.21	24.20
Loma Prieta	71.32	75.44	71.39	71.32
Northridge	69.06	71.43	69.12	69.07
Kobe	115.19	155.19	115.31	115.17

The energy accumulation plots account for the multi-resolution characteristics of wavelets and provide a more objective tool for investigating the dominant energy components in the signal in comparison to the magnitude of wavelet scalograms, as shown in Figure 5.9. The primary energy accumulation in time demonstrates a jaggedness indicative of the arrival of distinct energetic pulses. By compromising this temporal

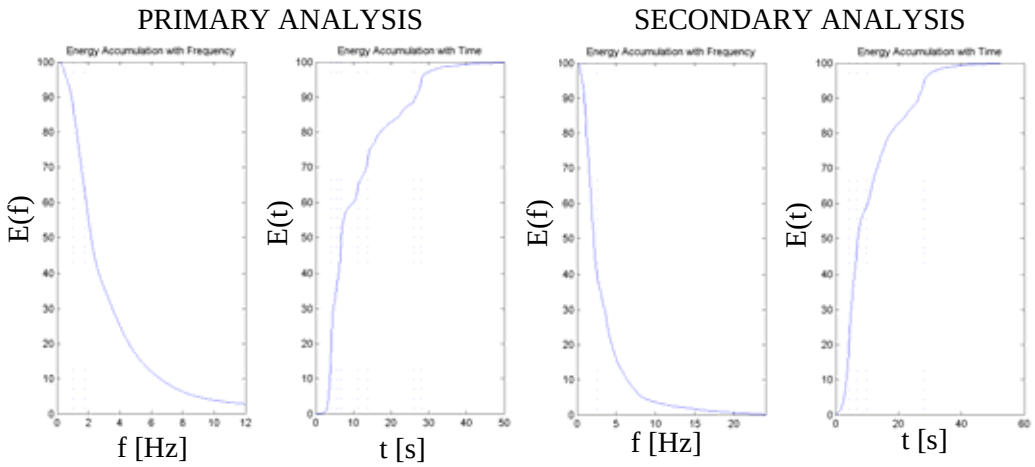

FIGURE 5.9. Energy accumulation in frequency domain and time domain for primary (left) and secondary analysis of El Centro

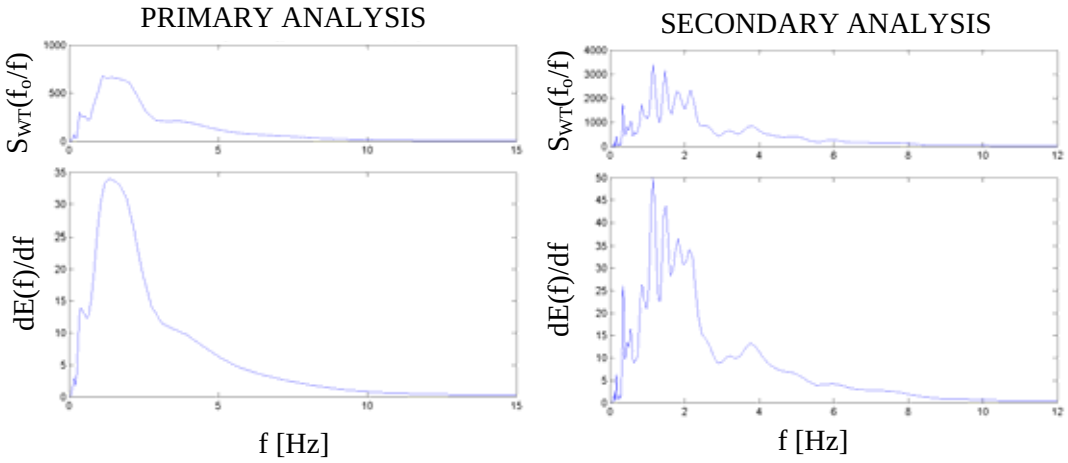

FIGURE 5.10. Wavelet marginal spectrum and rate of change of energy accumulation in frequency domain for primary (left) and secondary analysis of El Centro

resolution in the secondary analysis, a more precise measure of the energy accumulation in frequency is achieved. To enhance the discussion further, the rates of change of these energy measures in both frequency and time, are presented in Figures 5.10 and 5.11.

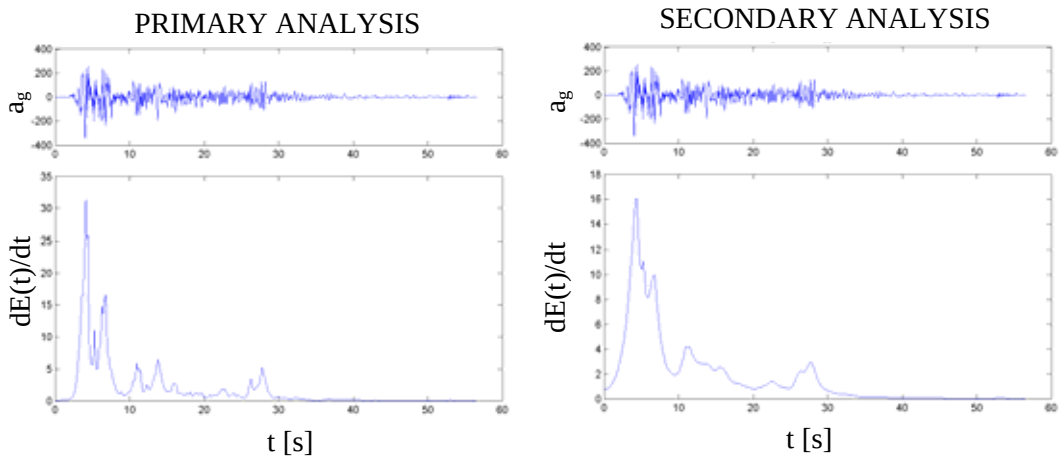

FIGURE 5.11. El Centro ground acceleration and rate of change of energy accumulation in time domain for primary (left) and secondary analysis

Looking first at the accumulation of energy in the frequency domain, from Figure 5.10, it is evident that the maximal rate of change in the primary analysis occurs at 1.35 Hz, though there is limited detail due to the loss of frequency resolution. The frequencies associated with these elevated rates of energy accumulation span a wide band from 1 to 1.9 Hz, with a minor change in energy associated with 0.4 Hz and no significant energy beyond 10 Hz. The secondary analysis, by virtue of a refined frequency resolution, identifies several distinct frequencies at which energy is contributed. Still the, maximum rate of change in the signal is constrained between 1.15 and 2.0 Hz. Beyond 2.5 Hz, there is little change in the energy accumulation within the signal. The steep ascent at 2.5 Hz in

Figure 5.9, marked by the dotted vertical line in the secondary analysis, affirms this concentration. Based on the noteworthy frequencies identified in Figure 5.10, an indication of the energy associated with these frequencies can be determined from the accumulation plots in 5.9. Dotted lines are used to indicate frequencies of interest.

In the primary analysis, the dominant influx of energy came from the frequencies between 1 and 1.9 Hz. At this time, the signal energy jumps from 61% to 88%. Investigating this in more detail through the secondary analysis, it is shown that 37.6% of the energy is associated with frequencies beyond 2.5 Hz. About 40% of the total signal energy is associated with frequencies between 1.15 and 2.5 Hz. Frequencies from 0.8 to 1.15 Hz account for only a few percent of the signal energy. Only 8% of the energy lies below 0.8 Hz. It is clear from the energy accumulation plot in Figure 5.9 that the single greatest jump in energy is associated with 1.15 Hz, where the cumulative energy rises from nearly 80% to 90%. From this analysis, it is evident that the range of frequencies from 1.15 to 2 Hz is the most energetic.

In the time domain, it is evident from Figure 5.11 that the primary analysis is superior in capturing many of the individual pulses in the record, though both analyses capture the same overall trends. The primary analysis indicates that most rapid changes in the energy within the signal occur between 4 and 7 s. Within this time frame, three distinct events are discernable: 4.1 s, 5.5 s and 6.7 s, with the most rapid change in energy being associated with the first in this series. The energy falls of very quickly following this flurry of activity. Beyond 10 s, there are 4 events, all bringing comparable levels of

energy: 11.1 s, 13.7 s, 26.2 s and 27.9 s. The occurrence of each of these events is denoted by dotted lines in the primary energy accumulation plot in Figure 5.9.

The accumulation of energy in time is not smooth due to the arrival of many small pulses associated with the arrival of the primary (P) and secondary (S) waves. With the arrival of the first pulse at 4.1 s, the energy accumulated doubles from 14% to 28%. The intermediate event at 5.5 s brings the energy levels up to 35.8%, with the next major event at 6.7 s causing a jump in accumulated energy from 41% to 55%. The accumulated energy tends to slowly level off near 8 s at about 60% of the total signal energy. The minor event at 11.1 s brings the accumulated energy to 65%, followed by the event near 14 s by which time the accumulated energy has reached 75%, steadily ascending. The last two minor events cause the accumulated energy to spike up from 89% to 93%, followed by a slow accumulation for the next 30 s. Though lacking the same level of detail, the secondary analysis affirms that the major pulse is associated with the fourth second and energy levels are generally sustained up to the seventh second, rapidly falling off after 10 s. Minor events do follow, with the most distinct near 28 s. This analysis is in agreement with the primary analysis that 50% of the signal energy is released in the first 7 s.

Based on these temporal analyses, four instantaneous spectra were extracted for more detailed analysis in Figure 5.12. Near 4 s, marked by the arrival of the P-waves, the primary analysis detects a very broadband spectrum holding 96% of the signal energy at this time, indicating a large suite of contributing frequencies. Though peaking at 1.6 Hz, the lack of frequency resolution implies that there are likely multiple distinct frequency components at this time. The secondary analysis sheds more light on the situation. The

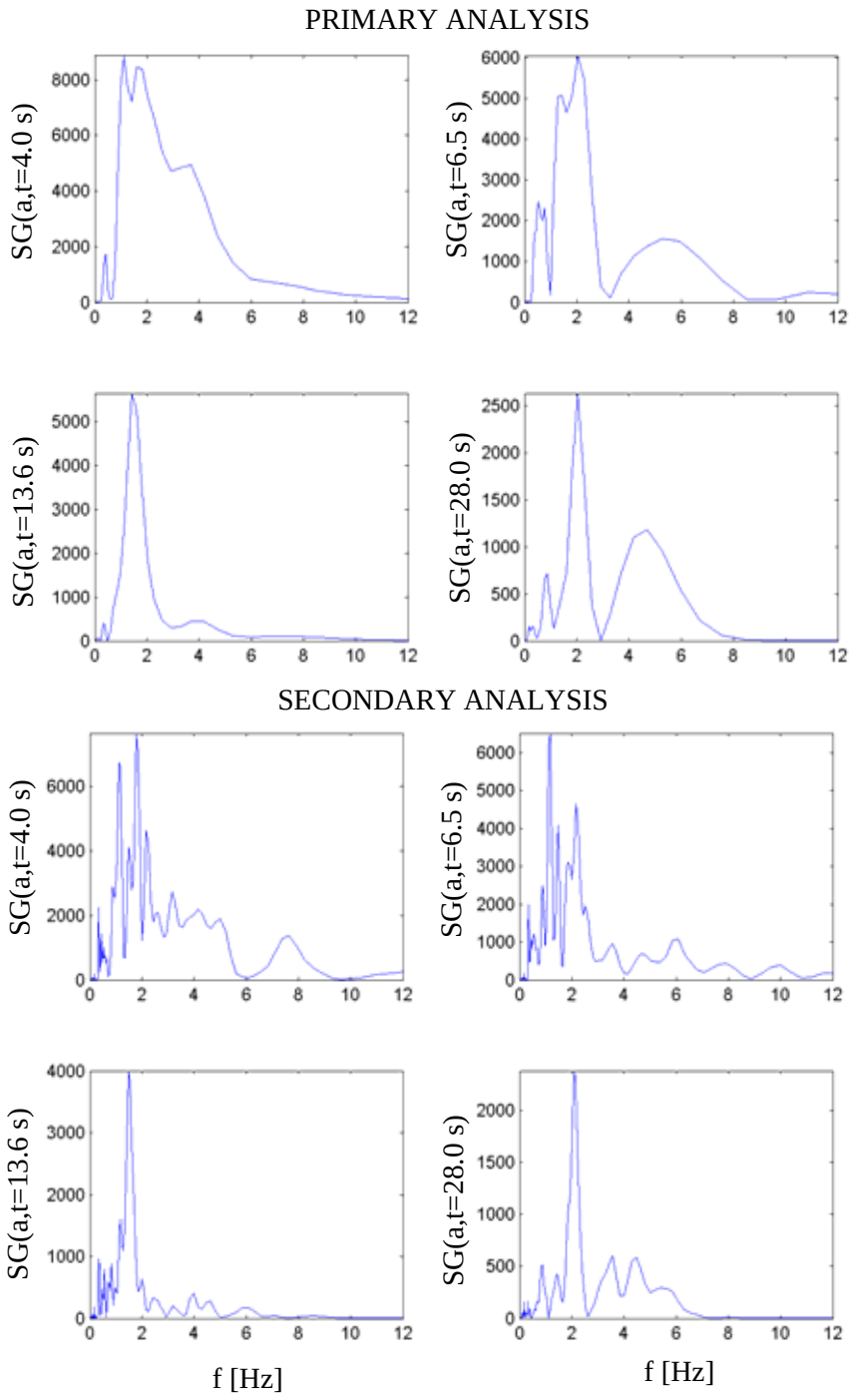

FIGURE 5.12. Wavelet instantaneous spectra taken at critical time steps in the El Centro event for primary (top) and secondary analysis

display has several peaks between 1 and 2 Hz, where most of the energy appears to reside. The level of energy between 3 and 6 Hz is fairly constant and holds 30.6% of the signal energy at this time. There is only a minor low frequency contribution centered at 0.45 Hz, with only 2.1% of the instantaneous signal energy. As listed in Table 5.5, there are distinct components in the vicinity of 1 and 2 Hz that contribute fairly equally to the overall instantaneous energy of the signal. In total, over 40% of the signal energy lies in this vicinity. An additional component of high frequency energy accounts for another 12.3% of the instantaneous signal energy. At 6.5 s, the primary analysis now identifies more distinct components, indicating that the wide array of frequencies was only present in that first pulse. The component centered at 0.62 Hz contributes 7.1% to the energy at this time. The second component, centered at 1.8 Hz, but essentially including contributions from 1.6 to 2 Hz by virtue of the reduced frequency resolution, captures 51.7% of the signal energy. A third component centered at 5.2 Hz includes energy from 4.6 to 5.8 Hz, holds 33.5% of the signal energy at this time. The added detail of the secondary analysis affirms a richness of energy from 1-3 Hz. Lumping this energy into two modes at 1.2 and 2.2 Hz, corresponding to 23.5% and 30.7% of the instantaneous signal energy, generally consistent with the distribution of energy noted by the primary analysis. Again, while visible, the low frequency component centered at 0.55 Hz contributes only 3.8% to the instantaneous signal energy. By 13.6 s, both the primary and secondary analyses concur that there is a single mode response near 1.5 Hz associated with over 60% of the overall instantaneous signal energy, as shown in Table 5.5. At 28 s, the last significant pulse arrives. With its arrival, a suite of frequency components returns. The primary analysis detects three major components. The component centered at 2.1 Hz

TABLE 5.5

RELATIVE CONTRIBUTIONS OF EACH COMPONENT TO INSTANTANEOUS SPECTRA FOR EL CENTRO EARTHQUAKE PRIMARY AND SECONDARY ANALYSES

t_j [s]	IF_1 [Hz]	$\hat{E}_1(t_j)$ [%]	IF_2 [Hz]	$\hat{E}_2(t_j)$ [%]	IF_3 [Hz]	$\hat{E}_3(t_j)$ [%]	IF_4 [Hz]	$\hat{E}_4(t_j)$ [%]	IF_5 [Hz]	$\hat{E}_5(t_j)$ [%]
Primary Analysis										
4.0			1.60*	96.0						
6.5	0.62	7.1	1.87	51.7			5.21	33.5		
13.6			1.47	79.4						
28.0			1.51	65.3	2.13	35.3	4.69	56.5		
Secondary Analysis										
4.0	1.13	11.6	1.88	16.7	2.16	13.3	4.0*	30.6	7.6	12.3
6.5	1.20*	12.5			2.20*	30.7				
13.6			1.55	62.0						
28.0					2.13	43.7	3.89*	48.6		

*broadband energy contribution centered or peaking at this frequency.

assimilates contributions from 1.9 to 2.4 Hz for a 35.6% share of the instantaneous signal energy. A broader-band component near 4.7 Hz with contributions from 4.19 to 5.19 Hz holds 56.5% of the instantaneous energy. Again, a low frequency component near 0.89 Hz is present but makes a contribution of only 4% to the energy at that time. The resolution of the secondary analysis is able to separate more of the high frequency components and affirms that the only significant components is actually at 2.13 Hz with 43.7% of the signal energy. A broadband characteristic, centered at approximately 4 Hz, appears to include the contributions of two modes and nearly one half the signal energy, as shown in Table 5.5. Though the Fourier spectrum agrees that energy is dominant between 1-2 Hz in this signal, the intermittent presence of specific contributions to the

overall signal energy can only be uncovered through time-frequency analyses such as those presented here.

Interestingly, a similar time-frequency analysis via Hilbert spectra was conducted by Huang et al. (1998) on the same El Centro record, but with startlingly different results. The analysis suggested that tall buildings with frequencies less than 0.5 Hz are the primary targets of seismic energy during this event, contrary to all that was previously observed. The authors suggest that this feature of seismic motion went previously unnoticed as a direct consequence of the limited Fourier perspective in earthquake engineering. In this controversial analysis, Huang et al. produced a marginal Hilbert Spectrum with its energy focused below 5 Hz and more importantly dominating the sub-0.5 Hz frequency range, in direct contrast to the Fourier spectrum. Their findings are shown in Figure 5.13.

Based on this, Huang et al. (1998) cautioned that the “high density and low frequency should cause major concerns for earthquake engineering, for this is exactly the range of resonance for high-rise buildings.” However, these findings seem suspicious. As demonstrated in Figure 5.14, a cursory inspection of the IMFs generating the Hilbert marginal spectrum in Figure 5.13 indicates that the largest decomposed amplitudes are associated with the first 4 IMFs, which by inspection contain predominantly higher frequencies. (Note that the amplitude ultimately plotted in the Hilbert spectrum and its marginal spectrum is merely the SRSS combination of the real and imaginary components of the Hilbert transform of each IMF, i.e. the signal and its quadrature component (This procedure is discussed in more detail later in Chapter 7). The last five

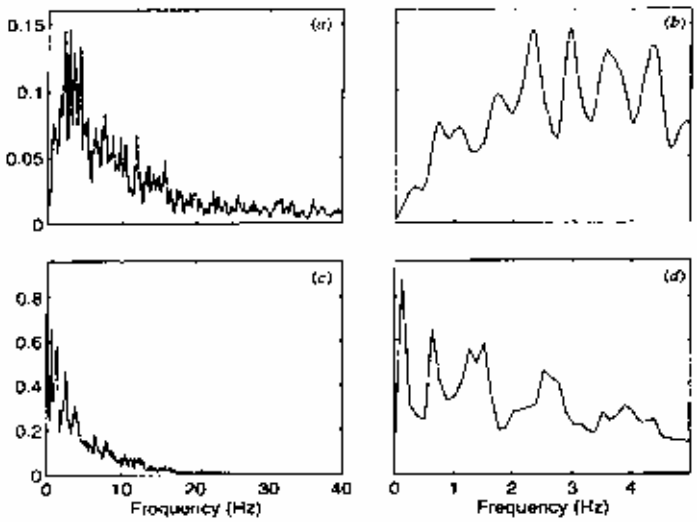

FIGURE 5.13. (a) Fourier spectrum and (b) low frequency zoom; (c) Hilbert marginal spectrum and (d) low frequency zoom for El Centro analysis conducted by Huang et al. (1998)

IMFs appear to be associated with the frequencies of less than 1 Hz. Note that the amplitudes of these IMFs are markedly smaller. It makes little sense then for these components to produce the largest Hilbert spectral coefficients, as suggested by Figure 5.13.

The concerns raised by Huang et al. (1998) were based upon a marginal Hilbert spectrum that misrepresented the nature of the seismic event. An explanation of the marginal Hilbert spectrum is given by Huang et al. (1998):

> …the frequency in either [the Hilbert Spectrum or Marginal Hilbert Spectrum] has a totally different meaning than the Fourier spectral analysis. [In the Hilbert Marginal Spectrum], the existence of energy at the frequency, ω, means only that, in the whole time span of the data, there is a higher likelihood for such a wave to have appeared locally...Consequently, the frequency in the marginal spectrum indicates only the likelihood that an oscillation with such a frequency exists.

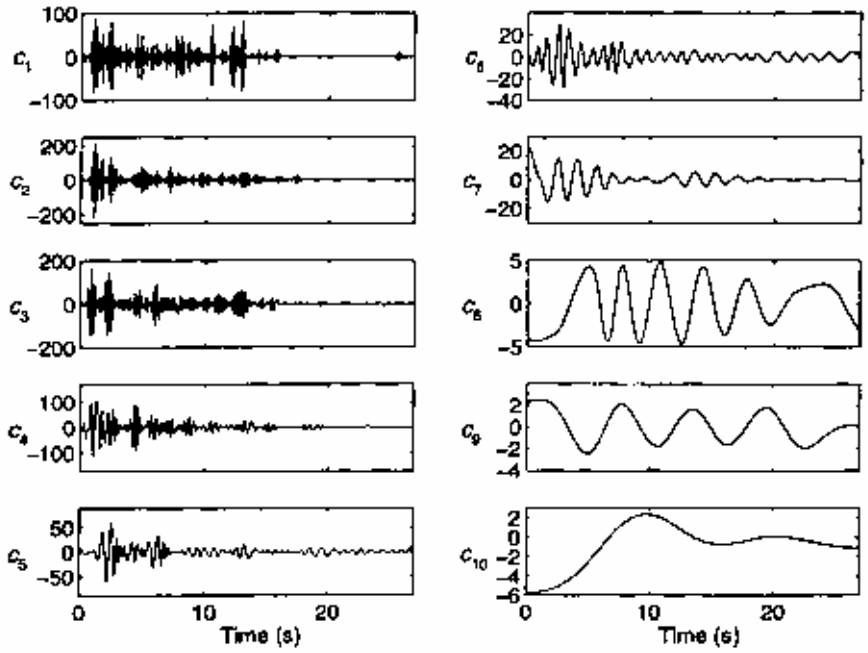

FIGURE 5.14. Ten IMF components from El Centro data provided by Huang et al. (1998)

Viewed from this perspective, the heavy concentration of low frequency components in the marginal Hilbert spectrum of Figure 5.13 only indicates that the low frequency components occurred locally most persistently throughout the time history. However, this does not imply that they carried the majority of the seismic energy, as the IMFs in Figure 5.14 affirm. As the scalogram and WIFS of the secondary analysis in Figure 5.7 demonstrate, the persistent presence of low frequency components can be rationalized, however the detailed analysis of these components reflects that their energy contributions are not dominant relative to other more energetic components between 1 and 2 Hz. As discussed previously in Figure 5.9 in the context of cumulative energy in the frequency domain, 90% of the signal energy lies below 1 Hz. Further, the instantaneous spectral analyses discussed previously affirm that, while these components are present, their

contributions to each instantaneous power spectrum was on the order of a few percent, and no components of any substance were observed below 0.4 Hz. On no account does the wavelet analysis herein affirm Huang et al.'s findings. In fact, the wavelet marginal spectra show good agreement overall with the Fourier representation, as expected.

It is not clear whether the calculation of the marginal Hilbert spectrum was erroneous or if its general tendency to display "likely components" as opposed to more "energetic components" is to blame for the counterintuitive perspectives in Figure 5.13. Regardless, any discussions based on time-frequency analyses must be conducted with care and verified against physical observations before unsubstantiated claims of ignorance on the part of earthquake engineers are levied.

5.4.2 Mexico City (1985)

This magnitude 8.1 earthquake that devastated Mexico City on September 19, 1985 remains in the minds of many as one of the most tragic quakes in North American history, as news cameras documented rescue attempts amidst the rubble of apartment buildings and hospitals. The quake, which occurred on the western coast of the Mexican peninsula, had tremendous impacts upon the valley of Mexico City as a result of unique soil conditions, which amplified the low frequency components. Though the frequencies of amplification varied from site to site within the city, the amplification was largely between 0.2 and 0.7 Hz. The concentrations of energy in the range of 0.2-0.6 Hz, being much higher than in previous quakes of comparable magnitude, led to heavy damage of structures in this period range (Jennings & Sanchez-Sesma, 1989). To demonstrate the pronounced impacts of soil conditions, a nearfield record taken near the epicenter in the

coastal regions of Mexico is first analyzed, recorded at Caleta de Campos, part of the Guerrero Array. To avoid confusion, this nearfield record will be referred to as the Guerrero MC (Mexico City) record in subsequent discussions. This coastal station had an epicentral distance of 27.1 km, making it well suited to capturing the nearfield characteristics of the quake. Subsequently, a free field record from the Mexico City valley, which typifies the low frequency amplification causing much of the damage in this quake, will also be analyzed. The nearfield Guerrero MC record is of considerable duration, although the peak ground accelerations are not as significant. The record, originally sampled at 200 Hz, is downsampled to 40 Hz for analysis.

The primary and secondary wavelet scalograms and WIFS for the Guerrero MC nearfield record are presented in Figure 5.15. For reference, the mean wavelet resolutions for each analysis are again provided in Table 5.3. The enhanced temporal resolution of the primary analysis isolates 3 energetic bursts: one event between 10 and 15 s and the other between 1 and 1.75 Hz, followed by strong shaking between 2 and 3 Hz accompanied by a low frequency component near 20 s. A slight burst of energy near 21 s is also apparent. From the scalogram and the associated WIFS, there is a collection of energy over 30 s and spanning a robust range of frequencies. Note in the primary WIFS that dominant ridges surface near 1.75 Hz and 0.5 Hz, the latter particularly in the vicinity of the strong shaking at 20 s. These are flanked by intermittent contributions in the high frequency range. The refined frequency resolution in the secondary analysis further affirms the richness of energy and the concentrations near 2.55 Hz and 1.75 Hz around the 20^{th} second, as well as the precursor to the strong shaking at 12 s. Though diminished in magnitude by virtue of the dilated temporal windows, a residual low

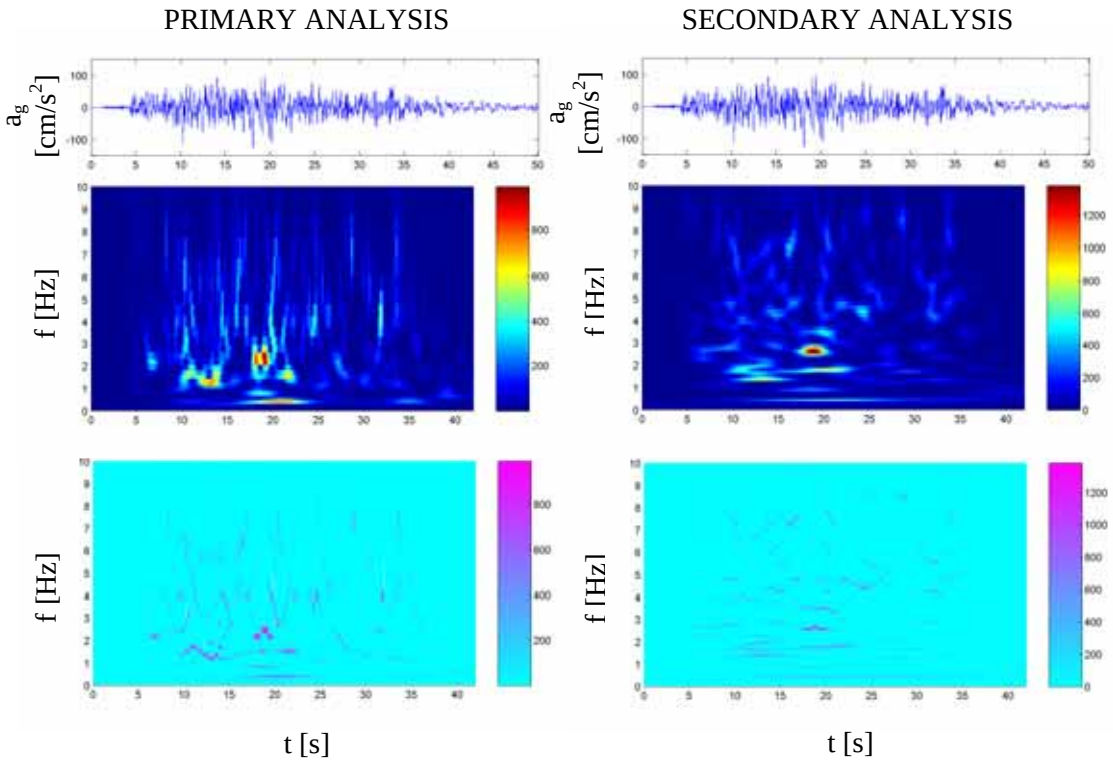

FIGURE 5.15. Guerrero MC nearfield ground motion, wavelet scalogram and WIFS (top to bottom) for primary (left) and secondary analyses

frequency component is still apparent and further affirmed by the ridges in the secondary WIFS. The secondary scalogram does give a better perspective on the intermittence of high frequency components within the record, though the resolutions in the low frequency lead to a dilation of the time windows evident by the elongated bands in the low frequency domain. The fluctuations of these high frequency ridges become more readily apparent in the secondary WIFS, as does the downshift of midrange frequencies and upshift of the low frequencies approaching the strong shaking near the 20th second.

A comparison of the Fourier spectrum and wavelet marginal spectrum is provided in Figure 5.16. From the Fourier spectrum, it is clear that there are two “tiers” of energy

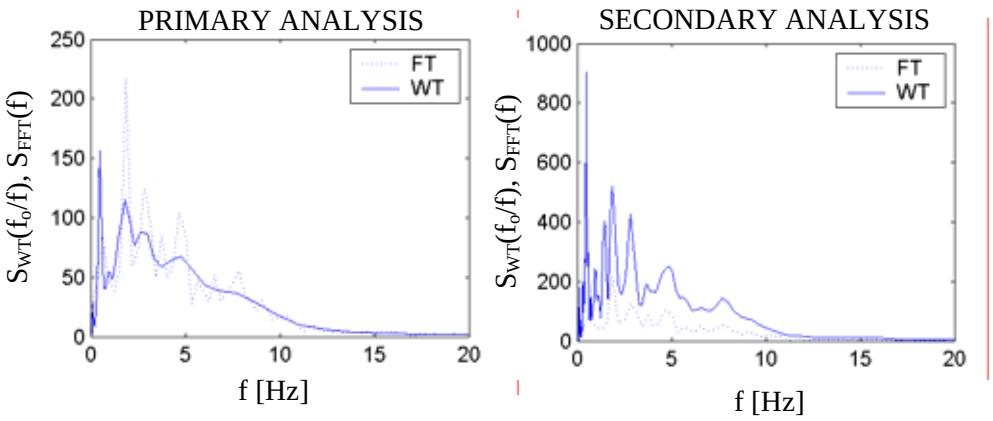

FIGURE 5.16. Wavelet marginal spectra with Fourier power spectrum for primary (left) and secondary analyses for Guerrero MC nearfield record

associated with this record. The first and more energetic tier has energy from 0.25 to 5 Hz, peaking at several distinct frequencies: 0.62, 1.86, 2.83, 3.75 and 4.72 Hz. The second tier from 5.3 to 9.6 Hz has diminished spectral amplitudes. The largest Fourier amplitude is associated with 1.86 Hz, as shown in the plot at the left in Figure 5.17. The wavelet marginal spectrum of the primary analysis accentuates the low frequency components of the record, though identifying a similar band of contributing frequencies, though with finer detail in the secondary analysis. Both analyses affirm the presence of a low frequency component as well as the presence of energy out to 5 Hz, then rapidly falling off by 10 Hz. The efficacy of both wavelets and Fourier transforms in capturing the signal energy is chronicled in Table 5.4.

Figure 5.17 presents the energy accumulation rates in frequency and time for the primary and secondary analyses. As the figure demonstrates, the primary analysis smoothes out many of the details of the energy accumulation with frequency. The rates of

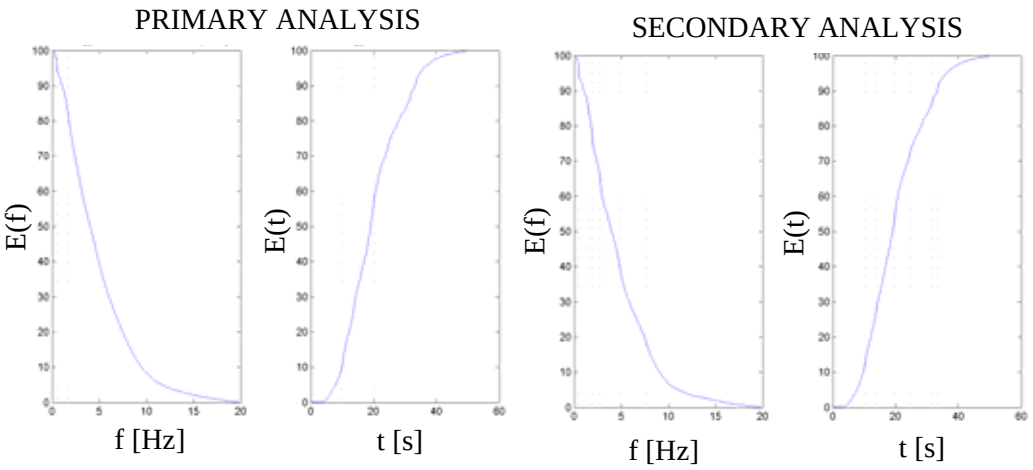

FIGURE 5.17. Energy accumulation in frequency domain and time domain for primary (left) and secondary analysis of Guerrero MC nearfield record

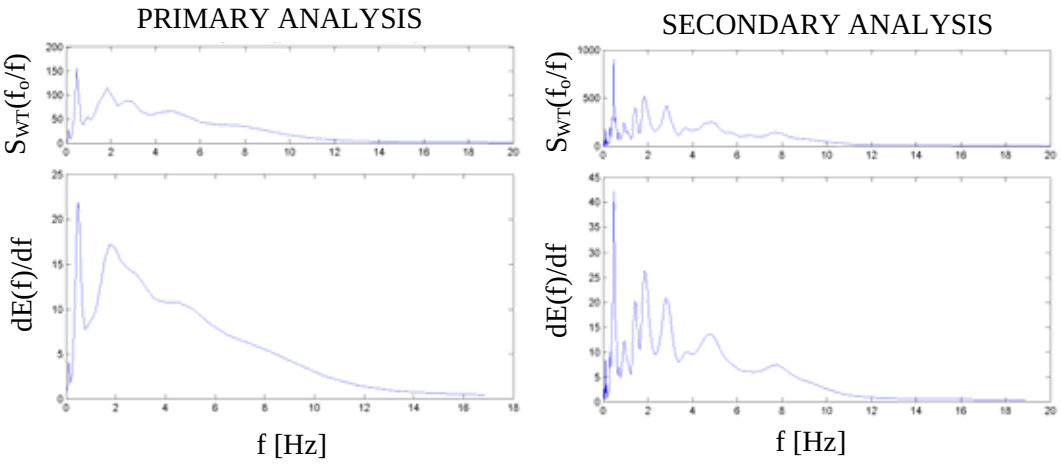

FIGURE 5.18. Wavelet marginal spectrum and rate of change of energy accumulation in frequency domain for primary (left) and secondary analysis of Guerrero MC nearfield motion

change of energy accumulation in frequency and time, shown respectively in Figures 5.18 and 5.19, offer a more complete description of the energetic components of the quake.

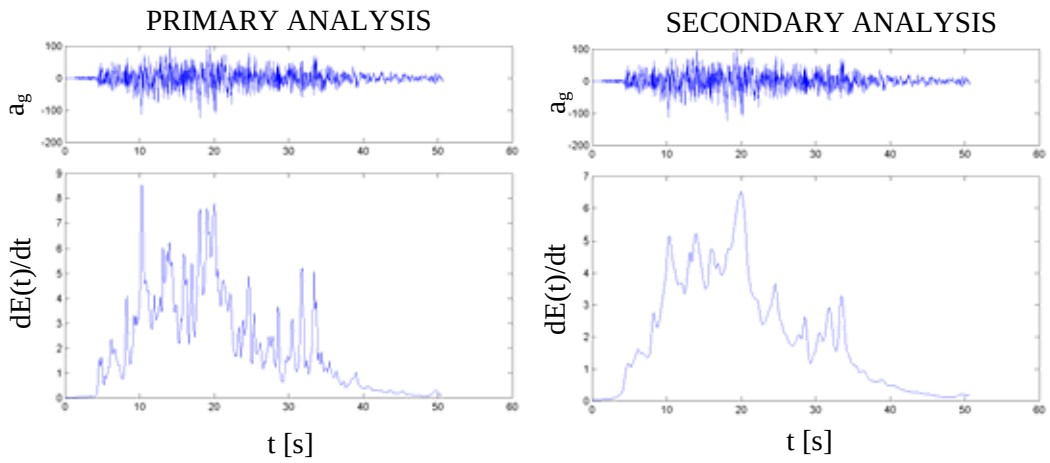

FIGURE 5.19. Guerrero MC nearfield ground acceleration and rate of change of energy accumulation in time domain for primary (left) and secondary analysis

Due to the compromised frequency resolution in the primary analysis, the rate of change of energy accumulation in the time domain in Figure 5.19 is able to isolate a very energetic component at 0.47 Hz followed by a more broadband contribution peaking at 1.76 Hz. The broadness of this peak implies that a bulk of the influx of energy into the system comes from frequencies in this vicinity. After plateauing at 4 Hz, the rate of change of energy accumulation in the frequency domain begins to fall off steeply by 12 Hz. The secondary analysis provides some additional details on the participating frequencies. The richness affirms that while the single most energetic component is at 0.48 Hz, a rather robust contribution from frequencies near 2 Hz is present. The peaks associated with influxes of energy into the system can be traced back to the accumulation

plot in Figure 5.17 to isolate specific contributions, as shown by the dotted vertical lines. This analysis reflects that approximately 6% of the signal energy lies at or below 0.49 Hz. Though several frequency components less than 2 Hz are shown to provide increases to cumulative energy in the signal, a total of approximately 20% of the nearfield signal resides less than 2 Hz. Another 20% resides at frequencies above 7.62 Hz, consistent with the findings from simulation studies, which found that the Guerrero gap might produce energy at a wide distribution of frequencies including high frequency motions (Jennings et al., 1989). The primary analysis affirms that 79% of the energy associated with this nearfield motion is associated with frequencies greater than 1.8 Hz, despite the sharp increase in energy accumulation near 0.5 Hz. The nearfield Guerrero MC record was found to contain only approximately 3% of its energy at frequencies under 0.5 Hz.

The intricacy of the rate of change in the time domain in Figure 5.19 highlights one of the unique characteristics of this event. Even with the reduced resolution of the secondary analysis, the energy influx into to the system is changing consistently between 10 to 20 s with a number of small events where the rate of energy accumulation suddenly increases. The most noteworthy of these events is at the twentieth second. Though falling off between 20 and 35 s, the level of activity in this event spans nearly 40 s. A number of these isolated events can be traced back to the accumulation plots in Figure 5.17. In doing so, it is shown that 13% of the energy arrives in the first 10.4 s. After which, the next 3 s bring an additional 13% of the energy. The ten seconds of shaking from 14 to 24 s brings over 46% of the signal energy, isolating the most energetic component near 20 s. The following seven seconds bring another 14% of the signal energy before quickly falling off beyond the thirty-first second. The accumulation in this event takes longer than the

other events considered in this study. The enhanced temporal resolution of the primary analysis, if anything, affirms the flurry of activity associated with this quake. The primary analysis generally confirms that the first 10 s is associated with only 10% of the signal energy, while 47% of the signal energy comes in the next 10 s of shaking.

The analyses of the instantaneous spectra taken at critical moments in the nearfield event are shown in Figure 5.20. In the primary analysis, the coarse frequency resolution results in the lumping of energy into wider frequency bands. At 10.3 s, despite the presence of a low frequency component near 0.5 Hz, a large concentration of energy is associated with the high frequencies. As shown in Table 5.6, the component near 1.87 Hz, which broadly captures contributions from 1.66 to 2.08 Hz, holds 18.6% of the instantaneous energy. The next component at 3.37 Hz representing frequency content from 2.99 to 3.74 Hz, is associated with over one-fourth of the instantaneous energy. The higher frequency bands from 6.42 to 8.05 Hz hold the most energy, 42.5%. The secondary analysis, though providing added detail, generally confirms that there is a robust distribution of energy noted in the primary analysis. Again the contributions near 0.5 Hz are just over 2%, as shown in Table 5.6. The first harmonic component of the primary analysis is now broken into two peaks at 1.41 and 1.87 Hz, which pool between them nearly 20% of the instantaneous signal energy. A very wide suite of energy from 3 to 6 Hz contains 33.2% of the instantaneous signal energy. A large contribution of energy near 7 Hz is also noted. The primary analysis at the twentieth second, now associated a more definitive share of the instantaneous energy with the mode near 0.5 Hz. By virtue of the enhanced temporal resolution, it is apparent that the majority of energy associated with this low frequency component is associated with the pulse at the twentieth second,

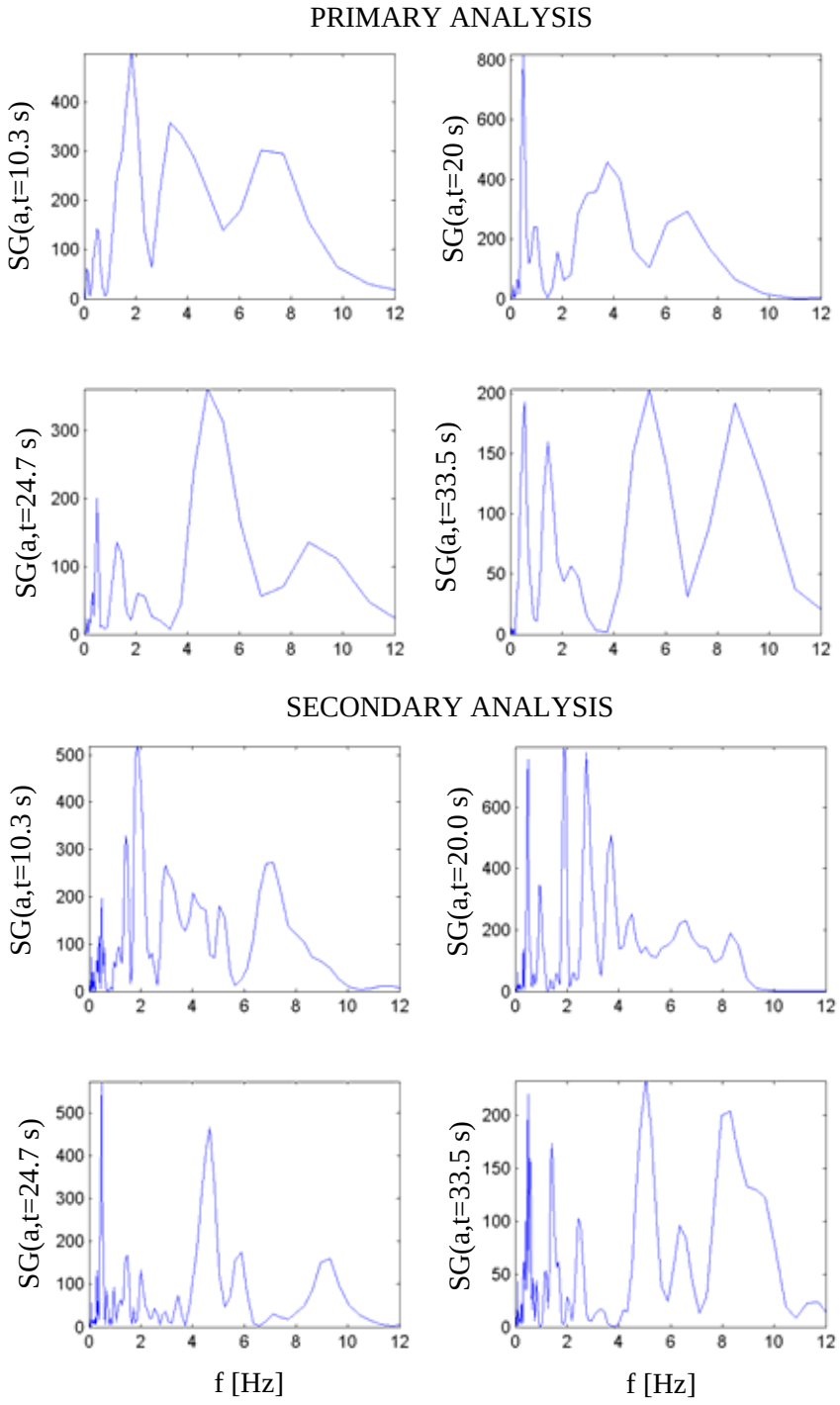

FIGURE 5.20. Wavelet instantaneous spectra taken at critical time steps in the Guerrero MC nearfield event for primary (top) and secondary analysis

as instantaneous spectral analyses at other time intervals fail to show such a strong component at this frequency. Despite this contribution, as shown in Table 5.6, a majority of the energy in this time interval remains in the high frequency ranges. The secondary analysis affirms that the low frequency components begin to more clearly separate into two distinct components less than 1 Hz, do retain more significance within the shaking near the twentieth second. They are coupled with contributions of similar order (see Table 5.6) from distinct frequencies near 1.93, 2.78 and 3.70 Hz. A very wide band of high frequencies attributes the remaining energy in this time interval. Moving away from the most energetic moment in the shaking, the emphasis on the low frequencies diminishes and the energy again moves toward the higher frequencies. Energy now is detected in significant quantities all the way to 8.62 Hz, as shown in Table 5.6, affirming the ability of the Guerrero gap to produce such excitations. The presence of high frequency shaking is affirmed in the secondary analysis in Table 5.6, though still retaining the significance of the low frequency component. This may be due to the fact that the compromised temporal resolution of this analysis leads to a smearing of energy with time at low frequencies.

By 33.5 s, some of the low frequency content has resurfaced in the primary analysis, though paling in comparison to the contributions at higher frequencies. The simultaneous presence of both high and low frequency shaking is a unique characteristic of the Mexico City event. The individual contributions are again noted in Table 5.6. The secondary analysis affirms a decided shift toward the higher frequencies, concentrating a majority of the instantaneous energy above 5 Hz. However, the persistent presence of the

TABLE 5.6

RELATIVE CONTRIBUTIONS OF EACH COMPONENT TO INSTANTANEOUS SPECTRA FOR GUERRERO MC NEARFIELD EARTHQUAKE PRIMARY AND SECONDARY ANALYSES

t_j [s]	IF_1 [Hz]	$\hat{E}_1(t_j)$ [%]	IF_2 [Hz]	$\hat{E}_2(t_j)$ [%]	IF_3 [Hz]	$\hat{E}_3(t_j)$ [%]	IF_4 [Hz]	$\hat{E}_4(t_j)$ [%]	IF_5 [Hz]	$\hat{E}_5(t_j)$ [%]
Primary Analysis										
10.3			1.87	16.7	1.87	18.6	3.37	26.3	7.24	42.5
20.0	0.49	12.1					3.77	41.6	6.72	34.76
24.7	0.49	2.56	1.34	5.43			4.82	53.4	8.62	29.9
33.5	0.56	5.54	1.47	11.9			5.34	25.9	8.68	42.2
Secondary Analysis										
10.3	0.49	2.2	1.41	6.8	1.87	13.5	4.03*	33.2	7.05	36.3
20.0	0.49	4.91	0.95	4.02	1.93	9.48	2.78	17.3	3.70	13.1
24.7	0.49	6.05			4.69	34.7	5.87	11.9	9.14	24.9
33.5	0.56	4.50	1.41	5.86	2.45	3.80	5.08	21.6	8.23	46.4

*midpoint of wide band energy distribution.

low frequency contributions at 0.5 Hz should be noted, as they will play a critical role once the seismic waves arrive in the Mexico City valley.

The collapse of a number of high-rise dwellings in the Mexico City earthquake emphasized the significance of site conditions in enhancing seismic risk, as it was observed that, at some locations in and near Mexico City, components in the vicinity of 0.5 Hz were dramatically amplified. Such amplification was not evident in coastal records, as shown in the preceding analysis and in Singh et al. (1989). In fact, ground motion at the lakebed sites in Mexico City were amplified nearly 75 times in the vicinity of 0.5 Hz in comparison to the costal sites of equal distance from the source (Singh et al., 1989). To demonstrate the dramatic amplification of the low frequency component, a free field record from the Mexico City Valley is analyzed by the aforementioned primary

analysis technique. The mean wavelet time and frequency resolutions are 0.113 s and 0.706 Hz, respectively, and the resolution of the accompanying Fourier analysis is 0.098 Hz. Upon comparing the farfield time history in Figure 5.21, recorded in Mexico City, with the nearfield Guerrero MC time history in Figure 5.15, the regular periodic characteristic of the farfield record and the elongation of period are immediately evident. An inspection of the marginal wavelet spectrum and the Fourier spectrum in Figure 5.21 demonstrates the amplification of the low frequency energy of the event that is largely credited with the heavy damage to structures of comparable period, as noted in the post-disaster surveys of Mexico City. A strong amplification of the 0.49 Hz component is apparent with only a slight presence at 1.46 Hz, which is comparatively negligible. Though this 0.5 Hz component was present in the coastal Guerrero MC record analyzed previously, the local site conditions clearly amplified this component of the shaking far above all others. The agreement between the wavelet marginal spectrum and the Fourier spectrum is excellent in this regard. The areas under the respective spectra also show good agreement with the signal variance. The signal had a standard deviation of 29.13 cm/s^2 in comparison to the 29.61 cm/s^2 estimated from the Fourier spectrum and the 29.16 cm/s^2 from the wavelet spectrum. The enhanced low frequency resolution of the wavelet analysis is particularly beneficial in capturing the energy of this record.

The scalogram also in Figure 5.21 affirms the concentration of energy at this frequency and identifies short duration pulses preceding the major pulse. The ridge extraction of the WIFS detects a subtle shifting of frequency. In comparison to the nearfield analysis in Figure 5.15, it becomes apparent that the amplification of the 0.5 Hz component dwarfs any residual contributions at the many other frequencies present in the

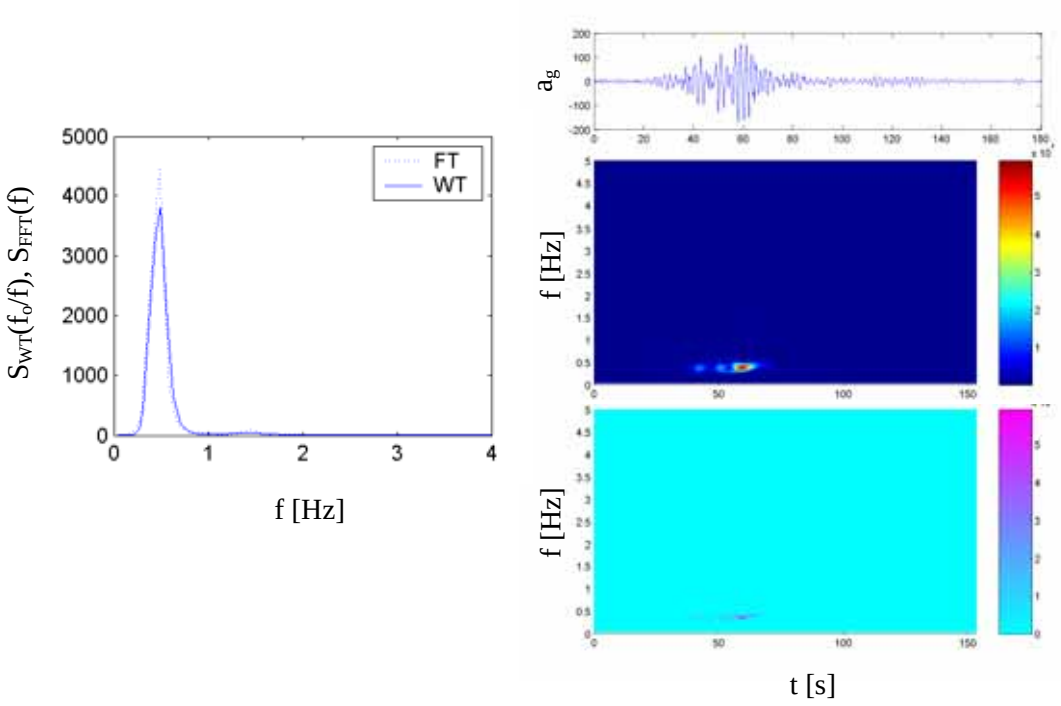

FIGURE 5.21. Comparison of Fourier spectrum and wavelet marginal spectrum (left) for Mexico City farfield ground motion with wavelet scalogram and WIFS (right, top to bottom)

quake. The energy accumulations in time and frequency and the rate of change in time are provided in Figure 5.22. The rate of change in the frequency domain (not shown), peaks at 0.47 Hz, as can be inferred from the accumulation plot in Figure 5.22 that has a steep descent in this vicinity. From this plot, it is demonstrated that 80% of the energy at this site comes from frequencies between 0.37 and 0.67 Hz. An additional 10% of the energy is associated with frequencies less than 0.37 Hz. The rate of change of energy accumulation in the time domain is actually more insightful, isolating the three pulses in the quake at 42.5s, 50.4 and 58.5 s, which happens to be most energetic. Relaying this information to the energy accumulation, it is demonstrated that one-quarter of the signal energy arrives with this main pulse. To determine the frequency content of the quake at

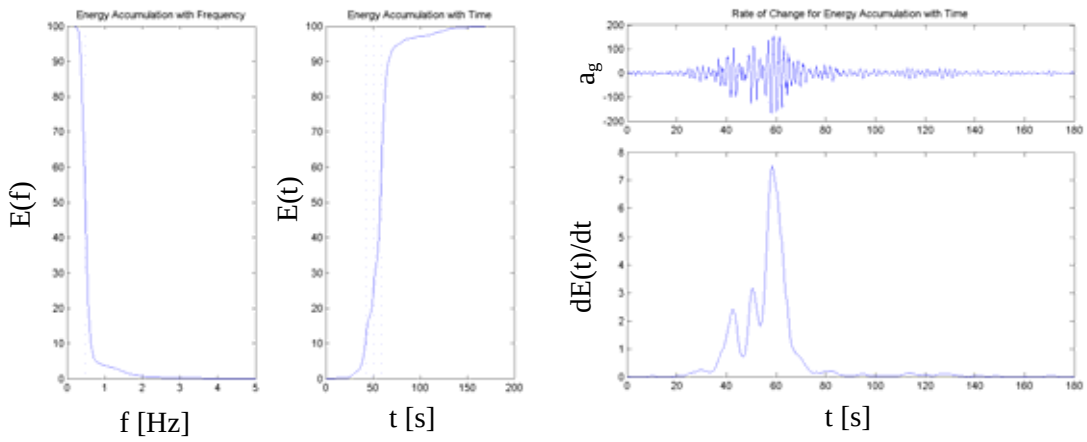

FIGURE 5.22. Energy accumulation in frequency and time (left), accompanied by Mexico City nearfield ground acceleration and rate of change of energy accumulation in time domain

these various time intervals, several instantaneous spectra are assembled in Figure 5.23. At each of the time steps associated with peaks in the rate of change of energy accumulation in Figure 5.22, the single component at 0.49 Hz dominates, with approximately 98% of the instantaneous signal energy at that particular time interval. Only after the shaking has subsided at 79.4 s does another frequency component surface, as approximately 20% of the energy surfaces at 1.47 Hz, the component just barely visible in the Fourier spectrum presented previously. This analysis affirms that shaking associated with the main three pulses are strongly focused at 0.5 Hz, while it is only in the residual shaking afterward that the additional component at 1.47 Hz emerges. The complexity of the instantaneous power spectrum in this latter stage of shaking reflects that under the diminished shaking, the amplitude of the 0.5 Hz begins to approach the energy levels associated with other harmonics.

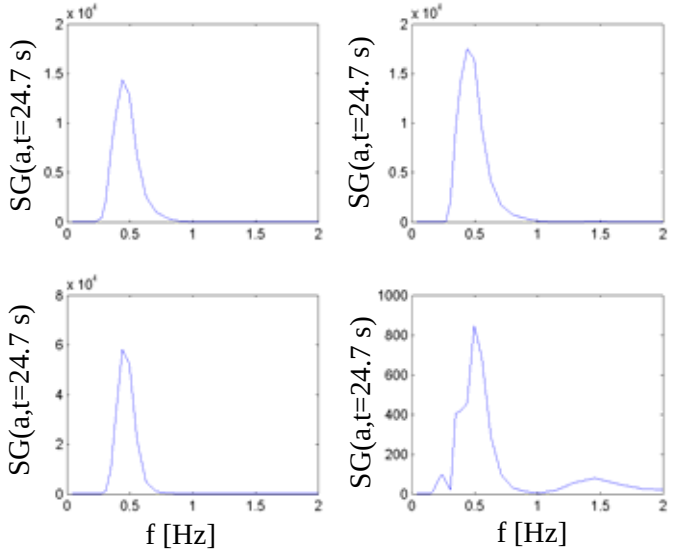

FIGURE 5.23. Wavelet instantaneous spectra taken at critical time steps in the Mexico City farfield record

5.4.3 Loma Prieta (1989)

An earthquake measuring 7.1 Ms occurred 18 km beneath the Santa Cruz Mountains in California on October 17, 1989, at 17:04 local time. The California Strong Motion Instrumentation Program (CSMIP) station closest to the epicenter of this so-called Loma Prieta event was the Corralitos station, located approximately 10 km away and very close to the San Andreas fault near the center of the aftershock zone. At this site, 0.64 g of motion was detected. At that time, this was the first nearfield record of a magnitude 7 event (Benuska, 1990). The ground motion record, with peak acceleration (PGA) of 0.6297 g, was fortunately relatively short in duration.

Again the two standard wavelet analyses used previously are presented in tandem for this event. The mean wavelet resolutions are given in Table 5.3. The signal was

downsampled from its original sampling rate of 50 Hz to 25 Hz to ease computation. Figure 5.24 shows the wavelet scalograms and the accompanying wavelet instantaneous frequency spectra for both analyses. Both the scalograms and WIFS affirm that the energy is primarily released within the first 10 s of the event. The primary analysis provides better temporal information and affirms that the energy lies between 2-10 s and concentrates at approximately 2.7-3 s, with the arrival of the largest pulse. The primary analysis detects a broad range of frequency contributions near 1 Hz and spanning all the way to nearly 4 Hz. Some secondary energy arrives near 5 and 7 s but pales in comparison to this initial pulse. The ridges in the primary analysis detect some slight high and low frequency contributions, which are minor in contrast to the persistent frequency contributions in the vicinity of 1.15 Hz, 1.5 Hz and 2.25 Hz. This latter component demonstrates a shift toward 3 Hz and then softens in frequency. Note that the most energetic burst at 2.8 s is tied to this higher frequency component.

The secondary analysis affirms that the primary burst of energy is concentrated near 2.75 Hz, though there are now more distinct bands of frequency evident, by virtue of the enhanced resolution, at approximately 1.25 Hz, 1.75 Hz, 2.25 Hz and 3 Hz. Interestingly these latter two components begin to approach one another, the 3 Hz softening toward the stiffening 2.75 Hz component. This stiffening and softening was crudely captured in the primary analysis by the increase and drop in the higher frequency component peaking near 3 Hz. The energy associated with higher frequencies between 3 and 4 Hz also is readily more apparent.

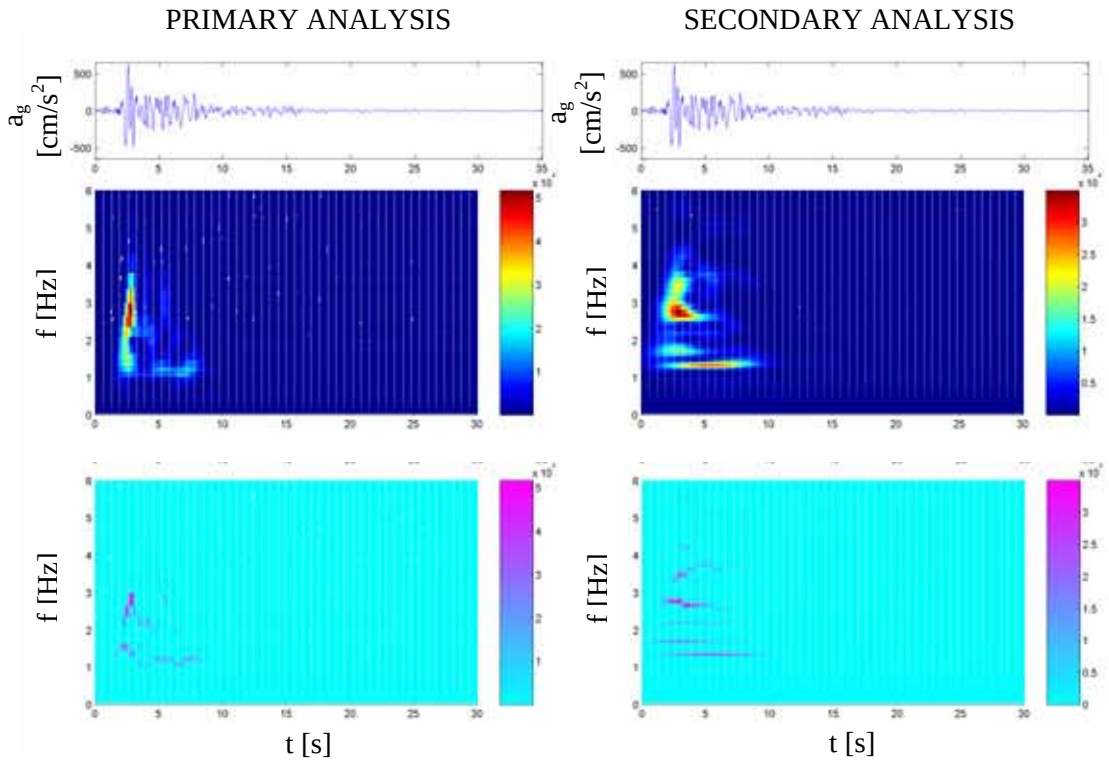

FIGURE 5.24. Loma Prieta ground motion, wavelet scalogram and WIFS (top to bottom) for primary (left) and secondary analyses

A comparison of the Fourier power spectrum and the marginal wavelet spectrum for each analysis is provided in Figure 5.25. The coarser primary analysis lumps the signal energy into two dominant bands of energy near 1.5 Hz and 3 Hz. However, revisiting Table 5.3, the frequency resolution of the secondary wavelet analysis is more akin to the resolution of the Fourier spectrum. As such, this secondary analysis detects many of the finer spectral details of the Fourier analysis. The Fourier analysis identifies a dominant contribution near 1.4 Hz coupled with an energetic component near 2.8 Hz. These two dominant modes are similar to those specified by the primary wavelet marginal spectrum. The differences in amplitudes are merely the function of the finer

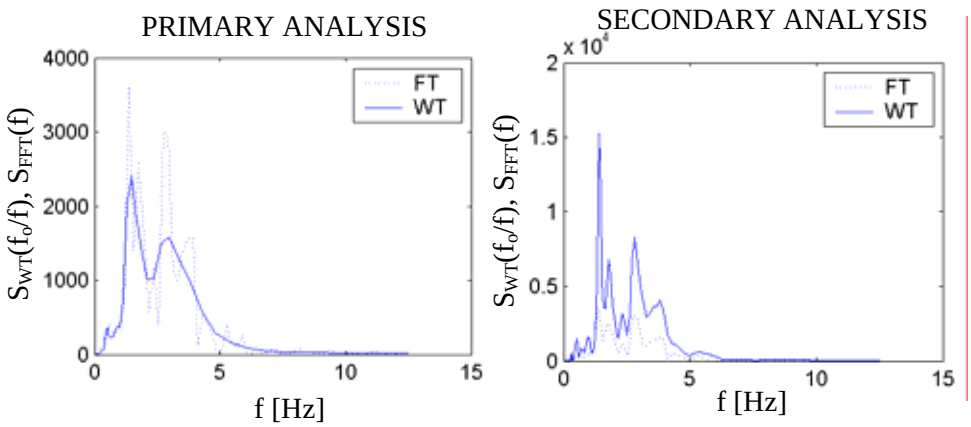

FIGURE 5.25. Wavelet marginal spectra with Fourier power spectrum for primary (left) and secondary analyses for Loma Prieta quake

bandwidth in the secondary wavelet analysis directly accounted for in the scaling by *a*. Still the energy is completely conserved in the wavelet representation and even more so than the Fourier analysis, as evidenced by Table 5.4 when comparing to the signal standard deviation σ. Note that at the low frequencies, the superior resolution of the wavelet provides some added detail. In general, both the wavelet and Fourier spectra confirm that there is only trace energy below 1 Hz and above 4 Hz.

The energy accumulation plots in Figure 5.26 account for the multi-resolution characteristics of wavelets and provide a more objective tool for investigating the dominant energy components in the signal in comparison to the magnitude of wavelet scalograms. The dotted lines on the energy accumulation with frequency are associated with the most significant spectral peaks identified in the primary and secondary analyses.

In the primary analysis, the energy accumulated up to 2.8 Hz is 46%, and by 1.5 Hz, 79% of the signal energy has been expelled. The four major peaks identified by the

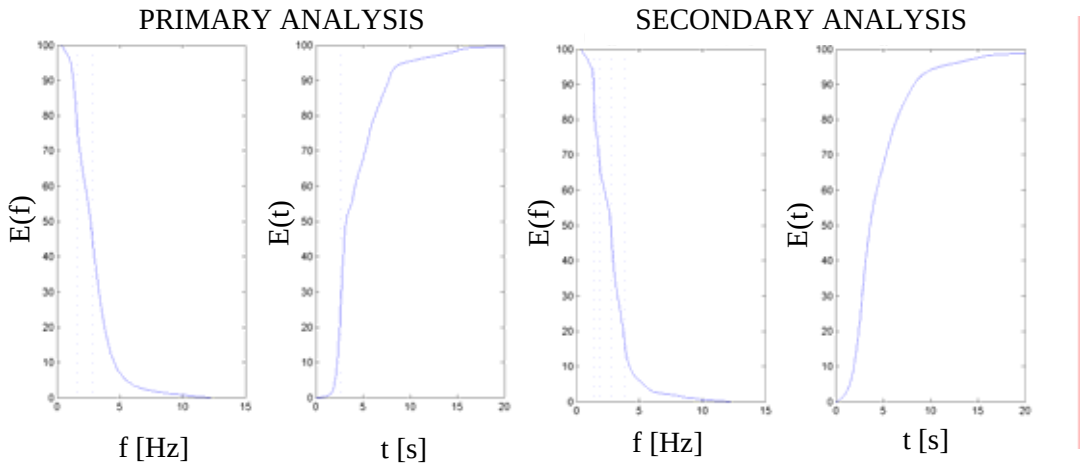

FIGURE 5.26. Energy accumulation in frequency domain and time domain for primary (left) and secondary analysis of Loma Prieta

secondary analysis verify that at 3.8 Hz, only 16% of the signal energy has been realized. By 2.8 Hz, this has jumped to 42% followed by a steep vertical ascent to 50% of the signal energy. This would indicate that nearly 35% of the total signal energy is associated with this component of the spectrum. 70% of the signal energy lies above 1.8 Hz with 81% of the energy above 1.4 Hz again followed by a very steep ascent to nearly 90% of the signal energy. Thus 20% of the signal energy is associated with this lower frequency component. The vertical ascents at 2.8 and 1.4 Hz are indicative of very rapid changes in signal energy. The frequencies at which these occur can be considered the most energetic frequency components in the signal. This can be more readily visualized by examining the rates of change of energy accumulation, shown for frequency in Figure 5.27. For the primary analysis, it becomes evident that the most energetic frequency component is associated with 1.5 Hz, which corresponds to the dominant frequency component in the Fourier spectrum. An additional energetic component at 2.8 Hz is also affirmed, along with a minor low frequency presence at 0.5 Hz. The accumulation curves in Figure 5.28

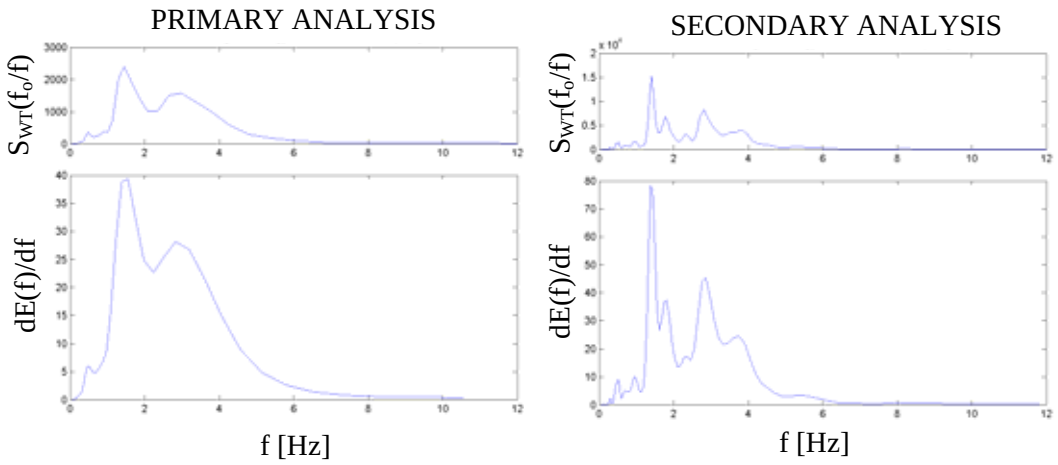

FIGURE 5.27. Wavelet marginal spectrum and rate of change of energy accumulation in frequency domain for primary (left) and secondary analysis of Loma Prieta

affirm that 90% of the signal energy is above approximately 1.25 Hz. In the secondary analysis, the findings are quite similar though more details are resolved. Still the energy is harnessed at 1.8 Hz and additionally near 3 Hz. The highest rates of change in energy accumulation are appropriately associated with the marginal spectral peaks and the analysis provides no evidence of significant high or low frequency contributions.

The rate of change of energy accumulations in the time domain is provided in Figure 5.28. The superior time resolution of the primary analysis is evident. Not only is the arrival of the major pulse at 2.8 s clearly identified, but also the sustaining of energy between 3 and 8 s, with the exception of occasional spikes at 4 and 5.5 Hz. The termination of the major energetic components occurs near 8 s. After this point, the energy drops off steeply and has hardly any contributions beyond 9 s. Returning to the energy accumulation in Figure 5.26, the dotted line indicates the arrival of the major

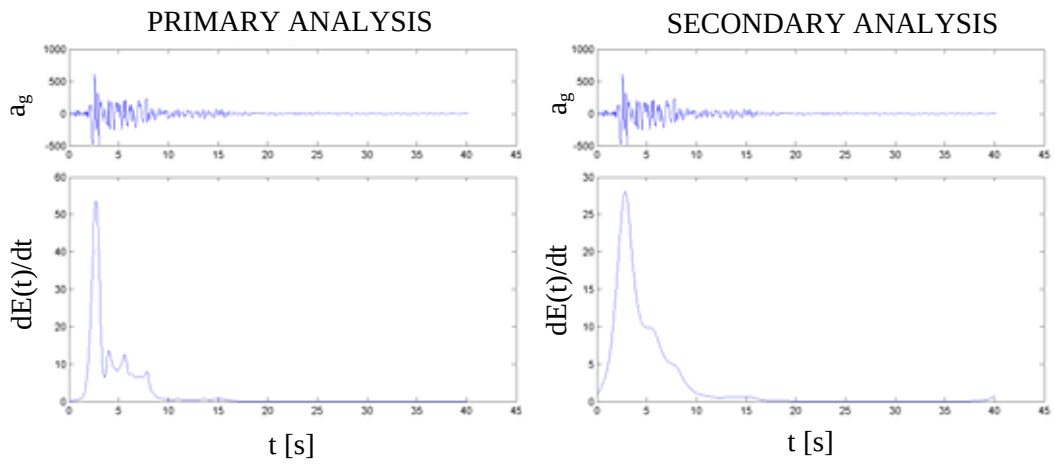

FIGURE 5.28. Loma Prieta ground acceleration and rate of change of energy accumulation in time domain for primary (left) and secondary analysis

pulse where signal energy jumps from 25% to 30% and sustains its intensity over the first 5 s, as over half the signal energy arrives. By nearly 7.8 s, 90% of the energy has passed, accounting for the drop off in *dE(t)/dt* beyond 8 s. The secondary analysis is incapable of providing such detail. It captures the major event at 2.8 s and the cumulative energy plot affirms a jump from 24% signal energy to 33%, followed by a rather gradual decline in energy terminating at 10 s. This loss of resolution is the consequence of the trade-offs between time and frequency resolution. Still the analysis sufficiently gauges the localization of energy, with the times and frequencies associated with the maximum rates of change in energy accumulation representing the most significant contributors to the event.

Four instantaneous spectra were extracted at key moments in the progression of the earthquake, as shown in Figure 5.29. At 2.8 s, the arrival of the major pulse of the quake, the primary analysis detects a bi-modal response peaking at 1.7 and 3.4 Hz. These two components respectively contribute 16.7 and 78.7 % of the energy at this time. The

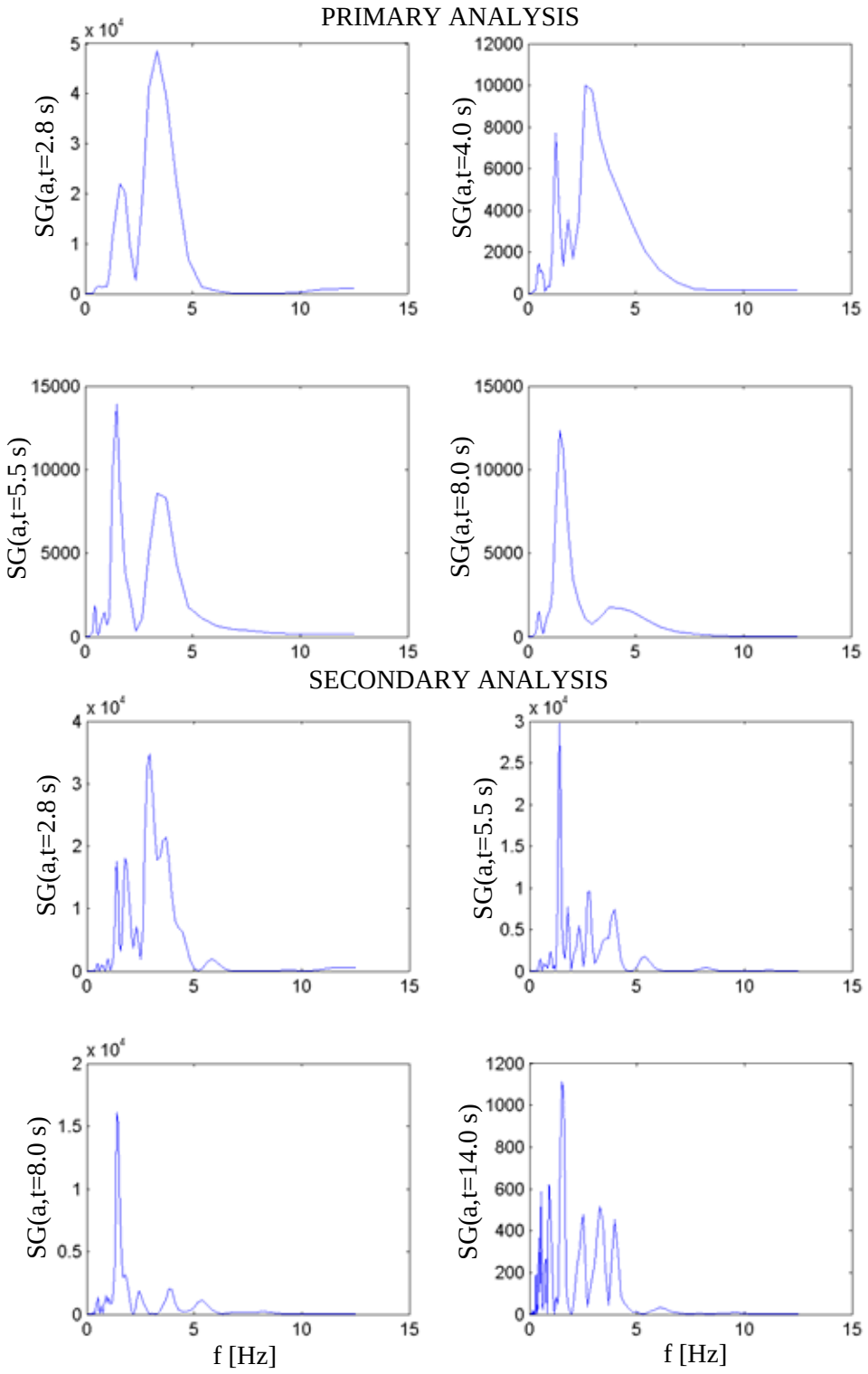

FIGURE 5.29. Wavelet instantaneous spectra taken at critical time steps in the Loma Prieta event for primary (top) and secondary analysis

enhanced resolution of the secondary analysis at this same time frame identifies two groupings of frequency contributions, each manifesting multiple peaks. The major grouping near 1.6 Hz holds 21% of the instantaneous signal energy and the grouping near 3 Hz holds 71% of the instantaneous energy at this time. These statistics are chronicled in Table 5.7. Both analyses confirm that this first and most energetic pulse contains dominant energy in the vicinity of 3 Hz. The next instantaneous spectrum at approximately 4 s, associated with the minor event, shows a slight low frequency component but two major peaks at 1.27 and 2.91 Hz, a down shift in frequency from the earlier pulse. Still the energy contributions are primarily associated with the higher frequency component (82.4%), with only 11.1% associated with the 1.27 Hz peak. By 5.5 s, the primary analysis continues to display two dominant modes with some minor low frequency content. The two peaks shift to the higher frequencies of 1.43 and 3.56 Hz with the arrival of this third event, also denoted in Figure 5.29. More energy is present in the lower frequency peak (31.6%) than previously observed, though the 3.56 Hz component still garners the most energy (63.6%). For the secondary analysis, this is better resolved to identify three major clusters of frequency contributions 1.5 Hz, 2.8 Hz and 3.9 Hz with respective instantaneous energy of 37%, 16% and 27%. While the primary and secondary analysis are in agreement with the energy contained in the 1.5 Hz vicinity, the increase in resolution identifies in greater detail that the energy in the higher frequencies is predominantly near 3.9 Hz.

By the 8th second, energy is known to drop off dramatically. The primary analysis identifies two components at 1.51 and 3.89 Hz, again shifting to higher frequencies, and energy now associated more so with the lower frequency component, 65.3% vs. 32.2%.

TABLE 5.7

RELATIVE CONTRIBUTIONS OF EACH COMPONENT TO INSTANTANEOUS SPECTRA FOR LOMA PRIETA EARTHQUAKE PRIMARY AND SECONDARY ANALYSES

t_j [s]	IF_1 [Hz]	$\hat{E}_1(t_j)$ [%]	IF_2 [Hz]	$\hat{E}_2(t_j)$ [%]	IF_3 [Hz]	$\hat{E}_3(t_j)$ [%]	IF_4 [Hz]	$\hat{E}_4(t_j)$ [%]	IF_5 [Hz]	$\hat{E}_5(t_j)$ [%]
Primary Analysis										
2.8			1.70	16.7			3.40	78.7		
4.0			1.27	11.1			2.91	82.4		
5.5			1.43	31.6			3.56	63.6		
8.0			1.51	65.3			3.89	32.2		
Secondary Analysis										
2.8			1.59	71.0			3.0	21.0		
5.5			1.50	37.0			2.8	16.0	3.9	27.0
8.0			1.43	60.0						
14.0	0.70	15.6	1.52	23.7	2.50	14.9	3.32	20.7	3.97	15.6

In the secondary analysis, the diminishing high frequency components are affirmed, as the instantaneous spectrum falls into a single modal response at 1.43 Hz, harnessing 60% of the instantaneous energy. The secondary analysis is extended to 14 s, where the energy release has mostly subsided. The response here still concentrates at 1.52 Hz (with 23.7% of the instantaneous energy), accompanied by a 0.70 Hz component (15.6%), a 2.50 Hz component (14.9%), a 3.32 Hz component (20.7%) and a 3.97 Hz component (15.6%). In terms of energy distribution, the energy of the quake following strong shaking is relatively broadband. A primary analysis (not shown) at this same time affirmed shared energy over a range of frequencies, with 28% localized near 1.5 Hz and 42% between 2.32 and 3.67 Hz, in general agreement with the secondary analysis.

When interpreting the primary analysis results, it is important to recall that a wider range of frequencies is contributing to the energy near 3 Hz, from 2.32 to 3.67 Hz,

giving it a consistently dominant share of the instantaneous energy. The secondary analysis identifies many contributors in this range whose individual share of the instantaneous energy generally sums to the energy associated with the higher frequency mode of the primary analysis. However, the rates of change of energy accumulation affirm that the frequencies near 1.8 Hz are responsible for the most sudden influx of energy. This is the single most dominant component of the quake, as also affirmed by Fourier, while the most dominant range of frequencies contributing to the shaking is near 3 Hz, corresponding to the spectral contributor with the greatest "bandwidth," a characteristic that also can be affirmed from the Fourier spectrum in Figure 5.25.

5.4.4 Northridge (1994)

The 6.7 magnitude Northridge earthquake on January 17, 1994 represented California's most devastating earthquake in recent history. Striking at 04:30 local time, collapses of residential dwellings caught many victims in their sleep, prompting a wave of seismic research to uncover the sources of numerous failures and deficiencies in constructed facilities. The particular record analyzed herein was taken 2.31 km from the epicenter, representing nearfield, strong shaking. The signal was sampled originally at 50 Hz and then downsampled to 25 Hz for the following wavelet analysis, whose resolutions are provided in Table 5.3.

As demonstrated by the primary analysis scalogram in Figure 5.30, with time, the energy associated with each pulse tends toward higher frequencies in a general hardening trend, observed near 4 s and 8 s. The first event has a distinctly higher frequency content, centered around 2 Hz, while the latter event shifts to 1.3 Hz. The majority of the signal

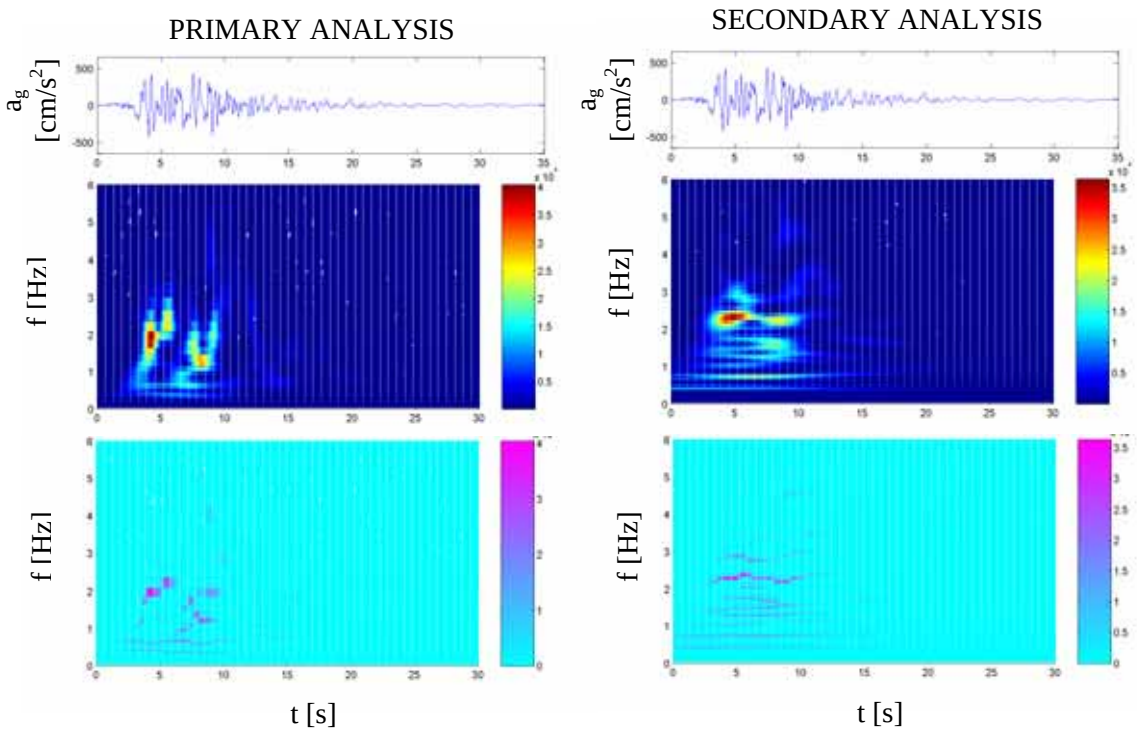

FIGURE 5.30. Northridge ground motion, wavelet scalogram and WIFS (top to bottom) for primary (left) and secondary analyses

energy is released within the first 10 s of the event. Though detecting a slight high frequency contribution, the WIFS affirms the dominance of energy between 1 and 2 Hz. The two signatures at 4 and 8 s share an ascending characteristic with neighboring frequency bands. Persistent components at 0.5 and 0.8 Hz are also noteworthy.

In the secondary analysis, also shown in Figure 5.30, the temporal bleeding noted previously is again present. The enhancement of frequency resolution isolates a few distinct frequency bands in the scalogram. The first event tends to focus primarily in the 2.3 Hz range. The latter event has more of a concentration near 2.21 Hz, flanked by a 0.76 Hz component. The abundance of low frequency ridges in the secondary WIFS may

be a direct consequence of an over resolution in the low frequency range. It does however detect two mirroring ridges near 2 and 3 Hz.

The Fourier spectrum in Figure 5.31 indicates that a wide band of energy from 0.46 to 3.01 Hz provides the driving energy in the earthquake. The largest Fourier amplitudes are near 2.3 Hz, but there also is a strong component near 0.8 Hz, as mentioned previously in the discussion of the scalograms. Beyond 3 Hz, the energy rapidly falls off. The wavelet marginal spectrum in the primary analysis captures largely the same trends, though the relative magnitudes emphasize the lower frequencies, as expected. The wider bandwidth of the components greater than 1 Hz implies that their amplitudes must be reduced in order to conserve energy. As noted in Table 5.4, energy is better captured by the primary wavelet analysis. The added detail in the secondary marginal wavelet spectrum reveals three contributing bands of energy near 0.6 Hz, 1.7 Hz and 2.4 Hz. These are consistent with the bands observed at different times in the wavelet scalogram and will be discussed in more detail in the instantaneous spectral analysis. The enhanced resolution in the secondary analysis, permits a better estimation of the overall energy, as shown in Table 5.4.

The energy accumulation plots in Figure 5.32 will now be discussed in parallel with the energy accumulation rates of change in the frequency and time domains, shown respectively in Figures 5.33 and 5.34. As noted previously, diminished resolutions in the time and frequency domains tend to smooth out the details of the energy accumulation plots, as seen from the primary and secondary analyses in Figure 5.32. In the frequency domain, as shown in Figure 5.33, the primary analysis, lacking sufficient detail, identifies

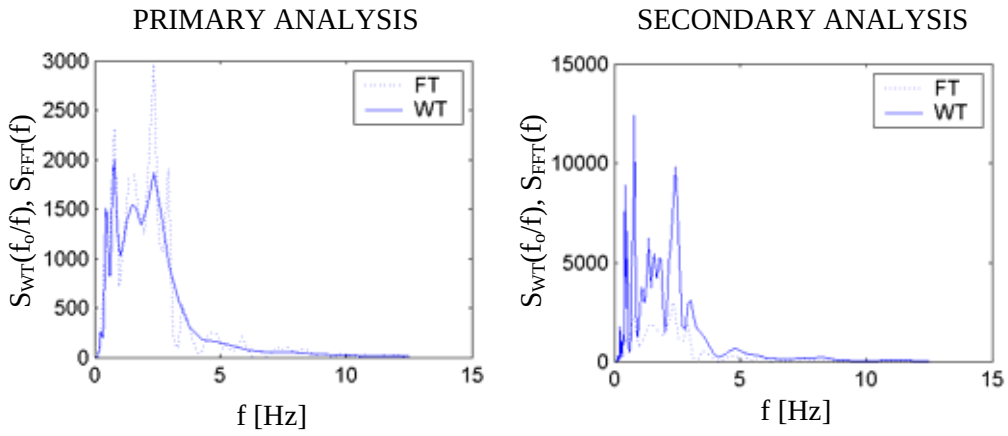

FIGURE 5.31. Wavelet marginal spectra with Fourier power spectrum for primary (left) and secondary analyses for Northridge quake

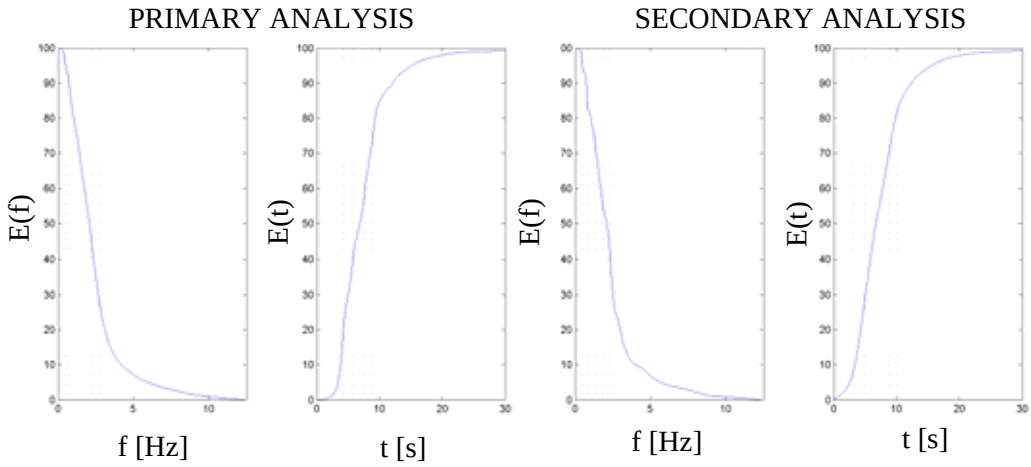

FIGURE 5.32. Energy accumulation in frequency domain and time domain for primary (left) and secondary analysis of Northridge

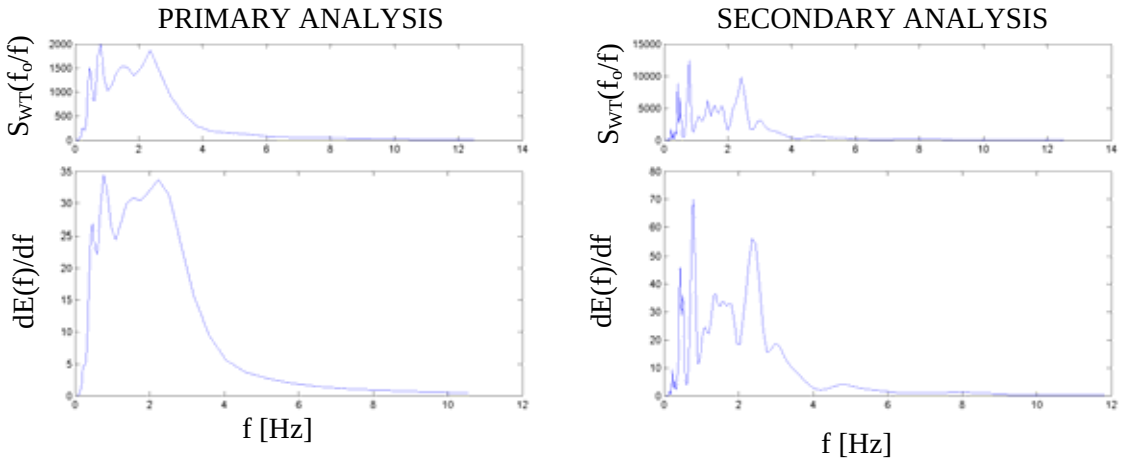

FIGURE 5.33. Wavelet marginal spectrum and rate of change of energy accumulation in frequency domain for primary (left) and secondary analysis of Northridge

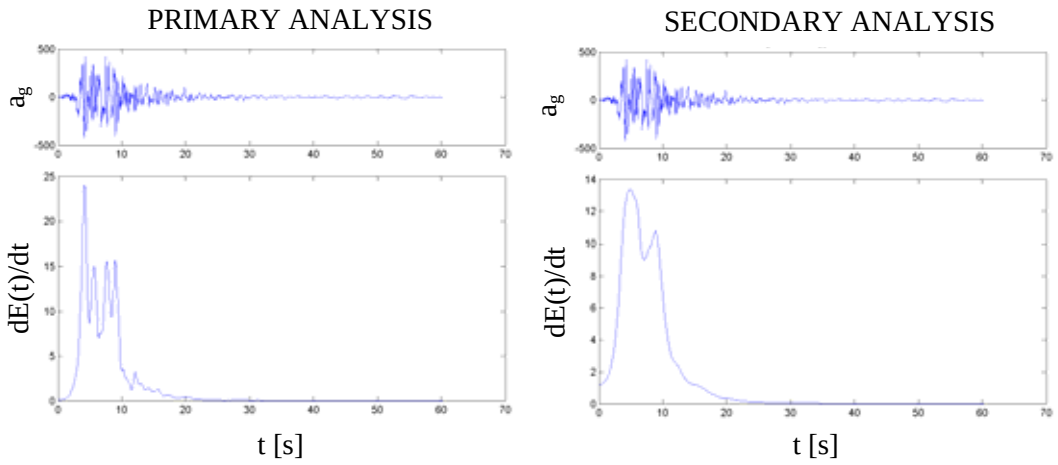

FIGURE 5.34. Northridge ground motion and rate of change of energy accumulation in time domain for primary (left) and secondary analysis

a large band of frequencies associated with the release of energy during the quake. This would indicate that a suite of frequencies from 0.4 to 2.7 Hz contributes in a comparable manner to the shaking. The frequency associated with the greatest change in energy accumulation is 0.76 Hz, closely followed by the component at 2.25 Hz. The bandwidths of contributing frequencies as well as the two aforementioned peak frequencies are denoted in Figure 5.32 by dotted lines. The energy accumulation plot in the time domain reflects that 27.3% of the energy lies above 2.76 Hz. 14% of the energy is between 2.3 and 2.7 Hz, while 40% of the energy is between 0.78 and 2.3 Hz, the broad range in which most of the scalogram energy was focused. Approximately 10% of the signal energy lies below 0.78 Hz.

The secondary analysis in Figure 5.33 provides some additional insights. Two distinct contributions to the rate of change of energy accumulation are observed at 0.48 and 0.79 Hz, followed by a constant influx of energy between 1.3 and 1.8 Hz. This is trailed by another influx of energy at 2.4 Hz. Again relating these particular frequency components to the energy accumulations in Figure 5.32 reveals that 38.4% of the signal energy is associated with frequencies higher than 2.4 Hz, while 13% are associated with frequencies from 1.9 to 2.4 Hz. The bands from 1.3 to 1.8 Hz and 0.8 to 1.3 Hz both are associated with approximately 12% of the signal energy. Only 6% of the energy is associated with 0.5-0.8 Hz. These analyses indicate that the dominant energy of the signal lies between 0.8-2.4 Hz, in agreement with the Fourier spectrum. However, the most energetic frequency contribution comes from 0.78 Hz. This frequency brings the single greatest influx of energy to the signal – a characteristic not evident from the Fourier spectrum.

From the time rate of change in Figure 5.34, the primary analysis denotes a constant energy contribution from 3.3 to 9.6 s, during which there are four distinct events at 4.24, 5.72, 7.64 and 8.92 s. These are the peak events creating the energy ascent demonstrated previously in the scalogram. These instances can be correlated back to the energy accumulation plots in Figure 5.32, as denoted by the dotted lines. This analysis indicates that 15% of the energy arrives in the first 4.14 s, at which point the cumulative energy jumps another 5%, marking the time with the highest energy influx. In the next two seconds, another 16% of energy is released. The following two seconds provide another 20% jump in energy. By 7.6 s, there is a spike in energy of 3% and then a 14% rise in energy up to 8.9 s. By this point, 75% of the quake's energy has been released, affirming the concentration of energy in the scalogram under 10 s. The secondary analysis smoothes out many of these details, as shown in Figure 5.34. Needless to say, the energy is still shown to lie between 3 and 10 s, peaking at 4.86 s, with a lesser peak at 8.95 s. A similar inspection of the accumulation plot in Figure 5.36 demonstrates that only 6.5% of energy lies in the first 3 s of shaking. The majority of the energy (45%) is released between 4.8 and 9 s, consistent with the primary analysis.

The primary instantaneous spectral analysis in Figure 5.35 provides more insights into the spectral distribution of energy during different critical events in the Northridge quake. The first spectrum, associated with 4.2 s, identifies one major energy component at 2.26 Hz, accompanied by some lower frequency content. As shown in Table 5.8, 88.9% of the instantaneous signal energy is associated with this single component. By 5.72 s, this low frequency component becomes more energetic, holding 18.37% of the instantaneous energy. At the same time, the dominant mode has stiffened and holds

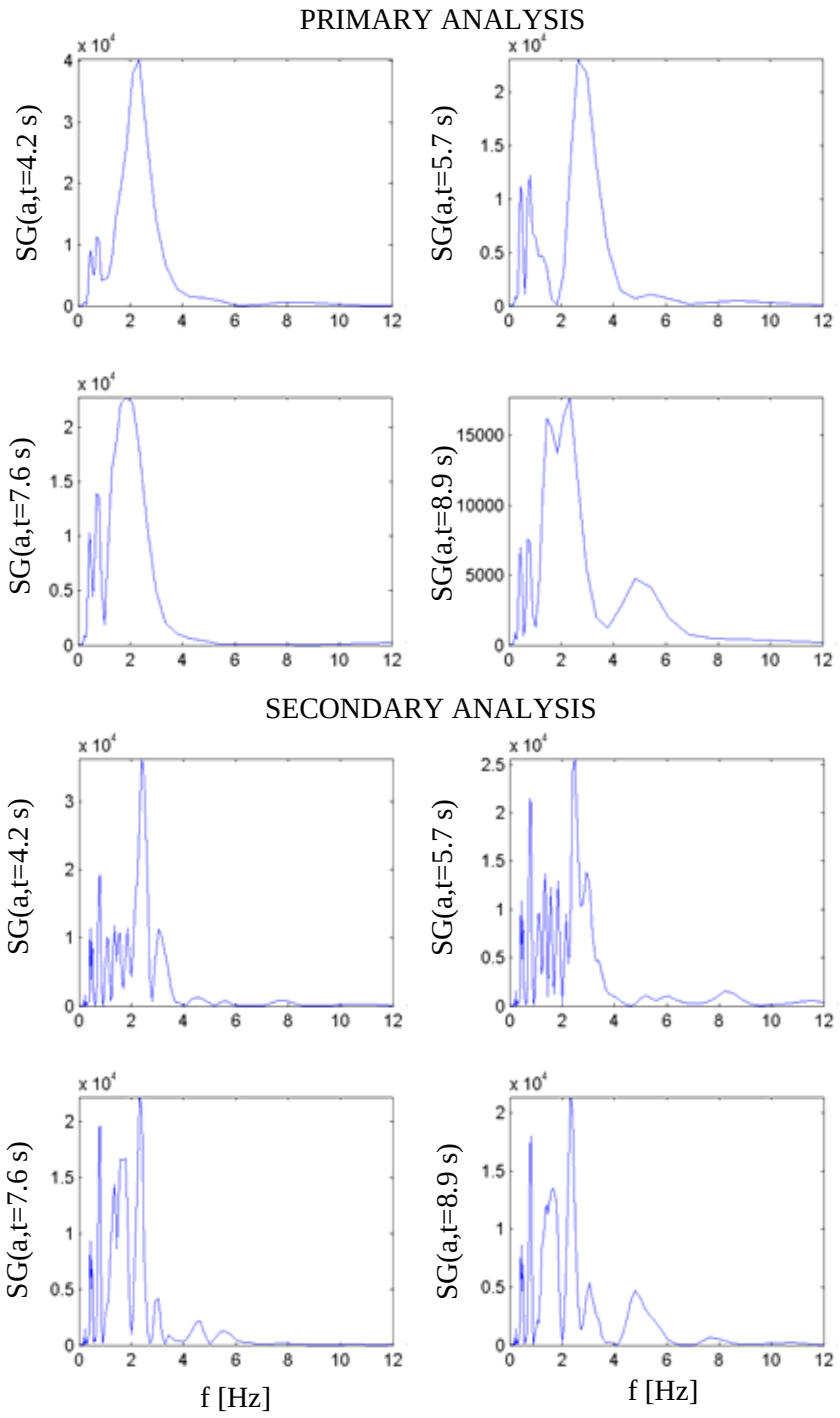

FIGURE 5.35. Wavelet instantaneous spectra taken at critical time steps in the Northridge event for primary (top) and secondary analysis

72.5% of the instantaneous energy. By 7.6 s, the response has focused toward a single mode at 1.8 Hz holding most of the energy, as shown in Table 5.8. Concurrently, the lower frequency mode has also shifted toward lower frequencies and holds 12.6% of the instantaneous signal energy. This tendency was reflected in the scalogram through a shift of energy toward lower frequencies in the two consecutive major events. By 8.9 s, the energy has been halved, though a low frequency mode at 0.62 Hz remains, with its energy content somewhat diminished. The combination of contributions at 1.8 and 2.3 Hz now hold 64.3% of the signal energy, with the addition of a high frequency component at 5 Hz, which represents a range of energy from 4.5 to 5.5 Hz. These analyses again demonstrate the importance of understanding that the energy under instantaneous spectra, and not the spectral amplitude, should be consulted to determine the dominant frequency within a signal. Marginal spectra demonstrated larger amplitudes at the lower frequencies, but the detailed analysis of energy distribution affirms that the dominant component in the quake was actually near 2.26 Hz.

The secondary analysis, also shown in Figure 5.35, provides potential over resolution of the low frequency components, but still discerns a dominant mode at 2.46 Hz at 4.2 Hz and is capable of separating out an additional mode at 3.11 Hz, whose respective energy contributions are given in Table 5.8. These two higher frequency modes then collapse into one peaking at 2.52 Hz and again comprising the primary energy source for the quake, accompanied by a broad band of energy in the low frequency range. By 7.6 s, these low frequency components become more distinct but still reiterating the strength of contributions in the vicinity of 2 Hz. At 8.9 s, the same

TABLE 5.8

RELATIVE CONTRIBUTIONS OF EACH COMPONENT TO INSTANTANEOUS SPECTRA FOR NORTHRIDGE EARTHQUAKE PRIMARY AND SECONDARY ANALYSES

t_j [s]	IF_1 [Hz]	$\hat{E}_1(t_j)$ [%]	IF_2 [Hz]	$\hat{E}_2(t_j)$ [%]	IF_3 [Hz]	$\hat{E}_3(t_j)$ [%]	IF_4 [Hz]	$\hat{E}_4(t_j)$ [%]
Primary Analysis								
4.2					2.26	88.9		
5.7	0.82	18.4			2.72	72.5		
7.6	0.75	12.6	1.80	84.0				
8.9	0.62	6.3	1.80	64.3	2.26	**	5.0	23.0
Secondary Analysis								
4.2	0.75*	28.9			2.46	43.6	3.11	16.0
5.7	0.75	34.0			2.52	47.0		
7.6	0.75	9.2	1.74	41.3	2.39	28.3		
8.9	0.75	7.7	1.67	30.0	2.39	26.2	4.88	17.3

*Broadband energy peaking at this frequency.
**Shares energy in one broad peak with previous frequency component.

contributors remain, joined however by an additional component near 5 Hz, whose instantaneous spectral energy contributions are listed in Table 5.8.

5.4.5 Kobe (1995)

One year after Northridge, on January 17, 1995 at 05:46 local time, a magnitude 7.2 earthquake hit Kobe, Japan, an area viewed previously to have relatively low seismic risk. The Nojima fault triggered the earthquake and subsequent rupture of several smaller faults in the Kobe area. The loss of 5600 lives and destruction of 100,000 buildings affirmed the devastation of this event. The Takatori N-S Kobe ground motion, measured approximately 10 km from the epicenter, is analyzed herein. The signal, sampled originally at 100 Hz, is downsampled to 25 Hz and analyzed by the aforementioned

wavelets to produce the scalograms and WIFS in Figure 5.36. Note the strong period of shaking in the time history in Figure 5.36 for the first 15 s, followed by a regular, periodic motion.

Both the primary and secondary analyses reiterate the same general finding: the Kobe event focused its dominant energy below 1 Hz. The primary analysis further affirms the arrival of a large low frequency pulse near 5 s and even lower frequency shaking subsequently. The scalogram is generally devoid of higher frequency content. The last meaningful shaking subsides by 15 s. The low frequency energy is flanked at three distinct locations by energy in the 2 Hz vicinity, in the primary event and in subsequent pulses near 10 and 15 s. The WIFS merely affirms the predominance of shaking below 1 Hz. In the secondary analysis, two predominant ridges are more clearly defined near 0.78 and 1.3 Hz. At the major pulse of the quake, some additional frequency components between these two also surface. This plethora of ridges may be the consequence of over resolution in the low frequency range. After 5 s, the components near 2 Hz split and move toward higher and lower frequencies.

Analysis of the traditional Fourier spectrum in Figure 5.37 affirms that the energy is focused in a narrowband between 0.4 and 1 Hz., peaking at a value of 0.9 Hz. The presence of minor yet constant energy between 1 and 3 Hz is also noted, though this energy falls off rapidly beyond 3 Hz. Both the wavelet marginal spectra and Fourier spectra in the primary and secondary analyses capture the frequency content of the signal. The amplification of amplitudes and the added detail in the higher frequencies in the secondary analysis is a consequence of the enhanced frequency resolution in the

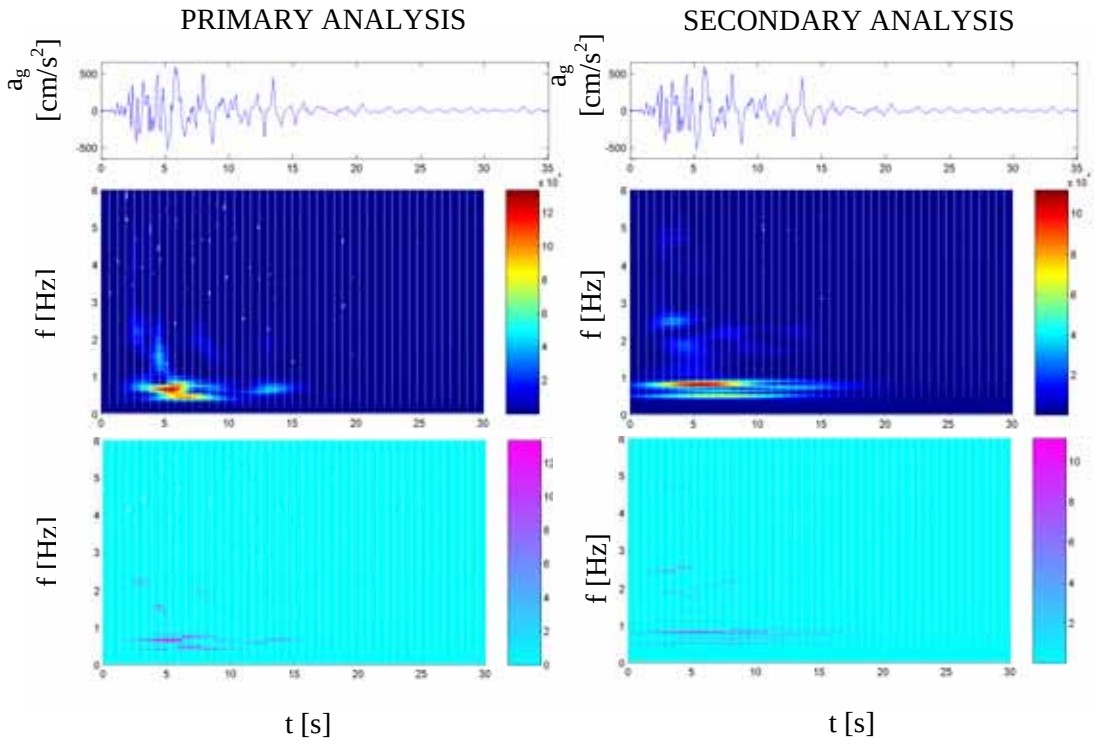

FIGURE 5.36. Kobe ground motion, wavelet scalogram and WIFS (top to bottom) for primary (left) and secondary analyses

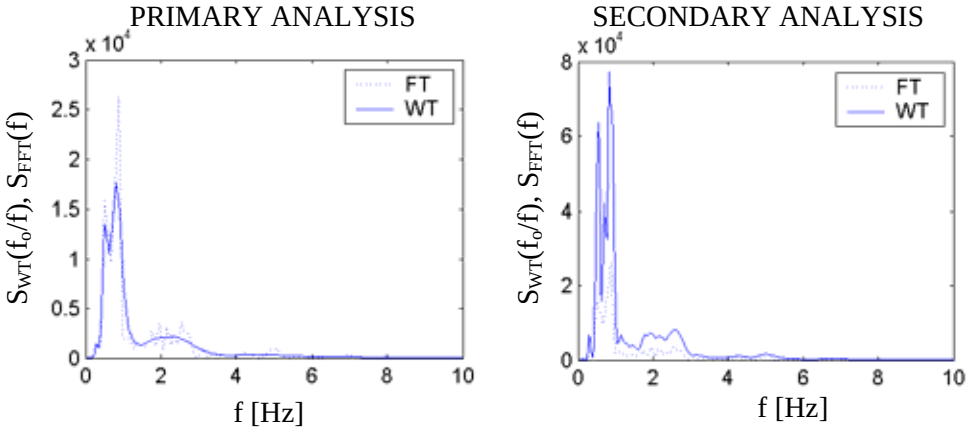

FIGURE 5.37. Wavelet marginal spectra with Fourier power spectrum for primary (left) and secondary analyses for Kobe quake

secondary analysis. The conservation of energy of all the spectral representations is again demonstrated in Table 5.4.

The energy accumulation plots in Figure 5.38, when viewed in conjunction with the energy accumulation rates of change in the frequency and time domains, shown respectively in Figures 5.39 and 5.40, provide a comprehensive perspective on the time and frequency characteristics and their energy contributions to the signal. In Figure 5.39, the rate of change of energy accumulation in the frequency domain from the primary analysis demonstrates a concentration of energy between 0.45 and 1.0 Hz, peaking at 0.76 Hz. Though some minor energy is infused between 1.5 and 3 Hz, the energy associated with this quake is concentrated in a relatively narrow band. The secondary analysis affirms this and provides more detail, identifying two events in that narrow band and then sharply dropping off at 1 Hz. The two peaks accentuated by the finer frequency resolution of the secondary analysis are at 0.54 Hz and 0.84 Hz. The frequencies are demarcated by dotted lines in the accumulation plots in Figure 5.38. From the accumulation plots in the primary analysis, the rapid ascent in energy is apparent. At 1 Hz, the accumulated energy rises from 38% to 41%. Further analysis shows that only 3% of the signal energy resides under 0.4 Hz. 20% of the signal energy lies between 0.4 and 0.76 Hz, and the frequency range of 0.76 Hz to 1 Hz holds 25% of the energy. As demonstrated by Figure 5.38, more than half the energy in the primary analysis is less than 1 Hz. The largest single jump in frequency occurs near 0.76 Hz, where the accumulated energy ascends from 66 to 74%. The secondary analysis confirms that 36% of the energy resides at frequencies greater than 1 Hz, in general agreement with the primary analysis. Further about 20% of the energy lies between 0.84 Hz and 1 Hz and

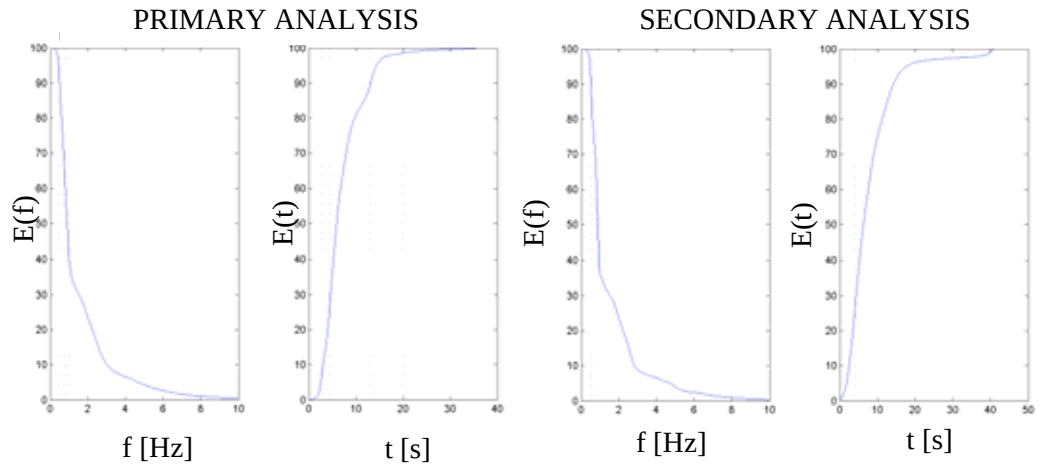

FIGURE 5.38. Energy accumulation in frequency domain and time domain for primary (left) and secondary analysis of Kobe

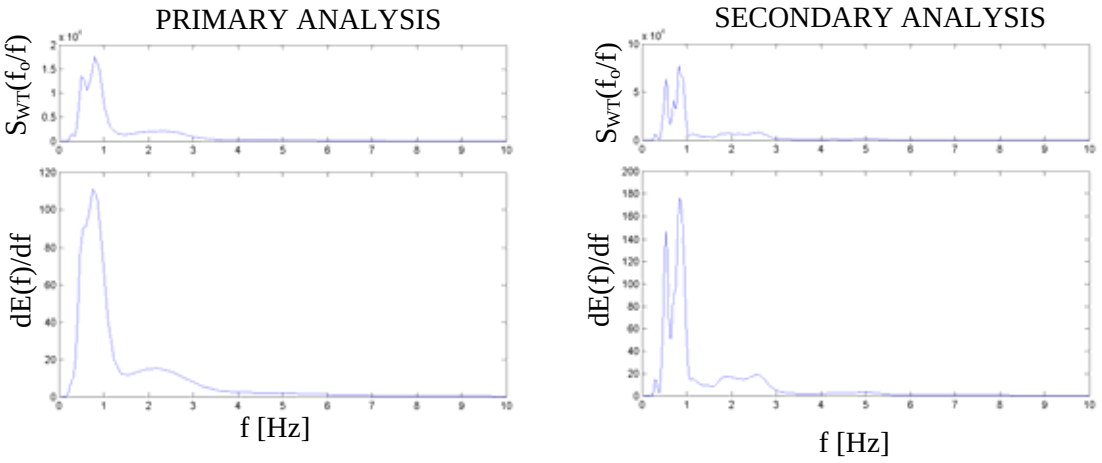

FIGURE 5.39. Wavelet marginal spectrum and rate of change of energy accumulation in frequency domain for primary (left) and secondary analysis of Kobe

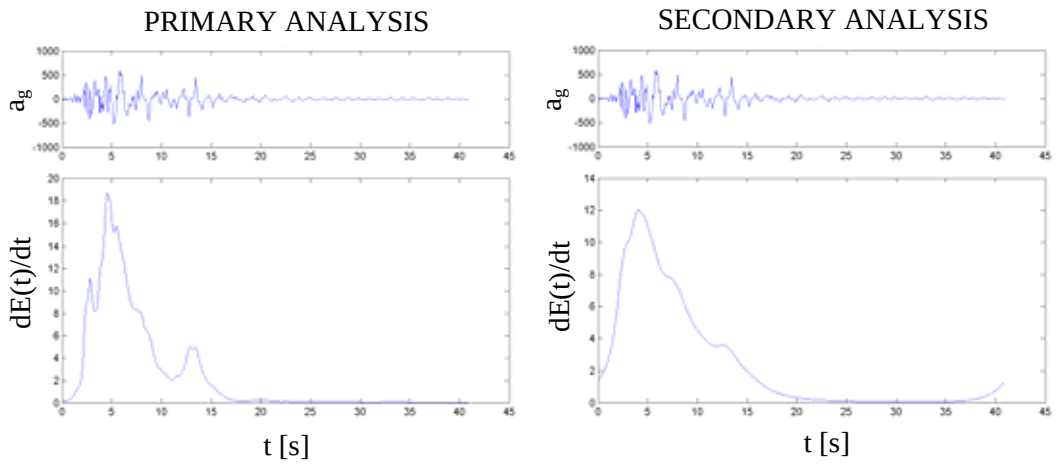

FIGURE 5.40. Kobe ground acceleration and rate of change of energy accumulation in time domain for primary (left) and secondary analysis

between 0.54-0.84 Hz, respectively. Ten percent of the signal energy is found at frequencies less than 0.54 Hz. The accumulated energy increases most drastically at 0.84 Hz, where it rises from 57.4% to 63.0%. The next major rise in energy is at 0.54 Hz, where the accumulated energy jumps from 86.4% to 92%.

Referring now to the rate of change in accumulated energy in the time domain, in Figure 5.40, the primary analysis affirms that a first event arrives near 3 s and is followed by the major event at 4.58 s. The energy rates fall of quickly until the arrival of a smaller event at 13.2 s, after which the infusion of energy falls quickly to zero within 20 s. Noting these critical time instants, an analysis of the accumulated energy in Figure 5.38 reveals that the event at 3.16 s was associated with only 3% of the overall energy. Subsequently, in the next two seconds the accumulated energy quickly rises another 10%. With the arrival of the event at 13.2 s, over 90% of the quake's energy has been recorded. Many of the details of the arrival of individual events are obscured in the secondary

analysis, due to the temporal smoothing. Still, the major pulse is identified at 4.06 s, after which the energy falls off, in tiers after 5 and 10 s.

A more careful analysis of the contributions by the various frequency components at particularly interesting sequences of the quake is provided in Figure 5.41 through the wavelet instantaneous power spectra. At 3.0 s, the primary analysis identifies 3 major components at 0.52, 0.84 and 2.60, with the former two being very closely coupled. Their respective energy contributions are tabulated in Table 5.9. They indicate that the low frequency component at 0.84 Hz is very strong. The component at 2.6 Hz, which represents contributions from 2.3 to 2.9 Hz, carries a significant portion of the instantaneous signal energy.

The secondary analysis, with a more refined resolution, gives a more precise depiction of the higher modes, identifying an energetic band between 1.5 and 2 Hz. A distinct mode at 2.67 Hz surfaces, carrying 22.2% of the instantaneous spectral energy. The lower frequency component at 0.84 Hz actually dominates in this analysis, carrying 27.6% of the instantaneous spectral energy. At 4.5 s, the energy has shifted in the primary analysis to one lower frequency mode at 0.8 Hz accompanied by a higher mode at 1.8 Hz. 41.2% of the instantaneous spectral energy resides in the narrow frequency band represented by the 0.8 Hz component. In the secondary analysis, the energy associated with 2.6 Hz has diminished somewhat, but the remaining characteristics of the spectra are largely unchanged from what was observed at 3 s. The coupled low frequency components in the primary analysis are still present at 7.4 s, with approximately 75% of the signal energy in this band of frequencies between 0.5 and 1 Hz. The presence of the

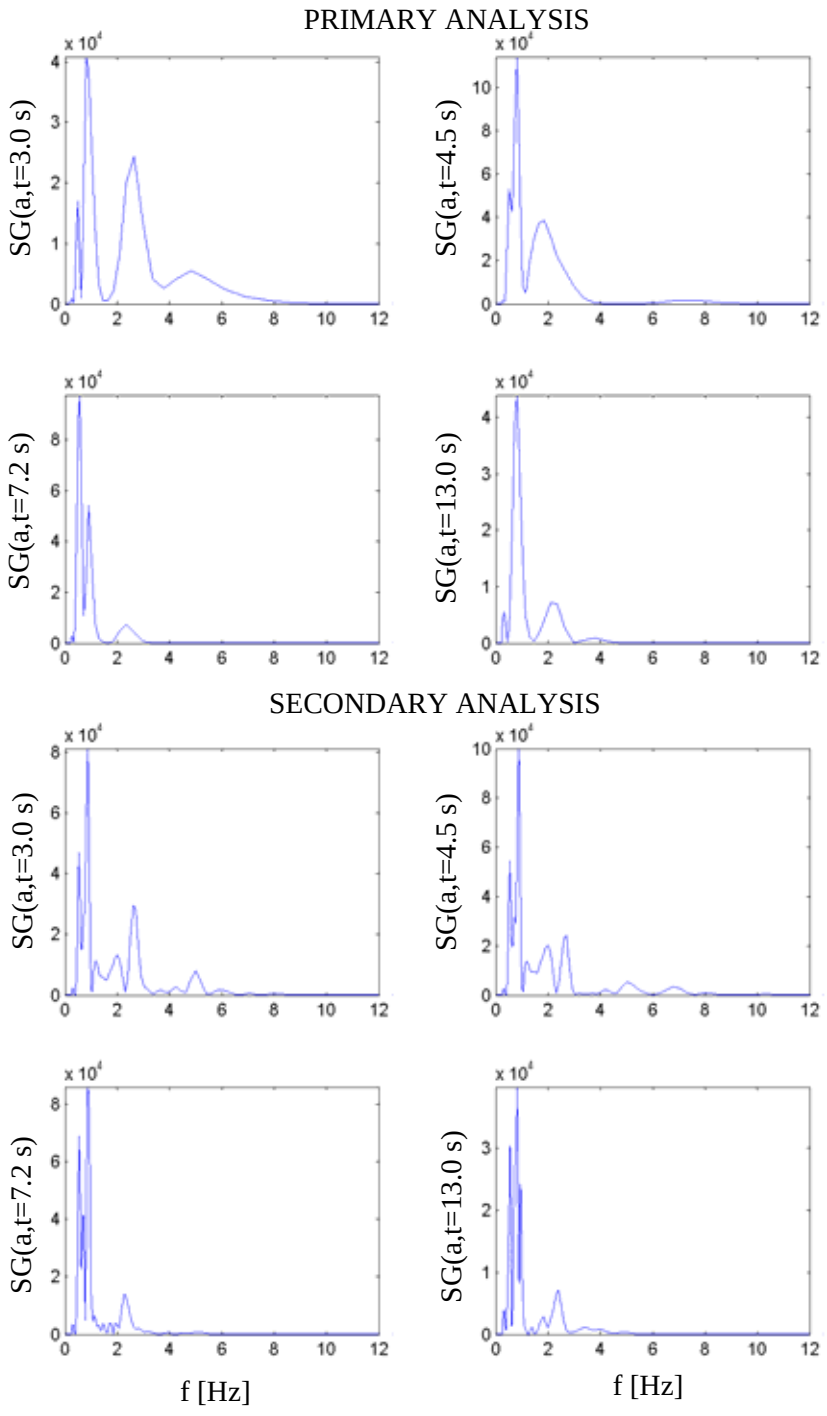

FIGURE 5.41. Wavelet instantaneous spectra taken at critical time steps in the Kobe event for primary (top) and secondary analysis

third mode at 2.38 Hz now becomes more visible, making a 12.5% contribution to the instantaneous spectral energy. The secondary analysis results shown in Table 5.9 confirm these findings and noting that the energy at this point is shifting to lower frequencies than the previous times analyzed. By the thirteenth second, the contributions of the higher and lower frequency components, in comparison to the energy associated with 0.84 Hz, are minor. The secondary analysis, with a finer resolution, indicates that the ground motion is not so periodic. As shown in Table 5.9, the energy in the second mode at 0.81 Hz dominates, though there is noteworthy energy at 0.55 Hz (21.0%) and 2.38 Hz (16.4%).

TABLE 5.9

RELATIVE CONTRIBUTIONS OF EACH COMPONENT TO INSTANTANEOUS SPECTRA FOR KOBE EARTHQUAKE PRIMARY AND SECONDARY ANALYSES

t_j [s]	IF_1 [Hz]	$\hat{E}_1(t_j)$ [%]	IF_2 [Hz]	$\hat{E}_2(t_j)$ [%]	IF_3 [Hz]	$\hat{E}_3(t_j)$ [%]
Primary Analysis						
3.0	0.52	4.0	0.84	28.9	2.60	43.2
4.5			0.80	41.2	1.80	53.1
7.2	0.55	41.1	0.91	34.6	2.38	12.5
13.0	0.38	3.17	0.84	67.7	2.24	24.7
Secondary Analysis						
3.0	0.55	10.9	0.84	27.6	2.67	22.2
4.5	0.55	10.9	0.88	29.2	2.67	14.3
7.2	0.55	29.1	0.88	41.3	2.31	16.6
13.0	0.55	21.0	0.81	42.9	2.38	16.4

*Broadband energy contribution centered or peaking at this frequency.

5.4.6 Comparison of Earthquake Properties

A comparison of the properties of the various nearfield earthquake records can be garnered from the wavelet energy accumulation rates. As the primary analysis had superior time resolution, its results are used to create the comparative energy accumulation in the time domain in Figure 5.42. Conversely, the secondary analysis is used to generate the same figure for the frequency domain. The richness of the Guerrero MC nearfield event is quite apparent, as its accumulation of energy is very gradual over a wide range of frequencies. The El Centro and Northridge events parallel each other, with very similar distributions of energy with frequency, though El Centro has elevated energy levels for frequencies greater than 3 Hz. The black horizontal lines delineate the 90 and 95% energy levels. The frequencies corresponding to these levels are tabulated in Table 5.10. As the table demonstrates, Loma Prieta comparatively has the least low frequency energy, evident from its curve's steep ascent followed by only modest energy gains under 2 Hz. Interestingly, the Guerrero MC nearfield record, similarly reflects a minimal energy contribution under 1 Hz, though this minor contribution was markedly amplified in the farfield record from the Mexico City valley, as shown previously in Figure 5.21. The Kobe record here provides the most dramatic energy profile in the frequency domain, emphasizing its concentration at low frequencies, a fact affirmed in Table 5.10 as it has the lowest frequencies at the 90 and 95% levels of the analyzed records.

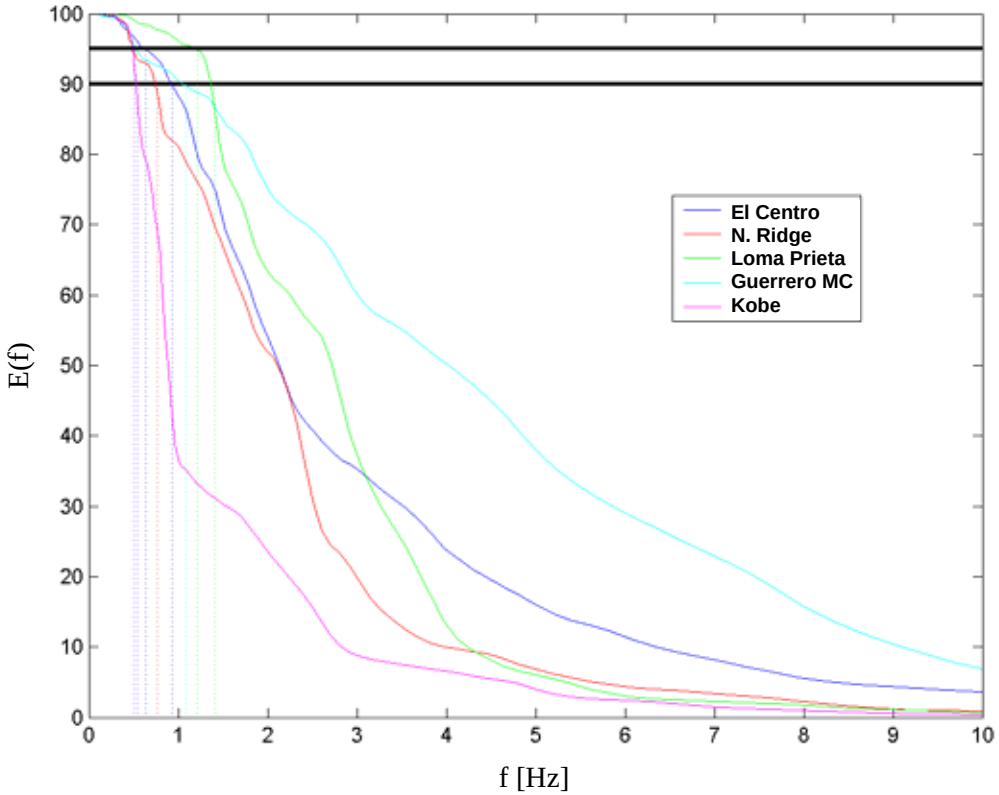

FIGURE 5.42. Comparison of energy accumulation curves in frequency domain for each of the five nearfield earthquake records

TABLE 5.10

COMPARISON OF ENERGETIC COMPONENTS AND ENERGY ACCUMULATION LEVELS IN TIME AND FREQUENCY FOR FIVE EARTHQUAKE RECORDS

	Most Energetic Component		90% of Signal Energy		95% of Signal Energy	
	f [Hz]	t [s]	f [Hz]	t [s]	F [Hz]	t [s]
El Centro	1.1	4.1	0.93	26.5	0.64	28.1
Guerrero MC	0.5	10.3	1.09	33.3	0.53	35.9
Loma Prieta	1.4	2.8	1.41	7.7	1.21	9.4
Northridge	0.8	4.1	0.76	12.1	0.50	15.2
Kobe	0.8	4.6	0.54	13.1	0.40	14.4

To further enhance the discussion, Table 5.10 also tabulates the most energetic components of these records, identified as those inducing the maximum rate of change of energy accumulation in the frequency and time domain. It is striking to note the parallels between Kobe and Northridge, occurring on the same day of the year and possessing very similar energetic components. Both have very strong energetic components at 0.8 Hz. The Fourier spectrum did detect sizeable energy in this range for both quakes, as shown in Figure 5.31 and Figure 5.37, however it can be implied that the enhanced low frequency resolution in the wavelet analysis was better suited to emphasize and capture the true energetic content at this frequency. For Loma Prieta and El Centro, again the most energetic component is consistent with the Fourier spectral representation shown respectively in Figures 5.25 and 5.8, though identified at slightly lower frequencies, perhaps again due to the enhanced resolution in this regime. Interestingly, the only record, which did not find agreement between Fourier spectral amplitudes and the wavelet energetic components listed in Table 5.10 is the Guerrero MC record. In the Fourier spectrum in Figure 5.16, though a low frequency presence is noted, it is dwarfed by the energy near 2 Hz. However, the wavelet analysis in Figure 5.18 detects that this single frequency component near 0.5 Hz in the Kobe quake is the most energetic component, though with narrow bandwidth. Eventually, the large contributions at a wide range of frequencies in the vicinity of 2 Hz ultimately dwarf this low frequency component in the Fourier spectrum in Figure 5.16, but the 0.5 Hz component consistently appears in the wavelet representation, again perhaps better detected due to the enhanced frequency resolution. Ironically, as the quake arrives in the Mexico City valley, it is this ever present component that is amplified and leads to widespread destruction.

The analysis of energy accumulation in the time domain is provided by Figure 5.43. Kobe, El Centro and Northridge each release their energy at a similar rate in time, though the intensity of El Centro trails off sooner than the other two events, having longer duration. The energy in Loma Prieta is released most quickly of all the records, as noted in Table 5.10. Mexico City tends to release her energy most gradually and does not manifest a single big event indicated by a steep ascent in the energy accumulation plot, making this earthquake very unique by conventional standards.

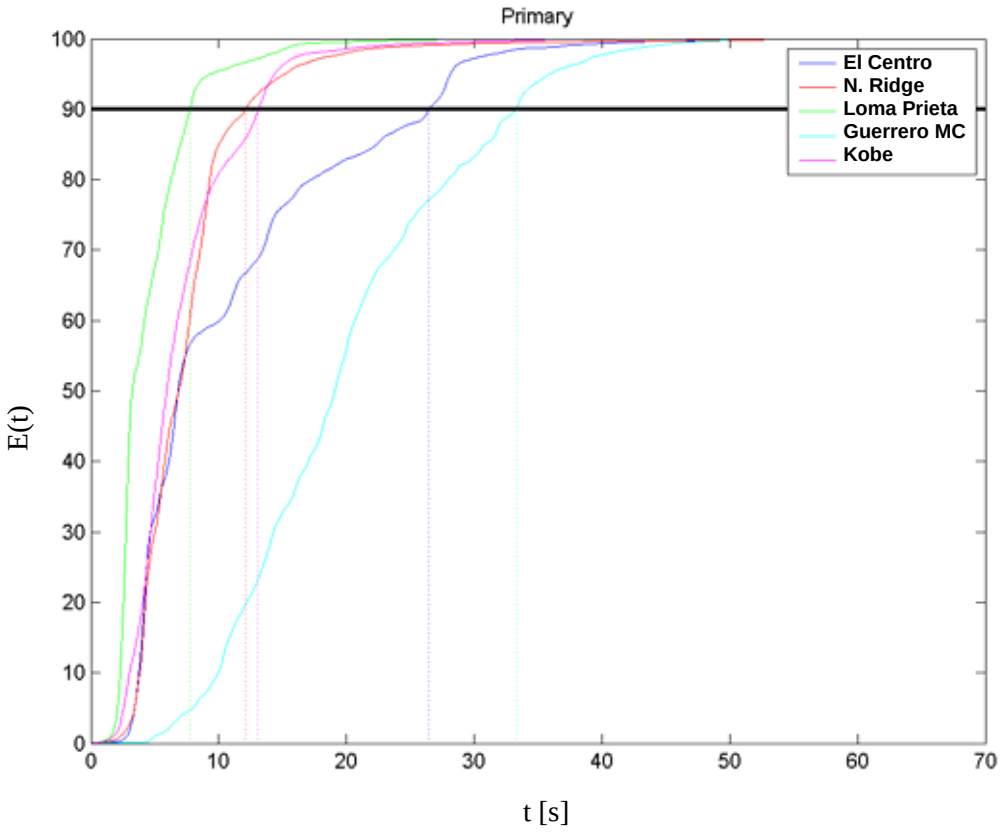

FIGURE 5.43. Comparison of energy accumulation curves in frequency domain for each of the five nearfield earthquake records

5.4.7 Seismic Response of a Building

The previous analyses have highlighted the wavelet's ability to capture the nonstationary characteristics of earthquakes and reveal the evolution of frequency content with time. Similar and more physically meaningful insights for Civil Engineers can be obtained by applying this tool for the analysis of structural responses under these highly nonstationary events. The unique ability of wavelets to capture these nonstationarities has made it equally useful in the simulation of structural responses to these events (Basu & Gupta, 1997; 2000). To demonstrate the ability of the wavelet to capture nonstationary characteristics of structural response, consider the roof level acceleration of a 13-story commercial building (Sherman Oaks), along its longitudinal (E-W) axis during the 1994 Northridge earthquake. The measured acceleration is shown in Figure 5.44a. A wavelet analysis of the signal, with central frequency of 2 Hz and a highly refined discretization (OF = 0.5), was conducted. The resulting marginal spectrum and its Fourier counterpart is shown in Figure 5.44b. From this spectral representation, it appears that the response is dominant in the first mode near 0.38 Hz, accompanied by lesser contributions from the second mode at 1.17 and the third mode at 2.34 Hz. The irregular shape of the wavelet marginal spectral peak in the first mode suggests the presence of nonlinearity. While the wavelet and Fourier representations are in good agreement in identifying the modes and their relative contributions, this detail in the fundamental mode is obscured by a comparable Fourier analysis. The wavelet spectrum further identifies the total energy of the system more accurately, with a standard deviation of 56.5 cm/s^2 verses the Fourier estimate of 60.0 cm/s^2, in good agreement with standard deviation of the signal itself

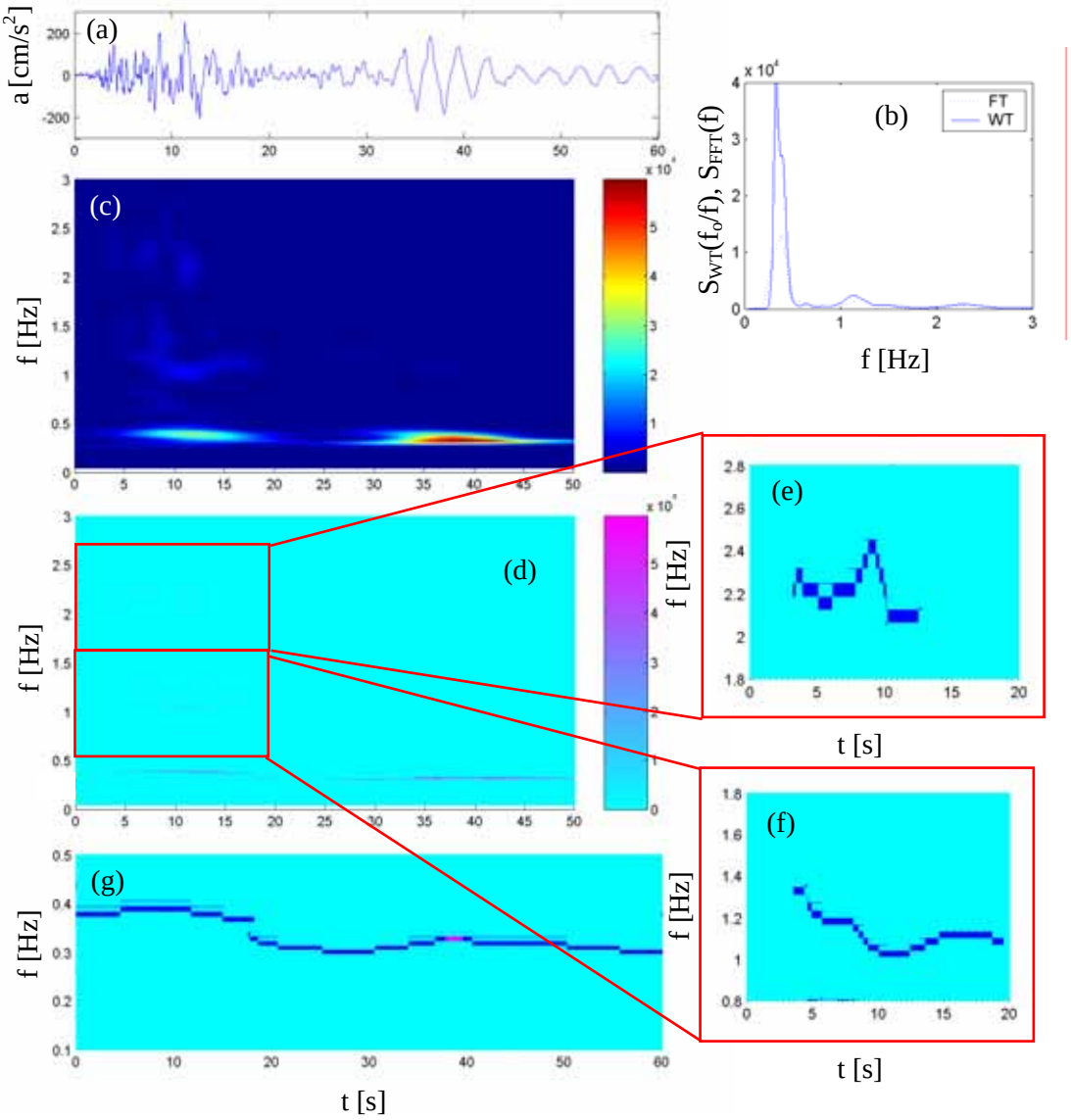

FIGURE 5.44. (a) Recorded structural response to Northridge ground motion, (b) Fourier and wavelet marginal spectra; (c) scalogram; (d) WIFS; (e) zoom of third mode ridge; (f) zoom of second mode ridge; (g) zoom of fundamental mode ridge

(56.6 cm/s^2). Despite capturing the energy accurately, any time-dependence has been completely lost.

The wavelet scalogram in Figure 5.44c preserves these evolutionary features, identifying two bursts of energy after the tenth and thirty-fifth seconds. As evident in the time series in Figure 5.44a, only the former large-amplitude response includes the two higher modes. An extraction of wavelet ridges produces the wavelet instantaneous frequency spectrum in Figure 5.44d. The ridges, though fainter for the higher frequency modes, manifest distinct fluctuations and an apparent softening of the fundamental ridge. Figure 5.44e zooms in on the third mode, darkening the plot and showing a hardening with the strong shaking, followed by a decrease in stiffness. The contributions of this mode are relatively isolated and manifest only with the strong shaking of the first 15 s. The second mode is present in both major shaking events, and when amplified and darkened in Figure 5.44f and echoes a similar characteristic of softening, again reaching a minimum stiffness following the major pulse near 10s. The dominant low frequency ridge in Figure 5.44g begins at a plateau near 10 s and then softens in the subsequent 10 s, manifesting some slight hardening during the second event, which primarily affects this lowest mode. It is apparent that by the conclusion of the shaking, this structure's fundamental period has softened, an indicator of some permanent damage in the structure. Interestingly, a comparison of the structural frequencies obtained through testing after the quake with some estimates taken before the quake may have detected this softening. However, without a baseline for comparison, the frequencies identified during or after the quake shed little light. On the other hand, the wavelet analysis allows the determination of frequency throughout the shaking, so that one record alone can be used

to document the onset of softening. In this context, wavelet-based analysis provides an attractive framework for structural health monitoring in the absence of such baseline data, which may not be available for most buildings.

The energy accumulation plots in Figure 5.45 reflect that energy is strongly accumulated near 0.347 Hz, corresponding to the first mode of the structure in its damaged state. The accumulation in the frequency domain plateaus at three distinct points, readily identifying the three modes and their relative contributions. The third mode contributions are quite scarce, while the second mode contributes 10-15% of the total energy and the first mode is responsible for nearly 70% of the total signal energy. Accumulation in time occurs distinctly in two events, representative two periods of activity sandwiching the lull between 20 and 30 s. The rate of change of energy accumulation in the time domain identifies the precise onset of the two events and the times of maximal energy influx, in this case occurring at 11.2 s.

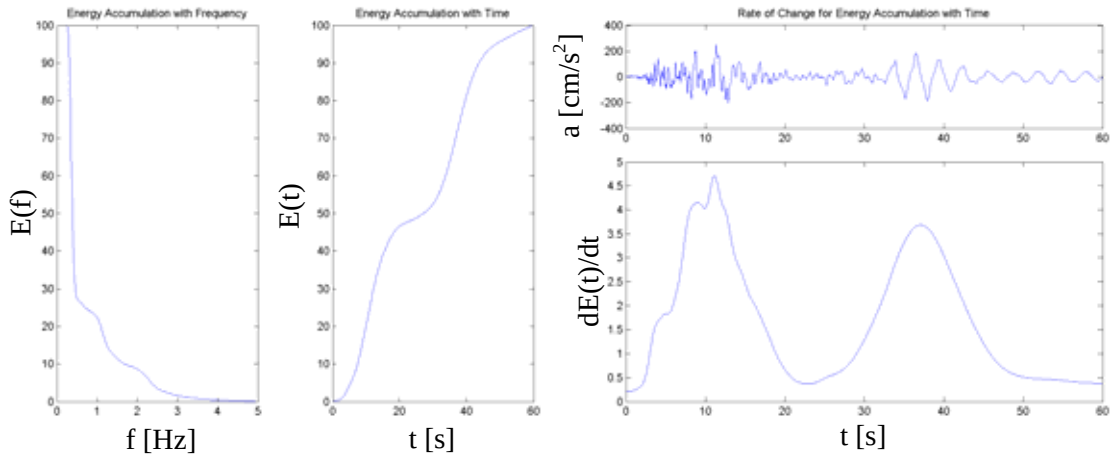

FIGURE 5.45. Energy accumulation in frequency domain and time domain (left) and structural accelerations and rate of change of energy accumulation in time domain for Sherman Oaks building under Northridge earthquake

A microscopic zoom of the energy distribution at distinct points within the response time history is provided by the instantaneous spectra in Figure 5.46. The first spectrum is associated with the plateau region in the rate of change in energy accumulation with time. This is a region where the rate of energy accumulation held relatively steady prior to strong shaking. At this time, all three modes appear to be present, though the two higher modes are sharing energy over a broad range of frequencies. The side lobes on the fundamental spectral peak indicate the presence of additional adjacent frequencies that could indicate a nonlinearity within that mode. Note also the surfacing of a fourth, high frequency mode. The relative energy contributions from these modes are listed in Table 5.11. The next two spectra are associated with peaks in that first strong shaking, denoted by the two peaks near 10 s in the rate of change in energy accumulation plot in Figure 5.45. At 8.7 s, there is a relatively larger contribution from frequencies in the vicinity of the second mode, diminishing the influence of the third mode. At 11.1 s, the energy has shifted dominantly towards the first mode coupled by a robust distribution of energy near the third mode. The last spectrum is associated with the final significant response within the structure. As evidenced previously, this response is dominantly in the first mode, as evidenced by Table 5.11, with a minor second mode contribution. The more detailed investigations of energy distribution with time, provided in the instantaneous spectra, indicate that the energy is more prominently associated with the higher modes in the first 9 s of the event. Even at 11.1 s, despite the surging first mode response, there is still a strong contribution in the vicinity of the third mode. It is only in the decline in energy accumulation rates symbolized by the dramatic fall off after 11 s in Figure 5.45 that the first mode overwhelmingly dominates the

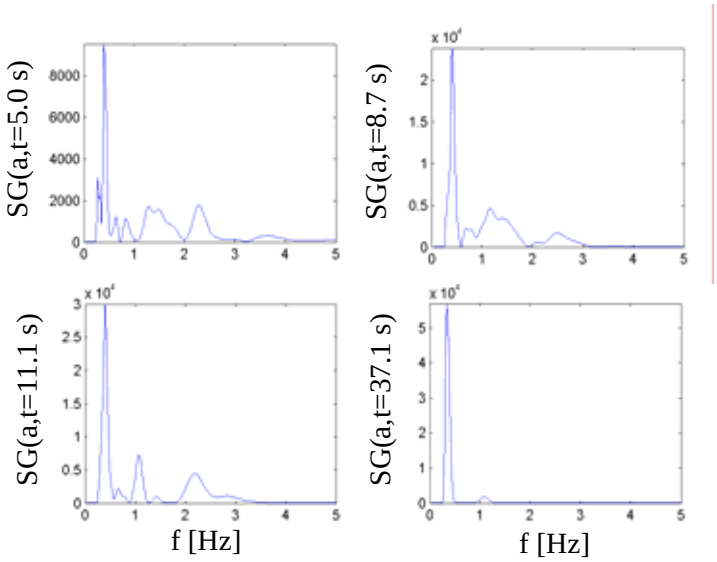

FIGURE 5.46. Wavelet instantaneous spectra taken at critical time steps in the Sherman Oaks building response in the Northridge earthquake

TABLE 5.11

RELATIVE CONTRIBUTIONS OF EACH COMPONENT TO INSTANTANEOUS SPECTRA FOR SHERMAN OAKS BUILDING IN NORTHRIDGE EARTHQUAKE

t_j [s]	IF_1 [Hz]	$\hat{E}_1(t_j)$ [%]	IF_2 [Hz]	$\hat{E}_2(t_j)$ [%]	IF_3 [Hz]	$\hat{E}_3(t_j)$ [%]
5.0	0.40	32.9	1.38	28.4	2.28	19.5
8.7	0.42	40.7	1.13	44.5	2.50	13.4
11.1	0.42	50.6	1.08	17.3	2.20	31.0
37.1	0.34	93.7	1.10	5.8		

response. The Fourier perspective cannot reflect such significance of higher modes over specific durations of the response.

5.5 Wind-Induced Response of a Tall Building

While relatively stiffer structures bear the brunt of most earthquakes, it is the tall, flexible buildings that produce dynamic responses driven primarily by wind. Under the action of wind, oscillations of high-rise buildings occur in three simultaneous directions: alongwind, acrosswind and torsion, as shown in Figure 5.47. The alongwind motion primarily results from the pressure fluctuations on the windward and leeward faces, which generally follow the fluctuations in the approach flow, at least in the low frequency range. The lateral motion, in the acrosswind direction, is introduced by pressure fluctuations on the side faces, induced by the fluctuations in the separated shear layers and wake flow fields. The wind-induced torsional effects result from an imbalance in the instantaneous pressure distribution on the building surface (Simiu & Scanlan, 1996).

The action of wind on structures may be one of the best-suited areas for the application of wavelets due to the time-dependency of the loading. As with most environmental loads, the magnitudes of loading are indeed time-varying; however, in the case of wind, this situation is further complicated by the fact that the direction of loading can also manifest marked time-variations within a single event. This unique situation can lead to rapid changes in the structural response as the alongwind and acrosswind directions of motion evolve with time, further complicated by the intermittent role of torsion arising from the instantaneous distributions of pressures on the structure. The

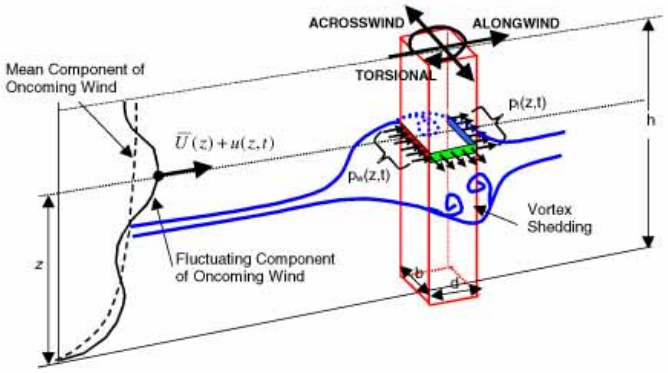

FIGURE 5.47. Response components for buildings under the action of wind loading (taken from Kijewski et al., 2001)

ability to examine the frequency content of the resultant response alongside the time-varying wind speed and direction was previously limited prior to the advent of time-frequency transformation tools. The following example demonstrates the utility of wavelet transforms in this regard.

5.5.1 Preliminaries

A five-year full-scale monitoring program was initiated between 1973 and 1978 on an 800-foot building in Boston that had manifested some undesirable response characteristics and failure of building envelope components (Durgin & Gilbert, 1994). Due to legalities, more specific details of the structure cannot be disclosed here. The extensive monitoring program included the collection of wind speed and accelerations at 8 locations in the building: with four sensors located on the 57th floor and another four at the 35th. In particular, these accelerometers at the higher elevation detected significant amplitude motions capable of causing occupant discomfort. The analysis of the data

obtained in the monitoring program is complicated by the fact that the structure is known to have both sway fundamental frequencies and its fundamental torsional frequency very closely aligned. Testing of the building indicated that the fundamental sway mode in the softer direction was 7.36 s (0.136 Hz) and the torsional mode was 6.37 s (0.157 Hz). The locations of the four accelerometers on the 57th floor are shown in Figure 5.48. The two sensors measuring the motion parallel to the long face of the building were termed the "NS" sensors by the original monitoring team. The other sensors capturing motions parallel to the building's shorter axis were termed "EW". The sensor pairs are positioned at opposite corners of the building plan and named based on the column they are associated with, i.e. 2 or 59.

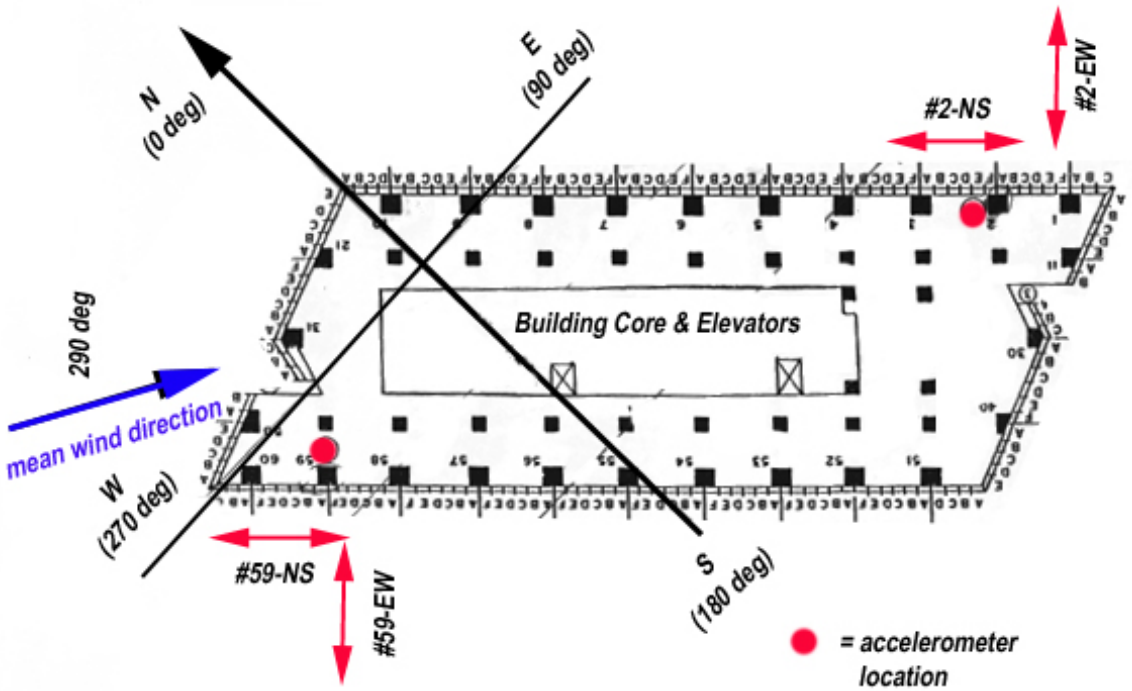

FIGURE 5.48. Plan view of monitored building with accelerometer locations and orientations

The record analyzed here corresponds to March 10, 1974 (record id: MR10743) and resulted in the largest levels of peak acceleration observed in the tower over the monitoring period. Over the course of this hour-long record, the mean wind speed, measured at 100 ft above the rooftop, was 53.7 mph, gusting to 77.3 mph, primarily out of the west-northwest at 290°. This mean wind direction and its orientation relative to the building's primary axes are shown approximately in Figure 5.48.

Knowing the close proximity of the sway and torsional frequencies, it is assumed that beating between these modes is a very probable occurrence. The first priority was to define the wavelet central frequency necessary to separate these modes. A 3 Hz Morlet wavelet was selected, capable of achieving this separation down to 0.012 Hz. An overlap factor of 1 and padding factor $\beta = 1$ were used in the analysis. Due to the potential for beating between modes, before analyzing the record, a baseline wavelet representation of this phenomenon was established. This is accomplished using the summation of two sine waves of identical amplitude and with fundamental frequencies of 0.13 Hz and 0.16 Hz, representing two closely spaced modes of vibration observed previously in data taken from this building. Two wavelet perspectives are provided in Figure 5.49. The first is the marginal wavelet spectrum, shown by the solid lines in Figure 5.49a. Its Fourier counterpart is shown by the dotted lines. Both representations detect a pair of spectral peaks at 0.135 and 0.165 Hz. Investigating the time-varying behavior of this system through wavelet instantaneous spectra at several time intervals unveils more details of the interaction between the two waveforms. At periods of high amplitude motion, the bandwidth of the two modes modulates and the two appear to merge into a single mode, though the individual peaks of the two modes are still discernable. At lower amplitudes

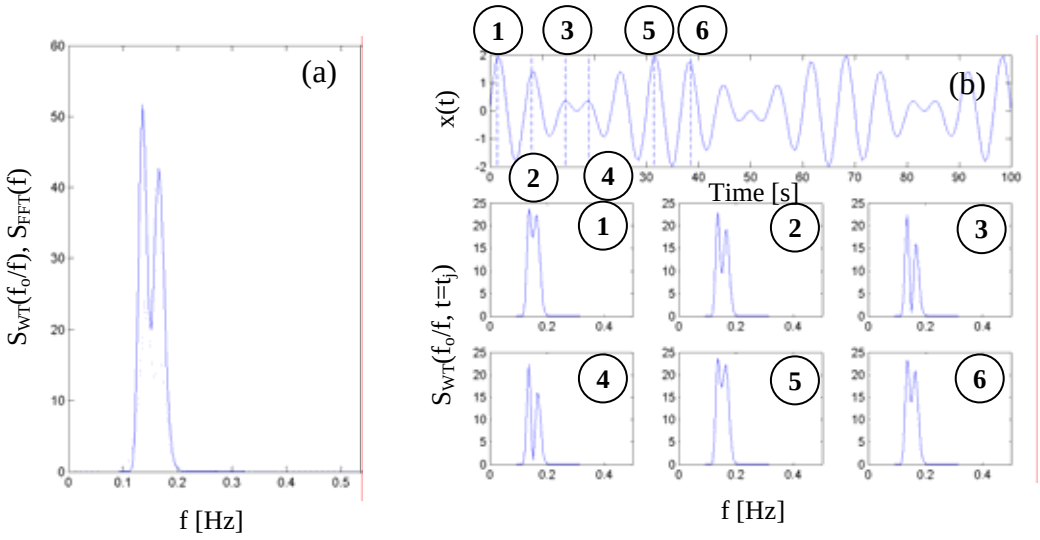

FIGURE 5.49. (a) Comparison of wavelet marginal spectrum (solid) and Fourier spectrum (dotted) for beating sines; (b) beating sine signal and wavelet instantaneous spectra at 6 locations in the time history

of motion, the two modes separate again into distinct yet closely-spaced modes, with the pattern repeating itself throughout the beating phenomenon. The wavelet consistently identifies the two peaks at 0.135 and 0.165 Hz in each instantaneous spectrum, indicating that while bandwidths may modulate the frequencies remain intact. However, this idealized system manifests no nonlinearities, which may further complicate the beating phenomenon as frequencies shift with amplitude. Further, these two sines maintain the same amplitude level throughout the simulated signal. Thus, if amplitude modulation is also introduced, the situation is complicated as either one of the spectral peaks may dwarf the presence of the other due to an unequal distribution of energy at that instant. As the subsequent analysis reveals, such amplitude fluctuations, the melding of two modes in a beating phenomenon and the presence of nonlinearity all play a role in the response of the monitored building in Boston. Finally, in this discussion there is no need to investigate

the energy associated with each component, as a cursory assessment of the relative magnitude of the wavelet coefficients will be sufficient, contrary to the statements in Section 5.3, since the spectral components are assumed to be in very close proximity, they have comparable bandwidths and therefore comparable amplitude reduction to account for increased bandwidth. Thus, in the subsequent discussions, wavelet coefficient amplitudes will be assumed to be an accurate direct indicator of the relative strength of each of these components.

5.5.2 Global Analysis

The analysis begins by examining the wavelet marginal spectra calculated from the entire length of the record, shown in Figure 5.50. These provide a similar perspective as that obtained by Fourier analysis, but through the discretization scheme in Chapter 4 these wavelet marginal spectra can provide a smoother representation with enhanced resolution at the lower frequencies. Note that due to the discrete frequencies chosen in the analysis the wavelet spectra will focus at the discrete frequency closest to the actual frequency of the system. Figures 5.50b and 5.50d manifest two modes, consistent with the closely coupled sway and torsional modes known to exist in this structure. The softer of the two is associated with the fundamental sway mode along the NS axis, while the higher frequency is associated with the first torsional mode. Note interestingly that in Figure 5.50a and 5.50c, the EW sway mode is oddly not present, with only dominant torsion detected. However, an investigation of the larger data set was able to identify the EW sway component in other records and found that the fundamental modal frequencies from lowest to highest are: sway detected by the NS sensors, followed by sway detected by the

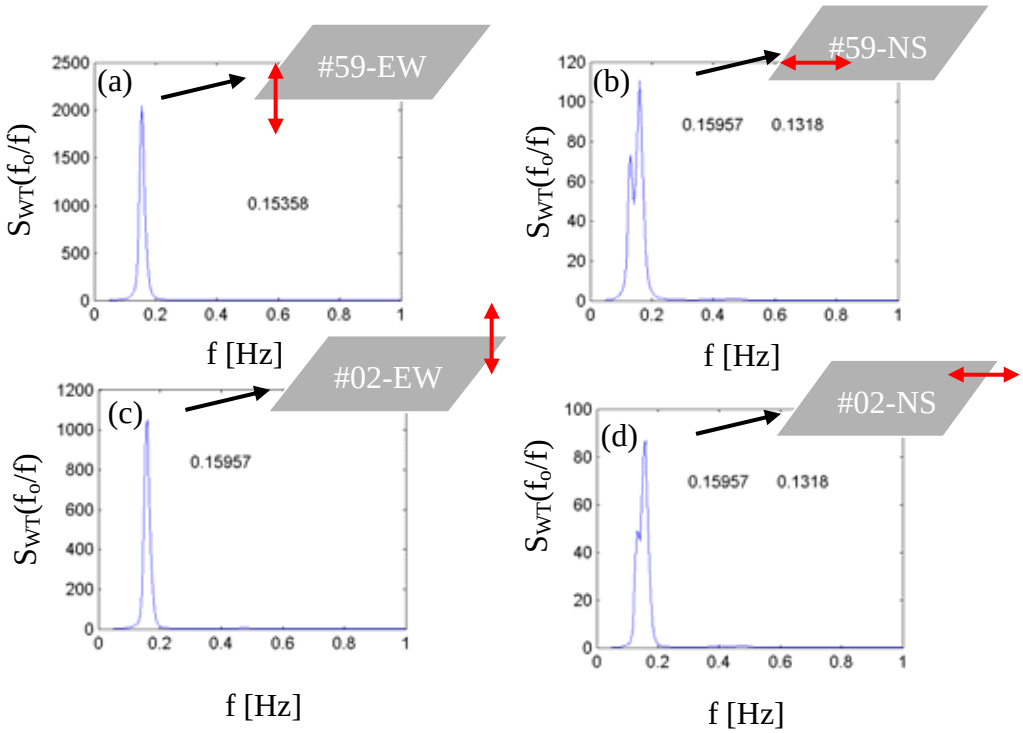

FIGURE 5.50.Wavelet marginal spectra for the four sensors at the 57th floor of Boston building

EW sensors, and finally torsion (Brown, 2003), indicating that all three frequencies lie in that order within a span of 0.136 to 0.157 Hz, though suggesting that the potential for coupled response between sway and torsion may be observed in those EW sensors. Nevertheless, the spectra associated with this event reflect that motion at the corners of the structure is dominated by torsion, facilitated by the larger torsional arm to that direction. In fact, even in the NS sensors, where torsional arms are shortened, torsion still overshadows NS sway. This is a disturbing feature since torsional accelerations are the most perceivable motions from an occupant comfort perspective.

The magnitudes of the spectra also manifest some interesting features, e.g. the windward EW torsional peak is twice the amplitude of its leeward counterpart's. While

this feature may be attributed to the inability of the floor diaphragms to sufficiently transmit the forces over the entire structural system (comprised solely of a moment resisting frame and core), this does not fully explain the discrepancy. On the other hand, the structure tends to twist and sway at comparable levels at both the leeward and windward ends of the building in the other direction, as shown in Figure 5.50b and 5.50d. Note however that the amplitudes of the spectral peaks are slightly diminished at the windward side of the building in Figure 5.50d, particularly in sway. The consistency between Figure 5.50b and 5.50d affirms a torsional frequency of 0.160 Hz and NS sway of 0.132 Hz, while the EW sway cannot be identified from the marginal spectra. The torsional frequency is confirmed as 0.160 Hz according to Figure 5.50c; however, Figure 5.50a provides the most interesting point of discussion in this analysis. Here at the windward face of the building the same torsional frequency that was found at #02-EW is not observed, but rather what appears to be a softened version (0.153 Hz). Hence, these global spectra for the EW sensors would indicate that the building is twisting at two different frequencies. Further, it is at this windward sensor that the largest amplitudes of motion are detected (note the spectral amplitude twice its counterpart #02-EW), indicating that the structure is effectively fishtailing in the wind due to an eccentricity between its mass and elastic centers. Recall also that this is the sensor set that would be measuring the sway mode closest to the known fundamental torsional frequency. Thus the building's response in both amplitude and frequency vary over the building's plan, an intriguing feature that will be explored utilizing wavelet instantaneous information.

The analysis of this feature and its explanation can commence through a wavelet analysis focused on distinct events within the time histories. As sensor #59-EW manifests

this very interesting behavior, six high amplitude events in its response were identified and the response of the other sensors during these six events is analyzed to determine the overall behavior of the building. The time histories recorded at each sensor are shown in Figure 5.51, with arrows demarcating the six events analyzed herein. Event 1 generates the highest amplitude shaking and will be discussed at great length for each of the four, recorded channels of data. Subsequently, analyses of some of the remaining events are provided to reinforce observations from Event 1. Only selected figures are included from these other events for brevity.

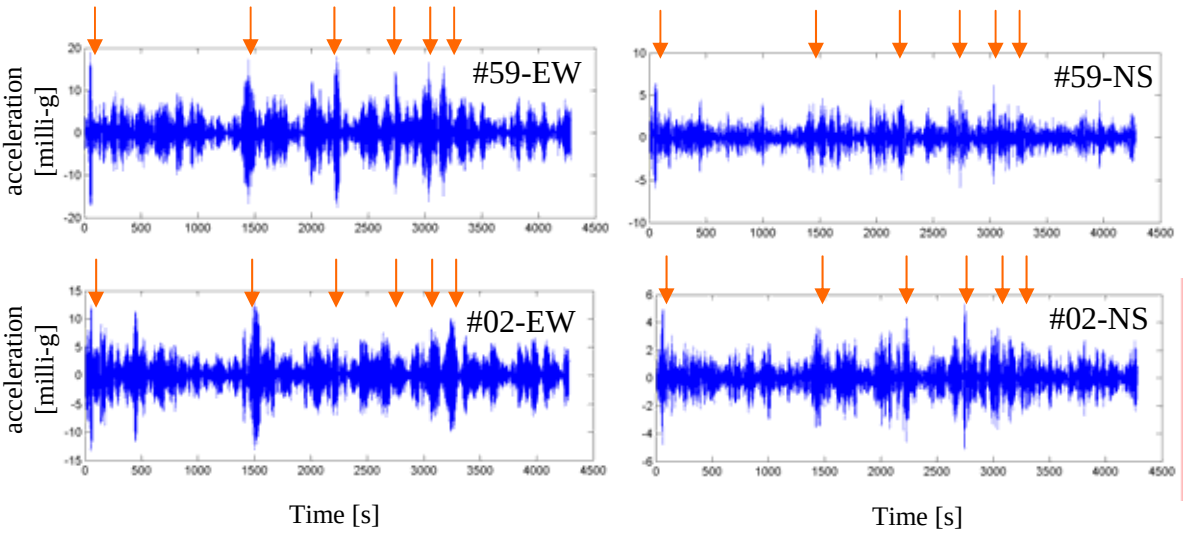

FIGURE 5.51. Time histories of acceleration response detected at four accelerometer locations. Events analyzed herein denoted by arrows

5.5.3 Event 1: 0-200 s

The images in Figure 5.50 can be viewed as global wavelet marginal spectra, as they represent an averaged perspective over the entire time history. On the other hand, local

wavelet marginal spectra can give an averaged representation of isolated signal features over particular events. The local marginal spectrum for sensor #59-EW is provided in Figure 5.52 and helps to unveil the particular behavior at this location during the first event shown in Figure 5.51, typified by an isolated high amplitude burst at the beginning of the record. Though the wavelet analysis retains the same resolution in every figure presented herein, this local marginal spectrum identifies two peaks, one at 0.153 Hz with very broad bandwidth and the indication of second mode sharing the same spectral band, an interesting finding considering this sensor is measuring that more likely coupled frequency pair. The presence of a higher mode contribution at 0.460 Hz is also noteworthy. Gurley & Kareem (1999) recommended the application of wavelets to identify the participation of higher modes in the response of tall buildings. Wavelets provide one of the few viable strategies to uncover such details, since the presence of these higher modes may depend greatly on the turbulent structure of the wind and its evolution with time. As a result, the relative contributions of each mode may suddenly increase for the same mean wind speed due to the instantaneous changes in the distribution of energy at different frequencies. As this is a time-varying phenomena, it cannot be identified through classical spectral techniques.

Analyzing the instantaneous wavelet details (Figure 5.53) during this event, the highest amplitude response occurs when the wind direction shifts and aligns with the corner of the building (270°) commensurate with the peak wind speed during this event. As the wind shifts back toward 290°, the response level subdues to an extent. It is just prior to and following this highly energetic burst that the single mode response, identified in the global marginal spectrum at 0.153 Hz, is observed, as shown in Figure 5.53. Note

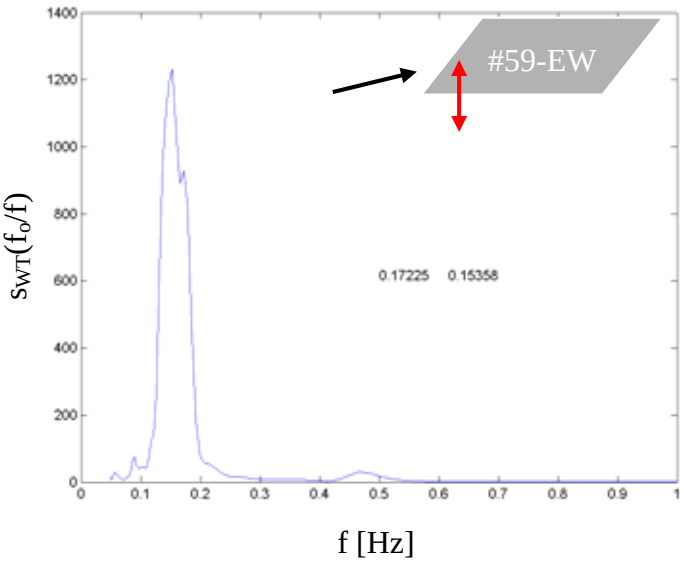

FIGURE 5.52. Local wavelet marginal spectrum for #59-EW (Event 1)

the large bandwidth associated with this spectral peak, broadening toward the high frequencies, suggestive of a coalescence of the two modes. The wide bandwidth of the response in conjunction with the wind direction supports the conclusion that both EW sway and torsional responses are sufficiently large and simultaneous in the response, leading to a melding of spectral bandwidth in the beating phenomenon similar to the example in Figure 5.49. This situation can be particularly energetic if both response components are of comparable amplitude. In spectra 1-3, this strong vibration is stimulated by the wind direction shift, proving critical for this building's geometry within the site-specific surroundings. Of the data collected, this wind direction shift is only observed in this record and this is also the only time motions of this structure reach the 20 milli-g levels. As the amplitude increases in the 3rd, 4th and 5th spectra, a shift of this spectral peak to a lower frequency of 0.148 Hz occurs. This is the characteristic softening of frequency that has been observed in full-scale measurements, (e.g. Tamura, 1998), as

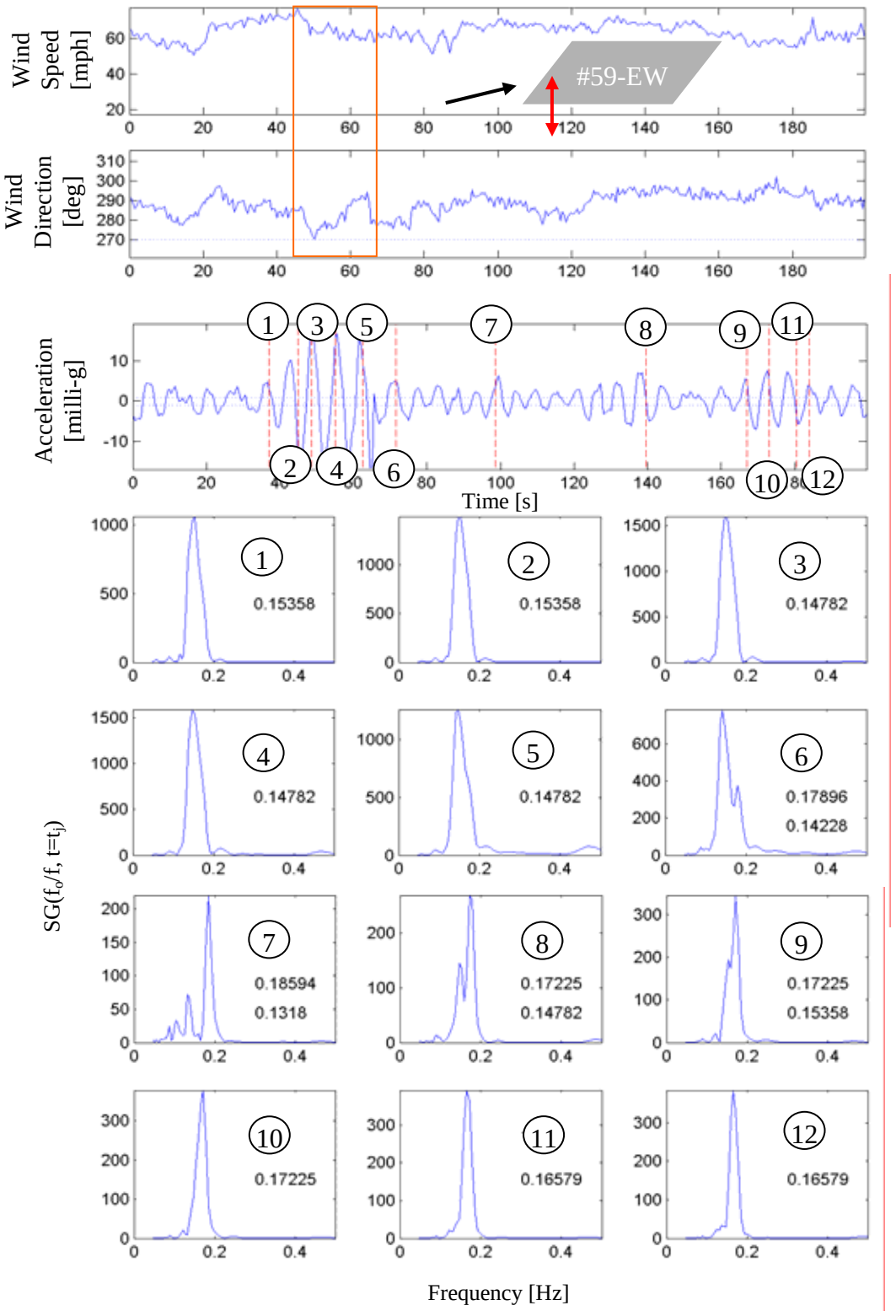

FIGURE 5.53. Wind speed, direction and response at #59-EW (Event 1) with wavelet instantaneous spectral analysis

the contacts between structural members diminishes and greater slip in joints reduces stiffness. This phenomenon is not indicative of permanent damage. At lower amplitudes of motion, contacts between surfaces again resume and a frequency increase is generally observed. More importantly, as the wind direction shifts back toward 280°, the response level diminishes and spectra 5 and 6 begin to separate into two peaks reminiscent of what was observed globally at the NS sensors in Figure 5.50. The torsional response gradually eases and separates toward the higher frequencies, allowing the sway to reappears as the dominant mode.

This behavior indicates that the isolated high amplitude motions here are facilitated by the presence of significant EW sway and torsion. Spectra 7 and 8 continue to manifest the bi-modal response, mostly torsional in nature, again an unsettling feature considering the significance of torsional motion in perception. As this occurs, in spectra 9 and 10, EW sway response gradually diminishes. Note the bandwidth of the dominant torsion in spectra 11 and 12 in comparison with the first few instantaneous spectra, further affirmation that this energetic event early in the time history was not a single mode response, but the product of modal coupling.

The ability of the structure to respond in such a manner is certainly facilitated by the beat phenomenon within the system and more importantly aided by the potential nonlinearities in stiffness and damping that can shift the torsional frequency toward the EW sway mode and markedly accentuate spectral bandwidths. However, the continuous beating in Figure 5.49 will not be observed in this structure due to the fact that both response components must be in equal measure and the dominance of torsion is

dependent on the instantaneous distributions of wind pressure on the building's faces. However, Event 1 demonstrates the ideal conditions to stimulate such behavior. As discussed by Yalla & Kareem (2001), in systems with closely coupled modes the bi-modal beat phenomenon is suppressed as the two modal frequencies coalesce into a single frequency, particularly facilitated through an increase in damping. Though the increase in damping was shown by the authors to induce this effect, it is hypothesized that the combinatorial effect of amplitude-dependence in stiffness, accompanied by a moderate increase in damping achieves the same effect, though this requires amplitude levels sufficient to induce the nonlinearity. An investigation of the behavior of the #02-EW sensor, measuring the same direction of motion but on the leeward side of the building provides added insights. At the leeward face, where global spectra in Figure 5.50c previously did not detect a discernable bi-modal response, the instantaneous wavelet spectra clearly manifest both modes prior to the high amplitude response, though torsion dominates (Figure 5.54). These two modes occupy the same spectral band as the single mode response shown previously in the instantaneous spectra numbered 1-4 in Figure 5.53. During high amplitude motion, spectra 2-3 manifest some melding and softening of torsion into the lower sway mode. At the highest amplitude of motion, the two modes nearly coalesce as observed at the windward face of the building, but this transformation is not ever fully realized, reinforcing the particular local features that facilitate this behavior. As a result, full melding never occurs in spectra 4-6, as torsion diminishes and sway starts to dominate. By the 7^{th} spectra, the sensor is now detecting a dominant torsional component. Recall, this is consistent with the other sensor. Moving toward the 9^{th} -12^{th} spectra, small hitches in spectra 9 and 10 are the only remnant of the

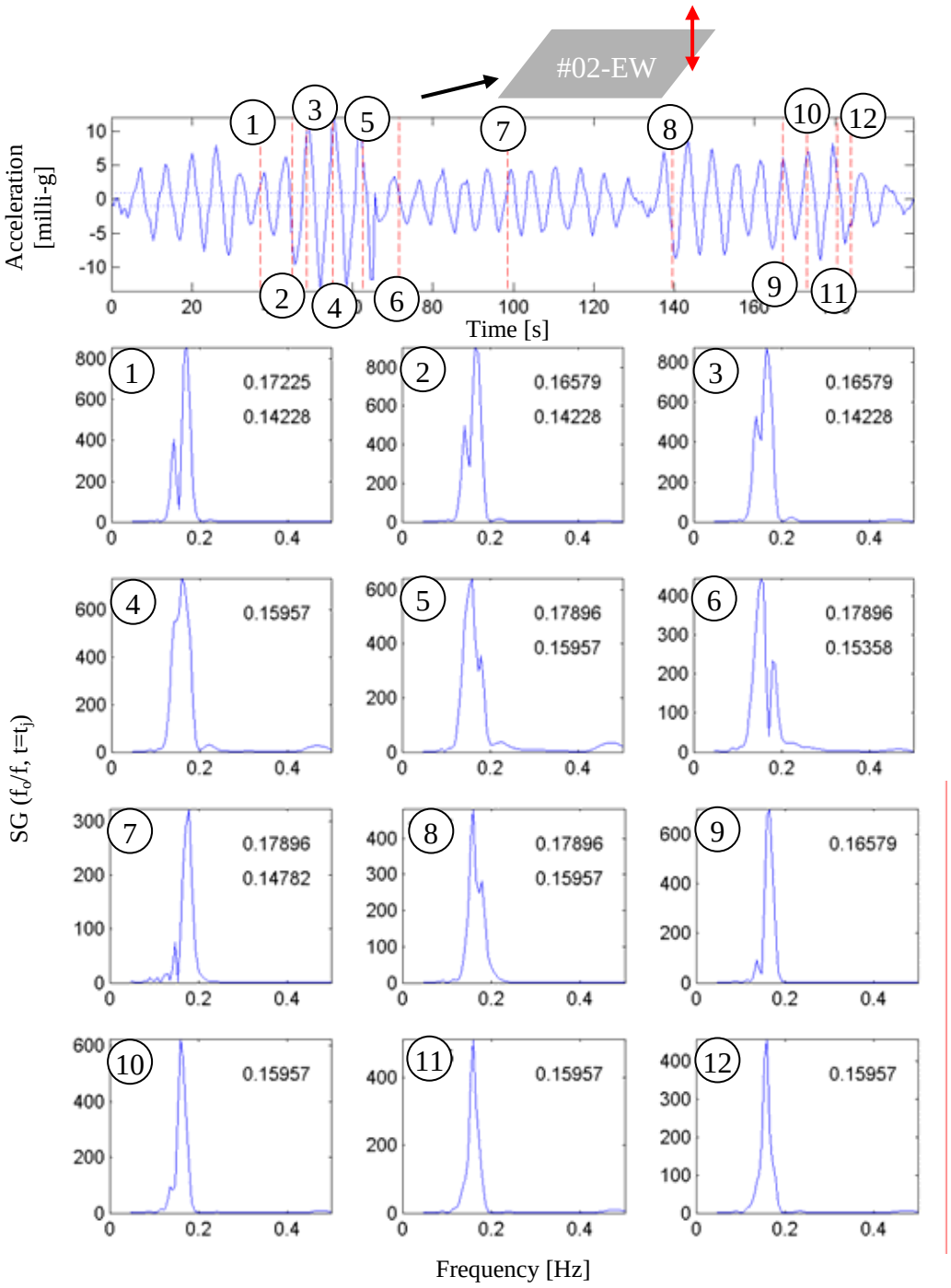

FIGURE 5.54. Response at #02-EW (Event 1) with wavelet instantaneous spectral analysis

sway response, and a single torsional mode response is observed to occur globally in both Figure 5.53 and 5.54, though interestingly, the building's torsion motion appears stiffer at the windward face than at the leeward. This again may be the localized by-product of fishtailing due to the orientation of the core, which is not aligned with the geometric center of the building and is shifted more towards the windward face of the building. Note that in the later spectra in Figure 5.54 there is no clear sway component but a widened bandwidth at the base of the spectra, though there is some trace sway at the windward sensor, emphasizing the localized features of this energetic event.

Examining the response in this event for #59-NS in Figure 5.55, the structure manifests two modes in spectrum 1 with NS sway dominant, but by the 2^{nd} and 3^{rd} spectra, the melding of the two fundamental modes due to a softening of torsion is evident. Further note the appearance of a higher mode of appreciable amplitude. By the 4^{th} and 5^{th} spectra, the melding of both modes into a single broadband peak is again observed. The coalescence phenomenon emerges at the highest amplitude shaking, facilitated again by torsion frequency softening and enhanced bandwidth due to damping increase with the amplitude of motion. The broad bandwidth of the coalesced mode in the 4^{th} spectra supports the premise of a merger between two independent modes of vibration. Because spectra 1-4 occur at the same amplitude level, the suppression of either mode is not the result of it being dwarfed by the other mode. Instead, the data reflects a physical manifestation of beat phenomenon interaction. The same holds true for the previous discussion of the EW sensors and the following discussion of the other NS sensor during this event.

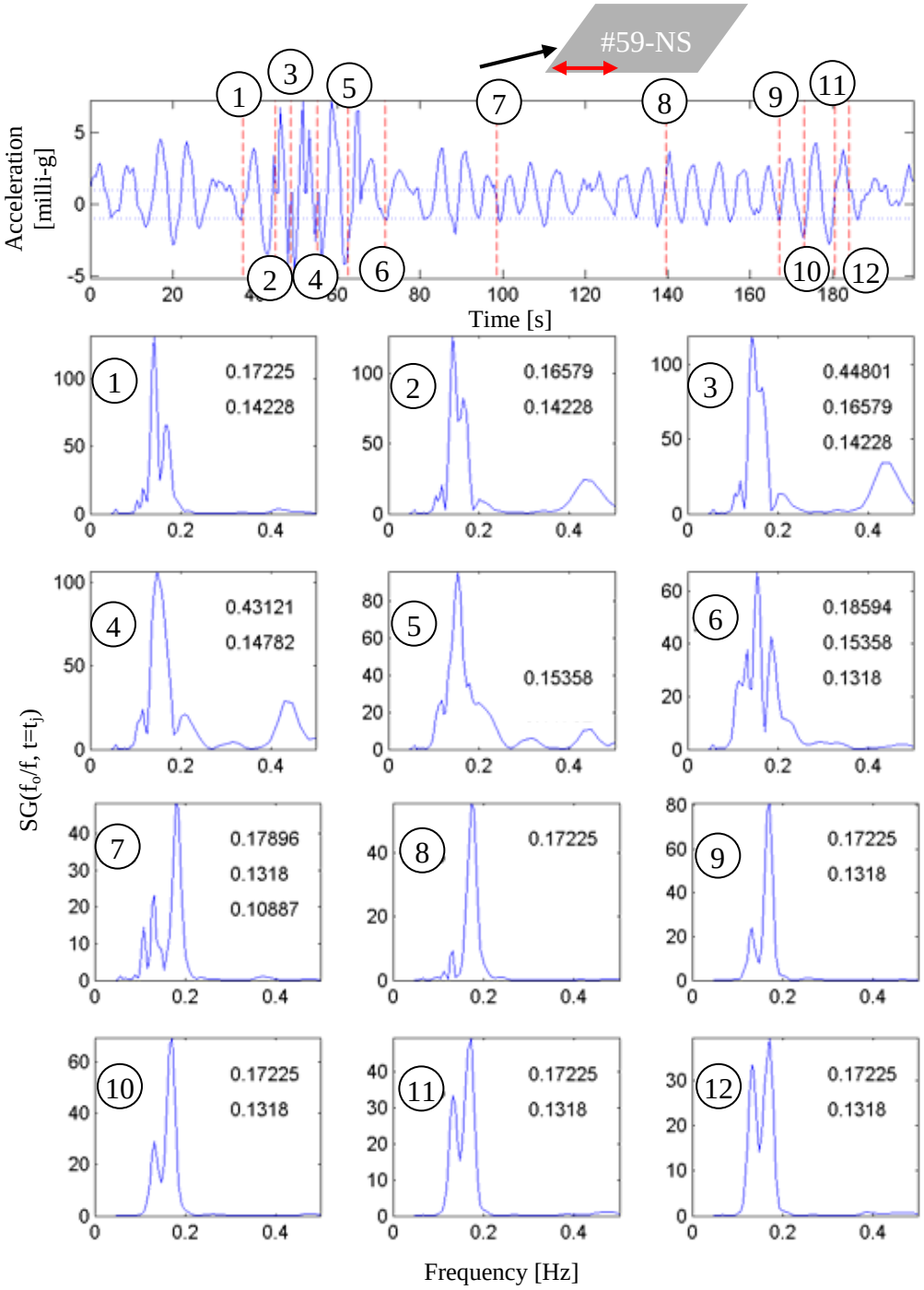

FIGURE 5.55. Response at #59-NS (Event 1) with wavelet instantaneous spectral analysis

Akin to spectrum 6 for the EW sensor at this same location, the melded modal response soon breaks down, but in a more dramatic fashion. The simultaneous presence of both a coalesced mode sandwiched between sway and torsion indicates the presence of all three characteristics within the local wavelet analysis window, though beyond this point the coalesced mode disappears leaving again the bi-modal response. Dominant torsion response ensues in spectra 7-10, though both modes are clearly present and better separated than in the other axis of the building. Note that the response observed here in the later stages of the event is one-tenth of the motion observed in Figure 5.53. Note also that at lower amplitude levels, the torsional response occurs at a higher frequency, consistent with the observed amplitude dependence mentioned previously.

At the leeward face, the first instantaneous spectrum in Figure 5.56, in comparison to Figure 5.55, has a comparable level of torsion motion, but diminished sway. Again, as observed in the #02-EW sensor, the two response components are not of comparable amplitude a melding in spectra 1-4 that never achieves the single mode response observed at the windward side. The lack of this feature is also due to absence of sufficient amplitude motion to soften the torsional mode and enhance the damping in the system. Soon after, spectra 5-8 show the emergence of the sway component, though the motion at this point is of lower amplitude. However, the sway component is only discernable due to the low amplitude of the torsional component at this time. By spectra 9-12, the appearance of this sway component is hardly evident and a low amplitude torsion component remains. Note that the residual torsional component is less than its counterpart at the windward side in Figure 5.55, due to structural eccentricities. Also comparing to Figure 5.55, these latter spectra more clearly reflect the more energetic

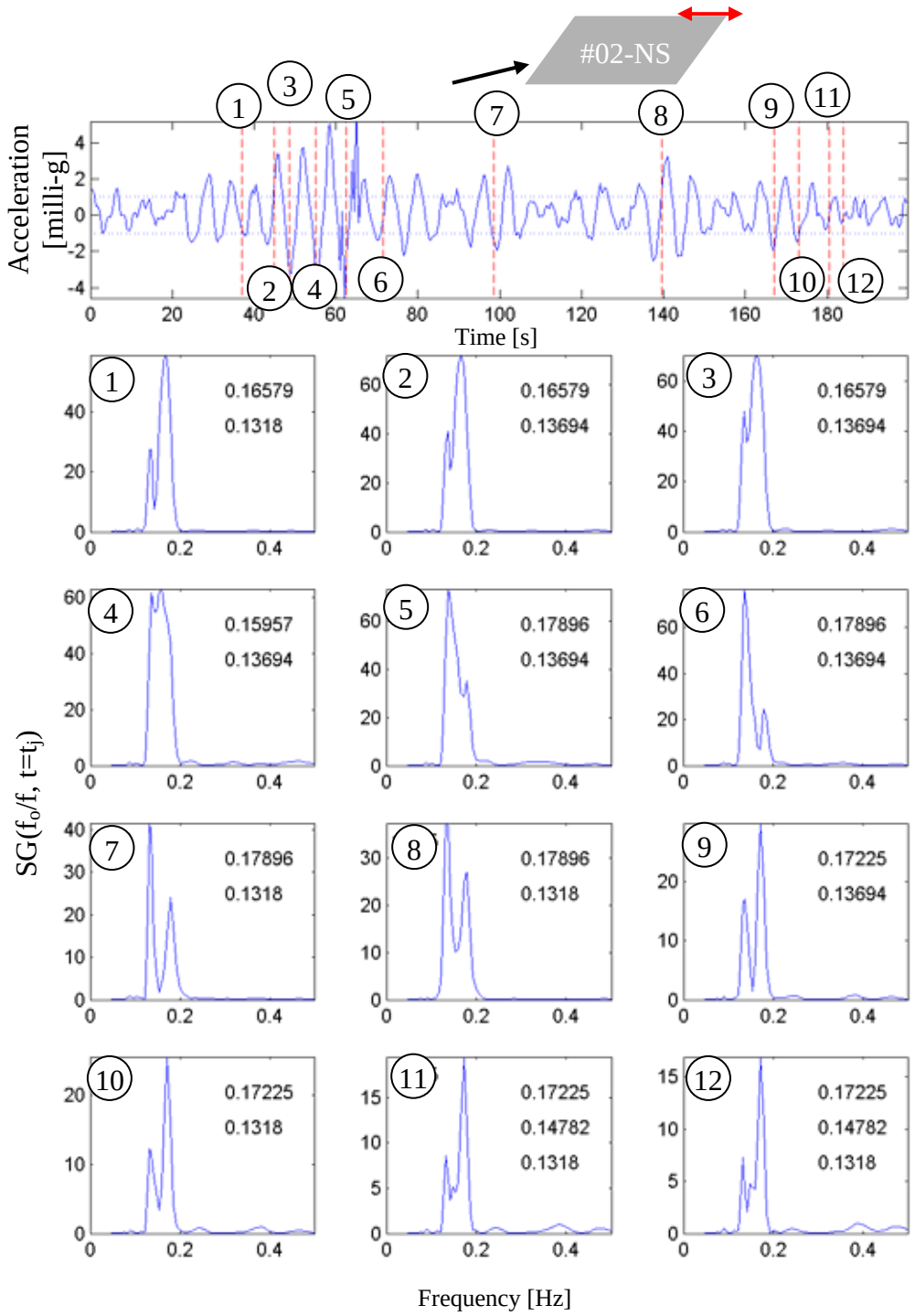

FIGURE 5.56. Response at #02-NS (Event 1) with wavelet instantaneous spectral analysis

sway response experienced in the windward corner is not present the other side of the building.

5.5.4 Event 2: 1350-1550 s

In Figure 5.57, it is again demonstrated that under similar spectral amplitudes, during the second noted event, the familiar coalesced response associated with high amplitude motion is observed again at sensor #59-NS, subsequently separating back into the two commonly identified modes. The presence of a coalesced mode at any frequency between the predominant sway and torsional modes (in this case at 0.153 Hz) is verified by the marked bandwidth of the spectral peak, particularly at the base and often asymmetric. As shown here, once separation occurs, due to a reduction of either response component, leading to lower amplitudes of motion, a decrease in damping, and increase of stiffness, the dominant torsional component remains. Again the prevalence of torsion is concerning and may perhaps again be attributed to an eccentricity between the geometric and elastic centroids of the building, as a result of the core being shifted from the centerline of the building and toward the leeward side, as shown in Figure 5.48.

5.5.5 Event 4: 2600-2800 s

Event 4 provides an opportunity to explore the effect of sway on dominantly torsional responses. Figure 5.58 compares the instantaneous spectra for #59-EW and #02-EW during part of this event. At the windward side of the building, the first spectrum indicates the notable presence of sway, as observed previously. This contribution is not present at the leeward side. In the ensuing amplification of the sway response, the torsion

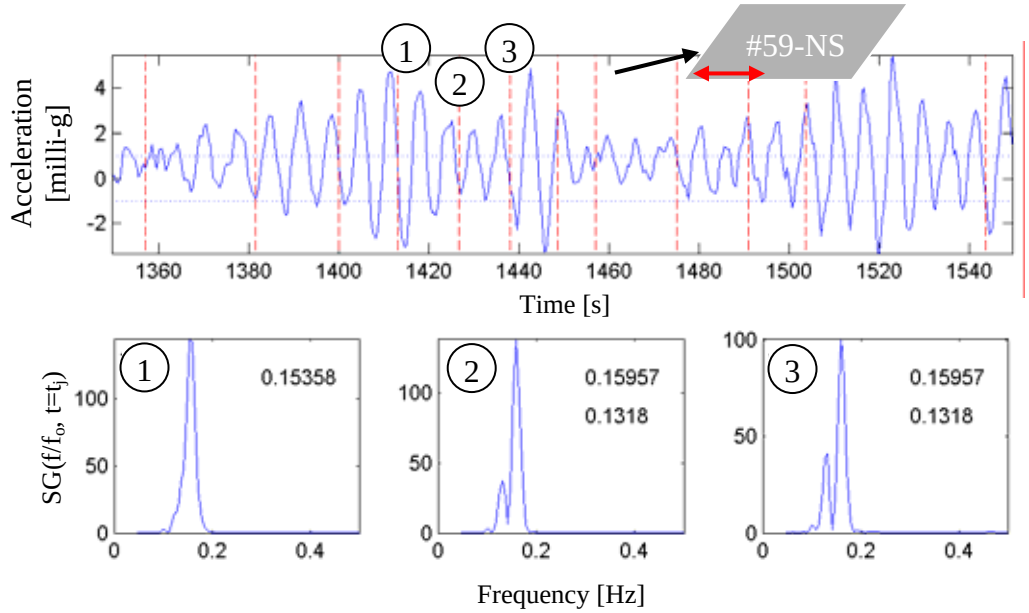

FIGURE 5.57. Response at #59-NS (Event 2) with wavelet instantaneous spectral analysis

present in the windward motions converges with the sway mode in the second spectra, resulting in a single mode response at a lower frequency and with larger bandwidth than the torsion response detected at the leeward side of the building. A comparison of spectra 2-4 for both sensors affirms this. This is the effect of torsion beating the sway mode at the windward side of the building, a local effect at that critical windward corner. As the amplitude level decreases in spectra 5 and 6, both sensors are beginning to detect similar torsional motions manifesting comparable spectral amplitudes, bandwidths and resonant frequencies. The windward sensor continues to manifest a low frequency asymmetry due to some residual sway component.

The WIFS provides another useful tool for macroscopic study of the response characteristics. The WIFS for #02-NS during Event 4 is provided in Figure 5.59. The WIFS manifests a bi-modal response in which the energy is dominantly focused with the

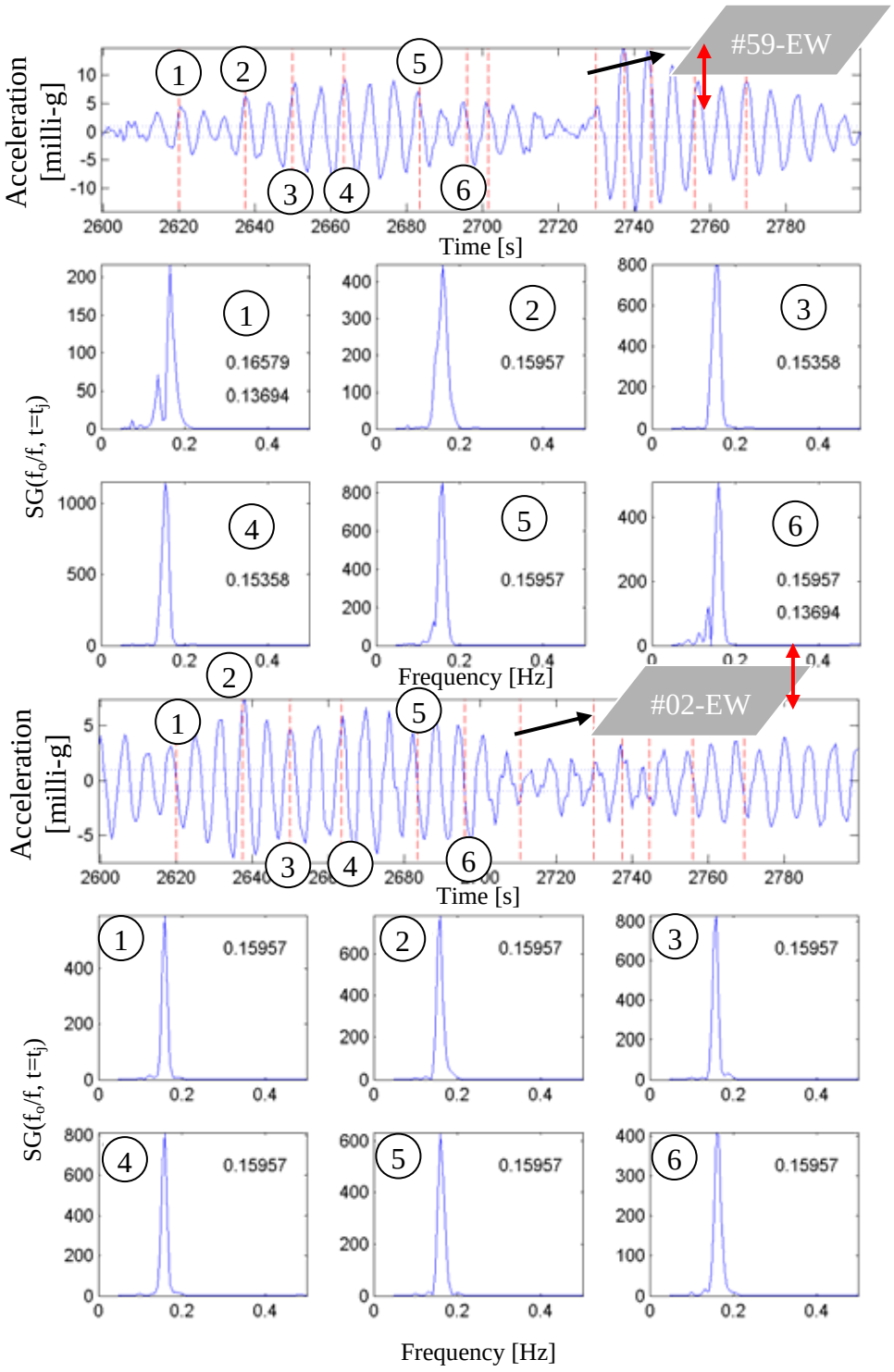

FIGURE 5.58. Response at #59-EW (top) and #02-EW (Event 4) with wavelet instantaneous spectral analysis

torsion component from 2600-2700 s and then transitions to dominant motions in the sway mode. Note that the higher frequency torsional mode shows far greater fluctuations in its instantaneous frequency ridge, demonstrating an increased sensitivity to amplitude variations than the lower frequency sway mode. During low amplitude events, e.g. 2700 –2730 s, the frequency is higher than during stronger vibrations, e.g. at 2660 s. This may explain why the torsional mode is often observed to soften into the sway mode and induced the coalesced response associated with beat phenomena.

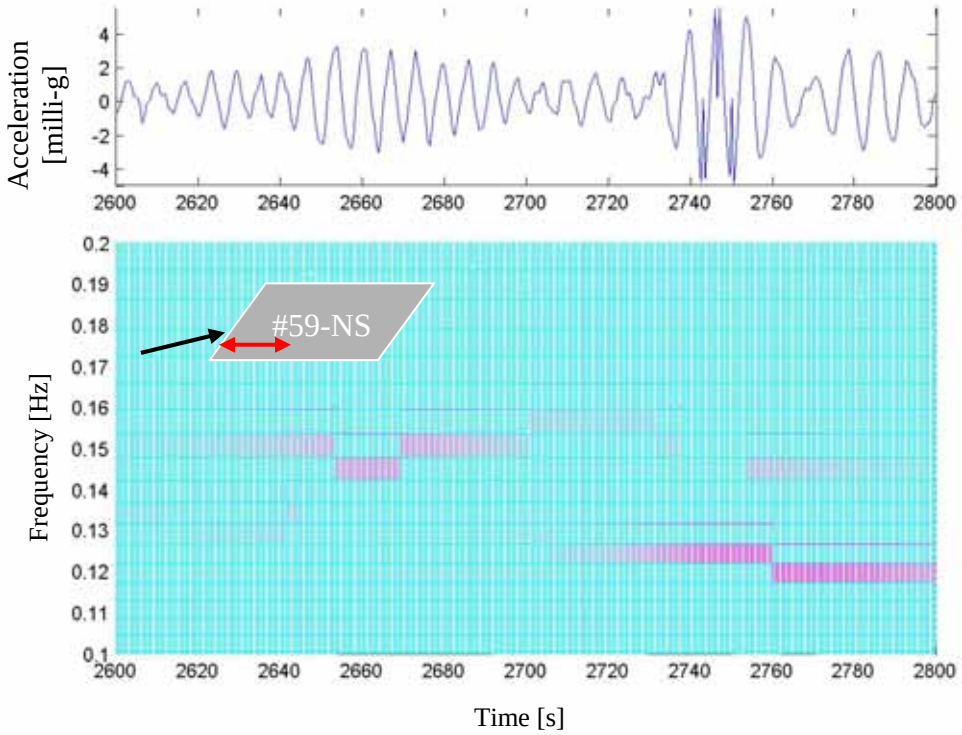

FIGURE 5.59. WIFS for #02-NS (Event 4)

5.5.6 Event 5: 3000-3200 s

Figure 5.60, spectra 1 displays a dominant torsion response of #02-EW during Event 5, a feature often expected at this sensor. In spectra 1-4 the separation between the dominant sway torsion and the diminished sway component is very evident. In this case, as the amplitude of motion increases, the dominant torsion mode associated dwarfs any sway component. Moving through spectra 5-9, the frequency of this torsional response softens, as the sustained amplitude of building motion increases. The bandwidth here does not indicate an expansion indicative of the coalescence observed previously. It may instead be hypothesized that the high amplitude torsional responses in Event 5 led to a softening of that modal frequency leading to the shift toward 0.153 Hz, a fact affirmed through the WIFS analysis shown in Figure 5.61. The WIFS shows only trace sway and a gradual softening of torsion frequency during the high amplitude response, after which it begins to stiffen again. It is this increased energy in the softened torsion mode led to heightened spectral amplitude, so much so that it completely dwarfed any sway response. Note that this softening is not evident in the global spectrum and only apparent in the local analysis presented here. Though omitted for brevity, the same dominant single mode torsional softening is observed at #59-EW in high amplitude responses, meanwhile, the NS sensors maintain the presence of both sway and torsion at low amplitudes. In this event, the motion is clearly dominated by torsion, obscuring any contributions due to sway. This prevalence of torsion is the infamous characteristic of this building.

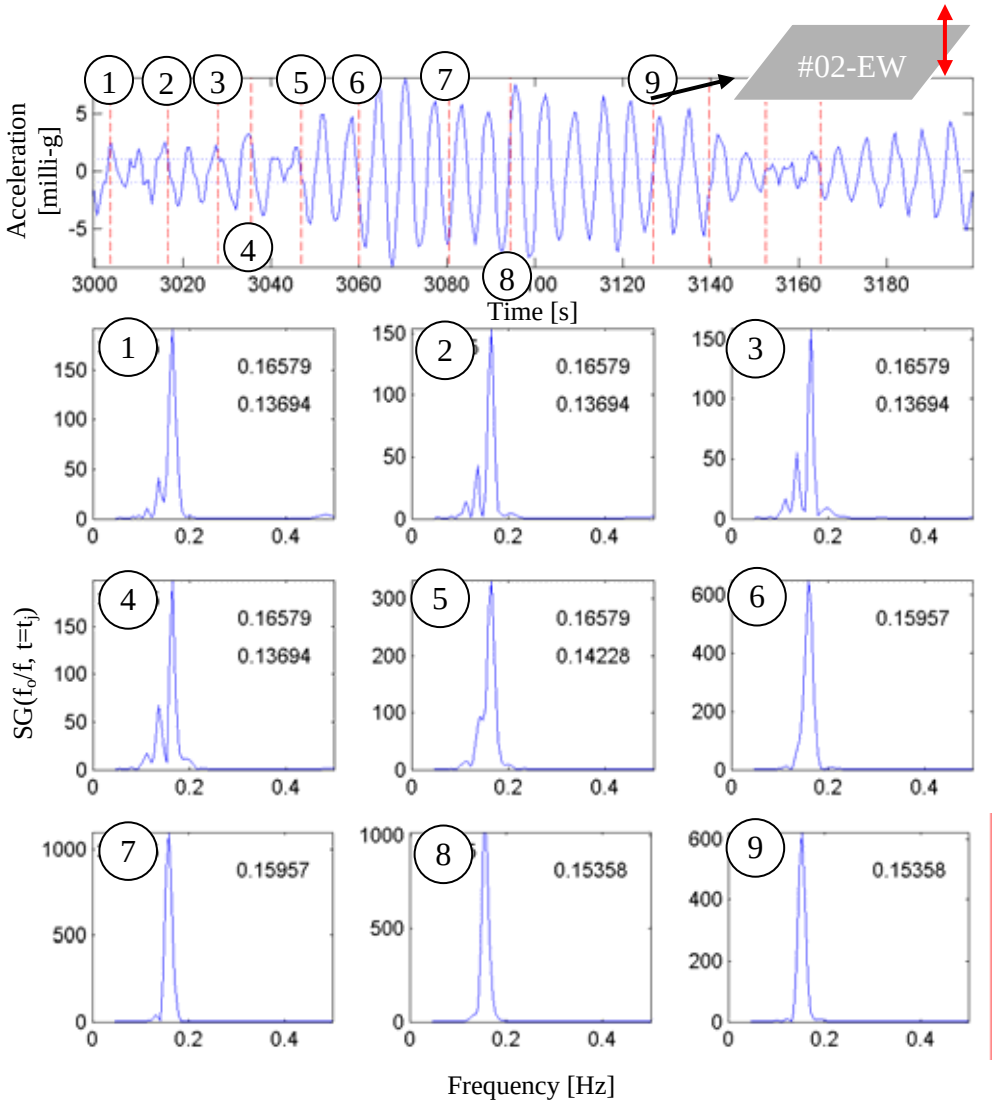

FIGURE 5.60. Response at #02-EW (Event 5) with wavelet instantaneous spectral analysis

5.5.7 Conclusions Based on Wavelet Spectral Analysis

In conclusion, the strongest and most sudden shaking was associated with Event 1, during which a sudden change in wind angle led oncoming winds directed toward the west corner of the building, an orientation more conducive to separation of flow, helping to further simulate strong torsional motions due to alternating vortices on the two long faces

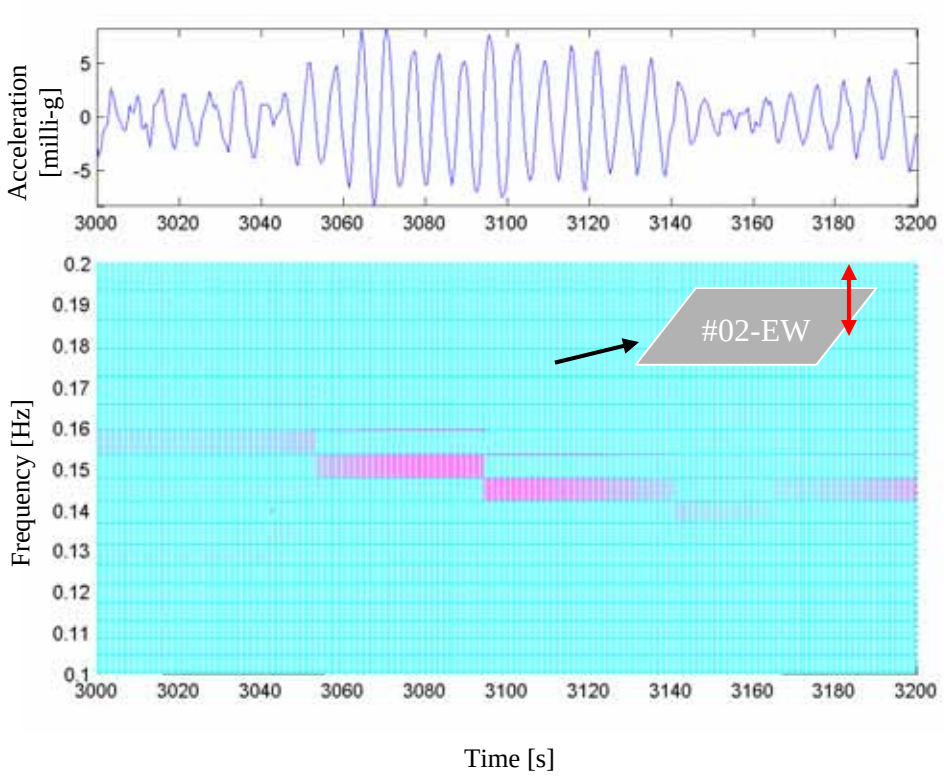

FIGURE 5.61. WIFS for #02-EW (Event 5)

of the structure. The comparable levels of sway and torsion in this event, and the high amplitudes of motion, facilitated a softening of the torsion mode and enhanced the damping sufficiently such that the beating of the two coalesced into a single mode response of high amplitude wide spectral bandwidth. As the wind direction changed quickly from this orientation, the isolated burst in response subsided, and the modes separated again, as the torsional component inducing beating diminished and nonlinearities in stiffness and damping were less pronounced. The coalescence associated with beat phenomenon only occurs under unique situations where the amplitude of motion is high enough to enhance nonlinearities and when torsional and sway contributions are significant. However, this phenomenon appears to be highly local, since

this coalescent phenomenon was only observed at the windward side of the building as a result of a fishtailing spurred by structural eccentricity. Further, since the NS sway frequency its orthogonal counterpart, the potential for coupling with the torsional mode is diminished, explaining the lack of coalescent behavior in these sensors.

Further, the potential for coupling of the sway and torsional modes often eliminates any physical decoupling of sway and torsion through a simple algebraic combination of the sensor outputs. It is important to note that the manifestation of amplitude dependence in dynamic properties and the evolution of a coalescent beat phenomenon are not apparent from just a global spectral representation, such as that of Figure 5.50. It is only in the in-depth investigations of time-frequency energy evolution that such interaction between modes can be uncovered to enhance understanding of building performance. Fortunately, these investigations of instantaneous modal properties are now made possible through the wavelet framework presented here.

5.6 Offshore Platforms

The previous analysis of wind and seismic response in buildings highlighted the ability of wavelets to uncover nonlinear and intermittent response characteristics. The final analysis in this chapter, focused on the response of tension leg platforms (TLP) under the action of wind and waves, will demonstrate the ability of the transform to capture time-varying low frequency content within the resulting response. The TLP response analyzed herein was obtained from experiments conducted through a joint industry project discussed in Gurley (1993). This experiment measured the response of a 1:160 scale model in six degrees of freedom, as shown in Figure 5.62, with longitudinal, transverse and vertical motions,

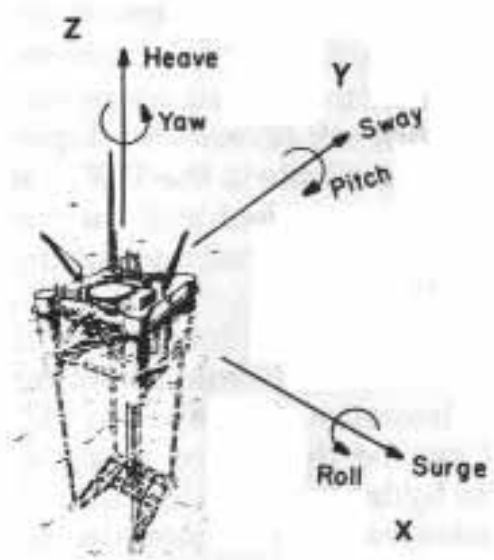

FIGURE 5.62. Schematic of response components for tension leg platforms (taken from Kareem, 1985)

referred to as surge, sway and heave, respectively, and angular motions in a transverse, longitudinal and horizontal plane: respectively, roll, pitch and yaw.

The thrust toward deep-water drilling gave birth to this class of compliant structure, designed to move with the environmental loadings rather than resisting them rigidly (e.g. Kareem, 187). One benefit of compliance is the ability to design these platforms with very low natural frequencies in surge, sway and yaw degrees of freedom, as shown in Figure 5.1. As wave motions have a narrow spectra centered about comparatively higher frequencies, compliant structures generally will not experience any dynamic amplification of wave-induced response, apart from second-order effects. However, they are relatively more susceptible to dynamic effects of wind than conventional fixed leg platforms and therefore must be designed to resist both dynamic

wind and wave loadings (Kareem, 1987). As these loading sources simultaneously produce low frequency wind and wave excitations, as well as higher frequency wave excitations, this situation is well-suited for a multi-resolution wavelet analysis, exploiting the wavelet's low-frequency resolution capabilities and the wavelet instantaneous spectral representations to distinguish the response components associated with wind and those resulting from wave action. Further, the ability of wavelets to track nonlinear features, as demonstrated in the previous analysis of building response, will have added utility in the analysis in light of the known system nonlinearities and those of the wave field (Kareem, 1985). Since the heave, pitch and roll are beyond the wave spectrum, they will not be considered at this time.

Before beginning the analysis of the platform response under the combined effects of wind and wave loads, some details of the oncoming wave field and the experimental model are defined. First, all discussions that follow will consider the scaled experimental data to give an indication of the likely behavior of this system at full-scale. Two sea states will be considered in this section, the first a mild sea state with significant wave height of 9.61 m and peak frequency, as determined from the Fourier power spectrum in Figure 5.63a, of 0.077 Hz. The severe sea state, whose Fourier power spectrum of wave height is provided in Figure 5.63b, is characterized by a wave frequency of 0.056 Hz and significant wave height of 20.23 m. Again, additional information on this experimental program, including the properties of the platform model and the experimental facilities, can be found in Gurley (1993).

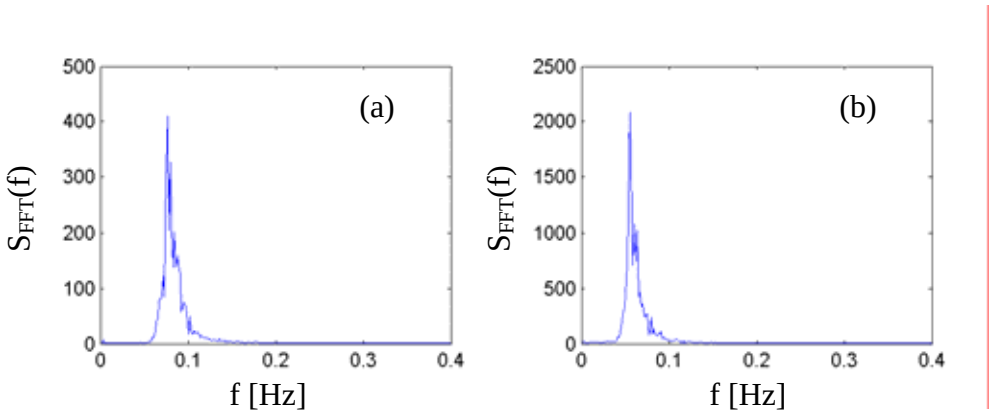

FIGURE 5.63. Fourier power spectra for wave field in (a) mild sea state and (b) severe sea state

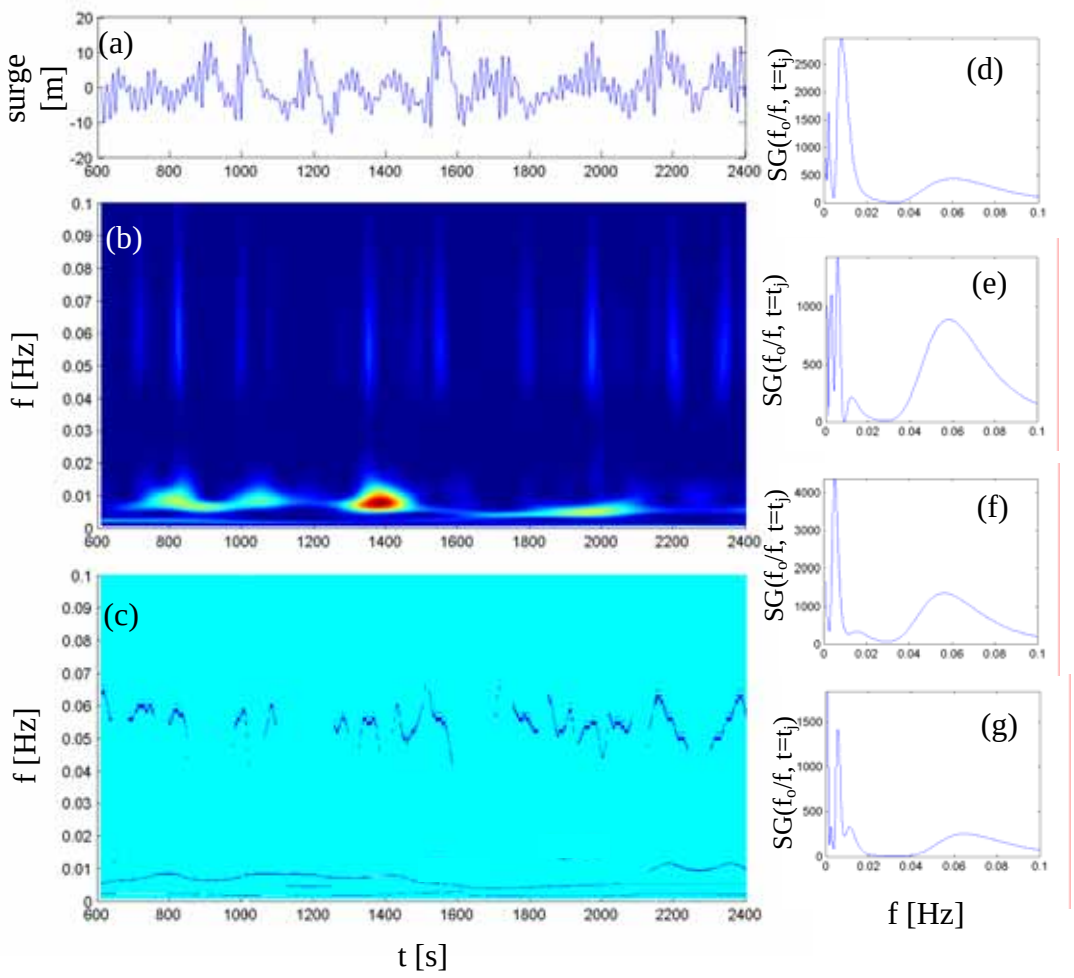

FIGURE 5.64. Severe sea state (a) surge response, (b) scalogram, (c) WIFS and instantaneous spectra at t_j = (d) 1007.8 s, (e) 1542.2 s, (f) 1970.3 s, (g) 2155.0 s

The surge response (Figure 5.64a) is analyzed first, using a wavelet analysis with f_o = 0.5 Hz to unveil any time-varying characteristics associated with wave loading. Considering that typical wave spectra are known to peak near 0.08 Hz and wind spectra at generally lower frequencies, the wave-induced response of the platform can be readily distinguished through the wavelet analysis. Both a mild and severe sea state are analyzed and compared herein to emphasize the relative role of wave action in each. The scalogram in Figure 5.64b identifies the wave frequency response with added intermittent components, which can be attributed to occasional slamming of waves on the platform hull in the severe sea state through the light, higher frequency bands. These oscillations of frequency are also observed later in Chapter 7 in the discussion of random sea states characterized by nonlinear waves. The precision of the WIFS in Figure 5.64c indicates that this wave component within the severe sea state manifests significant fluctuations in the instantaneous frequency. Also noted are the gradual fluctuations in the ridge associated with the resonant response of the platform near 0.007 Hz, manifesting nonlinearities consistent with the modeling of stiffness as a hard spring in the scaled model, increasing with displacement. Due to the long period of response, this occurs very gradually. Note the increase in instantaneous frequency between 800 and 1400 s followed by a softening between 1400-2000 s and a recurrent hardening beyond 2000 s. Meanwhile, the fluctuations in the wave component near 0.06 Hz follow the trends in the amplitude modulation of the time history. This is perhaps most clearly indicated by the two modulations in the WIFS between 2100 and 2400 s, following amplitude modulations of the same form in 5.64a. The low frequency ridges may also represent contributions from the second order, slowly varying drift forces at low frequencies,

caused by the second-order contribution resulting from interactions between components of the wave spectrum.

The WIFS demonstrates that the occurrence of peak surge response is not always commensurate with the wave frequency response, as large response excursions may also result from low frequency hydrodynamic loads due to the passage of large waves. For example near 1200s, a large surge response occurs without a strong wave frequency response component. This unique wavelet perspective allows differentiation of the relative contributions of wind and waves, both at the wave frequency and at lower frequencies, to a given event, readily garnered through examinations of the instantaneous spectra in Figure 5.64d-g. For example, Figure 5.64e has a significant high frequency contribution associated with wave frequency response while Figure 5.64g has a significant low frequency component. Comparing Figure 5.64d and 5.64e, it becomes evident that high amplitude surge response is not always driven by higher frequency wave frequency response and further distinguishes response due to higher frequency wave frequency response and low frequency wind/wave effects.

On the other hand, in the mild surge response, wind forces create a large response at the resonant frequency of the platform. The differences in the response characteristics between the mild and severe sea states are readily summarized by comparing their Fourier spectra and wavelet marginal spectra in Figure 5.65a. Both responses feature a low frequency component in the vicinity of the system's natural frequency, which arises due to nonlinear interactions between the inputs, resulting in forcing energy in a wider range of frequencies (Kareem et al., 1998). The wavelet marginal spectra are shown as

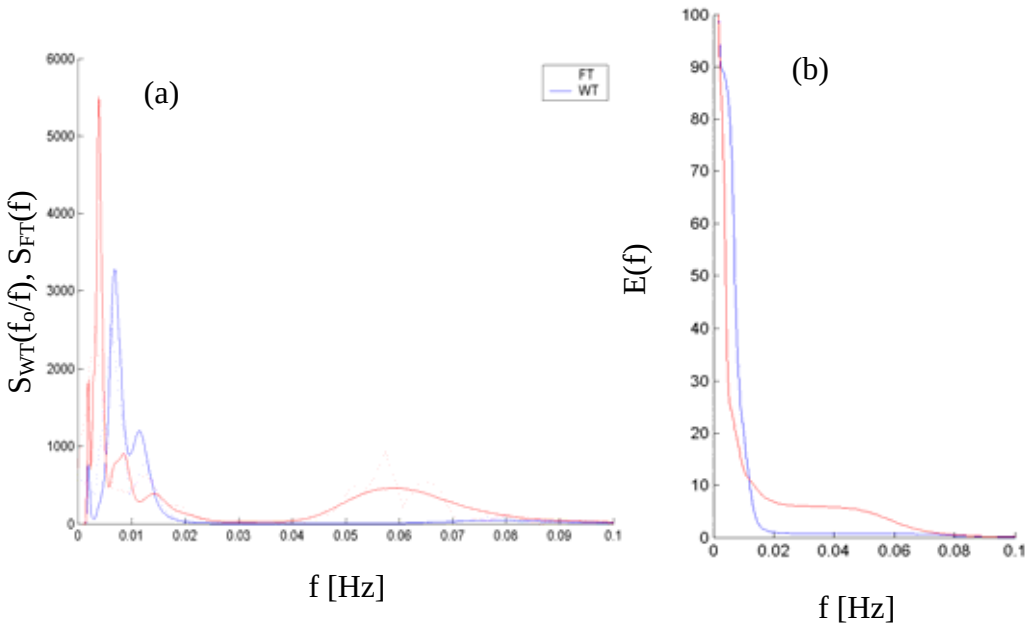

FIGURE 5.65. Comparison of surge response in mild (blue) and severe (red) sea states: (a) wavelet marginal spectrum (solid) and Fourier spectrum (dotted); (b) energy accumulation with frequency

solid lines and their Fourier counterparts are shown as dotted lines. The enhanced low frequency resolution capabilities of the wavelet become immediately apparent. In the severe sea state (red), the component associated with the high frequency wave excitations is immediately apparent. Though, as shown by the energy accumulation plots in Figure 5.65b, this wave component, while more pronounced, contributes less than 10% to the overall response: the severe sea state surge response is still dominated by the energetic low frequency wind and second order wave effects, as shown by the dark red hues in the scalogram of Figure 5.64b. The majority of energy in this case is associated with frequencies less than 0.01 Hz.

In the mild sea state, the energy concentrates at decidedly higher frequencies than the severe sea state, as shown again in Figure 5.65b. The mild sea state surge response (blue) has a richer distribution of energy in the frequency band under 0.02 Hz, where 98% of the energy is concentrated. Note the absence of energy at higher frequencies as further evidence of a lack of sizeable wave frequency response in the mild sea state. As shown by the scalogram in Figure 5.66b, the high frequency wave frequency response is minimal, though again manifesting an intermittent, time-varying frequency character. The WIFS in Figure 5.66c demonstrates the interchange of energy between second order wave components and resonant wind response. The hitches in these low frequency ridges in the vicinity of high amplitude events at 1800 and 2000 s may be due to hardening characteristic of the platform resonant response. In particular, the mild sea state surge analysis demonstrates that the primary effect of waves is not significant to the overall motion of TLPs, though it is well known that slowly varying drift forces at low frequencies caused by nonlinear interactions between wave components in wave spectrum may result in low frequency resonant oscillations of TLPs (Kareem, 1985). The prevalence of these low frequency components is highlighted by the instantaneous spectra in Figure 5.66d-g.

Ideally in the case of wind and waves approaching at a zero angle of attack, there should be no sway motion. However, due to the coupled nature of the TLP's degrees of freedom, the lateral motion may be induced by vortex shedding or through coupling that exists with the yaw motion. Sway may also result from any misalignment of the model in the wind/wave test facility. The resulting sway response in the mild sea state, garnered from a f_o = 1 Hz wavelet analysis, is characterized by a significant component of energy

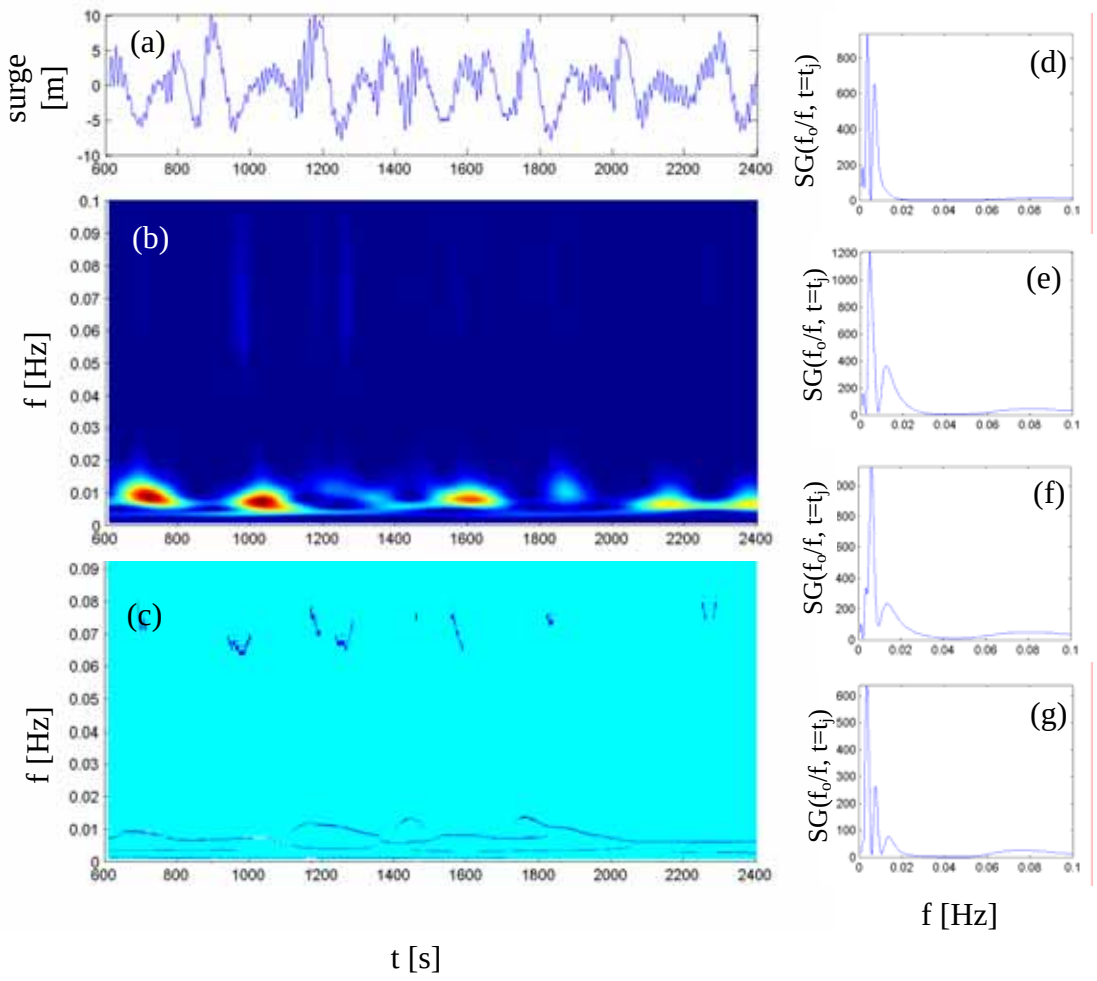

FIGURE 5.66. Mild sea state (a) surge response, (b) scalogram, (c) WIFS and instantaneous spectra at t_j = (d) 891.6 s, (e) 1168.0 s, (f) 1459.1 s, (g) 1772.2 s

in the wavelet marginal spectrum (blue) associated with the wave frequency response, as denoted by the energetic contribution near the peak of the wave spectrum in Figure 5.67a. This component contributes 30% of the total energy to the sway response, as shown by the accumulation curve in Figure 5.67b, a comparatively greater contribution that than observed in the surge response. As shown by the scalogram in Figure 5.68b and its associated WIFS in Figure 5.68c, this component of the response is highly energetic and

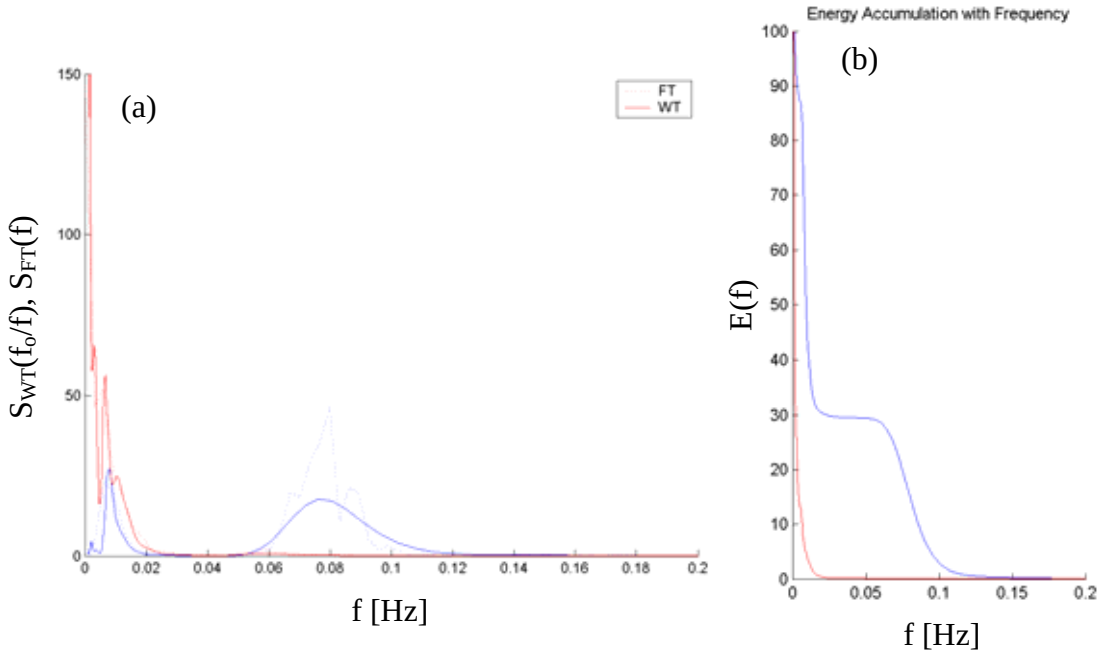

FIGURE 5.67. Comparison of sway response in mild (blue) and severe (red) sea states: (a) wavelet marginal spectrum (solid) and Fourier spectrum (dotted); (b) energy accumulation with frequency

shows marked fluctuations, similar to what was observed in the surge response of the severe sea state, a detail obscured in a conventional Fourier analysis.

Conversely, the severe sea state sway response has a strong, quasi-static component and the absence of any wave frequency response, a feature similarly affirmed by the energy accumulation plot in Figure 5.67b. This low-frequency component manifests trends consistent with that observed in the surge response. The scalogram associated with this sea state is shown in Figure 5.69. Note the increasing prominence of the resonant component of the response and the decreasing frequency of this response as the amplitude of sway declines beyond 1600 s, again suggesting the manifestation of the hardening spring action in the scaled model.

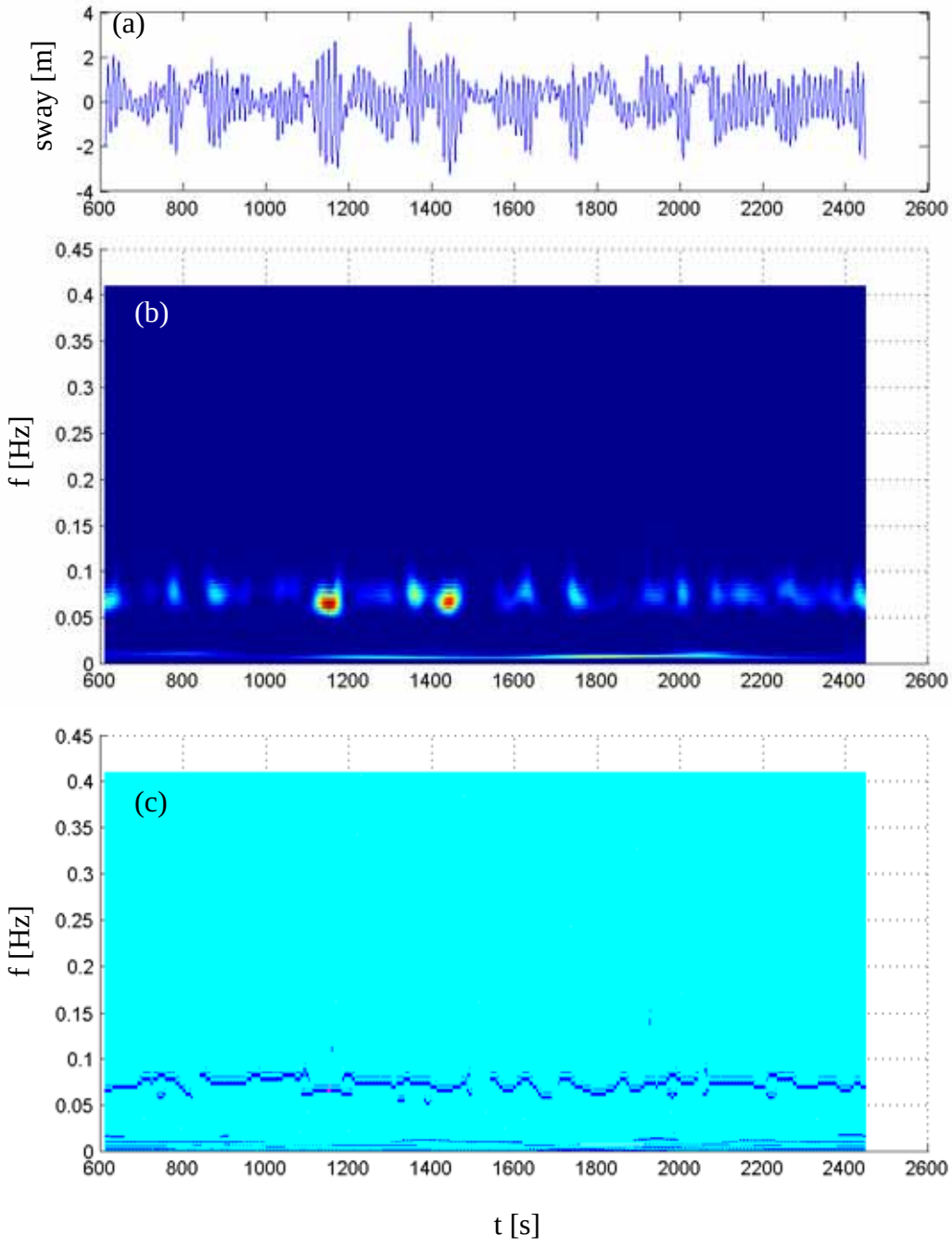

FIUGRE 5.68. Mild sea state (a) sway response, (b) scalogram and (c) WIFS

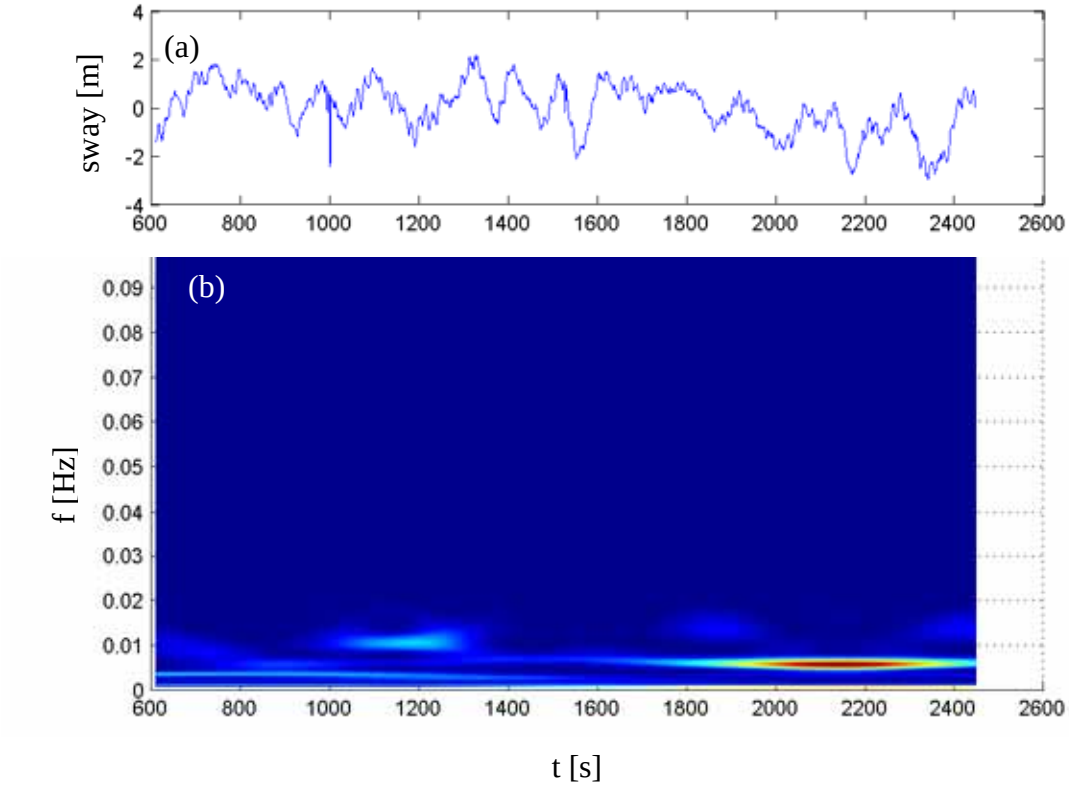

FIGURE 5.69. Severe sea state (a) sway response, (b) scalogram

The lateral motion induced by yaw is the final response component considered here using a f_o = 1 Hz wavelet analysis. This response component arises from asymmetrical distributions of the wind or wave loads but can be accentuated by uneven pre-tension in the tendons and potential eccentricity in the center of mass, which can induce surge-yaw coupling (Gurley, 1993). As shown by Figure 5.70b, the accumulation of energy in both the mild (blue) and severe (red) sea states is nearly identical, concentrated entirely in the low frequencies under 0.02 Hz. The difference lies in how this energy distributes within the low frequency range. As shown by Figure 5.70a both the wavelet (solid) and Fourier (dotted) spectra, the mild case manifests a sharp peak with a broad bandwidth and anti-symmetric shape. This spectral peak is flanked to the right by a slight, quasi-static

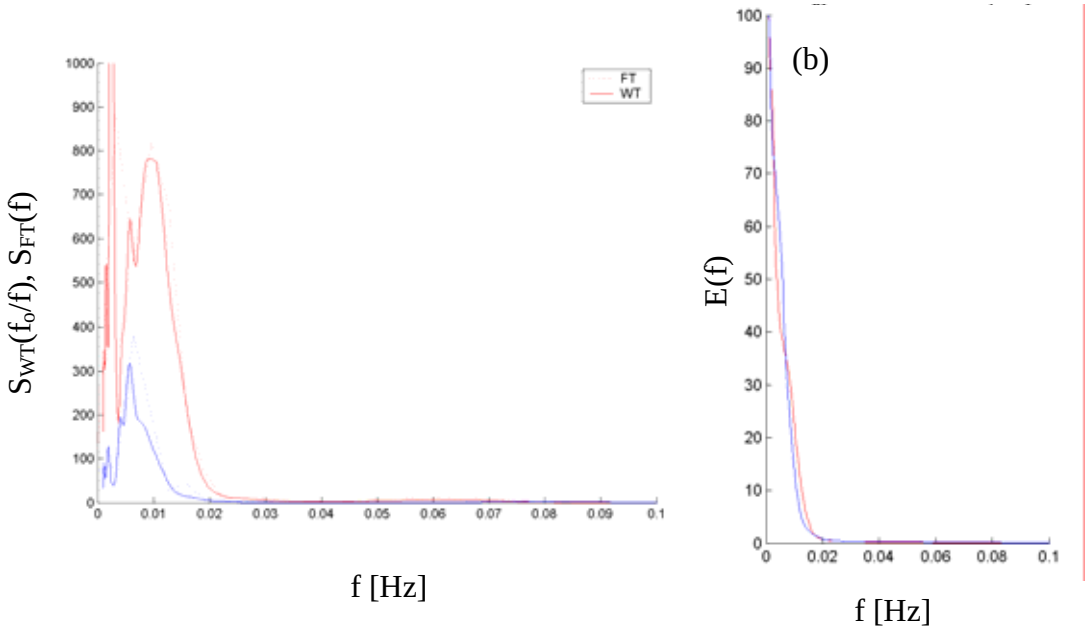

FIGURE 5.70. Comparison of yaw-induced lateral response in mild (blue) and severe (red) sea states: (a) wavelet marginal spectrum (solid) and Fourier spectrum (dotted); (b) energy accumulation with frequency

component. The severe sea state also shows this same quasi-static component but of a far more pronounced stature, however, the single response peak observed in the mild sea state has separated into a bi-modal characteristic, retaining the same resonant frequency as the mild state but now dwarfed by a higher-frequency component previously buried in the widened bandwidth of the mild sea state.

The averaged representation provided by the marginal spectrum fails to shed light on the true behavior of the yaw response. The scalogram in Figure 5.71b indicates that this bi-modal characteristic is present intermittently throughout the mild sea state time series in Figure 5.71a. The marginal spectrum merely represented the occasional presence of the higher mode in this pair as a widened bandwidth. The presence of both modes is very pronounced between 800 and 1200 s, concentrating at near 0.01 and 0.005 Hz.

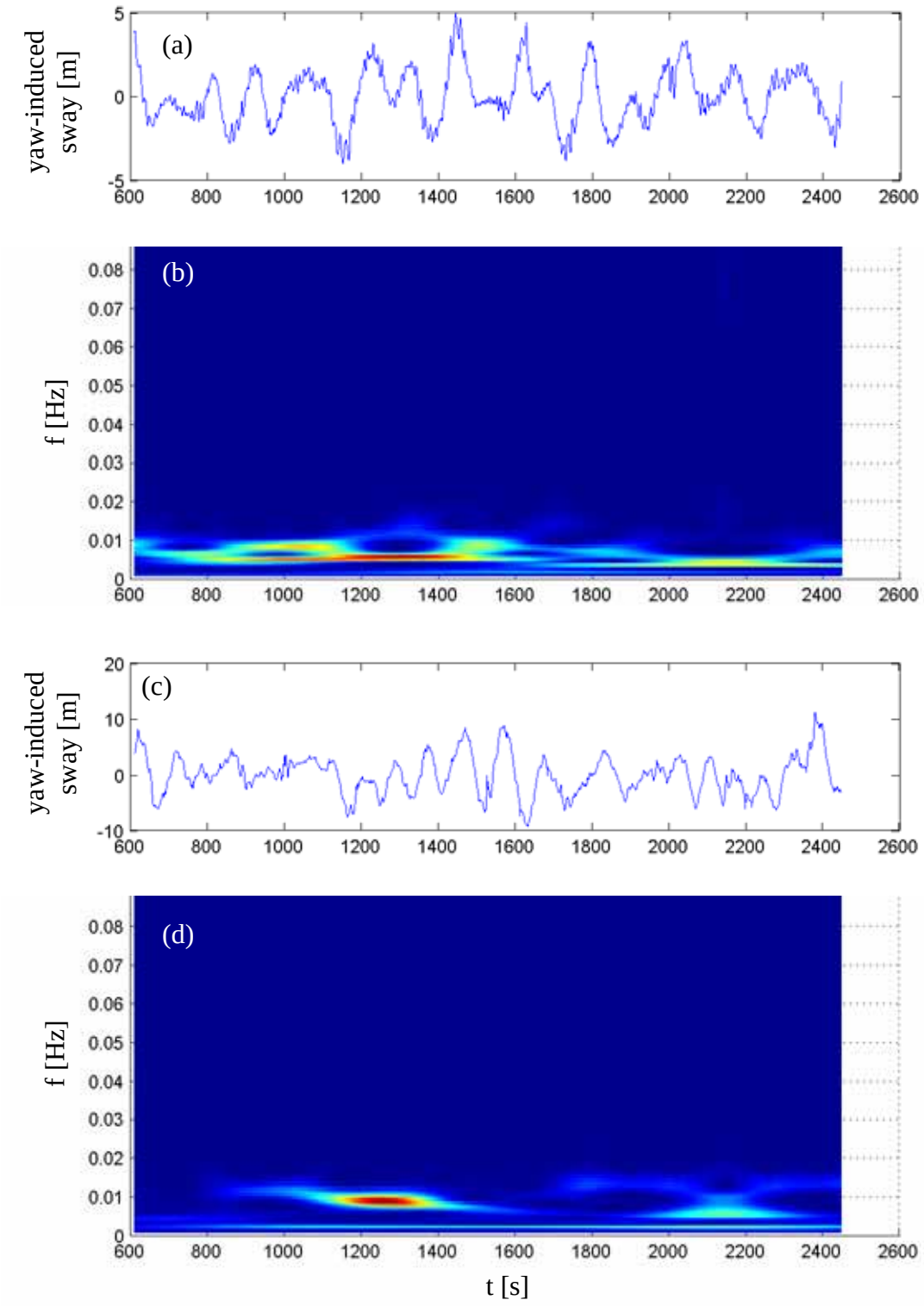

FIGURE 5.71. (a) Yaw-induced lateral response for mild sea state and (b) scalogram; (c) yaw-induced sway response for severe sea state and (d) scalogram

Between 1200 and 1400 s it reverts strongly back toward a resonant response at 0.005 Hz only revert back to this bimodal characteristic at 1400 s, repeating this trend later in the scalogram. The trace presence of a quasi-static component near 0.002 Hz is evident throughout though most pronounced between 1400 and 1800 s. The severe sea state produces a yaw scalogram in Figure 5.71c that demonstrates the enhanced presence of the higher mode in that bi-modal characteristic near 0.013 Hz, particularly between 800 and 1000 s and from 1800 s until the termination of the time series. Strong periodicity in the time series indicative of resonant response is identified by two isolated bursts of bright hues in the scalogram at 1200 and 2000 s. The quasi-static response is also very strongly evident in the severe sea state, becoming far more pronounced and persistent from 1000 s and on.

5.7 Summary

This chapter presented specific examples of wavelet analyses of environmental loads and associated response of Civil Engineering structures, highlighting the wavelet's ability to uncover intermittent and nonlinear characteristics through wavelet scalograms and instantaneous frequency spectra. In particular, the ability to detect and model nonlinear characteristics is particularly important for seismic analysis, where large amplitude response and structural damage can induce frequency variations. Further, in the design and modeling of compliant structures, wavelets can be beneficial in distinguishing wind and wave driven response of systems with nonlinearities in stiffness and subject to the action of nonlinear wave fields. In fact, this inherent nonlinearity in wave excitations will be a subject of further study in Chapter 7, where wavelets will be used in the analysis of

Stokian waves and to uncover the intermittent characteristics of random sea states. However, even under the lower amplitude excitations of wind, wavelets were shown in this chapter to be a critical tool in unlocking peculiar behavior trends in a tall building due to intermittent aerodynamic actions that were obscured in Fourier analyses. The following chapter will further demonstrate the utility of wavelets in unlocking such intermittent characteristics in wind fields through a wavelet-based coherence measure and its associated processing tools.

CHAPTER 6

WAVELET SYSTEM IDENTIFICATION II:

APPLICATIONS TO WAVELET COHERENCE

6.1 Introduction

As motivated in the preceding chapters, though transients have long defined signature characteristics across the engineering spectrum, available analysis tools like Fourier transforms have been ill equipped to represent this phenomenon. It was not until the time-frequency revolution of the 20th century that such signals could be adequately treated by the likes of the Gabor transform and the Wigner-Ville distribution. Today, wavelet transforms lead the transition to this new analysis domain, providing the ability to display time and frequency information independently and unveil the hidden features of evolutionary phenomena.

Particularly in the areas of aerodynamics and wind engineering, wind field fluctuations result in spatio-temporal pressure fluctuations on the surfaces of bluff bodies, e.g. buildings. These pressure fluctuations are manifestations of complex, nonlinear interactions that take place as the wind passes around a bluff structure. The spatio-temporal pressure fluctuations exhibit drastic transient features depending on their

location on the surface and, with the exception of the windward face, are not amenable to a functional relationship with the oncoming wind field. Efforts to identify significant linear correlation between wind and pressure fluctuations were unsuccessful, especially in the separated flow regions. This has led to the consideration of higher-order correlation, e.g. bicoherence (Gurley et al., 1997a). However, these efforts highlighted the inability of such Fourier-based measures to capture transient higher-order correlations that may exist between wind and pressure fluctuations.

With the availability of time-frequency analysis via wavelets, linear correlation analyses were enhanced by way of the coscalogram (Gurley & Kareem, 1999). This approach did identify some intermittent correlation between wind and pressure and will be further developed in this chapter as a tool for delineating any previously obscured intermittent relationship between certain wavelengths in the approach flow and the resulting pressure fluctuations. The potential for such insights have made wavelets an insightful tool for other applications in wind engineering. For example, early investigations of turbulent wind effects were conducted by Farge (1992), who applied wavelet-based spectral analysis to the modeling of atmospheric turbulence. Gurley & Kareem (1997a) later adapted this to the analysis of turbulence and resulting pressures in full-scale dynamic response data. In total, the use of wavelet transforms in this field continues to advance, as overviewed by Gurley & Kareem (1999) and applications of wavelets in wind, offshore, and earthquake engineering in Chapter 5.

This chapter continues the work in wavelets for both wind and waves by applying wavelet transforms to identify first-order intermittent correlation between measured

records. While this representation allows a display in terms of time and frequency, the influence of noise in the estimation of coherence over a localized time frame is significant, making a distinction between the true correlation and noise a major issue to be addressed. This chapter revisits the classical approach for reduction of variance, averaging, in the multi-resolution context of wavelets, and later discusses three tiers of denoising schemes, which minimize the need for localized averaging in order to preserve temporal information. While hard thresholding based on global maxima of the wavelet coherence map can be used to isolate meaningful coherence, other thresholding simulation schemes are proposed to provide a reference noise map to more accurately separate spurious noise effects from true signal content. These reference maps are generated using independent realizations of time histories to establish a statistical measure of the expected noise in the estimated coherence. The robustness of these schemes is established using both simulated and measured data. The method is shown to significantly reduce the presence of spurious coherence, even in cases where variance and leakage are prevalent.

6.2 Wavelet Coherence Background: Scalogram and Coscalogram

The localized wavelet coefficients are well suited for analyzing non-stationary events, with their squared values plotted on a time-scale (time-frequency) grid. This visualization, called the scalogram or mean square map, reveals the frequency content of the signal at each time step to pinpoint the occurrence of transients while tracking evolutionary phenomena in both time and frequency. However, in some recent studies, the concept of the scalogram has been advanced to identify correlation between signals in

which the squared coefficients are replaced with the product of the wavelet coefficients of two different processes (e.g., Hudgins et al., 1993; Gurley & Kareem, 1999). This coscalogram produces a view of the coincident events between the processes, revealing time-varying pockets of correlation over frequency.

To demonstrate this concept, full-scale pressures measured on a building and the upstream wind velocity fluctuations were analyzed by Kareem & Gurley (1999). The scalogram of wind velocity and simultaneously measured pressure are presented along with their coscalogram in Figure 6.1a-c. The light hues of the coscalogram identify areas of correlation. Figure 6.1d-f presents the same information for two uncorrelated records. The resulting coscalogram (Fig. 6.1f) of these two unrelated processes shows no distinct correlation. The coscalogram contains wavelet coefficients determined from segments of the signal isolated by the sliding window of the scaled parent wavelet. At each time step, the calculated wavelet coefficients comprise a single raw spectrum across the range of scales, equivalent to a spectrum obtained from a single time history in the traditional Fourier analysis. These raw spectra that are assembled along the time axis in the scalogram and coscalogram lack the ensemble averaging necessary in traditional Fourier methods to reduce the variance in the estimate, resulting in noisy displays where correlated events are difficult to differentiate from random coincident coefficients. Though this simple measure of correlation has been used to qualitatively identify first-order wind velocity and pressure relationships (Gurley & Kareem, 1999), it is refined in this chapter by the introduction of a wavelet coherence measure.

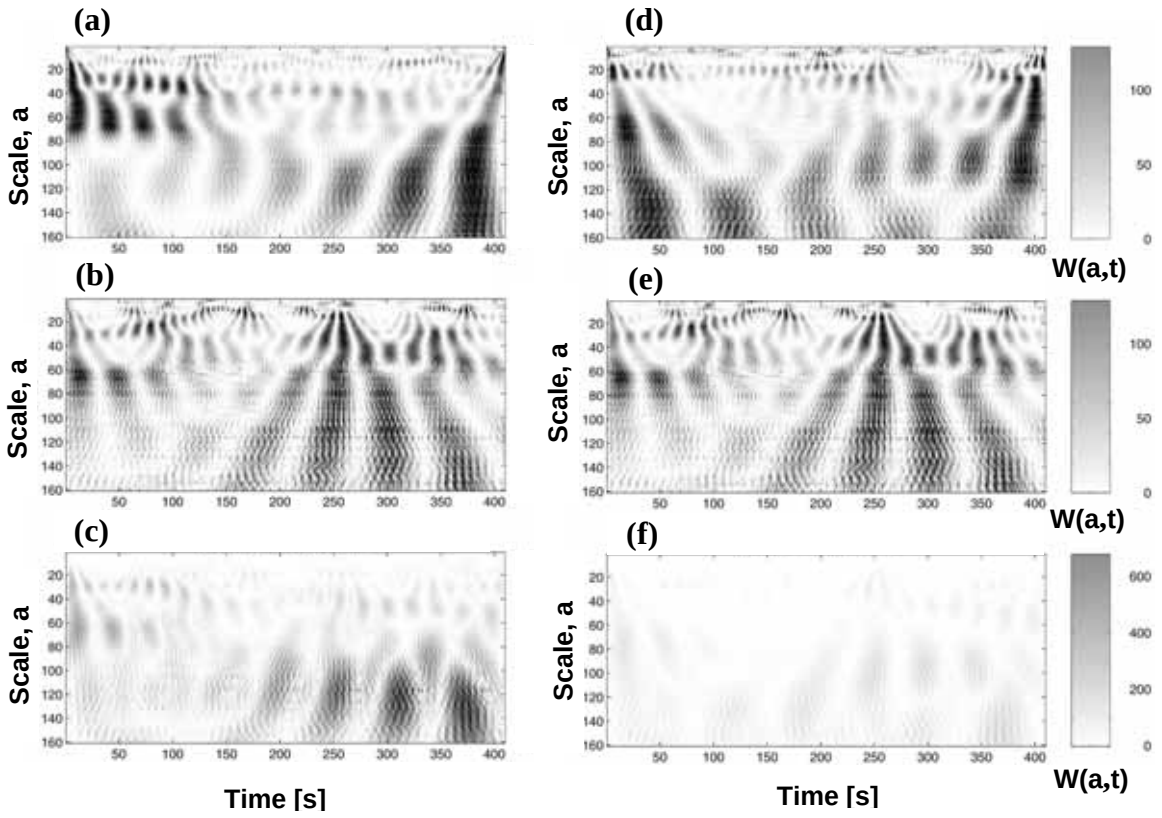

FIGURE 6.1. (a) Scalogram of upstream wind velocity 1; (b) scalogram of rooftop pressure; (c) coscalogam of these two correlated processes; (d) scalogram of upstream wind velocity 2; (e) scalogram of rooftop pressure; (f) coscalogram of these two uncorrelated processes (taken from Gurley & Kareem, 1999)

6.3 Wavelet-based Coherence Map

As the Morlet wavelet introduced in Chapter 4 is merely a localized form of the Fourier transform, it can intuitively be substituted into classical spectral measures to uncover time-varying frequency content, effectively windowing the Fourier analysis. For this reason, it is again the preferred wavelet in this application. The equivalence of traditional Fourier measures with those newly recast using Morlet wavelets was previously shown in Gurley & Kareem (1999) for quantities such as scalogram and coscalogram, analogs to

the auto-spectrum and cross-spectrum. Their abilities to capture marginal spectral characteristics and measures of signal energy were further validated in Chapter 5. In this chapter, the classical coherence definition is modified utilizing spectra defined locally by Morlet wavelets to yield a time-frequency coherence function. The traditional form of the coherence function can be retained as the ratio of the wavelet cross-spectrum to the product of the wavelet auto-spectra of the two signals *x(t)* and *y(t).* The wavelet coherence map is thus defined as

$$\left(c^{W}\left(a,t\right)\right)^{2} = \frac{\left|S_{xy}^{W}\left(a,t\right)\right|^{2}}{S_{xx}^{W}\left(a,t\right)S_{yy}^{W}\left(a,t\right)}, \tag{6.1}$$

where the localized power spectra discussed above are given by

$$S_{ij}^{W}\left(a,t\right) = \int_{T} W_{i}^{*}\left(a,t\right)W_{j}\left(a,t\right)d\tau \tag{6.2}$$

with the subscripts on the wavelet coefficients indicating their association with each signal.

The localized time integration window in Equation 6.2, $T = \left[t - \Delta T, t + \Delta T\right]$, is selected based on the time resolution desired in the resulting coherence map and essentially performs the same ensemble averaging operation, albeit localized in time, as traditional Fourier analysis to obtain an auto-spectrum or cross-spectrum of two signals. The map is bounded between 0 and 1 and provides a view of the localized correlation with respect to both time and frequency. Equivalence of this proposed time-frequency coherence map with its classical formulation is demonstrated in the following section.

It should be noted that discussions in Torrence & Compo (1998) highlight that an earlier coherence measure defined by Liu (1994), similar to that used by Shin et al. (1999), had limited physical meaning without the smoothing introduced here by T in Equation 6.2, and hint that averaging to some extent is necessary to provide a useful measure of coherence. The parameter T in Equation 6.2 addresses this concern, although, being somewhat arbitrary, it also presents the potential for a loss in time localization.

6.3.1 Comparison of Wavelet- and Fourier-based Coherence Estimates

The validity of the coherence map in Equations 6.1-6.2 is demonstrated by first applying the wavelet-based coherence to stationary signals. The standard Fourier-based coherence estimate is directly compared with the wavelet-based coherence by averaging out the time information in the wavelet coherence map, according to

$$\left(c^W(a)\right)^2 = \frac{1}{nt}\sum_{i=1}^{nt}\left(c(a,t_i)\right)^2 , \tag{6.3}$$

where nt is the number of discrete time steps resulting from the localized time window, T.

The signals being analyzed in this example are the upstream wave elevation and the resulting surge response of a tension leg offshore platform (TLP) 1:200 scale model, measured experimentally in a wind/wave tank facility and shown in Figure 6.2a,b. Sampled at 1 Hz, 4096 s of data is used in this analysis. This is a part of the larger data set investigated in Section 5.6. Standard Fourier coherence estimation and Equations 6.1-6.3 are applied to these signals with the results shown in Figure 6.2c. The coherence is well represented by both estimates, demonstrating the accuracy of the wavelet-based

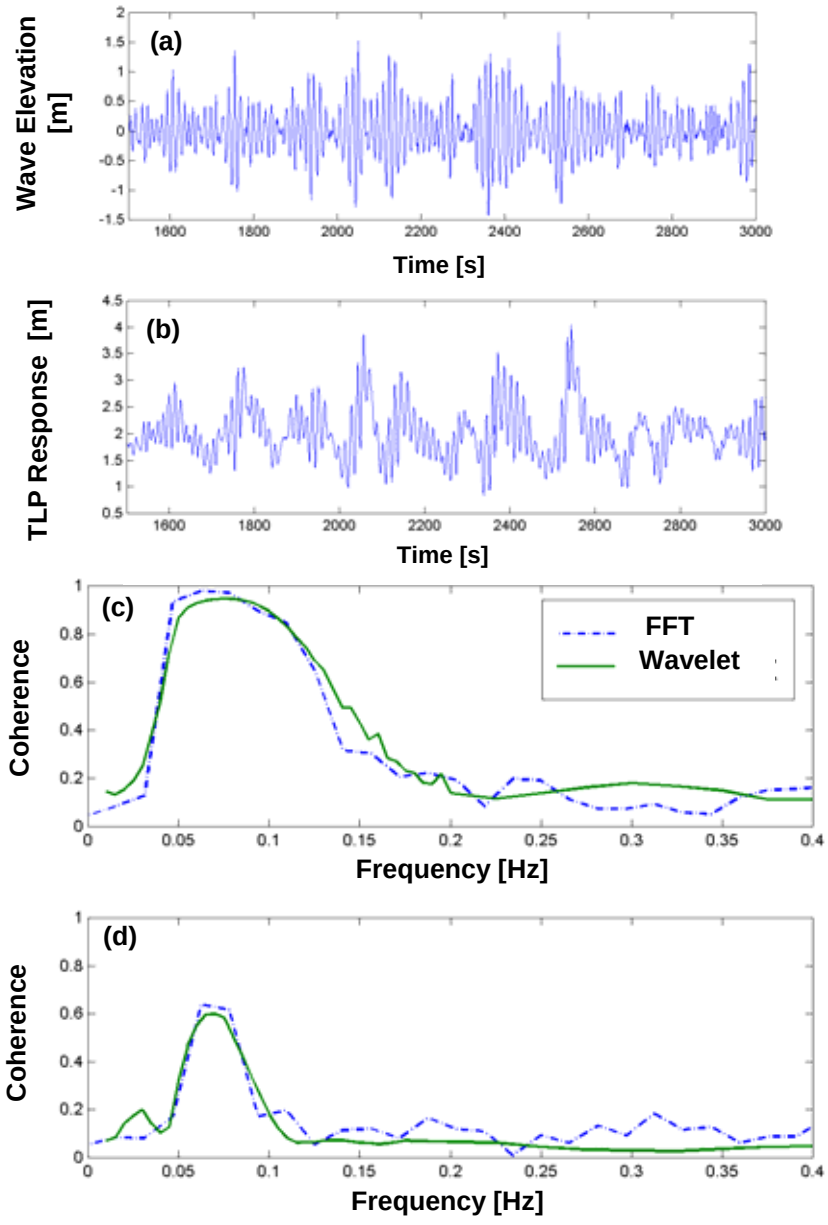

FIGURE 6.2. (a) Incoming wave surface elevation; (b) TLP surge response; (c) wavelet and FFT coherence estimates between wave elevation and TLP response; (d) wavelet and FFT coherence estimates between wave elevation and TLP response with incoherent nose added to each

coherence estimate with respect to both magnitude and frequency. A second example demonstrates that wavelet-based coherence can accurately estimate smaller levels of linear correlation. In this case, independent white noise vectors are added to the wave surface and TLP response time histories to reduce the level of correlation, and coherence estimates are again produced. Figure 6.2d shows the wavelet coherence representing the reduced correlation accurately.

6.3.2 Application of Wavelet-Coherence to Non-stationary Signals

The previous section demonstrated that wavelet-coherence viewed only with respect to frequency provides an effective coherence estimate. The advantage of wavelet-based coherence in identifying the time at which coherence between two signals occurs is now demonstrated by its application to velocity and pressure signals with known pockets of short duration correlation. Two independent Gaussian wind velocity signals ($v_1(t)$, $v_2(t)$) are simulated for 2048 s at 1 Hz. A pressure record is then created by combining independent white noise $\varepsilon(t)$ with the $v_2(t)$ wind record and a quadratic term

$$pr(t) = \varepsilon(t) + v_2(t) + G(\varepsilon(t)^2 + v_2(t)^2) \,. \tag{6.4}$$

For this example, G = 0.05. Two small segments of the pressure record, over the time interval *t'*, are then replaced with signals generated by

$$pr(t') = \varepsilon(t') + v_{1f}(t') + G(\varepsilon(t')^2 + v_{1f}(t')^2) \,, \tag{6.5}$$

where $v_{1f}(t')$ indicates $v_1(t')$ after band pass filtering is applied to correlate the pressure and the velocity record over selected frequency ranges. The use of Equation 6.5 produces a pair of signals, $pr(t)$ and $v_1(t)$, correlated only from 512 to 768 s between 0.0625 and 0.25 Hz and from 1536 to 1792 s between 0.19 and 0.37 Hz, and uncorrelated everywhere else.

The standard Fourier-based coherence between $v_2(t)$ and $pr(t)$ and between $v_1(t)$ and $pr(t)$ are displayed in Figure 6.3. Note that the intermittent coherence between $v_1(t)$ and $pr(t)$ cannot clearly be distinguished, suggesting that the signals are uncorrelated, whereas the relationship between $v_2(t)$ and $pr(t)$, as expected, appears fairly strong.

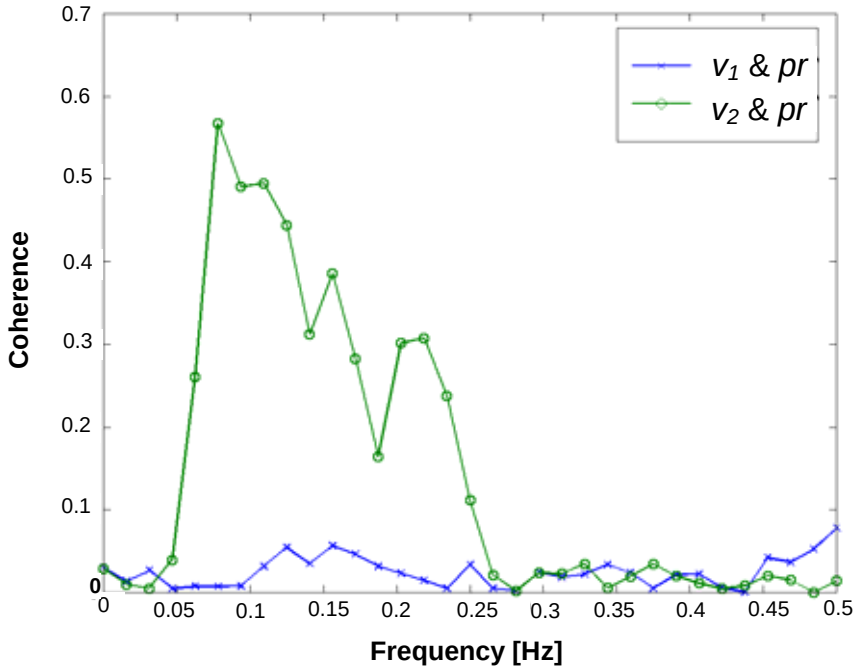

FIGURE 6.3. Coherence between $v_2(t)$ and $pr(t)$ and between $v_1(t)$ and $pr(t)$

Isometric and overhead views of the wavelet-coherence map between $v_1(t)$ and $pr(t)$, as generated by Equation 6.1, are shown in Figure 6.4. For this example, and those which follow, a value of $f_o = 5/(2\pi)$ was deemed sufficient to provide the necessary time and frequency resolutions, though a more precise frequency resolution (larger f_o) may be required in other cases, as discussed in more specifically in Chapter 7. A time integration window of T = [t - 64 s, t + 64 s] was applied. Pockets of strong correlation can then be identified in these displays that include the time and frequency regions of introduced correlation, approximately boxed. However, the coherence estimate also displays phantom correlation in regions where no correlation exists, particularly in the low frequency regions as emphasized by the semi-logarithmic plot in Figure 6.4. This noise is similar to that seen in Fourier-based spectral methods, where, due to a finite number of ensembles, variance errors are introduced. In the case of the wavelet coherence map, the localized time integration window T determines the number of ensembles used in the estimation of coherence in Equation 6.1. Increasing T can reduce the noise in the coherence estimate at the expense of temporal resolution.

6.4 Minimization of Spurious Coherence

Classically, the presence of variance in raw spectral estimates necessitates the use of averaging in order to obtain more reliable results. However, the transient information sought in a time-frequency analysis may be obscured through excessive averaging, especially in the low frequency regime, where spurious coherence seems most prevalent. A variable integration scheme is proposed in the following section to address this issue,

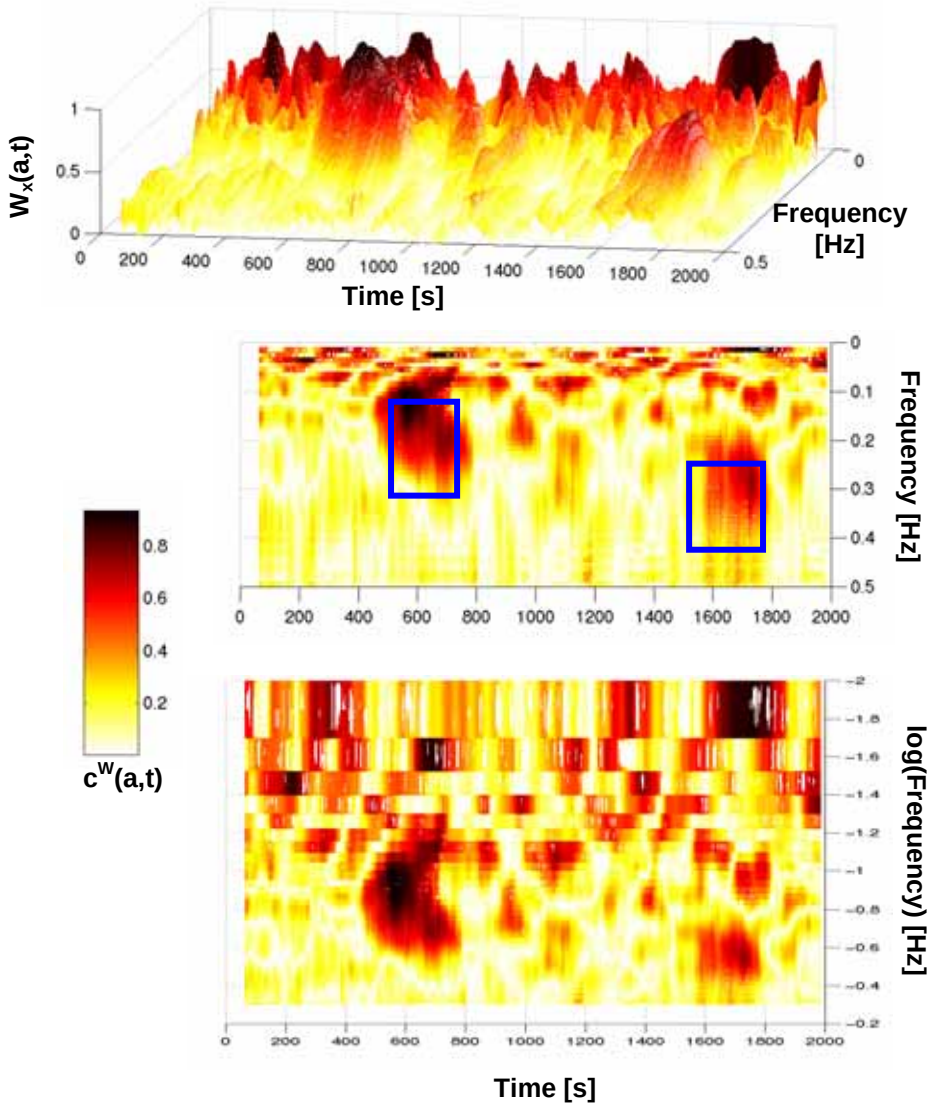

FIGURE 6.4. Wavelet coherence map between $v_1(t)$ and $pr(t)$, also shown as semi-logarithmic in frequency, emphasizing low frequency content

followed by alternative approaches designed to better preserve temporal resolution using simulated signals to build reference noise maps.

6.4.1 Multi-Resolution Integration Windows

In the initial formulation of the wavelet coherence, the localized time window is constant throughout the analysis. However, unlike its Fourier counterpart, the wavelet transform is multi-resolution, having scale-dependent time and frequency resolutions. Each wavelet coefficient, at given (frequency) scale a_i and time t_j, is the result of analyzing a local section of the time history windowed by the scaled Gaussian function of the Morlet wavelet. Thus, the signal's content Δt_i before that point in time and Δt_i after that point in time is used to estimate the wavelet coefficient $W(a_i,t_j)$, where Δt_i is dictated by a_i according to Equation 4.5. Note that the central frequency implicitly dictates this resolution and becomes one of the parameters influencing the extent of the spurious coherence in the wavelet coherence map. This is demonstrated in Figure 6.5 using the simulated velocity and pressure signals with known coherent pockets boxed in the figure. In this demonstration, a constant 64-second integration window was used to evaluate the coherence every 10 seconds to expedite calculations. The larger values of central frequency elongate the temporal windows of the scaled wavelets, reducing the averaging achievable in the analysis and leading to extensive spurious coherence. The spurious coherence diminishes for lower wavelet central frequencies as more averaging is achieved, but this also implies that the frequency resolution capabilities are lost, leading to a smearing of energy. A balance between the two extremes is achieved for $f_o=5/2\pi$ and thus this is why it is used as the baseline case in this discussion. The influence of central

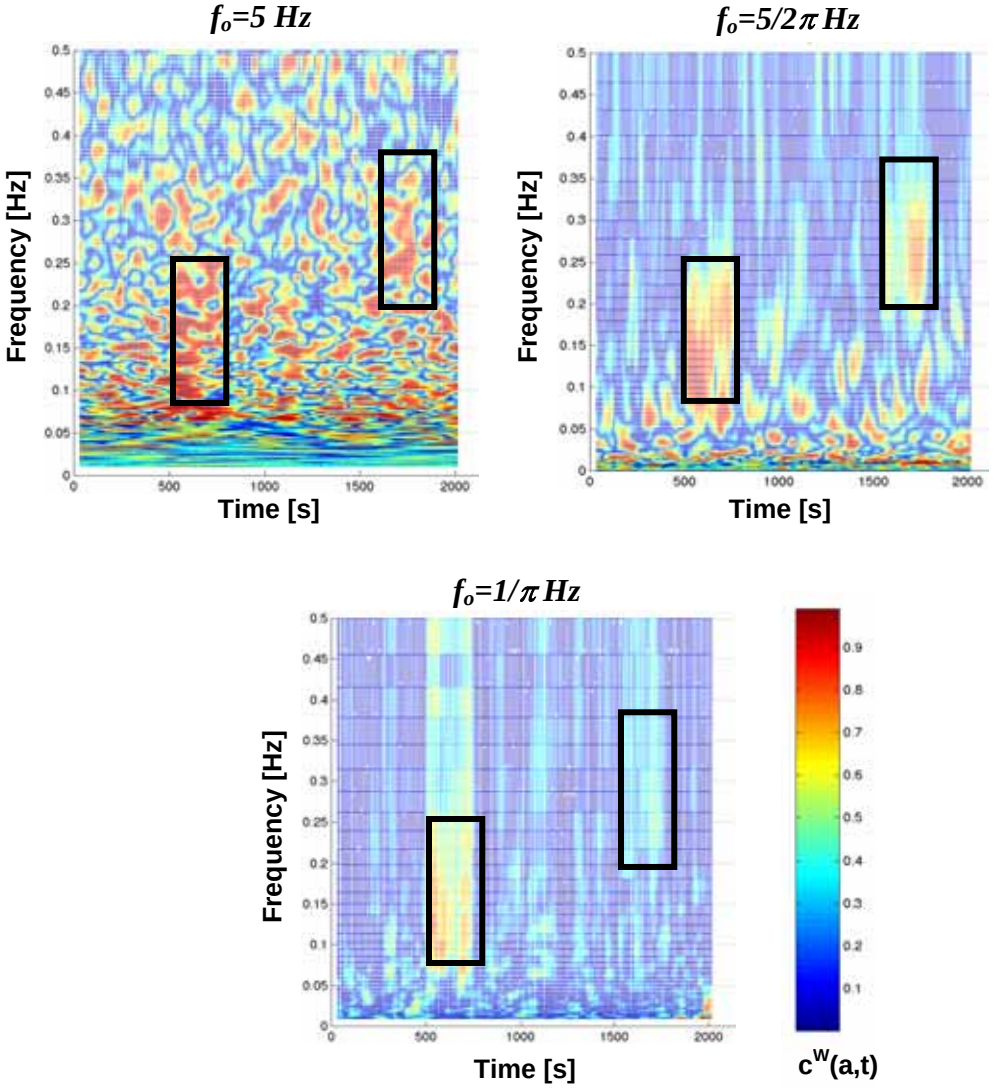

FIGURE 6.5. Influence of central frequency on the occurrence of spurious coherence in wavelet coherence map. Known coherent pockets between $v_1(t)$ and $pr(t)$ designated by boxes

frequency in the context of the developments in Chapter 4 should be kept in mind throughout the subsequent discussions.

For the analysis conducted in Section 6.3.2 and shown in Figure 6.4 (referred to herein as the baseline example), the choice of a constant window spanning a total of 128 s implies that at very low frequencies, as little as one unique local section of the time history is effectively being included in the estimate of the wavelet local spectrum in Equation 6.2. For $f_o = 5/2\pi$, at 0.01 Hz nearly all the wavelet coefficients in that 128 s time span are estimated from the same section of the time history, approximately 112 s long (Δt_i~56.27 s), and are thereby virtually non-unique. Thus their subsequent averaging does little to reduce the variance, as conceptualized by Figure 6.6a. The figure illustrates that at low frequencies there can be considerable overlap of the Morlet wavelet's Gaussian window within the analysis horizon *T*, yielding only three unique wavelet windows, shown in white. Conversely, at higher frequencies, the same *T* affords five unique wavelet windows. The ramifications parallel the estimation of power spectra from Fourier-transformed blocks of a time history. Consider a signal of finite duration from which five raw spectra can be generated only by heavily overlapping the blocks of the time history being Fourier transformed. These five spectra are highly dependent and thus only minimally reduce the variance when averaged. However, if the signal were long enough to estimate five raw spectra from non-overlapping segments of the signal, their averaged result would have far less variance, just as in the case of the higher frequencies in Figure 6.4, whose wavelet coefficients are estimated using windows with temporal duration of only a few seconds. The localized spectra in Equation 6.2 at these frequencies include markedly more wavelet coefficients generated from independent segments of the

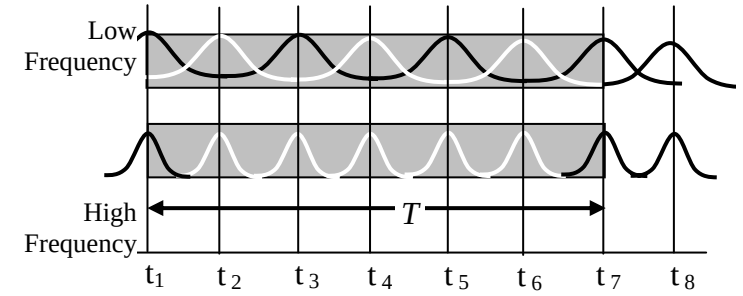

(a) FIXED INTEGRATION

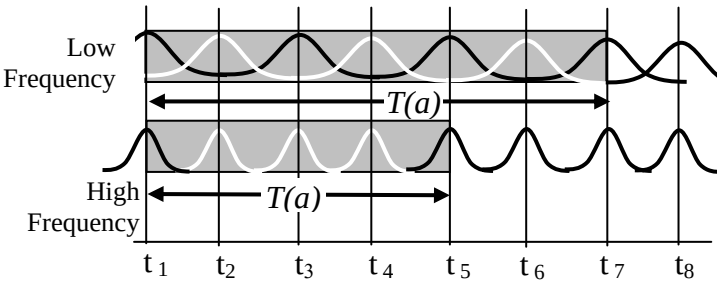

(b) VARIABLE INTEGRATION

FIGURE 6.6. Illustration of variable integration window concept

time history. Now the same f_o = 5/2π Morlet wavelet, at 0.5 Hz, produces a wavelet coefficient from only 2.24 s of data (Δt~1.12 s), affording over fifty coefficients from non-overlapping segments of the 128 s analysis window for averaging and sizeable reductions in variance. This explains why lower frequencies in the coherence map seem to be heavily plagued by spurious coherence, as emphasized when the coherence map is plotted as semi-logarithmic in frequency in Figure 6.4.

The use of a fixed integration window (FIW) in Equation 6.2 actually provides differential treatment to the high frequency components, in terms of the number of uniquely estimated wavelet coefficients included in the averaging process. Due to the multi-resolution character of the wavelet analysis, T in Equation 6.2 should be replaced

by *T(a)*, so that the integration in Equation 6.2 averages the same number of "ensembles" over all frequencies, as also conceptualized in Figure 6.6b, where at both high and low frequencies there are at least three unique wavelet windows, shown in white.

A scheme predicated upon variable integration windows (VIW) proceeds by defining the window of integration for each frequency as an integer multiple (β_T) of the temporal resolution of the analyzing wavelet at that scale, given as

$$T(a) \geq 2\beta_T \Delta t = \frac{2\beta_T a}{\sqrt{2}} = \frac{2\beta_T f_o}{f\sqrt{2}} \tag{6.6}$$

for the Morlet wavelet. Thus β_T would be chosen as a constant for the entire map, dependent on the number of desired averages in the coherence measure, and *T(a)* would vary, inversely proportional to the frequency being analyzed. The inequality in Equation 6.6 arises from the fact that the times at which the signal is sampled will not coincide with the effective initiation and termination of an arbitrary dilated wavelet, such that *T(a)* must be rounded to the nearest sampled point. This fact leads to the overlapping which may occur at lower frequencies, as visualized in Figure 6.6. Note that Equation 6.6 insures that there is a minimum of β_T independent time segments being windowed in the estimation of wavelet coefficients, but there certainly may be additional overlapping ensembles present, especially in the lower frequencies. As the number of independent ensembles makes the most significant contributions to variance reduction, it allows the simplest and most direct criteria for defining *T(a)*.

In Figure 6.7, the benefits of variable integration are evaluated by comparing the baseline case to three other cases: β_T = 10, 20 and 50. Note that in the baseline case, the fixed integration window yielded approximately β_T = 50 in the high frequencies while affording as little as β_T = 1 in the low frequencies, accounting for the prevalence of spurious coherence in this region. As shown in Figure 6.7, by averaging over a horizon long enough to permit a sufficient number of wavelet coefficients to be estimated from non-overlapping windowed sections of the time history, much of the low frequency spurious coherence is minimized. The higher frequencies still appear to be plagued in comparison to the baseline case, as expected, since the baseline essentially had β_T =50 in this region. Increasing the number of ensembles being averaged to β_T =20 and 50 yields further improvements in the higher frequencies, though the known pockets of coherence are now beginning to bleed temporally, a consequence of increasing the time frame for local averaging. This loss of temporal resolution in the coherence map is an unavoidable consequence of increasing the number of ensembles in the averaging process. However, the examples provided in Figure 6.7 illustrate that meaningless coherence can be attributed to the effective number of ensembles in the averaging process in Equation 6.2 and justifies the use of a variable time window for this integration, as defined by Equation 6.6.

Note that spectral averaging in general makes implicit assumptions of stationarity. The stationary assumption is rarely justified in the wavelet analysis, as the suspicion of evolutionary characteristics motivates the use of wavelet analysis in the first place. Still, by viewing the problem as one with locally stationary blocks, this localized averaging process can be reasonably justified. It is then left to the discretion of the user to determine

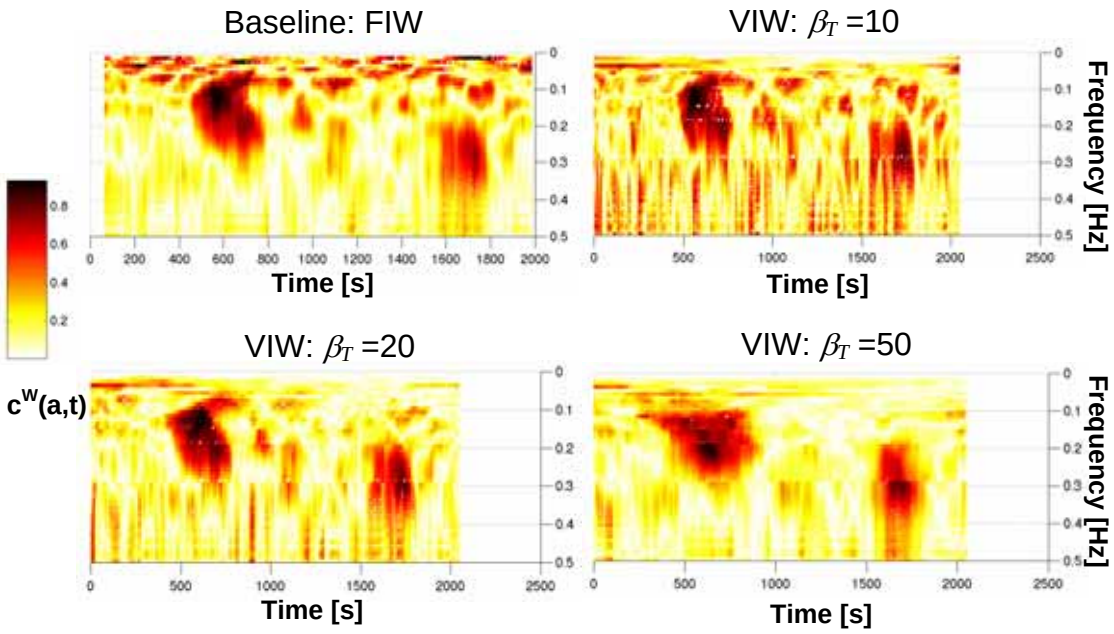

FIGURE 6.7. Examples of variance reduction by variable integration window

how transient the process is when specifying integration windows so that evolutionary behavior is not masked. The averaging operation provides a more reliable description of coherence as opposed to the raw coscalogram, providing a smoothed, yet biased estimate, however it becomes evident that there is a delicate balance between a sufficient integration window to minimize variance and one that is so long that it obscures relevant time-varying information. In cases where highly evolutionary characteristics are suspected, integration windows must be tightly localized, placing practical limits on the use of localized integration to diminish spurious coherence, motivating more sophisticated techniques to remove noise from the map, introduced below.

6.4.2 Ridge Extraction by Hard Thresholding

As wavelet analysis is used commonly for the study of evolutionary behavior with relatively short duration data, the possibility of significant amounts of averaging becomes increasingly difficult if not impossible, particularly if the signal contains transient information that would be completely obscured in the averaging process. An alternative approach is to separate the signal from the noise surrounding it. In the case of analyzing wavelets whose Fourier transforms are sharply focused near a fixed frequency value (e.g. Morlet wavelet), the maxima of the resulting wavelet transform reflect the locations where the energy of the signal concentrates, defining a curve in the time-frequency plane termed the ridge – quite useful in situations where frequency-modulated signals are imbedded in noise. Recall this concept was discussed more fully in Chapter 4 and has been repeatedly exploited thus far in Chapter 5 and will continue to be revisited in future chapters. Although noise is spread throughout the time-frequency plane, the contribution of the signal is much greater than the noise in the vicinity of the ridges, which can be extracted as discussed in Section 4.4.

However, in the coherence analysis presented here, the coherent pockets are intermittent and not suitable for extraction techniques geared for smooth, continuous ridges. Still, the theory of ridges implies that globally, as the truly coherent pockets will show stronger coherence than the surrounding noise, leading to larger coefficients. As a result, the truly coherent pockets may be separated by globally identifying the maximum coherence ($max[c^w]$) in the map and applying denoising schemes such as hard thresholding. This process is defined by

$$c^{W,hard}(a,t) = \begin{Bmatrix} 0 & if & c^{w}(a,t) < \lambda_T \max[c^{w}] \\ c^{w}(a,t) & if & c^{w}(a,t) \geq \lambda_T \max[c^{w}] \end{Bmatrix}. \quad (6.7)$$

This process roughly approximates a ridge identification procedure, effectively extracting the locations where the true coherence lies. Here λ_T is the assigned threshold factor, taking on a value between 0 and 1 to define the percentage of the maximum coherence deemed meaningful. The thresholding not only removes spurious coherence as the result of variance, but also removes the effects of the Gaussian windowing operation in the Morlet wavelet transform, which introduces a known enhancement of spectral bandwidth discussed previously in Chapter 4. Though lesser values of coherence surrounding a point in time and frequency are produced as a result of this window, the highest coherences will still manifest along these ridge points, which carry all the meaningful coherence information.

The thresholding operation in Equation 6.7 was applied to some of the cases considered in the previous section, as the combination of ridge extraction by hard thresholding and variable integration provides a simple means to extract meaningful coherence from the wavelet coherence map. For β_T=10, increasing the threshold factor to 0.75 approximately isolates both pockets of known coherence, as clearly shown when comparing the results from Figure 6.7 to the filtered results in Figure 6.8. However, by selecting too stringent a threshold (λ_T = 0.90, not shown), only a portion of the first pocket of coherence is retained, while the second is completely lost. When the number of ensembles is more sizeable, the threshold factor can be relaxed considerably, as β_T = 50, λ_T = 0.50 illustrates. Recall that this thresholding approach is merely another strategy to

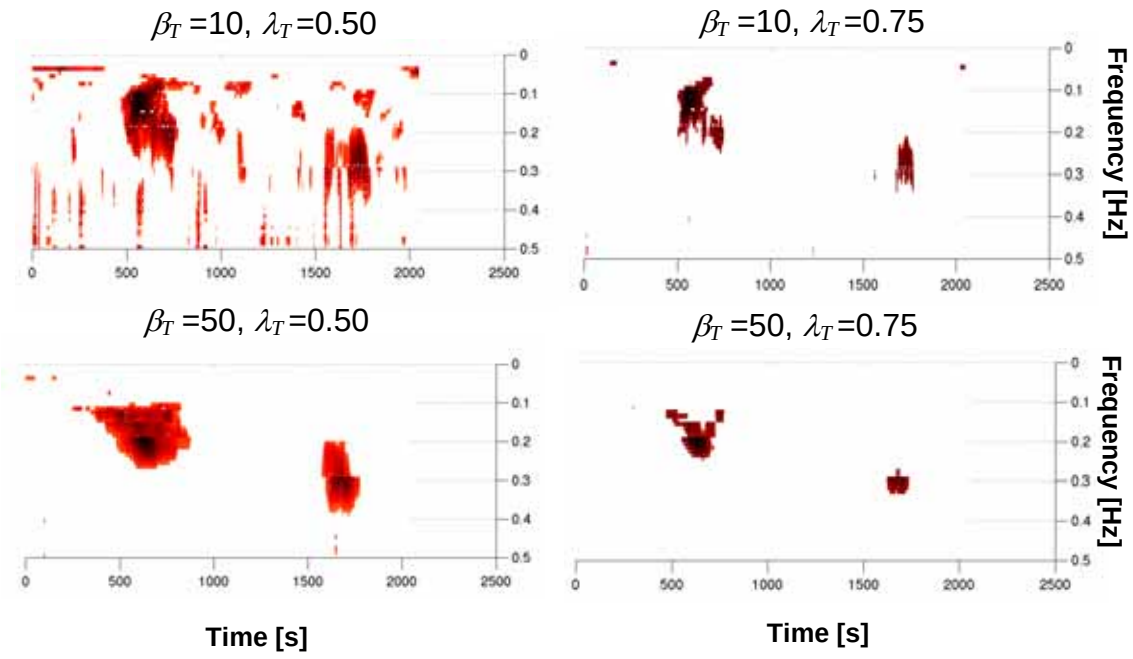

FIGURE 6.8. Examples of coarse ridge extraction by thresholding

separate true coherence from noise. As the noise is primarily the byproduct of variance, or a lack of averaging, in cases where variable integration has insured a large number of ensembles in the average (e.g. β_T =50), the noise has already been considerably alleviated (see Fig. 6.7). In such cases, the noise is less dominant, taking on lower amplitudes in comparison to the coherent ridges, thereby relaxing the necessary threshold value λ_T. Note again, that the bleeding of temporal information, particularly for the first pocket of known coherence, is an unavoidable consequence of increasing the number of ensembles in the averaging process. Thus far, Sections 6.4.1 and 6.4.2 have discussed two techniques for reducing the appearance of spurious wavelet coherence that, while simple, are quite subjective. The following sections discuss more sophisticated techniques that remove much of this subjectivity and provide an effective means to separate meaningful pockets of coherence without requiring the use of variable integration windows.

6.4.3 Filtered Wavelet Coherence Map Based on White Noise

Though the coarse ridge extraction by thresholding is a simple means to identify meaningful coherence, the insouciant use of hard thresholding based on global maxima may obscure meaningful coherence that is weaker than the dominant coherent components. Any coherence, real or noise-induced, falling below the threshold value is neglected. Recognizing that the spurious coherence is the result of inherent randomness, one alternative would be to conduct repeated Monte Carlo simulations of white or colored random noise in order to determine the likely levels of variance in a given wavelet spectral measure. By this approach, peaks in a wavelet scalogram, for example, are deemed statistically significant if they surpass a given confidence level defined by the random noise simulations. This type of approach was detailed in Torrence & Compo (1998) for statistical significance of wavelet power spectra. J. Huang et al. (1998) applied a similar technique to define a reference map for multi-resolution Fourier cospectra. This approach is extended herein to wavelet coherence.

This process initiates with the generation of a reference coherence noise map through repeated simulation of independent, zero mean, Gaussian white noise processes at the same sampling rate and of the same duration as the original signals. The wavelet coherence of the two simulated white noise signals is delineated by $\left(c_i^{wn}(a,t)\right)^2$ and is repeatedly calculated for *N* independently simulated white noise signal pairs, according to Equations 6.1 and 6.2. These simulated coherence maps, which should represent spurious coherence associated with random signals, are then averaged to produce a mean noise reference map

$$\left(c_{mn}(a,t)\right)^2 = \frac{1}{N}\sum_{i=1}^{N}\left(c_i^{wn}\ (a,t)\right)^2 \tag{6.8}$$

with standard deviation $c_{st}(a,t)$. The threshold value of a statistically meaningful correlation can them be defined as the sum of this mean and the standard deviation weighted by a factor *g*

$$c_{th}(a,t) = c_{mn}(a,t) + g\left(c_{st}(a,t)\right). \tag{6.9}$$

The noise factor *g*, which need not be an integer value, must then be selected based on the desired likelihood of noise exceeding the threshold, providing a quantitative measure of statistically meaningful correlation, where the distribution of the random noise map is taken as Gaussian, consistent with the simulated noise. As a result, selecting $g = 1$ implies a probability of suppressing 68.3% of the spurious coherence, $g = 2$ sets a more stringent level at 95.4%, and $g = 3$ raises that level to 99.7%. With the reference map $c_{th}(a,t)$ now in place, the actual wavelet coherence of *x(t)* and *y(t)* can be generated by Equation 6.1 and then subjected to a thresholding scheme, yielding a *filtered coherence map* according to

$$c_F^W(a,t) = \begin{Bmatrix} 0 & if \quad c^W(a,t) < c_{th}(a,t) \\ c^W(a,t) & if \quad c^W(a,t) > c_{th}(a,t) \end{Bmatrix}. \tag{6.10}$$

The noise factor *g* in Equation 6.9 must be selected judiciously, as a choice that is too large may negate statistically meaningful, albeit reduced, levels of correlation, as observed in the thresholding procedure in the previous section. While the choice of *g* may be rather arbitrarily defined, e.g. Hangan et al. (2001), a less subjective choice for *g* may

be determined based on the probability distribution of the noise coherence maps, as recommended here.

To demonstrate the efficacy of this approach, N = 100 pairs of statistically independent, zero mean, Gaussian white noise signals of the same length and sampling rate of v_1 and *pr* are simulated and the threshold of statistically meaningful correlation is determined by Equation 6.9 for g = 1, 2 and 3. The unfiltered wavelet coherence map of v_1 and *pr* and the filtered maps for the varying levels of g are shown in Figure 6.9. By progressively increasing the factor g, a more stringent thresholding condition is achieved. The latter two figures clearly demonstrate the minimization of spurious coherence in the low frequency range by virtue of this approach. Note that these results were achieved without the use of any variable integration schemes but merely assuming ΔT = 64 s, leading to the strong coherence in the low frequency range. By assuming a uniformly distributed noise field and then performing the wavelet coherence operation, the spurious coherence that results from implicit biases in the transform are recreated in the reference thresholds and can be removed through the aforementioned thresholding operations through minimal computational effort. For g = 3 the two known coherent pockets are identified with some scattered, minor spurious coherent pockets remaining.

6.4.4 Filtered Wavelet Coherence Map Based on Signal Characteristics

The technique in the preceding section is more generalized assuming that a threshold level representative of the spurious coherence can be generated using generic white noise signals. However, this approach does not incorporate any specific information on the spectral or probabilistic structure of the analyzed signals, perhaps leading to those

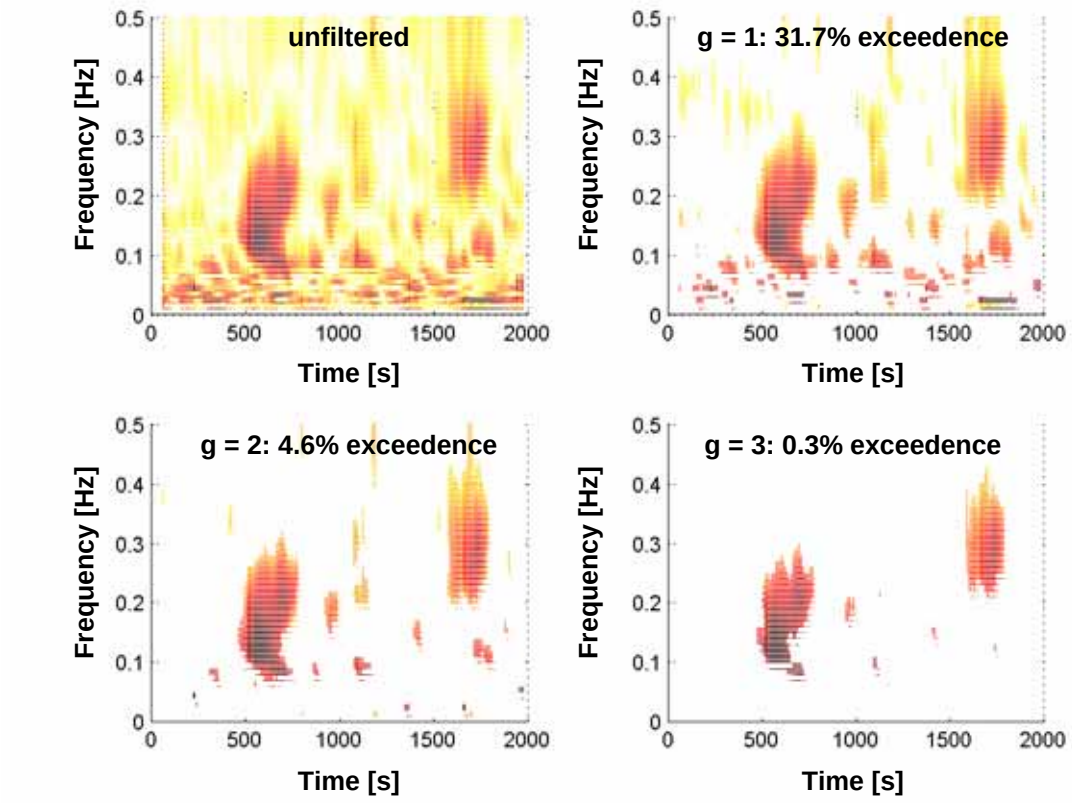

FIGURE 6.9. Filtered wavelet coherence map between $v_1(t)$ and $pr(t)$ with g selected for varying noise exceedence levels, based on white noise

residual trace coherent patches in Figure 6.9. As a result, a more sophisticated tool was proposed by Dunyak et al. (1997) through a method to quantify the statistical relevance of wavelet coefficients when detecting coherent wind gusts. These sustained gusts are delineated from short incoherent bursts by establishing a reference distribution of wavelet coefficients from simulated Gaussian signals with no sustained gusts. This notion can be extended for the purposes of wavelet coherence analysis by employing a "smart" thresholding scheme that exploits both the spectral and probabilistic information from the

signals being analyzed to generate a map describing the expected noise threshold (Gurley et al., 2003).

In this case, the expected noise map associated with the wavelet coherence for a given pair of signals, *x(t)* and *y(t)*, is developed by first generating multiple simulations of the second signal, denoted $y_s(t)$. These simulated signals are independent of each other and *x(t)* and are statistically identical to the original signal *y(t)* in both the power spectral density and probability density function, through the use of a recently developed non-Gaussian simulation algorithm (Gurley & Kareem, 1997a). The wavelet coherence between *x(t)* and each of the simulated versions of the second signal ($y_s(t)$) is calculated using Equation 6.1. The resulting wavelet coherence, denoted $\left(c_i^{nc}(a,t)\right)^2$, takes the place of $\left(c_i^{wn}(a,t)\right)^2$ in Equation 6.8. The mean noise reference map is then calculated by this modified version of Equation 6.8 and the thresholding operations in Equations 6.9 and 6.10 are repeated using this "smarter" reference threshold incorporating the spectral and probabilistic structure of the signals.

The non-Gaussian probability distribution of the random noise map in this case must be approximated by considering higher-order statistics collected from the multiple simulated noise maps, in addition to their mean and standard deviation. As the extreme regions of the established distribution are used to determine the threshold, the probability model used must reliably reflect the actual distribution of noise. An extreme value-type distribution that does not explicitly include any information on the higher-order statistics is disregarded in favor of more advanced four parameter models. A modified Hermite polynomial-based model and a maximum entropy-based model are used in Gurley et al.

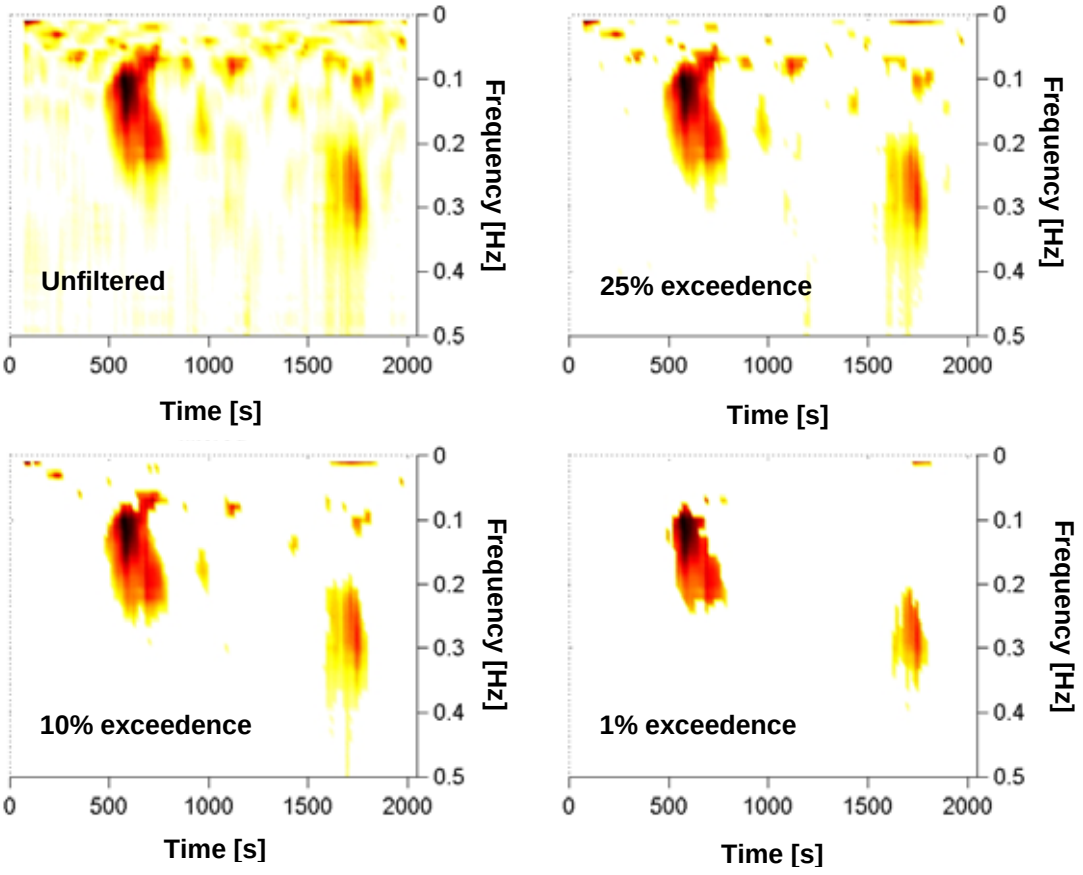

FIGURE 6.10. Filtered wavelet coherence map between $v_1(t)$ and $pr(t)$ with g selected for varying noise exceedence levels, based on signal characteristics

(2003). Both of these have been shown to be very effective in representing the tail region of non-Gaussian processes (Gurley & Kareem, 1997b) and produced almost identical results for the examples used in this chapter. The tail region of the resulting PDF represents the probability of noise exceeding the selected threshold that demarcates correlation in the wavelet coherence map.

To illustrate the proper selection of the factor g, in light of this modified thresholding scheme, as well as the robustness of this approach, a filtered wavelet coherence map is generated using $N = 100$ for the baseline analysis of the velocity and

pressure signals, $v_1(t)$ and $pr(t)$, discussed in Section 6.3.2. Note that this baseline case also does not exploit the use of the variable integration windows (see Section 6.4.1) and thus provides significant low frequency noise, just as the example in Section 6.4.3. As Figure 6.10 illustrates, the performance of the unfiltered map is greatly enhanced as the noise exceedence criterion is made more stringent. At the 1% exceedence level, both regions of known coherence are completely isolated, even in the low frequency range, indicating that the technique can remove spurious coherence that results from variance, in the low frequency regime. Note that the trace pockets of spurious coherence that remained in Figure 6.9 using a very strict thresholding condition of $g = 3$ were mitigated fully by this "smarter" thresholding scheme thanks to the incorporation of the probabilistic and spectral features of the signals themselves.

To further illustrate the application of the filtered wavelet coherence map, measured full-scale incident wind velocity fluctuations and their corresponding pressure variation over a building surface are analyzed. Note the strong low frequency correlation evident in the time histories of velocity and pressure shown in Figure 6.11a,b. The filtered wavelet coherence map is generated using a threshold reference map based on 500 simulated realizations of the data. Figure 6.11c-f shows the resulting filtered wavelet coherence map at several levels of the noise factor g. Extraneous noise again is removed as g increases, leaving a clearer portrait of the pockets of strong correlation. Though relatively intensive, the application of these filtered wavelet coherence estimates to wind data may be useful for identifying intermittent variations in the relationship between the velocity and pressure introduced by a change in wind direction or due to the evolution of a flow structure under the separation zone. Such maps can enhance the understanding of

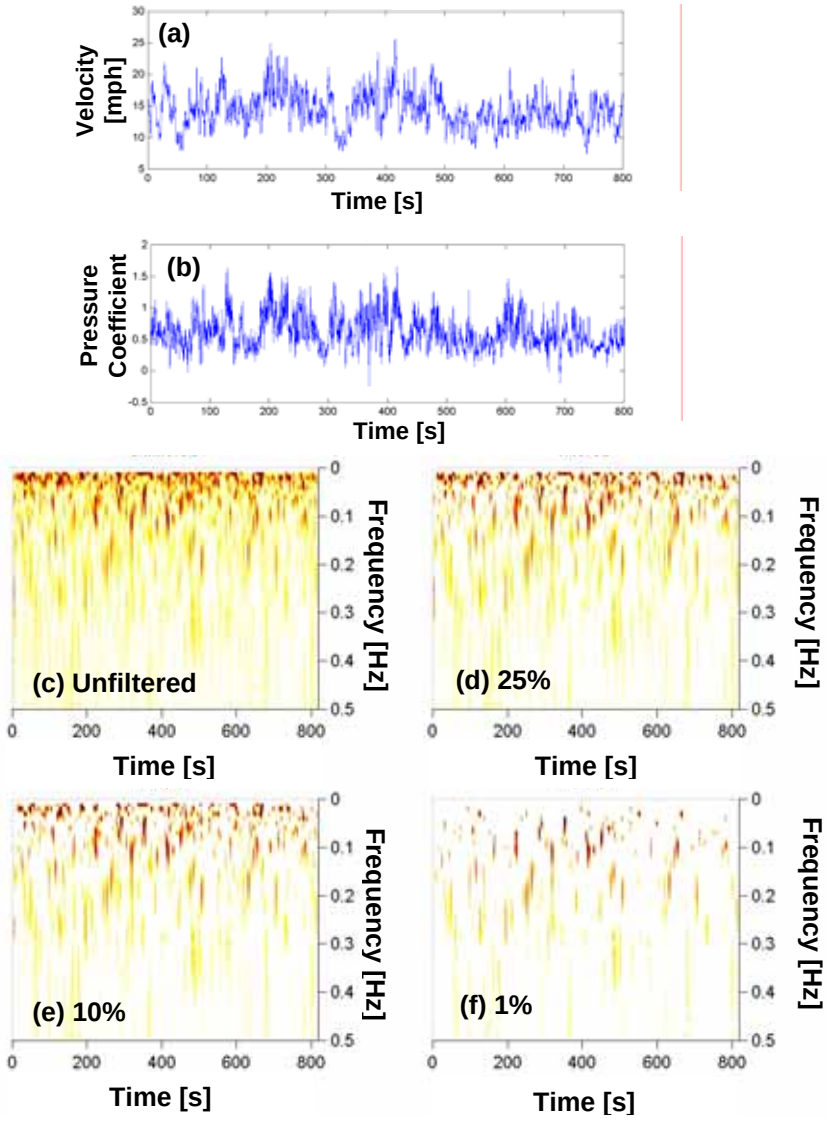

FIGURE 6.11. (a) Measured wind velocity; (b) measured wind pressure; (c) unfiltered wavelet coherence map; filtered wavelet coherence map with *g* selected for varying levels of noise exceedence: (d) 25% exceedence; (e) 10% exceedence; (f) 1% exceedence

complex wind-structure interactions and open new avenues for data analysis, modeling, and simulation.

6.5 Scale/Frequency-averaged Wavelet Coherence Map

Traditionally, coherence is displayed as a function of frequency only, averaged over the entire time duration, as shown previously in Figure 6.3. As a result of the dual character of wavelet transforms, the resulting coherence maps may be manipulated in order to view coherence with respect to time. The wavelet coherence between two signals and those between the first signal and simulated versions of the second signal are each averaged over the scale component. In doing so, a display of the scale-averaged coherence, $\bar{c}(t)$, mean noise reference coherence, $\bar{c}_{mn}(t)$, and threshold coherence, $\bar{c}_{th}(t)$, between the two signals can be generated with respect to time rather than frequency. Such an interpretation for the simulated velocity and pressure, $v_1(t)$ and $pr(t)$, is displayed in Figure 6.12a. The intermittent correlated regions clearly stand out as those surpassing the noise threshold, determined as a percent exceedence in the Hermite polynomial-based probability distribution model derived from the first four moments of the noise coherence maps as shown in Figure 6.12b.

6.6 Conclusions

In this chapter, wavelet decomposition was used to produce a time-frequency display of the coherence between signals intermittently correlated. Unfortunately, raw spectral estimates used in the definition of coherence were inherently laden with statistical noise.

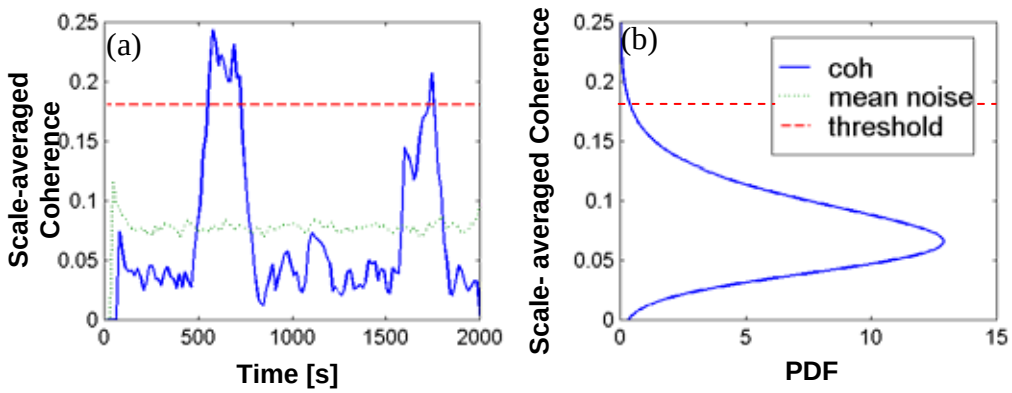

FIGURE 6.12. (a) Scale-averaged coherence along with mean coherence and noise threshold; (b) Hermite polynomial-based PDF model of reference noise maps

The classical approach for reduction of variance is to perform ensemble averaging by using localized time integration. In this case, the introduction of a variable integration window predicated on the multi-resolution character of wavelets highlighted that the lack of ensemble averaging results in much of the observed spurious coherence. Insuring sufficient ensembles in the average reduced the spurious coherence, though the loss of temporal resolution was a limiting factor. As a result, a three-tiered thresholding approach was introduced to isolate meaningful coherence. Hard thresholding, when coupled with sufficient ensembles in the variable integration scheme, was shown to enhance performance. However, to preserve evolutionary characteristics while removing significant noise, more sophisticated approaches were required which do not involve extensive averaging and VIW. The use of reference maps to filter the wavelet coherence and distinguish meaningful coherence from bi-products of the transform was shown to be quite effective in isolating known coherent pockets. This was first achieved by simply using repeated simulations of white noise processes, which provided quite reasonable

results that could be further enhanced by the third tier: a “smart” thresholding simulation scheme. In both approaches, the noise was filtered from the display map by comparison with a threshold describing the likely noise level. In the latter approach, this threshold was created by averaging a series of reference correlation maps between one signal and uncorrelated simulations of the second signal. Examples demonstrated that this technique was capable of identifying first-order correlation and effectively reducing the presence of noise in the correlation displays for both simulated and measured data. Though relatively intensive, these approaches facilitated the removal of significant levels of all of the various contributing noise sources.

Unfortunately, even with such refinements, the wavelet fails to reveal the instantaneous higher-order correlations that may exist in the transient spikes of fluctuating pressures. On the other hand, while Fourier-based higher-order spectral measures such as bicoherence can capture higher-order correlations, they have difficulty detecting such intermittent nonlinear interactions. The same can be said for the case of high amplitude, nonlinear extreme waves, whose first- and second-order components are phase coupled over relatively short intervals (Powers et al., 1997). This motivated the need for wavelet-based measures such as bicoherence to study nonstationary and nonlinear characteristics of random waves and the resulting response of floating offshore platforms, as well as prompting their consideration in Gurley et al. (2003) for higher-order intermittent correlation analysis of wind velocity and fluctuating pressures. In this latter study, it is shown that this analysis framework can also be extended to a higher-order wavelet bicoherence measure to capture intermittent second-order correlation. In total, when combined with the wavelet capabilities demonstrated in Chapter 5, the

wavelet correlation detection analysis schemes presented here offer immediate applications where the determination of intermittent correlation between linear and even nonlinear processes is required, e.g. bluff body aerodynamics in turbulent flows, wave-structure interactions in nonlinear random seas, and the nonlinear and non-stationary seismic response of structures. The next chapter will extend these wavelet frameworks to the identification of frequency and damping in Civil Engineering structures.

CHAPTER 7

WAVELET SYSTEM IDENTIFICATION III:

ANALOGS TO HILBERT SPECTRAL ANALYSIS

7.1 Introduction

Recently, the merits of the Hilbert transform with Empirical Mode Decomposition (EMD), or Hilbert Spectral Analysis (HSA), have been explored for time-frequency analysis by a number of studies. The use of this approach has been advocated widely by illustrating its superior performance in comparison to the continuous wavelet transform through a number of nonlinear and nonstationary examples. Although HSA itself provides a new and useful tool for time-frequency analysis, at times, its comparisons with wavelet transforms may be misleading and cast significant doubt on the wavelet's ability to provide satisfactory time-frequency analysis. This chapter shall revisit many of the examples used to establish the Hilbert spectral analysis within the wavelet analysis framework overviewed in Chapter 4 to offer a different perspective to these commentaries, illustrating cases where the two approaches perform comparably and highlighting situations where one is truly superior to the other. It is demonstrated that the two approaches provide comparable evidence of nonlinear and nonstationary behavior for

a number of classical examples, though this evidence is presented in distinctly different manners with Hilbert spectral analysis relying solely on instantaneous frequency and the wavelet using information from both this measure and the instantaneous bandwidth. The intent of this chapter is not to advocate the use of one over the other, but rather to objectively assess their efficacy and clarify some of the misconceptions surrounding these applications.

7.2 Theory of Hilbert Spectral Analysis

As discussed in Chapter 3, the Hilbert transform cannot separate multiple frequency components at any given point in time. Therefore, the application of this transform to multi-component signals requires pre-processing of the data by bandpass filtering or other appropriate methods to separate the various components (Lee & Park, 1994). Huang et al. (1998) introduced the concept of Empirical Mode Decomposition to accomplish this decomposition using empirical bases termed Intrinsic Mode Functions (IMFs), permitting the application of the HT. These IMFs are defined so as to insure that they have well-behaved Hilbert Transforms. These conditions are based on the fact that the instantaneous frequency is accurately defined by restricting a function to be symmetric with respect to the local zero mean level and by requiring that, within a given time series, the number of zero crossings and extrema must be equal or at most differ by one. This latter condition is established to insure that the IMF is monocomponent in nature. The term monocomponent is somewhat ill defined, as discussed in Section 3.7.5; therefore, Huang et al. (1998) had adopted a narrowband condition, based on the traditional characteristics of a stationary, narrowband Gaussian process.

While the full details of EMD can be found in Huang et al. (1998), the procedure can be summarized as follows, retaining here the notation used in that study. The process initiates with identification of the local extrema. These extrema are then used in conjunction with a cubic spline fit to construct an upper and lower envelope for the signal. The average of the upper and lower envelopes, as a function of time, is defined as the envelope mean, which may not correspond to the local signal mean. The difference between the signal and envelope mean is defined as the first component, h_1.

To eliminate riding waves and make the wave profiles more symmetric, this first component h_1 is treated as the data, and the process of fitting extrema and determining their mean is repeated in the so-called sifting process such that

$$h_{1k} = h_{1(k-1)} - m_{1k} . \tag{7.1}$$

Thus, in the k^{th} iteration, the previous component's extrema are fit and the mean is again removed. This process of sifting is repeated until the two conditions placed on a proper IMF are satisfied. Then the resulting sifted data is treated as the first IMF component, $c_1=h_{1k}$. This component will contain the finest scale. This finest scale represented by the first IMF is then removed from the data, leaving the residue,

$$r_1=x(t)-c_1 \tag{7.2}$$

and the residue r_1 is now treated as the data and the entire sifting process is repeated to obtain the second IMF, c_2, and so on to obtain all remaining IMFs such that

$$r_n = r_{n-1} - c_n . \tag{7.3}$$

The process will terminate when r_n or c_n become very small, or r_n is essentially monotonic. The subsequent IMFs obtained in this manner will progressively capture the coarser scales remaining in the signal. The signal can then be reconstructed by the superposition of these N IMFs according to

$$x(t) = \sum_{i=1}^{N} c_i + r_N \tag{7.4}$$

It should be noted that the determination of appropriate IMFs is predicated on the restrictions levied by the Hilbert Transform to provide an accurate instantaneous frequency, requiring the IMFs to be symmetric with respect to the local zero mean and have the same number of zero crossings and extrema. If the IMFs generated in this process meet these conditions, then the monotonic signal conditions surrounding the HT should be satisfied and the HT can be applied to each IMF to obtain an estimate of the IF with time. Constructed in this fashion, the IMFs are entirely empirical, and a given IMF may even contain two distinct frequency components, though at each point in time, the IMF is entirely monocomponent. Thus, the decomposition is different from Fourier transforms, where each component is related to a given frequency for its entire duration. In this decomposition, the data are expanded in a basis derived from the data itself.

As Huang et al. (1998) reiterates, an IMF on its own has little meaning and the true physical meaning can only be garnered from the complete Hilbert spectrum. This Hilbert spectrum (HS) is generated by converting each IMF into an analytic signal by Equation 3.23. The resulting amplitude of the analytic signal for each IMF is plotted as a dual function of instantaneous frequency, as determined by Equation 3.27, and time. The result is often viewed in two dimensions by studying the contours of the HS in the time-

frequency plane. This total process employing EMD and the HT is termed the Hilbert Spectral Analysis. The fact that the performance of wavelet transforms are heavily dependent upon the parent wavelet chosen was a motivating factor for developing the HSA, as the IMFs serving as basis functions are derived from the data itself and thus maintains physical resemblance.

7.3 Preliminaries

It should be noted that the ability of this technique to characterize the instantaneous frequencies within the data rests upon two critical elements: first upon the ability of EMD to separate the various components within the signal, and secondly, upon the ability of the Hilbert Transform to truly yield the quadrature component of the signal, dictating the accuracy with which the instantaneous frequency is identified. As will be discussed throughout this chapter, limitations in either one of these areas can affect the performance of Hilbert Spectral Analysis. Before discussing these and other issues by example, a few additional preliminary discussion points must be established.

7.3.1 Resolutions of Hilbert Spectral Analysis

The accuracy of IF estimation is dependent upon the resolutions of the time-frequency transform. The resolutions associated with the Morlet wavelet transform were discussed in considerable detail in Chapter 4. On the other hand, the resolutions of the Hilbert Transform are difficult to clearly quantify. The transform's temporal localization is verifiable, as the signal is being convolved with *1/t* in Equation 3.24. As a consequence of the Heisenberg Uncertainty Principle, the good localization in the time domain implies

poor frequency resolution, necessitating the incorporation of bandpass filtering, or in this case EMD, to insure modal separation. As a result, the inherent accuracy of these pre-processing tools indirectly dictates the frequency resolution of HSA. Therefore, the frequency resolution of HSA is based upon EMD's frequency resolution, essentially the narrowband condition on the maxima and zero crossings. The implications of this will be discussed in subsequent examples.

7.3.2 End Effects in Hilbert Spectral Analysis

Just as with wavelet transforms, the implementation of numerical schemes using Fourier transforms can introduce end effects. It was shown in Chapter 4 that these end effects are attributed to this but more importantly to an additional source in wavelet transforms. Huang et al. (1998) had also observed end effects, attributed to the spline fitting in the EMD procedure and due to the fact that the Hilbert Transform was implemented via Fourier Transforms. The authors remedied this using characteristic waves to extend the data and reduce discontinuities at the ends. This can be likened to the reflective padding scheme presented for wavelets in Chapter 4.

7.3.3 Introduction of Instantaneous Bandwidth

While the notion of instantaneous frequency has been generally accepted in the literature as the average of the frequencies at each point in time (Priestley, 1988), the discussion has not fully extended to consider the instantaneous bandwidth or spread of frequencies contributing to this mean. In recent years, a few definitions of instantaneous bandwidth have surfaced within the literature, though these discussions have not fully demonstrated

the utility of this measure. However as the examples in this chapter will later show, in the case of wavelet analysis in nonlinear systems, the spread about the instantaneous frequency is equally as important as the mean frequency itself.

As discussed in Cohen & Lee (1990), the squared bandwidth can be classically defined as

$$B^2 = \int_{-\infty}^{\infty} \left(\omega - \langle\omega\rangle\right)^2 \left|S(\omega)\right|^2 d\omega \tag{7.5}$$

where $S(\omega)$ is the Fourier transform of some arbitrary signal $s(t)$ and $<\omega>$ is the mean frequency defined by

$$\langle\omega\rangle = \int_{-\infty}^{\infty} \omega \left|S(\omega)\right|^2 d\omega \,. \tag{7.6}$$

As discussed in Jones & Boashash (1990), these spectral measures in Equations 7.5 and 7.6 can similarly be normalized by the area under the power spectrum. Regardless, this bandwidth can then be related to the amplitude and phase of the signal by

$$B^2 = \int_{-\infty}^{\infty} A'^2(t)dt + \int_{-\infty}^{\infty} \left(\phi'(t) - \langle\omega\rangle\right)^2 A^2(t)dt \tag{7.7}$$

where the first term is independent of phase and the second defines the deviation of the instantaneous frequency from the mean frequency of the signal. What this relation implies is that contributions to the signal bandwidth arise from two sources, the

amplitude variations (first term) and frequency variations (second term), i.e. from AM and FM sources.

Replacing $S(\omega)$ with a time-frequency energy distribution (e.g. Wavelet or Short Time Fourier Transform), changes Equation 7.6 into an expression for instantaneous frequency or mean frequency of an instantaneous power spectrum. Similarly Equation 7.7 becomes a measure of instantaneous bandwidth or the deviation from the instantaneous spectral mean.

Cohen & Lee (1990) later show that an instantaneous bandwidth measure can be equivalently obtained from the analytic signal itself. Consider again the analytic signal introduced in Equation 3.25. The amplitude term $A_Z(t)$ can be viewed as an envelope function, and provided that the this envelope varies more slowly than the phase, as discussed previously in the theory of asymptotic signals in Section 3.7.2, the instantaneous frequency can be identified from the derivative of the phase. According to Cohen & Lee (1990), the instantaneous bandwidth can then be obtained from the derivative of the analytic signal's envelope:

$$B_i(t) = \left(\frac{A'_Z(t)}{A_Z(t)} \right)^2 . \tag{7.8}$$

Based on this definition, the concepts of instantaneous frequency and bandwidth make sense only for signals that are locally narrowband (Ristic & Boashash, 1996). However, Boashash (1992a) has been critical of this definition, as it focuses entirely on the amplitude modulations and implies that if no amplitude modulation is present, i.e. $A_z(t)$ is

constant, then the signal would have zero bandwidth and only one frequency present. These intuitive difficulties have presented concerns for this definition, though in the case of amplitude modulated signals, it has been shown by Cohen & Lee (1989) that this definition produces the same value of instantaneous frequency as the classical definition.

Despite this attractive theoretical framework, the resulting instantaneous bandwidth measures are not always physically meaningful. For example, Jones & Boashash (1990) concluded that the Wigner-Ville and Choi-Williams distributions could produce negative spectral bandwidths due to the inherent negativity in the distributions themselves. As a result, only a measure of spread derived from a positive definite distribution such as the Short Time Fourier Transforms are physically useful, as demonstrated by Barnes (1992) in the analysis of seismic reflection data and the aforementioned examples by Cohen & Lee (1989). Fortunately, the wavelet similarly provides the opportunity for meaningful analysis of instantaneous bandwidths.

The calculation of derivative in the instantaneous bandwidth of Equation 7.8 can be difficult, prompting authors to use other approaches, e.g. maximum likelihood estimators (Ristic & Boashash, 1996). Similarly, approaching the problem as an integral operation on an instantaneous spectrum, as suggested by Equation 7.5, is complicated for multi-component signals, as it can be difficult to isolate the spectral band associated with each component in order to identify its instantaneous bandwidth. In such cases, limits of integration must be imposed, a task which is somewhat ambiguous and arbitrary. As a result, it is suggested herein to make use of a different estimator that is localized in the vicinity of the spectral peak, making it easy to apply in multi-mode scenarios and

circumventing the aforementioned concerns. The half-power bandwidth measure first introduced and discussed in Section 4.2.2.2 can provide such an estimator in a simplified and straightforward manner. Though arbitrary in its definition, this bandwidth measure allows the tracking of variations of the instantaneous bandwidth in time to uncover the presence of nonlinearity in the signal, within a computationally efficient framework. It is this relative bandwidth variation that is of most utility in the subsequent discussions.

Finally, it should be noted that the spectral bandwidth is often exaggerated by the window effects introduced by local transforms. This detail must be kept in mind when analyzing instantaneous spectral bandwidths. Cohen & Lee (1989, 1990) investigated the relationship between signal bandwidth and window bandwidth for Short-Time Fourier Transforms. Though the exact relations can be found in the cited reference, the study overall conveys the fact that the bandwidth of the spectrogram (B_{SP}) includes both the signal's true bandwidth B_s and the B_w bandwidth associated with the window of the transform:

$$B_{SP}^2 = B_s^2 + B_w^2 \,. \tag{7.9}$$

Cohen (1999) has also investigated the moments of the wavelet transform. Although he noted the more complicated entanglement that occurs as the result of scaling, the first and second moments contain the contributions of both the window and the signal bandwidth, as noted previously for the Short Time Fourier Transform. Despite this fact, the half-power bandwidth measure presented earlier in Chapter 4 can be used to identify relative changes in spectral bandwidth, as the window contributions remain constant throughout the analysis. These relative fluctuations in bandwidth represent variations in the range of

frequencies present locally in time, vital information for nonlinear systems, when viewed in conjunction with the dominant frequency in that locality, provided by the traditional instantaneous frequency.

7.4 Proper Conditions for Comparison of Hilbert Spectral Analysis and Wavelet Transforms

A critical reason for advocating the use of HSA over a WT analysis has been its ability to provide a clearly defined time-frequency skeleton plot. In contrast, the WT is shown in Huang et al. (1998) to provide a somewhat smeared and less precise representation as frequency ranges are plotted in a color contour map. However, by examining closer the theory behind both approaches, one can identify the rationale behind this discrepancy in performance. Recall that the wavelet transform is inherently a two variable transform, being a function of scale (frequency) and time. Thus, a wavelet analysis directly provides an energy density that is simultaneously a function of both frequency (scale) and time. In particular, as the Morlet wavelet considers windowed sections of the signal in its analysis, these windows modify the bandwidth of the signal, as discussed in the previous section. This characteristic helps to explain the “smeared” appearance of a continuous wavelet scalogram as noted in Huang et al. (1998), though the extent of this leakage can be minimized by adjusting the Morlet wavelet’s central frequency.

Like the WT’s scalogram, Hilbert spectra also yield the time-frequency energy density; however, in this case the transformation is not inherently a function of both frequency and time. Instead, the use of the HT allows the complex analytic signal to be formed, which is not a function of frequency but merely a function of time. It is only in

the subsequent calculation of the instantaneous frequency from the phase of this analytic signal that a frequency variable can be obtained for the HSA. By calculating the frequency from the phase relationship, the Hilbert spectrum provides a single frequency coordinate for each component in the signal. This is an important distinction that helps to further explain the reason for the poor performance of the WT in its initial comparisons to the HSA in Huang et al. (1998).

Since the WT provides a complex signal directly, as a function of both frequency and time, it too can be used to determine the instantaneous frequency of the signal. In a similar manner, the scalogram values at these instantaneous frequencies may be plotted at each point in time to yield the wavelet ridge (Staszewski, 1997; 1998). Such representations, defined previously in Chapter 4, are termed wavelet instantaneous frequency spectra in this study, to simply reinforce its parallels with the Hilbert spectra. In this way, the performance of the HSA and WT can be compared via equivalent standards by examining the ability of each to identify the evolution of the instantaneous frequency with time. It should be reiterated that the HT would not be able to provide an estimate of frequency without invoking the calculation of instantaneous frequency, just as the WT will never be able to provide a point estimate of frequency without also calculating an estimate of IF. As previous comparisons in Huang et al. (1998; 1999) did not consider this, the WIFS is used throughout this chapter to revisit these continuous wavelet comparisons to the HSA.

7.5 Examples

The following sections shall revisit a number of examples presented originally in Huang et al. (1998), examining the HSA results against revised Morlet wavelet analyses performed within the framework offered by this study. The current continuous wavelet results simulated by Equation 3.9 feature enhanced resolution by adjusting the central wavelet frequency, include the proper discretization and appropriate padding for end effects, discussed in Chapter 4, and are presented in a form analogous to the HS via the WIFS. In these comparisons, Hilbert spectra adapted directly from Huang et al. (1998), which provided the first meaningful comparison between HSA and WT, will be considered in order to give complete justice to HSA. Any differentiation of phase data to estimate the instantaneous frequency is accomplished by determining the slope of a piecewise linear fit to the phase data by a least squares approach. For comparison, the original continuous wavelet analyses conducted by Huang et al. (1998) are also provided. Note that the quality of these analyses depend on the discretization of the time-frequency domain as well as the central frequency f_o of the Morlet wavelet applied. Specific details on these parameters used in Huang et al. (1998) were not provided.

7.5.1 Example 1: Localized Sine Wave

The first example presented is a single cycle of a 1 Hz sine wave. Figure 7.1a,b displays the signal and the scalogram generated using the Morlet wavelet. What should be noted in this case is that an analysis of such transient phenomena requires a wavelet with a localized temporal resolution, adjusting f_o to 1 Hz. The dark red patch in the center of the wavelet map has pinpointed the time location and frequency content of the signal. The

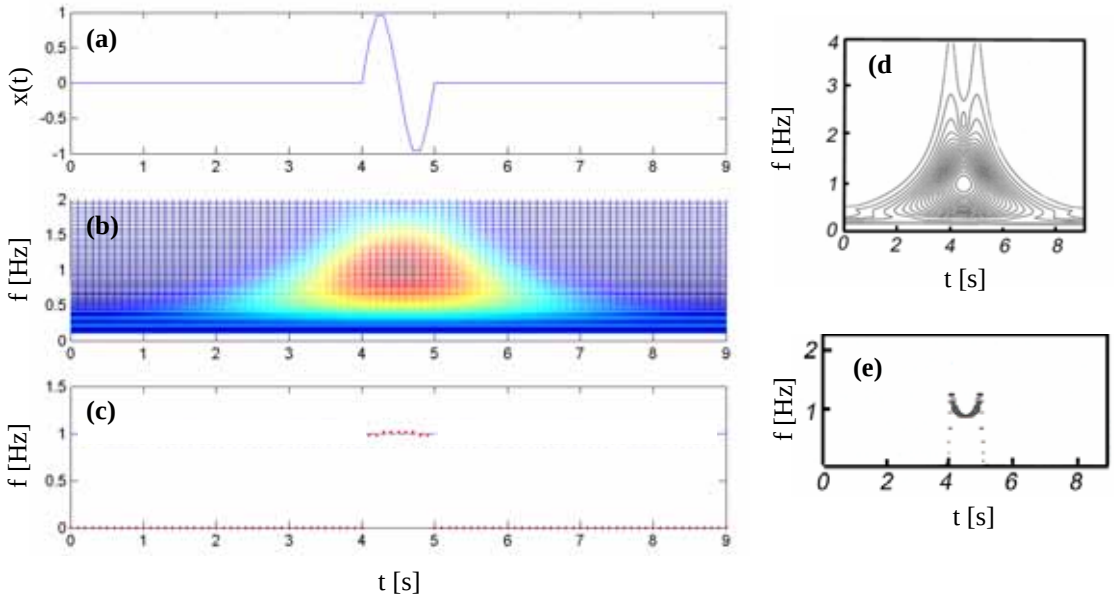

FIGURE 7.1. Example 1: (a) isolated cycle of 1 Hz sine wave; (b) wavelet scalogram; (c) WIFS (red dotted) with frequency of sine wave (blue dashed); (d) Huang et al.'s (1998) Morlet wavelet result; (e) Huang et al.'s (1998) Hilbert spectrum

"bleeding" of the wavelet scalogram is the result of inherent window effects in the time and frequency domains; however, these Gaussian windows will produce maximum wavelet coefficients at the time and frequency where the signal's energy content is concentrated, pinpointing the ridge. Using a global search for maxima of the wavelet modulus, the actual value of instantaneous frequency identified by the wavelet is shown by the WIFS in Figure 7.1c. By this approach, the wavelet will precisely identify the instantaneous frequency of the signal in the range of 4.1-4.2 seconds and 4.8-4.9 seconds as 0.98 Hz. This identification becomes even more exact at the heart of the transient, between 4.3 and 4.7 seconds with the identified value of 1.08 Hz. The continuous wavelet transform was previously criticized by Huang et al. (1998) for using spurious harmonics to isolate the transient (Fig. 7.1d). However, the wavelet analysis in Figure 7.1b does not

rely on higher harmonics, as the maxima of the transform, colorized in red, are restricted to the 1 Hz range. In fact, the localization in time and frequency of the WIFS is comparable to that generated by the HSA (shown in Figure 7.1e) and may even surpass its performance at the initiation and termination of the single cycle of oscillation.

7.5.2 Example 2: Sine Wave with Frequency Discontinuity

Another example of a sudden change of a signal's frequency is given in Huang et al. (1998) by a 0.03 Hz sine wave that suddenly shifts to a 0.015 Hz frequency of oscillation. The occurrence of this shift is highly localized in time, occurring suddenly at the 500^{th} second, as shown in Figure 7.2a. In the continuous wavelet analysis by Huang et al. (1998), the smearing of information in both frequency and time is highly undesirable (Fig. 7.2e) and pales to the pinpoint precision of the HSA (Fig. 7.2d). Revisiting the continuous wavelet example again using a Morlet wavelet with better frequency resolution properties (f_o=5 Hz), two distinct frequency bands are identified in Figure 7.2b, although the transition between the two is masked by an apparent smearing of the wavelet coefficients due to window effects. However, upon examining the WIFS, a plot of the identified wavelet instantaneous frequency, analogous to the quantity portrayed in the Hilbert spectrum, is shown in Figure 7.2c and illustrates the precision with which the continuous wavelet can identify both the frequency and time characteristics of this signal.

7.5.3 Example 3: Quadratic Chirp

To examine if the temporal smearing of the scalogram is problematic for a case where nonlinear frequency changes occur continuously throughout the signal, the example of a

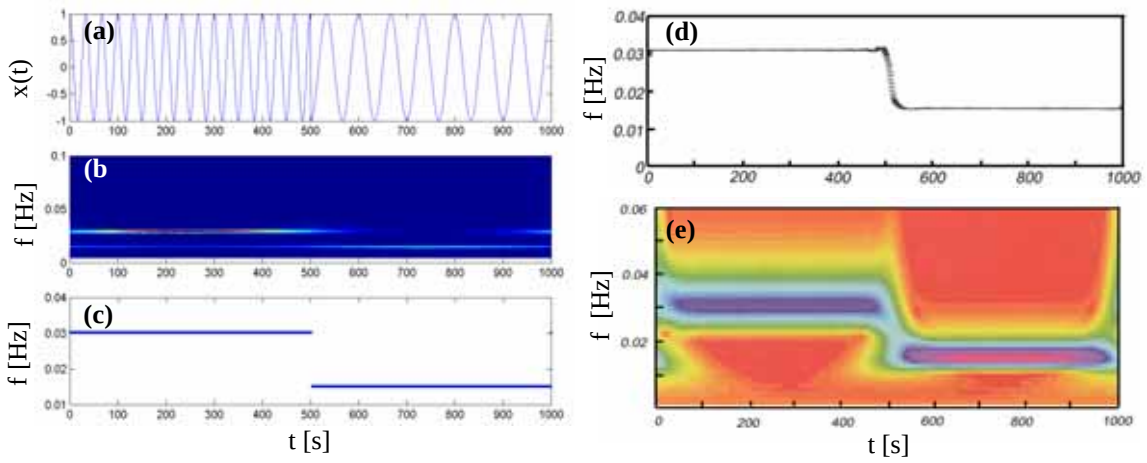

FIGURE 7.2. Example 2: (a) cosine wave with frequency halved midway through signal; (b) wavelet scalogram; (c) WIFS; (d) Huang et al.'s (1998) Hilbert spectrum; (e) Huang et al.'s (1998) Morlet wavelet result

quadratic chirp is considered. The chirp (shown in Figure 7.3a) quadratically varies from 0.2 Hz at 0 seconds to 0.17 Hz at 120 seconds. Hilbert and continuous wavelet (f_o=3 Hz) analyses were conducted, with the scalogram shown in Figure 7.3b and the identified instantaneous frequencies for the Hilbert transform (red) and continuous wavelet transform (blue) shown in Figure 7.3c. Note that the analysis of this chirp signal does not require pre-processing by EMD, as it possesses a unique frequency component at each instant in time. Both capture the quadratic variation in frequency, despite some end effects problems. The padding operation discussed previously is performed on the quadratic chirp signal and the continuous wavelet and Hilbert transforms are again determined. The result in shown in Figure 7.3d-e and demonstrates that the padding operation, not only enhances the performance of the continuous wavelet transform, but improves the Hilbert result as well – diminishing the large swings at the ends. Note

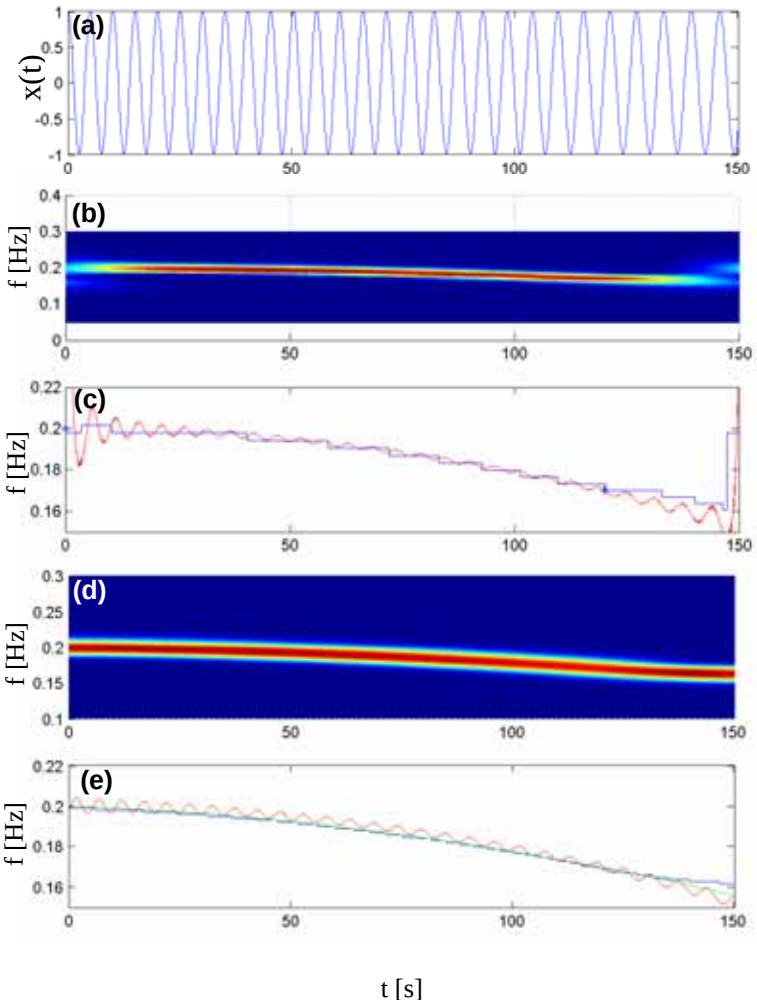

FIGURE 7.3. Example 3: (a) quadratic chirp; (b) wavelet scalogram; (c) identified instantaneous frequency by WT (in blue) and HT (in red); (d) wavelet scalogram using padded signal and finer discretization of scales; (e) identified instantaneous frequency by WT (in blue) and HT (in red) and actual quadratic frequency law (green) using padded signal and finer discretization of scales

however that the two transforms treat the signal in different ways. The HT manifests oscillations of the instantaneous frequency in addition to the global quadratic decay. The WT does not detect this oscillatory behavior and instead provides equivalently piecewise fit of the IF law to capture the overall quadratic nonlinearity. Note that in Figure 7.3c, the nature of this piecewise fit was rather coarse; however by choosing a finer discretization of scales in the wavelet analysis in Figure 7.3e, the identified IF law is far smoother. This piecewise fit arises from the fact that the wavelet fits small waves or "wavelets" to the signal at each point in time – as expected, a locally linear approximation to the quadratic. Note that in Figure 7.3e, the actual quadratic frequency relation used to simulate the chirp is plotted in green to demonstrate the accuracy of HT and WT in identifying the frequency variations. The WT result in blue nearly overlays identically with the theoretical result in green. The HT result in red is slightly less accurate and manifests an oscillatory behavior that is not present in the actual quadratic IF law. Thus far, Examples 2 and 3 respectively illustrate the equal ability of both techniques to identify changes in frequency occurring over a range of frequencies and at an isolated instant in time.

7.5.4 Example 4: Stokes Wave

The true significance of the Morlet wavelet's central frequency can be discerned in the example of the idealized Stokes wave in deep water. The use of a perturbation analysis to solve this system illustrates the common practice of representing nonlinear phenomena as a summation of harmonic components, with the second-order approximation to the Stokes wave profile given by

$$X(t) = \frac{1}{2}a^2 k + a\cos(\omega t) + \frac{1}{2}a^2 k\cos(2\omega t) \tag{7.10}$$

in which a is the amplitude and k is the wave number. By choosing a=1, k=0.2 and ω=2π/32, as discussed in Huang et al. (1998), Figure 7.4a is generated. By inspecting the instantaneous wavelet modulus taken at an instant in time, as demonstrated in Figure 7.4b, a component at 0.0320 Hz is evident, representing the 0.0313 Hz harmonic. The presence of a higher mode at 0.0622 Hz, though evident only in the wavelet modulus in Figure 7.4b due to its small magnitude relative to the dominant ridge of the scalogram in Figure 7.4c, confirms the presence of the 0.0625 Hz component. Figure 7.4c displays the resulting Morlet wavelet scalogram for f_o=5 Hz, whose color scale does not clearly reflect the second mode, though the WIFS in Figure 7.4d detects the two frequencies identified from the local maxima shown in Figure 7.4b. The Morlet wavelet with 5 Hz central frequency, though having a refined frequency resolution, will have a poor temporal resolution of over 100 seconds. Thus it behaves much like a Fourier harmonic analysis and is well suited to capture the dual harmonics used in Equation 7.10 to simulate the second-order approximation to the Stokes wave. It unfortunately has no ability to capture the local nonlinearities of the wave profile. Note that the degree of smearing has been minimized in the current continuous wavelet analysis in Figure 7.4c in comparison to the previous findings in Figure 7.4e. This perspective offered by the wavelet analysis reflects the philosophy used to simulate the nonlinear system – represent the nonlinearity by a sum of harmonics.

In contrast, Figure 7.4f displays the HSA result, which oscillates about 0.0313 Hz and shows no evidence of the second mode. To justify this result, Huang et al. (1998)

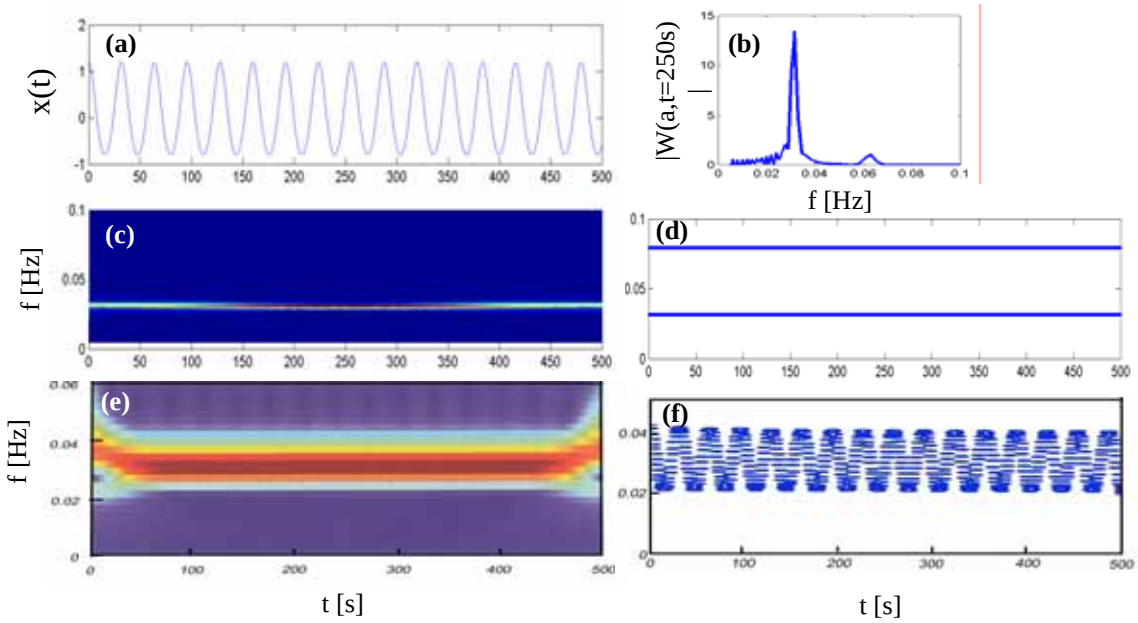

FIGURE 7.4. Example 4: (a) Second order approximation to the Stokes wave; (b) wavelet modulus at t=250 s; (c) wavelet scalogram; (d) WIFS; (e) Huang et al.'s (1998) Morlet wavelet result; (f) Huang et al.'s (1998) Hilbert spectrum

explained that Stokes waves could similarly be modeled as a cosine with modulated frequency

$$X(t) = \cos(\omega t + \varepsilon \sin(\omega t)), \tag{7.11}$$

which is much like the frequency modulated signal in communication theory, with ω serving as the carrier frequency and the second frequency term being the transmitted signal. As argued by Huang et al. (1998), if there are any frequency changes within the wave's oscillation, then its profile can no longer be a simple sinusoid. A visual inspection of the simulated Stokes wave in Figure 7.4a demonstrates that there is such a subtle departure from the simple sinusoidal shape. This deviation from a simple sinusoid

observed in Stokian waves is the result of intrawave frequency modulation, represented by the second frequency term in Equation 7.11.

An enhanced temporal wavelet analysis echoes this behavior. Inspecting the time series, peaks have a frequency of around 0.03 Hz or a period of about 32 s. The resolution of the wavelet in both time and frequency must be sufficient to capture this. From the relations in Equation 4.5 and Equation 4.8, a central frequency of 0.5 to 1 Hz will be required to balance the time and frequency resolution capabilities. Thus the wavelet analysis of the Stokian wave simulated by Equation 7.10 (shown again in Figure 7.5a) is repeated with f_o=0.5 Hz. In this analysis, the scalogram (in Figure 7.5b) still concentrates near 0.03 Hz, however there is no evidence of a higher harmonic. Instead there is an oscillatory variation toward the high frequency range, evidenced by the light blue hues. Inspection of the WIFS (Figure 7.5c) still does not confirm this, as it manifests a single frequency component at 0.0303 Hz that does not vary with time. Looking at the instantaneous frequency estimated from the phase of the wavelet transform, a nearly constant frequency value is again identified, though more precise, at 0.0312 Hz. Still, the scalogram behavior indicates that the wavelet is detecting some variation of evolutionary energy content. As discussed previously in Section 7.3.3, the spectral characteristics of a system are not merely defined by the instantaneous frequency. As a result, the bandwidth of each instantaneous spectra produced from the wavelet analysis is provided in Figure 7.5d and demonstrates that this value oscillates about a mean value with a period of approximately 32 seconds in the same manner as the HS in Figure 7.4f.

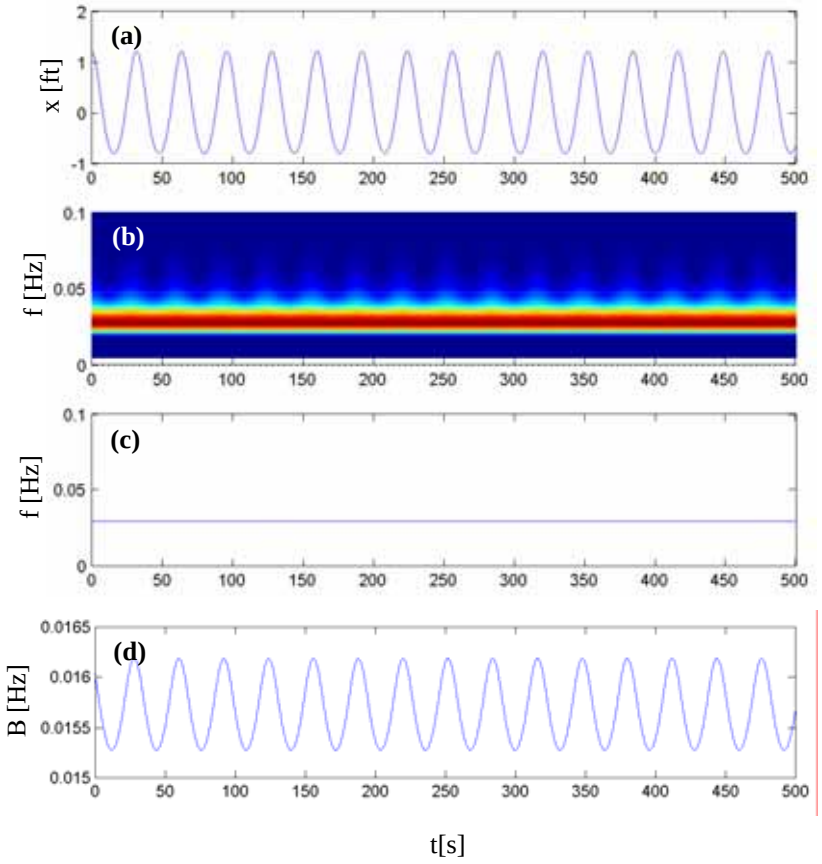

FIGURE 7.5. Example 4 via refined wavelet analysis: (a) second order approximation to the Stokes wave; (b) wavelet scalogram; (c) WIFS; (d) wavelet instantaneous half-power bandwidth

Application of a similar wavelet analysis on measured surface elevation of wave tank data verifies these characteristics of Stokian waves. Figure 7.6a displays wave data generated mechanically by a 1 Hz sinusoidal excitation with +/- 9 mm amplitude. Note that the time series manifests narrowed peaks and widened toughs, highlighting a subtle

deviation from a simple sinusoidal shape. By inspection of the time series, the peaks are separated by approximately 1 s, necessitating a temporally refined wavelet capable of determining variations occurring over less than one second and frequency sensitivity a

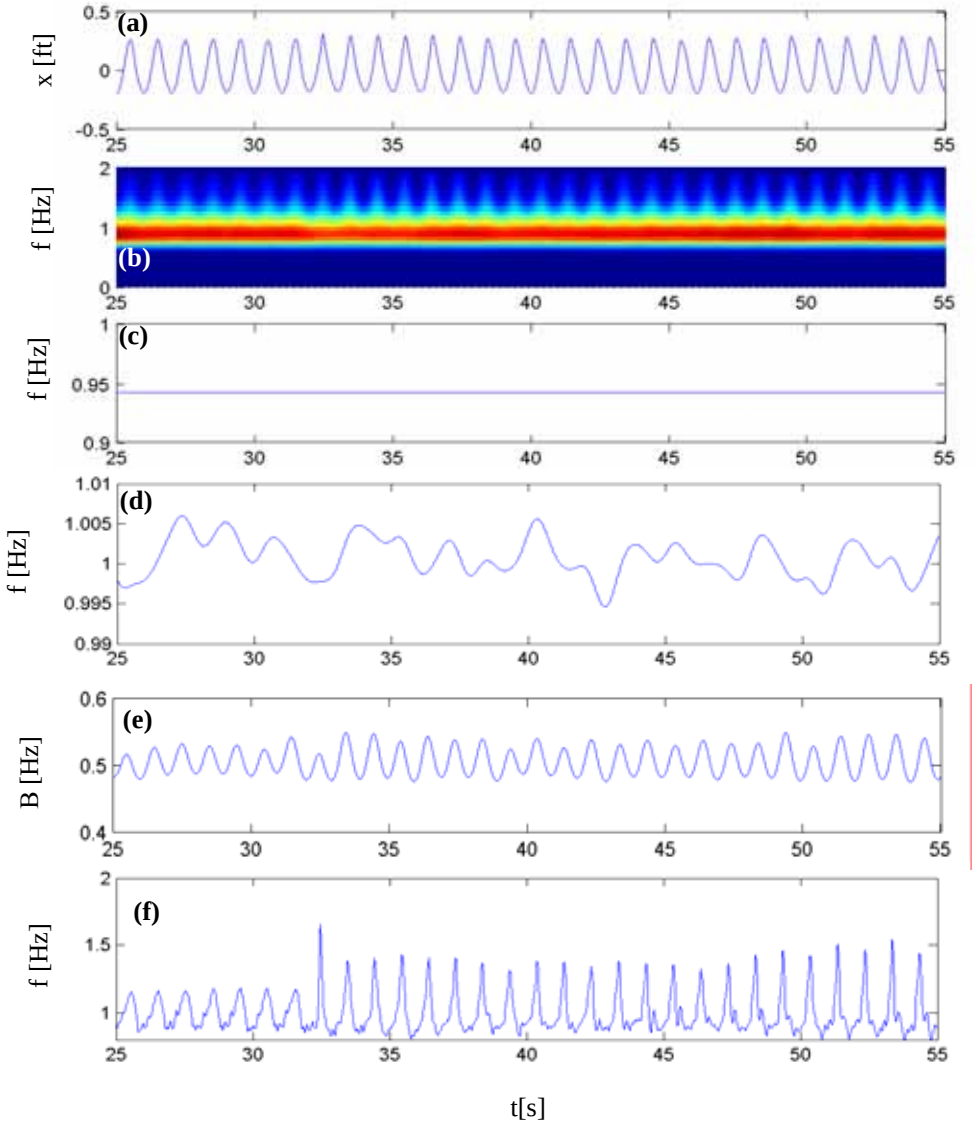

FIGURE 7.6. (a) 30 seconds wave tank surface elevation; (b) scalogram of wave tank data; (c) WIFS; (d) instantaneous frequency from wavelet phase; (e) instantaneous half-power bandwidth estimate; (f) instantaneous frequency from Hilbert transform phase

fraction of 1 Hz. With f_o=0.5 Hz, a temporal resolution of 0.35 s is possible, with a 0.22 Hz frequency resolution. The scalogram for this analysis, shown in Figure 7.6b, again concentrates near 1 Hz with its warm hues, but the lighter shades of blue fluctuating in the higher frequency scales again indicate the presence of time-varying frequency content. The WIFS in Figure 7.6c, as observed in the previous example of Stokian waves, remains constant at 0.94 Hz, giving an averaged interpretation of the instantaneous frequency as a result of the wavelet approximation. Zooming in on the more precise phase-based instantaneous frequency estimate, in Figure 7.6d, the minor modulations reveal time-variance in the local mean frequency. Further fluctuations about this mean frequency are then identified in the instantaneous bandwidth in Figure 7.6e, which provides a rich display of nonlinear characteristics beyond that of the numerically simulated Stokes waves in Figure 7.5. The bandwidth in this case oscillates again at the frequency identified in the WIFS, however, the periodic modulations of the bandwidth indicate a regular variation of frequencies concomitant at each instant in the signal. A Hilbert Spectral Analysis by Huang et al. (1998) of measured wave data affirmed similar phenomena, albeit displayed solely in the instantaneous frequency. The direct application of the Hilbert transform in Figure 7.6f can affirm the variations of the frequencies present in the system, though this perspective is far noisier without the filtering afforded by EMD.

This example illustrates two important facts: first, that a wavelet analysis with poor temporal resolution inherently treats the signal in the same manner as Fourier analysis, while a wavelet analysis with refined temporal resolution is capable of detecting nonlinear wave characteristics. It is the resolutions tied to a specific analysis that

ultimately dictate whether the nonlinear system will be viewed in terms of harmonics or intrawave modulated waves, i.e. waves deviating from a simple sinusoid with subcyclic oscillations. While the resolutions of HSA, though temporally precise, remain fixed, the flexibility in wavelet transforms allowed both of these perspectives to be realized. Secondly, but perhaps more importantly, the wavelet does not necessarily manifest these indicators in the instantaneous frequency, but instead in the instantaneous bandwidth. Recall again that the wavelet fits small waves or "wavelets" to the signal at each point in time. In the case of the Morlet wavelet, these localized waves are sinusoidal in nature. The IF identified in Figure 7.5c is then the frequency of the best fit widowed sinusoid. However, as the Stokian wave profile subtlety deviates from the simple sinusoid, it is not unreasonable to expect that additional neighboring frequencies are required to capture these deviations. The involvement of such adjacent frequencies is represented by the bandwidth measure. Thus in the truest sense indicated by Priestly (1988), the wavelet IF is the mean frequency and the bandwidth reflects the deviation of these frequencies from this mean as they evolve in time.

7.5.5 Example 5: Linear Sum of Two Closely-Spaced Cosines

As the previous example demonstrated, the temporal resolution of HSA is fixed, yet precise. The time resolution is a consequence of the Hilbert transform's convolution in Equation 3.24 involving a highly localized function. The following example will demonstrate a situation in which the sacrificed frequency resolution in HSA can be problematic. A pair of closely spaced cosine waves was generated by

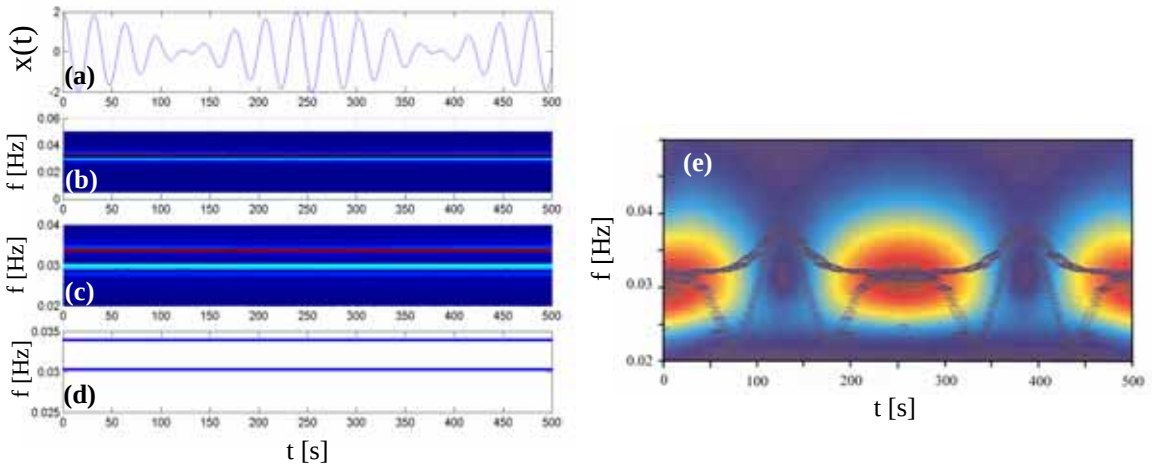

FIGURE 7.7. Example 5: (a) linear combination of two closely-spaced cosine waves; (b) wavelet scalogram; (c) wavelet scalogram (zoom); (d) WIFS; (e) Huang et al.'s (1998) Morlet wavelet analysis with Hilbert spectrum contours superimposed

$$x(t) = \cos\left(\frac{2}{30}\pi t\right) + \cos\left(\frac{2}{34}\pi t\right) \tag{7.12}$$

The frequencies of these two harmonics are approximately 0.0294 and 0.0333 Hz. Figure 7.7a shows the signal with characteristic beat phenomena. In order to separate the two components, a given analysis technique must have a refined frequency resolution, consistent with the findings of Delprat et al. (1992). In Huang et al. (1998), it was shown that neither a continuous wavelet analysis nor HSA could identify two distinct harmonic components, as shown in Figure 7.7e. Revisiting this problem using f_o=5 Hz for the Morlet wavelet, presumably different from Huang et al.'s (1998) analysis, the wavelet scalogram (Fig. 7.7b) was generated. As the zoom in Figure 7.7c illustrates, two distinct bands of energy are revealed, shown in red and light blue. Searching the localized maxima, two instantaneous frequency components can be identified at 0.0303 Hz and 0.0340 Hz, within 3% of the actual signal frequencies, as shown by the WIFS in Figure

7.7d. Figure 7.7e again displays the wavelet scalogram obtained by Huang et al. (1998) with the Hilbert spectrum superimposed as contours. Though the signal is the linear combination of two distinct harmonics, according to Huang et al. (1998), neither approach accurately captures this. The wavelet scalogram indicates a high concentration of energy at approximately 0.03 Hz, but does not distinguish between the two components. However, the continuous wavelet's inability to separate the harmonics in Huang et al. (1998) should not be interpreted as a failure of the continuous wavelet in theory, but rather a byproduct of the selection of an insufficient central frequency f_o in the analysis.

Likewise, the Hilbert spectrum localizes in the same vicinity but also shows some spurious oscillatory behavior in the instantaneous frequency between 0.025 Hz and 0.035 Hz, treating the beat phenomena as a frequency modulated wave. As shown in the previous example, the presence of multiple components in an IMF will result in nonlinear phase terms once the HT is applied. In such cases, the HT treats the closely spaced harmonics by some non-physical modulated wave. The misrepresentation in this example may be a direct consequence of EMD. In this case of two closely spaced modes, the EMD required a very stringent condition of 3000 siftings to obtain only eight IMF components, which still could not represent the true signal (Huang et al., 1998). The inability to distinguish between two distinct components may be traced to the definitions of the IMFs to satisfy the restrictions of the Hilbert transform. As discussed previously, Huang et al. (1998) used a more relaxed narrowband condition, placing conditions on the number of zero crossings and maxima. In doing so, the resulting IMFs are narrowband in character but not strictly monocomponent, potentially encapsulating in that narrow band both

closely spaced harmonics, leading to the inability of the Hilbert spectrum to capture the dual harmonic character of this signal. Unfortunately, the frequency resolution of EMD cannot be readily refined.

7.5.6 Example 6: Amplitude Modulated Signal with Constant Frequency

In another example provided by Huang et al. (1998), the physical significance of the HSA result is again called into question. In this case, an amplitude-modulated (AM) wave is generated by

$$x = \exp(-0.01t)\cos\left(\frac{2}{32}\pi t\right) \tag{7.13}$$

which represents the impulse response function of a single-degree-of-freedom mechanical oscillator with frequency of 0.0313 Hz and damping ratio of approximately 5%, shown in Figure 7.8a. Although the signal is completely amplitude-modulated in theory, there is a minor frequency modulation revealed upon applying the Hilbert transform, as shown later in Figure 7.9b. Huang et al. (1998) argue that this result should be expected as amplitude variations influence the bandwidth of a process, viewed in terms of traditional power spectra as a spread of frequencies about the mean frequency. Based on that argument, the authors contend that this spread of frequency may be manifested in time as a slight deviation of the IF from the mean frequency of the process, in this case yielding oscillations about a frequency of 0.0313 Hz (see Figure 7.9b). This spread of frequencies about the IF at each instant in time is one means to account for the many neighboring frequencies produced by AM, however, the IF should theoretically surface as the average of the frequencies at each point in time, as discussed in Priestley (1988) and would be

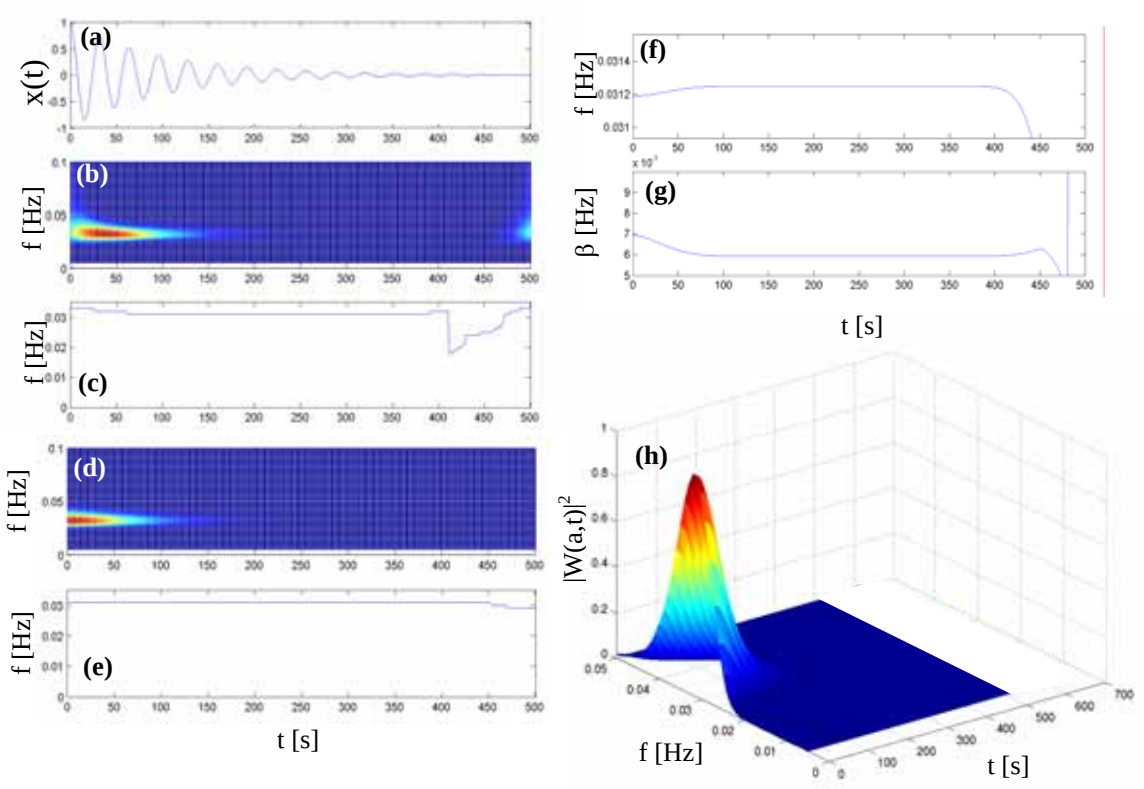

FIGURE 7.8. Example 6: (a) amplitude-modulated cosine; (b) wavelet scalogram; (c) WIFS; (d) wavelet scalogram with application of padding; (e) WIFS with application of padding (zoom); (f) WIFS determined from wavelet phase with application of padding (zoom); (g) wavelet estimate of HPBW with application of padding; (h) 3D view of wavelet scalogram with application of padding

expected not to oscillate for this linear system. As the signal has no true frequency modulation, how should the oscillatory component detected by the HT be interpreted?

On the other hand, the analysis by the continuous wavelet transform (f_o=1 Hz), shown in Figure 7.8b, captures the transient nature of the signal, with the reds denoting the maximum energy content concentrated near 0.03 Hz. Examining the WIFS in Figure 7.8c illustrates that the extracted estimate of the IF (0.0315 Hz), though lacking accuracy at the initiation of the signal due to an end effect, is within 1% of the theoretical

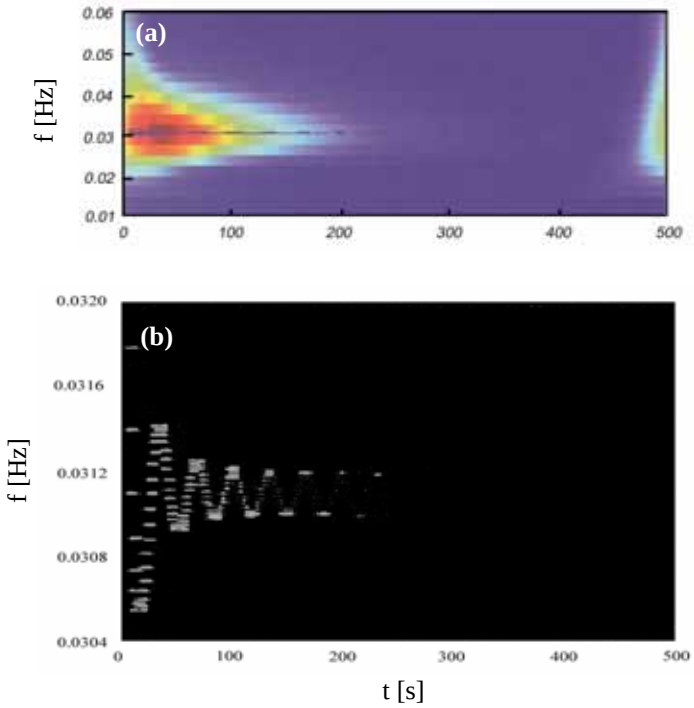

FIGURE 7.9. (a) Huang et al.'s (1998) Morlet wavelet result; (b) Huang et al.'s (1998) Hilbert spectrum (zoom)

frequency, shown by the dotted line. Beyond 400 seconds, the identification of the IF is no longer accurate, as the signal energy is fading. Note, as shown in Figure 7.9a, that Huang et al. (1998) similarly observed end effects anomalies in their wavelet analysis. As

discussed previously, end effects can pose a significant limitation to the quality of wavelet analyses, particularly for short duration signals. To insure local preservation of spectral characteristics, the signal in Equation 7.13 is padded using the reflective padding scheme previously introduced. The resulting scalogram and WIFS are shown in Figure 7.8d-e. The use of this technique eliminates the poor performance at the initiation of the signal and greatly enhances its accuracy at the conclusion of the signal, though there are

still some deviations due again to the fact that the signal, at that point, has nearly damped out completely.

To further validate the ability of the wavelet to analyze this signal and demonstrate the dual potential of the wavelet, the instantaneous frequency is also identified using the derivative of the wavelet phase. As this often can be a more precise means of identifying the instantaneous frequency, it is a useful exercise to see if the wavelet can detect any physical influence of amplitude decay in the instantaneous frequency. As shown in Figure 7.8f, the wavelet instantaneous frequency extracted from phase takes on a constant value of 0.0313 Hz and when zoomed in to a scale of +/-1% of the oscillator frequency, there is no evidence of oscillation. There is a slight deviation early in the signal, corresponding to a residual byproduct of end effects. At the end of the signal, the estimation quality rapidly degrades due to the difficulty of phase identification once the signal energy is nearly completely damped out.

It was also demonstrated in previous examples that instantaneous bandwidth can manifest evidence of nonlinearity or physically meaningful intrawave frequency modulation. SDOF oscillators like the one considered here, the half-power bandwidth has a unique relationship to the oscillator frequency and its damping. The HPBW of each instantaneous spectra produced from the wavelet analysis is provided in Figure 7.8g and demonstrates that this value holds relatively constant throughout the decay in the signal, as expected, since the expression in Equation 7.4 represents an oscillator with constant frequency and damping for which both the resonant frequency and bandwidth should not vary with time. Note that at the beginning of the signal, the bandwidth suffers from a

more visible inaccuracy, attributed to the fact that the bandwidth measure is far more sensitive than the instantaneous frequency to end effects, as discussed in Chapter 4 and demonstrated by several additional examples in Chapter 9. As discussed later in Chapter 9, even with the addition of padding, bandwidth measures within $3\Delta t$ of the beginning and end of the signal can have some residual inaccuracy. For this analysis, that region would encompass 68 seconds at the ends of the signals, clearly marked by the rounded characteristic in Figure 7.8g. Neglecting these two regions, the bandwidth holds constant, as expected. The sudden drop off beyond 450 s is again the consequence of attempting to identify a signal for which has almost entirely damped out. Figure 7.9b similarly affirms that the Hilbert Spectrum can also no longer identify frequency content beyond 200 seconds, again to the decay of signal energy.

Contrary to the HSA result, oscillatory frequency modulations are not reflected in the wavelet HPBW measure, or in the instantaneous frequencies identified using either the amplitude or phase of the wavelet. In fact, the presence of amplitude modulations in this signal are ultimately observed in the three-dimensional perspective offered by the wavelet scalogram in Figure 7.8h, where the amplitudes of wavelet coefficients reflect the decay of energy in the signal. This information has been used in system identification applications where nonlinearities in damping and stiffness are detected via changes in the wavelet amplitude and phase, respectively, with time (Feldman, 1994a,b; Staszewski 1998). This example illustrates that the harmonic wavelet analysis will identify the true frequency of the signal and does not identify an amplitude-induced FM in either its IF or bandwidth, though identification of the amplitude modulation can be retained from the amplitude of the wavelet coefficients.

While the notion of intrawave frequency modulation may be physically meaningful in some cases, in this example the presence of this phenomenon is not, effectively indicating a slight nonlinearity in a linear the system, though it is noted in Huang et al. (1998) that the magnitude of this intrawave modulation is only +/- 1.5%. Still it must be clarified if this frequency modulation is due to physical changes in frequency or due to a numerical byproduct of the HT. The analytic signal generated using the HT will always provide a unique complex representation, however, as Boashash (1992a) has stated, "whether or not it corresponds to any physical reality is another question." This indeed depends on the extent to which asymptotic signal assumptions are met. In this case, the presence of frequency modulation in a constant frequency oscillator can be deceiving and may actually be the consequence of a violation of asymptotic signal assumptions. The definition of the instantaneous frequency in Equation 3.27 is only valid if the envelope and phase are well separated. For an arbitrary signal in the form of

$$y(t) = a(t)\cos(\phi(t)) \tag{7.14}$$

as in Equation 7.13, this implies that the Fourier transform of *a(t)* must be well separated from and less than the Fourier transform of *cos(ϕ(t))*, as discussed in Chapter 3. This is because the HT inherently selects the highest frequency component of the signal as the complex phase term. If the Fourier spectrum of the oscillatory component of the signal is not located at a frequency higher than and well separated from the envelope's spectrum, then the Hilbert transform operation will be a result of overlapping and phase-distorted functions. This will give rise to a waveform that can no longer be described by a purely AM law, even though it was generated by an AM process (Rihaczek, 1966). In such

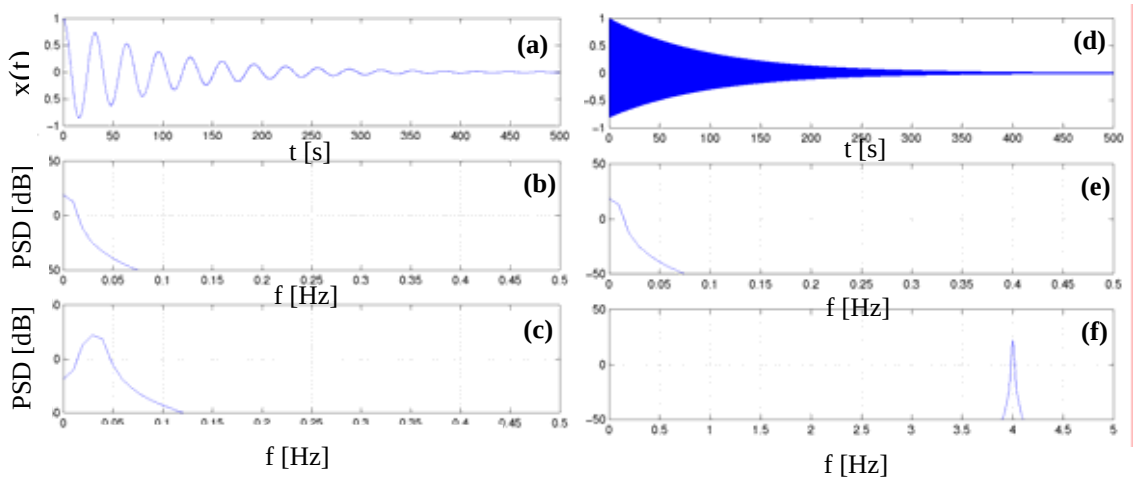

FIGURE 7.10. (a) Amplitude-modulated cosine in Example 6; (b) Fourier spectrum of envelope *a(t)*; (c) Fourier spectrum of phase *cos(ϕ(t));* (d) Amplitude-modulated cosine in with envelope and phase well separated in frequency; (e) Fourier spectrum of envelope *a(t)*; (f) Fourier spectrum of phase *cos(ϕ(t))*

cases, "the HT and the analytic signal are not always interpretable in a way which is physically meaningful and representative of physical phenomena" (Boashash, 1992a).

Examining the signal generated in Example 6 (Fig. 7.10a), a plot of the Fourier spectrum of its exponential envelope and phase term at 1/32 Hz is shown in Figure 7.10b,c. In this case, it is clear that there is some overlap in these two spectra, indicating that the envelope and phase may not be well separated in frequency and may cause phase-distortions for the Hilbert transform. Figure 7.10d-f provides an example of a signal with no significant spectral overlap between the amplitude and phase, as the cosine frequency in Equation 7.14 is increased to 4 Hz. It is interesting then to examine the implications of these overlapping envelope and phase spectra on the estimation of the instantaneous frequency using the Hilbert transform. Figure 7.11b,c shows the estimated instantaneous frequencies of these cases. The axis on the frequency coordinate is scaled

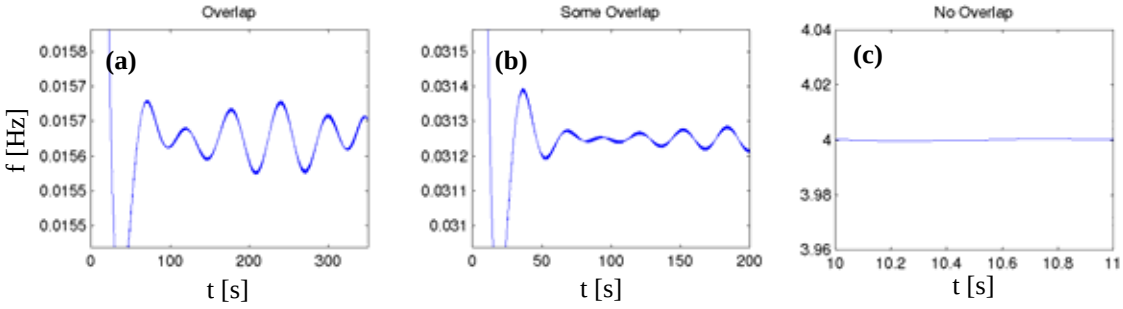

FIGURE 7.11. Instantaneous frequencies identified from the Hilbert transform: (a) case where envelope and phase spectra overlap significantly; (b) case where envelope and phase spectra overlap somewhat (Ex. 6), shown in Figure 7.8; (c) case where envelope and phase spectra do not overlap significantly

to +/-1% of the true frequency in each case to provide an equivalent basis for comparison. For further illustration, a case where the level of overlap is greater than in Example 6 is also provided in Figure 7.11a by decreasing the cosine frequency in Equation 7.13 to 1/64 Hz. In this case, where the overlap is most significant (Fig. 7.11a), the level of this intrawave modulation is more marked. As the overlap is lessened in Example 6 (Fig. 7.11b), the intrawave modulation is still present but reduced. In case of the higher frequency signal in Figure 7.11c, the presence of this oscillation is hardly notable. It can be inferred that the intrawave modulation in this case actually results from the Hilbert transform not being able to clearly identify the phase and misinterpreting contributions from the envelope as a result of their overlap in the Fourier domain.

In the case of this exponentially decaying envelope, by increasing the frequency of the oscillatory term in Equation 7.14, the degree of overlap is not only being minimized, but also the bandwidth of the system is also being increased. Note that the product of the bandwidth and duration, or BT product, was introduced in Chapter 3 as a

measure of the richness of the signal. The exercise in Figure 7.10 equally illustrates the role of the BT product in the reliability of an IF measure produced by the HT. For signals with small BT, e.g. a low frequency, well damped oscillator, the IF is difficult to identify at an instant since there is no dominant frequency (Boashash, 1992a). This does not preclude the use of the HT for small BT signals – it only raises concerns for the interpretation of results.

In practice, it is desirable to examine asymptotic signals, which are characterized by a finite duration, bandwidth and energy, but with large BT product; however, the term "large" is quite ambiguous. Although, Slepian et al. (1961) determined that 99% of a signal's energy is typically preserved within the limits of $B_xT_x > 5$, Boashash (1992a) suggested limiting analysis to signals with $B_xT_x >10$ such that the approximation error resulting from assuming band and time limited functions is minimal. This will include, in practice, signals used in communications and seismic applications. In Boashash (1992a) it is shown that for a given signal, the analysis of short duration records (small BT) will manifest significant leakage in the time-frequency energy density. Increasing the duration (larger BT), reduces this effect so that the deviations from the true IF diminish.

Thus, the demonstrations in Figure 7.11 further illustrate that the estimated IF approaches the anticipated result, with levels of IF oscillation decreasing, as the bandwidth of the signals, and thereby the BT product, increases. Either the possibility of spectral overlap between the phase and envelope or the implications of a small BT product serve as viable explanations for the apparent "intrawave frequency" modulation

cited by Huang et al. (1998) and demonstrate that this characteristic is not physical but a numerical byproduct of the Hilbert transform.

7.5.7 Example 7: Duffing Equation

Huang et al. (1998, 1999) explore a variety of classical nonlinear problems with distinctly different frequency nonlinearities using continuous wavelets and HSA. The simplest of these systems is the Duffing oscillator under harmonic excitation, in accordance with the second-order differential equation

$$\frac{d^2x}{dt^2} + \left(1 + \varepsilon x^2\right)x = \gamma \cos \omega t \tag{7.15}$$

where ε, γ are constants and ω is the harmonic forcing frequency. The term in parenthesis represents nonlinearity in the stiffness of the oscillator, which will lead to a frequency that changes with amplitude. As discussed in Stoker (1966), Duffing (1918) noted that the motions of this system were periodic but not simple harmonic, resulting in a period that is “a unique function of amplitude”. The variation of frequency with time observed in the Duffing oscillator is a physical reality due to the nonlinearity of the stiffness in Equation 7.15 and has been identified by other authors using both Hilbert (Feldman, 1994a,b) and wavelet transforms (Staszewski, 1998). Huang et al. (1998, 1999) investigated the solution for a strongly nonlinear case (Fig. 7.12a) using HSA and identified 3 IMF components contributing to the system response, as shown in Figure 7.12b, for ε = -1, γ = 0.1 and ω = 1/25 Hz. The dominant component of the oscillator displays marked intrawave oscillations of both long and short period, expanded upon in

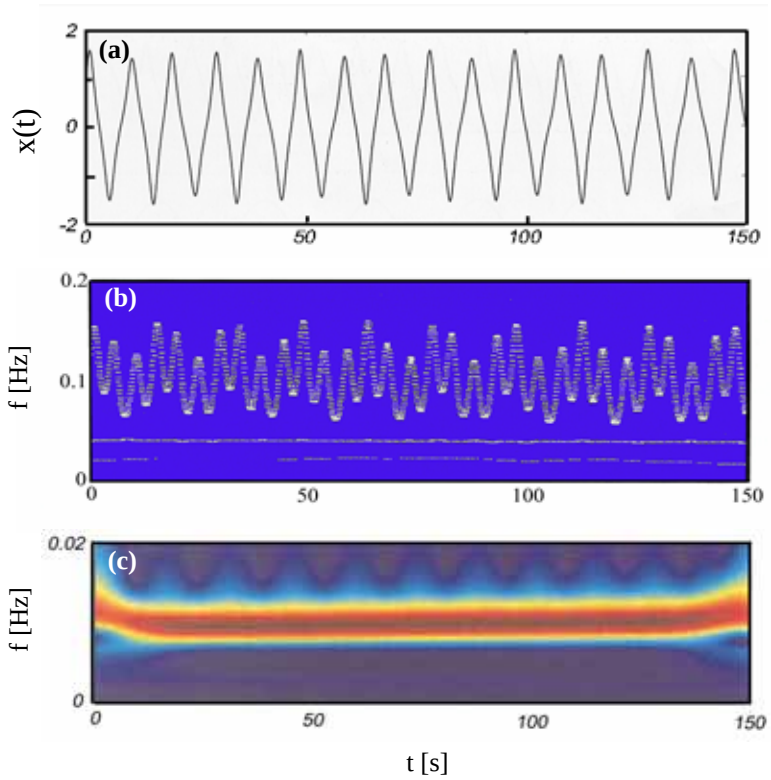

FIGURE 7.12. Example 7: (a) Duffing oscillator under harmonic excitation; (b) Huang et al.'s (1998) Hilbert spectrum manifesting 3 IMF components; (c) Huang et al.'s (1998) Morlet wavelet result

Huang et al. (1998). Meanwhile, the low frequency component, represented by the IMF near 0.04 Hz, is attributed to the forcing function (at 1/25 Hz). The lowest frequency component is attributable to a slow wobbling of the phase. Huang et al. (1998) noted that the Morlet wavelet could not capture this nonlinear behavior in terms of the intrawave frequency modulations, though identifying the dominant frequency content in the region near the intrinsic frequency of 0.124 Hz as shown by Figure 7.12c. Note however that even this basic wavelet analysis by Huang et al. (1998) manifests some oscillatory characteristic in the high frequency range, indicating a time-varying bandwidth and

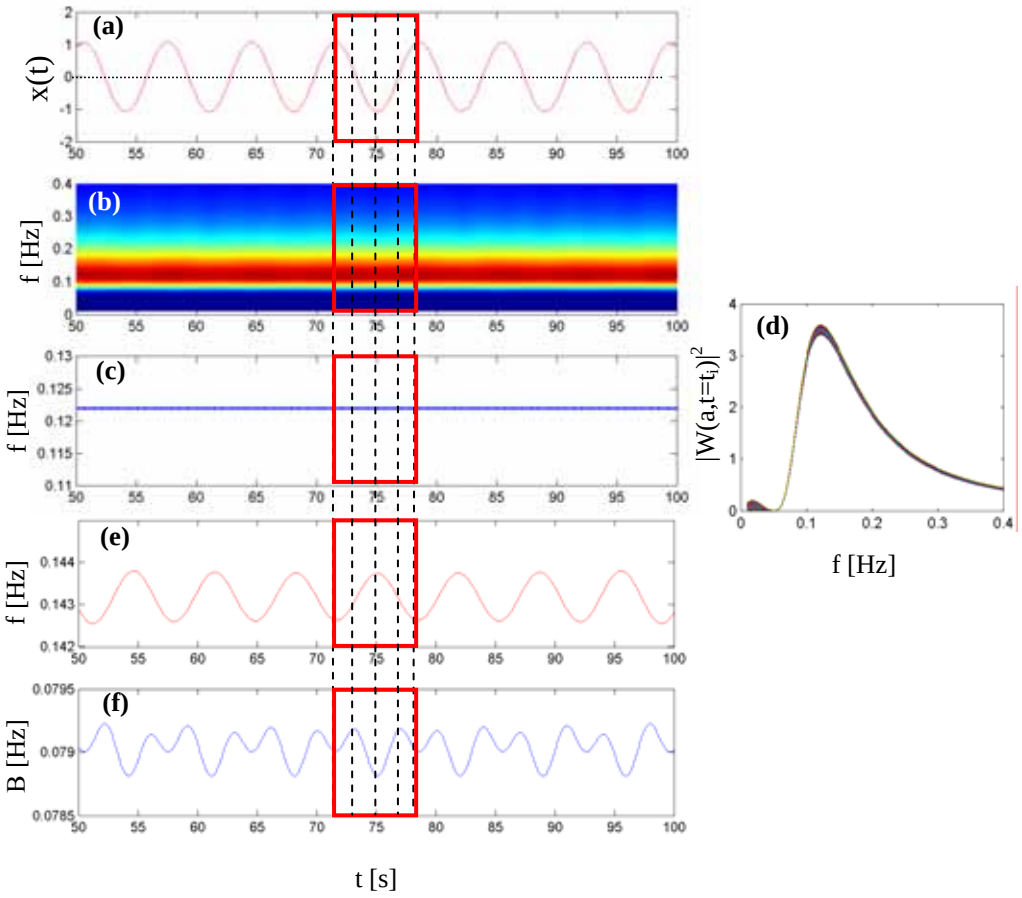

FIGURE 7.13. Example 7: (a) Duffing oscillator in free vibration, zoomed in from 50 to 100 s; (b) wavelet scalogram; (c) WIFS; (d) wavelet instantaneous frequency spectra at each time step plotted one atop another; (e) instantaneous frequency identified by phase of WT; (f) instantaneous half-power bandwidth

demonstrating again that the wavelet's ability to detect nonlinear behavior lies in its bandwidth measure.

In order to expand upon these findings, the response of the system in Equation 7.15 is generated using a 4^{th} order Runga Kutta simulation to determine if the wavelet is sensitive enough to detect even subtler nonlinearities, embodied by a Duffing oscillator with ε = -0.22, γ = 0.1. For a more basic understanding of the wavelet interpretation, the

system is first released from the initial conditions of $x(0) = 0$ and $x'(0) = 1$ and allowed to freely vibrate, as shown in Figure 7.13a. From the time series itself, the frequency of oscillation can be estimated as 0.14 Hz. Applying the Morlet wavelet with f_o=0.25 Hz, in order to achieve a refined temporal resolution, yields a scalogram capturing the dominant harmonic component, shown in Figure 7.13b. The extracted WIFS shown in Figure 7.13c reiterates this finding through a single ridge near 0.12 Hz. The lack of accuracy in this identified instantaneous frequency ridge can be justified in light of the reduced frequency resolution for f_o=0.25 Hz, which was conceded to enhance the temporal resolution. Plotting the instantaneous spectra at each time step one atop another (Fig. 7.13d), essentially collapsing the scalogram in time, confirms the presence of a single response component, however the thickness of the profile indicates that there is some variation in the amplitude, peak position and bandwidth. Although the maxima of the wavelet scalogram cannot be used to directly identify the instantaneous frequency accurately for such a fine time resolution analysis, the phase of the wavelet transform can still be used to provide a more precise identification of instantaneous frequency. The IF determined from the wavelet skeleton's phase along the ridge in Figure 7.13c is provided in Figure 7.13e and affirms the presence of a frequency component near 0.143 Hz. The oscillation of the phase instantaneous frequency reflects at the subtle nonlinearity of this system. The findings in Figure 7.13e imply that the peaks of the instantaneous spectra in Figure 7.13d are gradually shifting back and forth about 0.1431 Hz. By examining the instantaneous half-power bandwidth, Figure 7.13f provides additional evidence of the subtle nonlinearity of this system with oscillations occurring at twice the frequency of the oscillation of the Duffing system. The fluctuations of the bandwidth measure describe the

variation of the spread of frequencies about the instantaneous frequency in Figure 7.13e, the source of the thickened line on the backside of the instantaneous power spectra. As the red frames in Figure 7.13 help to demonstrate, the bandwidth, sensitive to signal amplitude, takes on its lowest values in the signal's troughs and peaks at the zero crossings of the signal, where the Duffing oscillator is essentially a linear system, while intermediate troughs occur at the signal maxima. As the envelope of the signal in Figure 7.13a is constant due to the lack of dissipative term, one may expect a constant bandwidth in the response. However, the subtle bandwidth fluctuations are a result of the nonlinearity in frequency and affirm the bandwidth sensitivity to even very mild nonlinear phenomenon. It should be reiterated that if f_o were chosen too large, much of this behavior would be obscured, as also demonstrated previously in the Stokes wave analysis.

Looking at the forced response of the same system for $\omega = 1/50$ Hz in Figure 7.14a, the envelope of the signal manifests a low frequency oscillation as a result of the forcing function. Inspection of the wavelet scalogram in Figure 7.14b reveals that the warmest hues indicate the frequencies at which the signal concentrates, which again are focused at 0.12 Hz due to the loss of frequency resolution in the scalogram discussed previously. The bright blue band at the foot of the scalogram indicates the 0.02 Hz forcing function. While the energy is clearly concentrated in the vicinity of the oscillator's dominant frequency, the higher frequencies of the scalogram manifest a rippling indicative of fluctuations in the frequency content with time. The instantaneous frequencies were identified from the ridges of the transform and are shown in Figure 7.14c. Two dominant components were observed: one near 0.12 Hz and one

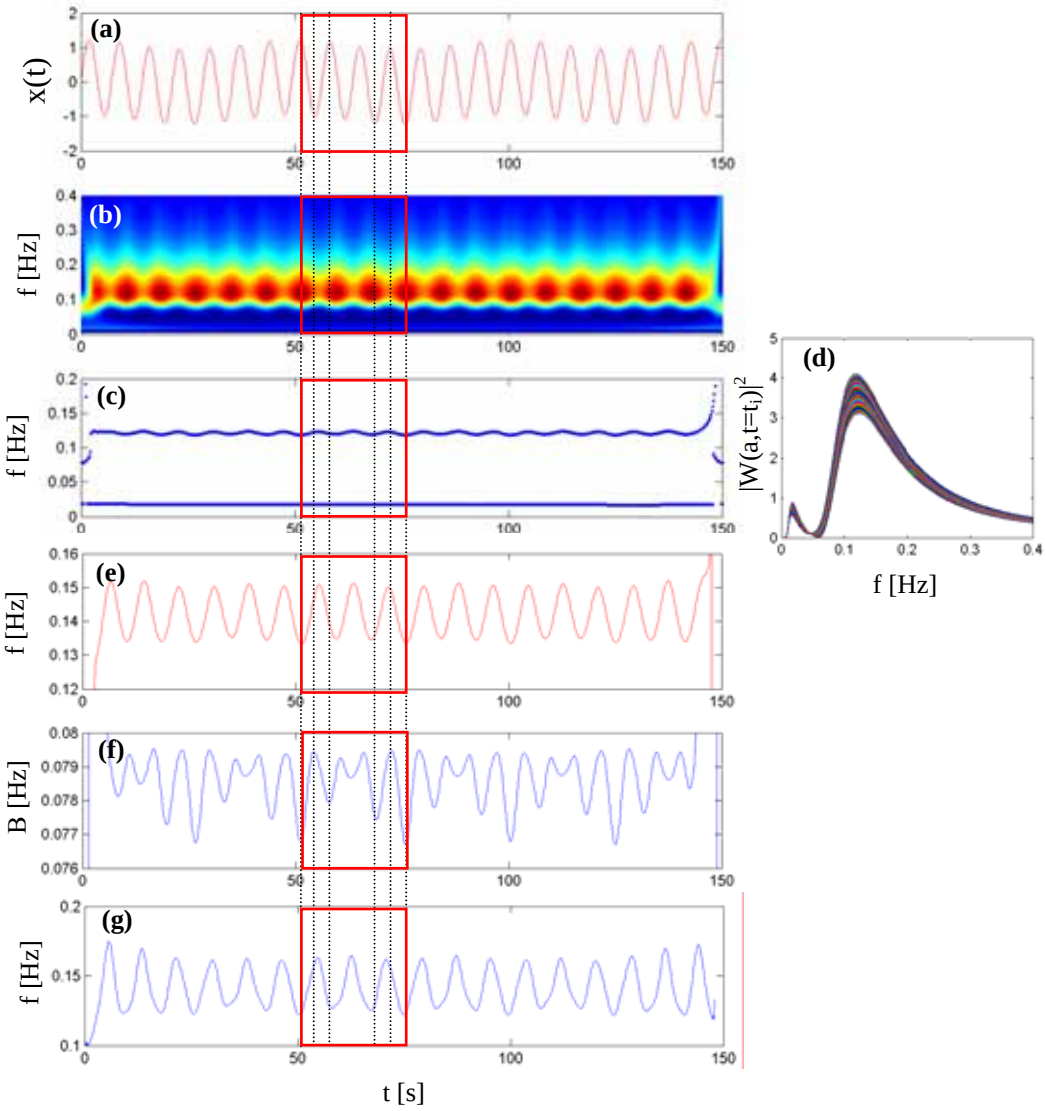

FIGURE 7.14. Example 7: (a) Duffing oscillator in forced vibration; (b) wavelet scalogram; (c) WIFS; (d) wavelet instantaneous frequency spectra at each time step plotted one atop another; (e) instantaneous frequency of high frequency component identified by phase of WT; (f) instantaneous half-power bandwidth of high frequency component; (g) estimate of instantaneous frequency by Hilbert Transform

corresponding to the forcing frequency near 0.02 Hz. Contrary to Figure 7.13b, the ridge associated with the nonlinear oscillator now manifests some fluctuation. The same overlay of instantaneous spectra in Figure 7.14d reveals that a more marked spread in bandwidth, peak frequency and amplitude of the spectral peak than in its counterpart in Figure 7.13b, indicative of more prominent time-varying characteristics. Turning again to the instantaneous frequency estimate from the wavelet phase in Figure 7.14e, the range of oscillation of the instantaneous frequency is identified more precisely in the vicinity of 0.14 Hz, as before. Note that the wavelet instantaneous frequency estimate, grounded in Fourier harmonics, manifests a smooth regular periodicity. Again recalling that the wavelet analysis fits small waves to the data, the instantaneous frequency estimate is more representative of the best-fit frequency over some short time interval but may not fully capture subcyclic characteristics. Turning to the instantaneous bandwidth in Figure 7.14f, a different perspective with a far more oscillatory characteristic is evident. The red box denotes a region of downshift, during which the local signal mean shifts to lower amplitudes. Each downshift is followed by an upshift. These trends occur in a periodic manner as a consequence of the forcing frequency, thus the duration of downshift region is half the forcing period or 25 s. The initiation and termination of the downshift are marked by troughs in the wavelet instantaneous frequency in Figure 7.14e and the deepest troughs of the instantaneous bandwidth in Figure 7.14f. This pattern repeated in the bandwidth is a consequence of the amplitude modulation arising from the forcing function, while the higher frequency fluctuations spanning the downshift region reflect the nonlinearity of frequency in the signal. Note that both the frequency and bandwidth qualitatively manifest local symmetry over the downshift region. This result can be

compared to the instantaneous frequency estimated via the Hilbert transform, shown in Figure 7.14g. This result shows more irregularity when compared to the wavelet instantaneous frequency in Figure 7.14e, as expected. The wavelet instantaneous frequency is characteristically smooth as discussed above, being a best-fit local mean to the frequency at that time. For the wavelet, any fluctuations or spread about this mean are carried in the bandwidth in Figure 7.14f. The Hilbert result does not separate these two contributors of frequency evolution and provides an instantaneous frequency estimate whose peaks and troughs shift and lean, though in a repeating pattern, as a result of intrawave fluctuations. The appropriateness of either representation depends entirely on the perspective desired.

This example again reiterates the distinction between these two techniques: the HSA will in general detect these subtle changes in frequency due to some nonlinearity, essentially identifying subcyclic frequency changes, while the Morlet wavelet's instantaneous frequency will only detect changes in the instantaneous frequency in its truest mean sense, as it locally fits windowed sinusoids to the data and is thus capable of detecting only nonlinearities evolving over entire cycles of oscillation or following significant changes in amplitude, which will be referred to herein as supercyclic oscillations. One period of oscillation in the Duffing oscillator corresponds to a marked amplitude change, easily detectable by the Morlet wavelet's instantaneous frequency extracted from the phase.

However, the rippling manifested in the scalogram, particularly in the high frequency range, suggests that the wavelet is detecting some of the subcyclic oscillations

of the Duffing oscillator, not through its ridges or instantaneous frequency, but through its spectral bandwidth, as introduced in Example 5. The bandwidth fluctuations, being more sensitive than instantaneous frequency, are not as precise near end effects regions, as discussed in more detail later in Chapter 8. Even so, they capture repeating patterns of frequency spread with time. Further, they demonstrate a secondary fluctuation in the bandwidth with a periodicity that corresponds to the time between a signal peak and its subsequent trough – a subcyclic phenomenon. Thus, it appears that while the wavelet's instantaneous frequency captures only supercyclic oscillations and mean behaviors of frequency over small windows, the additional insights provided by the bandwidth affirm the deviations from the instantaneous frequency, affirming the presence of subcyclic phenomenon or a frequency that continuously varies with amplitude for the same reasons as discussed following the Stokes wave examples.

7.5.8 Example 8: Lorenz Equation

The Lorenz equation, initially proposed to study deterministic non-periodic flow, has become a fundamental system for the investigation of chaos and was considered in Huang et al. (1998) as another classic nonlinear system for investigation using HSA. The system is described by

$$\dot{x} = -\sigma x + \sigma y \qquad \dot{y} = rx - y - xz \qquad \dot{z} = -bz + xy \tag{7.16}$$

where *s*, *r* and *b* are positive constants, assumed to be 10, 20 and 3, respectively, for the purpose of this example. The system is released from its initial position of (10, 0, 0), resulting in the x-component response shown in Figure 7.15a, illustrating the transient

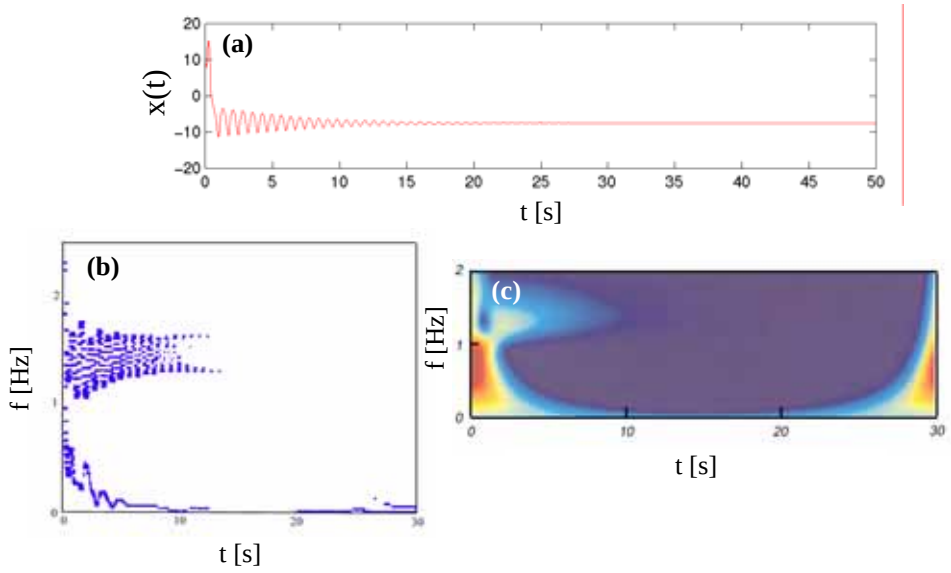

FIGURE 7.15. Example 8: (a) Lorenz equation x-component; (b) Huang et al.'s (1998) Hilbert spectrum of Lorenz equation, x-compnent; (c) Huang et al.'s (1998) Morlet wavelet result

characteristics of the system. The Hilbert spectrum generated by Huang et al. (1998) is provided in Figure 7.15b and reveals the characteristic intrawave frequency modulation observed in other non-linear systems as a result of subcyclic frequency variations. The Hilbert spectrum also manifests a low frequency component, which rapidly drops from 1 Hz and lingers around 0.1-0.2 Hz. This mode corresponds to the rapid transient drop occurring in the first few seconds of the Lorenz response. After this transient period, the oscillator tends to behave as a damped nonlinear system. Note the decaying of the instantaneous frequency indicating supercyclic FM due to the damping characteristic as well as the oscillations about 1.4 Hz due to subcyclic nonlinear behavior. Linearization of the system in Huang et al. (1998) yielded a dominant frequency of about 1.46 Hz, consistent with the main frequency about which intrawave modulations occur.

The continuous wavelet analysis by Huang et al. (1998) shown in Figure 7.15c captures the transient nature of the signal, but the frequency resolution may not be sufficient to disclose the nonlinearities present. The revisited Morlet wavelet analysis of the Lorenz x-component response (Fig. 7.16a) is shown in Figure 7.16b. While the scalogram indicates that the wavelet has captured the transient behavior with the intense red patches, it is the wavelet instantaneous frequency spectrum (Fig. 7.16c) that truly provides clear representation of the behavior. Consistent with the HSA in Figure 7.15b, the Morlet wavelet with f_o=0.5 Hz, chosen for more precise temporal resolution, was capable of detecting the marked frequency shifts due to the transient behavior in the first few seconds of the signal. This is characterized by a shift in the low frequency component from about 0.75 Hz to 0.019 Hz. After this transition range, the wavelet detects a bi-modal response, with the low frequency response near 0.019 Hz and the oscillator's response at about 1.4 Hz, near the 1.46 Hz theoretical prediction of the linearized system. The estimation of instantaneous frequency of this mode becomes unreliable beyond 10-15s, as the signal's energy decays, shown by the diminishing light blue patch in the scalogram. This observation is consistent with the HS in Figure 7.15b, which indicates that the instantaneous frequency estimate about 1.4 Hz is scarcely detected beyond 10 seconds, though the lower frequency response is still clearly present. The subcyclic oscillations about 1.4 Hz, occurring essentially in the decaying component of the response, are subtly evident in the WIFS in Figure 7.16c, apparently becoming more pronounced as the signal dissipates. To more closely inspect these subcyclic oscillations, the instantaneous frequency of this component is also identified from the wavelet phase. The result, shown in Figure 7.16d demonstrates that subtle oscillations are

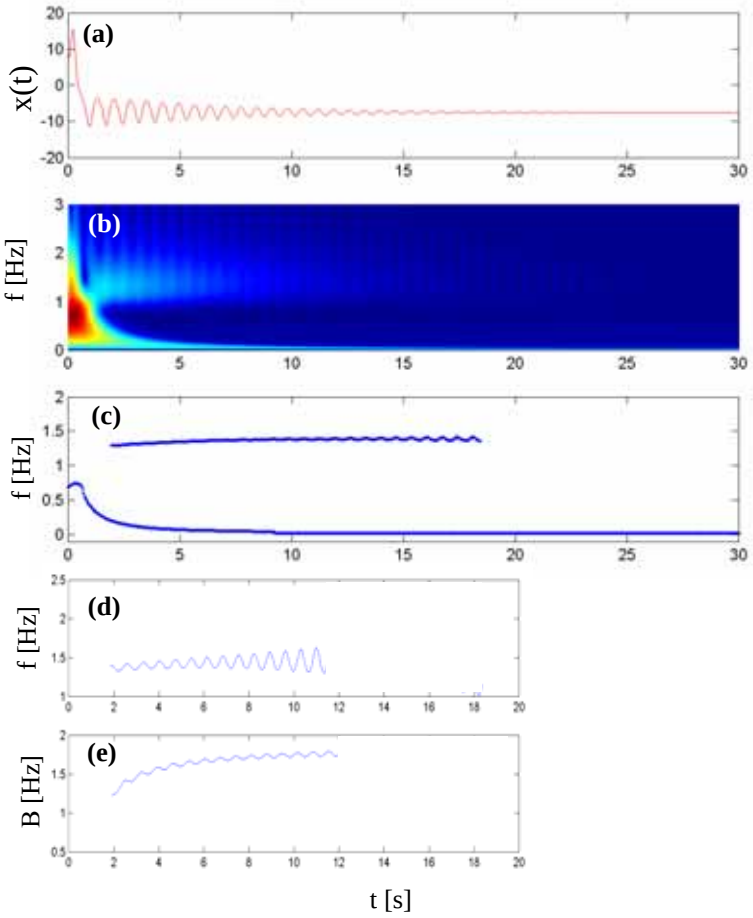

FIGURE 7.16. Example 8: (a) Lorenz equation x-component; (b) wavelet scalogram; (c) WIFS; (d) instantaneous frequency of high frequency component identified by phase of WT; (e) instantaneous half-power bandwidth of high frequency component

detected by the wavelet phase, though not of the magnitude detected in HSA. These oscillations grow in amplitude slightly, however, this is not a physical reality but rather a bi-product of the increasing difficulty in estimating the instantaneous frequency accurately from the phase as the signal's energy rapidly diminishes. The amplitude of wavelet coefficients during this decaying phase of the higher frequency component

initiate at a maximum value of around 8.5 and fall beneath 10% of this value by the tenth second, becoming essentially zero by the twentieth second.

The dual characteristic of the continuous wavelet transform allows the investigation of instantaneous spectra, taken as slices of the wavelet scalogram along the time axis. These spectra provide snapshots of the system's frequency domain behavior. Critical points in the response of the Lorenz equation's x-component are labeled in Figure 7.17 by asterisks, and their associated instantaneous spectra are provided. The first three points are part of the rapid transient decay. Their instantaneous spectra reveal the predominantly monocomponent nature of this transient region, with the broad spectral peak shifting from near 1 Hz to a lower frequency value near 0.5 Hz. By the fourth point, the system has entered into an essential free vibration about 1.4 Hz accompanied by the persistent low frequency component. The presence of both modes continues through points 5 and 6, though the magnitude of the second peak associated with the free vibration oscillations is steady decreasing as the system's energy is dissipated. Simultaneously, the low frequency component approaches DC and becomes highly concentrated, reflecting the permanent offset of the system as the response decays. An investigation of the half-power bandwidth of the second peak is provided in Figure 7.16e, affirming again the presence of nonlinearity in the frequency spread at each instant in time, with a periodicity similar to that observed in the phase-identified instantaneous frequency. It should be noted that the diminished values of the bandwidth at the beginning of the signal is a consequence of enhanced sensitivity in the end effects region, discussed more fully in Chapter 8. Again, the WIFS and wavelet bandwidth concur with the findings of HSA: observing an oscillatory characteristic in the high frequency

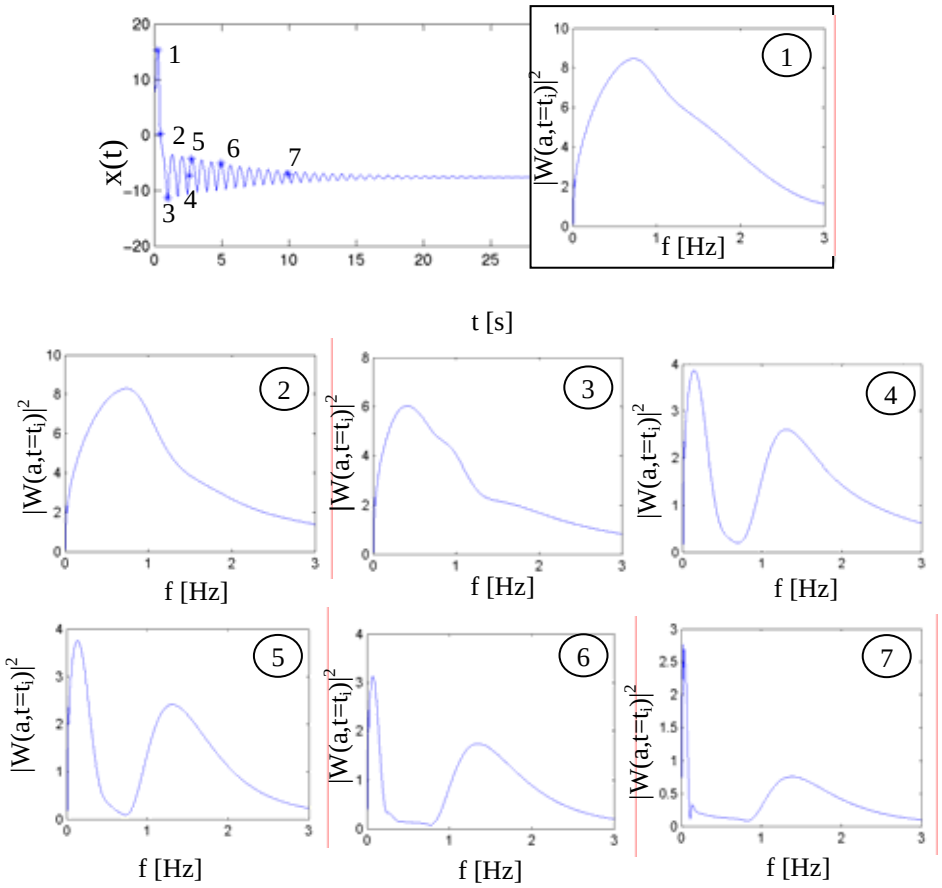

FIGURE 7.17. Example 8: Lorenz equation, x-component, instantaneous spectrum from wavelet transform at critical points in the response

component of this nonlinear system and identifying the transient behavior of the constant offset.

7.5.9 Example 9: Rössler Equation

Huang et al. (1998) also investigated the Rössler Equation for the famous period doubling event described by

$$\dot{x} = -(y + z) \qquad \dot{y} = x + \frac{1}{5} y \qquad \dot{z} = \frac{1}{5} + z(x + \mu) \tag{7.17}$$

where μ = 3.5. The system simulated by a first-order forward difference technique from the initial conditions {*x(0)* = -4, *y(0)* = 4, *z(0)* = 0} is shown in Figure 7.18a. The Hilbert spectral analysis of the x-component of the Rössler system, as performed by Huang et al. (1998), is provided in Figure 7.18b. Note that the EMD of the data yielded 2 meaningful IMF components, one oscillating between 0.17 and 0.25 Hz, representing the dominant nonlinear characteristic of this system. The lower frequency component, near 0.1 Hz, is assumed to be the result of some numerical error, as it is quite low in energy and is surfacing in a system known to have only two dominant scales.

Huang et al. (1998) states that "to represent such a [system] with either Fourier spectrum or wavelet analysis, one would need many harmonics." Indeed, a continuous wavelet analysis may represent globally this system by a series of harmonics if the temporal resolutions are insufficient to resolve the nonlinearities, as shown by Figure 7.18c. Inspecting the signal shown again in Figure 7.19a, there are large amplitude peaks occurring about every 11 seconds, indicating that there is some frequency content in the vicinity of 0.1 Hz. Temporally, smaller peaks occur approximately 5 seconds after a large peak, so the wavelet chosen must not have a time resolution greater than 5 seconds in order to detect the changes in the signal with time. Wavelet analyses can often be performed in stages. In the first stage, it is often desirable to identify components within the signal by choosing a wavelet with sufficiently fine frequency resolution. As the dominant peaks have a frequency in the vicinity of 0.1 Hz, one may seek a wavelet with a resolution 10% of this value, or 0.01 Hz. This can be achieved using f_o=5 Hz, though the

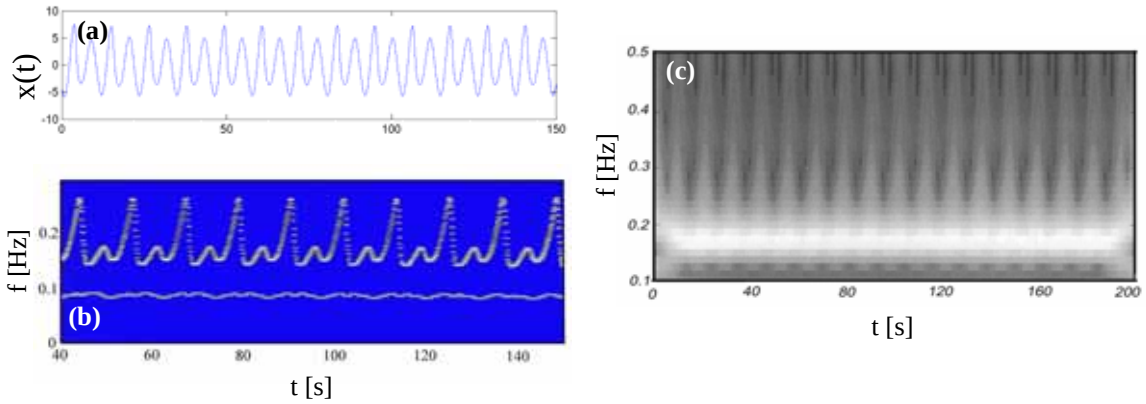

FIGURE 7.18. Example 9: (a) Rössler equation x-component; (b) Huang et al.'s (1998) Hilbert spectrum; (c) Huang et al.'s (1998) Morlet wavelet result

temporal resolution for this wavelet is about 7 seconds and thus will not capture the variations which occur every 3-4 seconds. Using this fine frequency resolution first, in stage 1 of the analysis, two distinct components are identified at around 0.09 and 0.17 Hz, demonstrated in Figures 7.19b-c. This information then defines two frequency ranges over which to apply a more temporally refined analysis in stage 2. The first component near 0.1 Hz was cited by Huang et al. (1998) as some numerical artifact from the simulation of the system. As this component does not manifest marked temporal variation in the refined analysis, it will not be included in subsequent discussions. However, it will be shown that the component near 0.17 Hz does reveal interesting phenomena in a refined analysis. Again, to track the time-evolving amplitude changes, a wavelet with fine time resolution must be chosen. For f_o=0.25 Hz, the temporal resolution is enhanced to approximately 1.75 s. Using this wavelet to analyze the second component of the system as stage 2, the scalogram in Figure 7.19d is obtained. Note that the color contours of the wavelet scalogram mimic the same oscillatory peaking of the frequency observed in the Hilbert spectrum in Figure 7.18b. The WIFS is generated in Figure 7.19e and reveals that

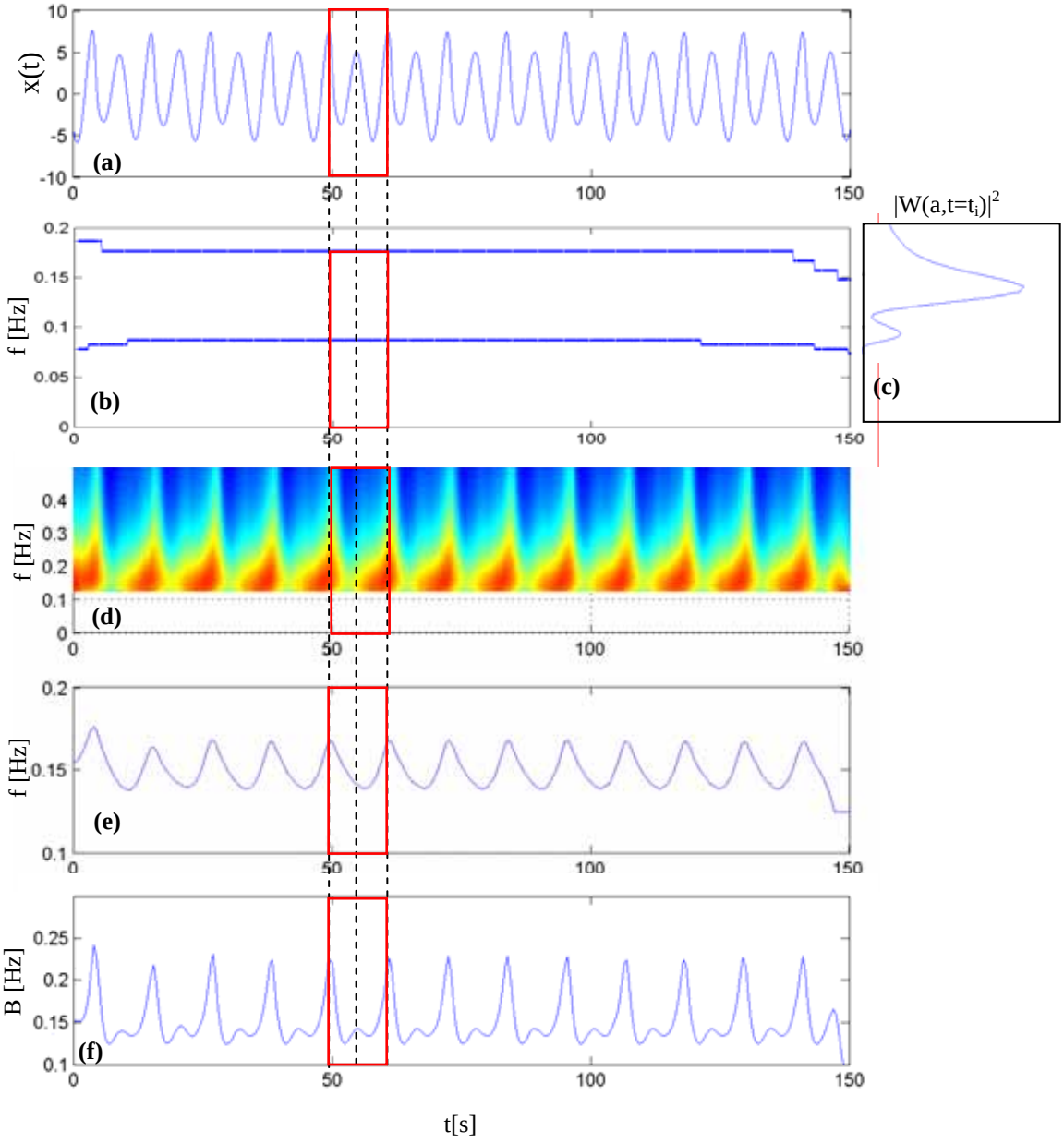

FIGURE 7.19. Example 9: (a) Rössler equation x-component; (b) WIFS for analysis stage 1; (c) sample instantaneous spectra; (d) wavelet scalogram for analysis stage 2; (e) WIFS for analysis stage 2; (f) instantaneous half-power bandwidth for analysis stage 2

the energy is primarily concentrated in an oscillatory pattern between 0.1375 and 0.1665 Hz, with a period of oscillation of 11.4 seconds, capturing the period of the large peaks in the time series.

As the scalogram fluctuations in the high frequency range indicate some variation of energy in time, a half-power bandwidth analysis is performed as part of stage 2 on this second component. The results, shown in Figure 7.19f, clearly demonstrate the behavior identified by Huang et al. (1998) in Figure 7.18b, with large peaks interlaced with smaller, rounded humps. The period between the major peaks in bandwidth is 11.4 seconds, corresponding to the period of the large peaks in the signal. Approximately 5.5 seconds after each major peak in the HPBW, a smaller peak follows, as also observed in the time series. The period between the smaller peaks of the HPBW is also 11.4 seconds. Thus the dual identification of the instantaneous frequencies and bandwidth from the wavelet transform illustrates the ability of the Morlet wavelet to characterize this nonlinear behavior, albeit differently than the HSA, and dispute the claim by Huang et al. (1998) that “no other methods can match the resolution power displayed here.” As demonstrated in previous examples, while the instantaneous frequency can signal the presence of nonlinear behavior in response to marked amplitude changes in the signal, it does so in a more averaged sense. It is the sensitivity of the instantaneous bandwidth that detects the presence of waves of neighboring scales indicative of a deviation from a perfect sinusoid – a trademark of the nonlinear system.

7.5.10 Example 10: Random Wave Data

While the wavelet analyses presented thus far have considered a number of nonlinear and nonstationary systems, Huang et al. (1998) extended the time-frequency analyses to measured wave data. While the intent of this chapter is not to provide such an exhaustive array of examples, the analysis of measured wave data was included in the discussions of the Stokes wave. To enrich this discussion further, the analysis of experimentally observed random sea waves is presented herein. The waves were generated by a JONSAWP random excitation with amplitude of 64 cm. The power spectrum of the excitation affirms discernable frequency content up to approximately 2 Hz, although this broad peak focuses at approximately 0.4 Hz. The resulting waves at one measuring station are provided in Figure 7.20a for 200 seconds of the total measured record. From inspection of the time series, the fundamental period of oscillation is approximately 2 seconds, though the wave profiles are not smooth, indicating the presence of other frequencies or nonlinearities in the data. A continuous wavelet analysis with f_o=1 Hz produced the scalogram shown in Figure 7.20b. The scalogram reflects several pockets of intense energy bursts, associated with high amplitude events in the data, and concentrated at around 0.5 Hz. The presence of lighter hues fading into the high frequency range again suggests the detection of a distribution of energy beyond the fundamental observed frequency. Ridge extraction from the wavelet modulus revealed up to three local maxima for any given instantaneous spectrum. The maxima take on the highest values in the vicinity of 0.5 Hz, as shown in red on the WIFS in Figure 7.20c, accompanied by intermittent lower amplitude components in a relatively lower and higher frequencies, shown in light green and yellow. Individual analyses of the occurrence of the three ridges

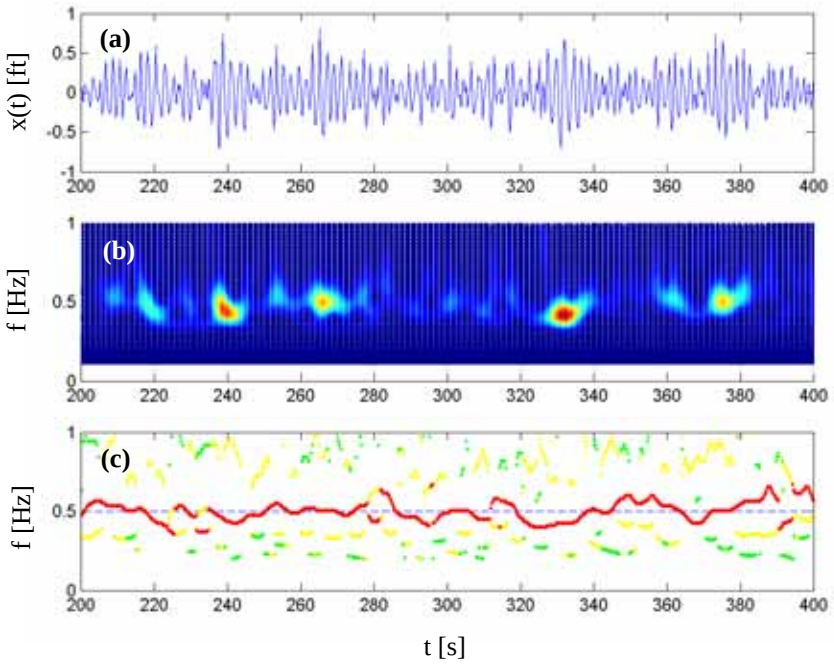

FIGURE 7.20. Example 10: (a) measured random wave data; (b) wavelet scalogram; (c) WIFS for up to three ridges (red → green indicates highest to lowest energy components at each time step)

are provided in Figure 7.21. Figure 7.21a displays the instantaneous frequency associated with the simplest harmonic representation observed in the signal – for which there is only one dominant oscillatory component near 0.5 Hz, typified by the instantaneous spectrum to the right. The frequency content of the signal often shifts then to a bi-modal characteristic, centered around 0.5 Hz, as shown in Figure 7.21b, but alternating its dominant peak between approximately 0.4 and 0.6 Hz, as shown by the two example instantaneous spectra. The occurrence of a third peak is usually an intermittent phenomenon of relatively lower energy and accompanies the dominant presence of the same two harmonics centered near 0.5 Hz. It is important to reiterate that wavelet instantaneous spectra, when viewed in tandem with the wavelet instantaneous frequency

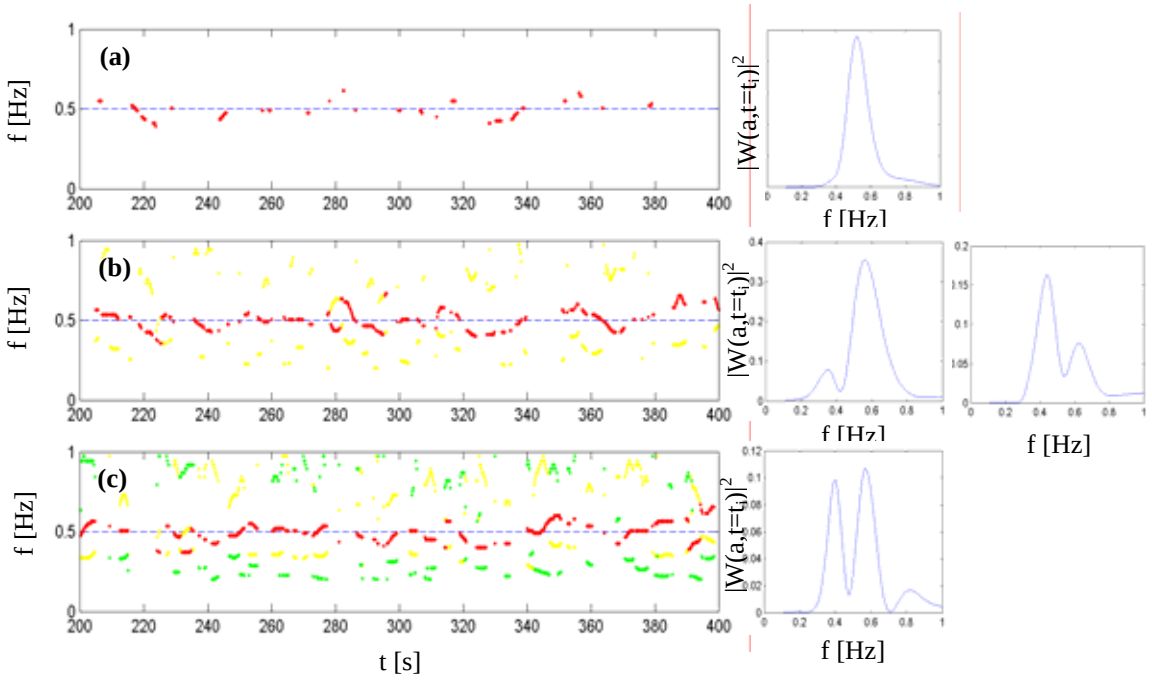

FIGURE 7.21. Example 10: instantaneous frequency identified from (a) single mode spectra; (b) bi-modal spectra; (c) multi-mode spectra (red → green indicates highest to lowest energy components at that time step), with example of each instantaneous spectra class shown at the right

spectrum, serve as a microscope for studying the evolution of multiple harmonic components within the response. In particular, the alternating characteristic of the two dominant components centered near 0.5 Hz represents a temporal variation of the fundamental wave frequency that would be obscured in traditional Fourier analysis. This observation, coupled with the intermittent characteristics, further highlights the richness of the energy distribution in the wave profile, similar to the findings in Huang et al. (1998).

7.6 Discussion: Processing Concerns and Performance in Noise

While the examples provided herein have reassessed the performance of the continuous wavelet transform and the Hilbert transform with Empirical Mode Decomposition for a number of nonlinear and nonstationary systems, these results are not achieved without a proper understanding of each approach. For example, the successful application of the Hilbert transform is predicated on the IMFs satisfying certain narrowband and symmetry conditions. The quality of the IMFs produced by EMD is dependent upon the spline fit procedure employed, particularly near the ends, where cubic spline fits have wide swings that may eventually propagate inward and corrupt the entire data span. Corrective measures such as the inclusion of characteristic waves are discussed in Huang et al. (1998) and should be applied as needed to insure optimal performance. The use of spline fitting or oversampling of the data will additionally be required to determine the derivatives of the phase with sufficient accuracy. This is true of the wavelet analysis as well if the phase is used to estimate the instantaneous frequencies, though in the examples provided it is often sufficient to use the maxima of the transform for this identification, alleviating the need for any differentiation.

The sifting process used to generate the IMFs should also be used with care, since when applied in excess, it can completely obliterate meaningful amplitude modulations and yield purely frequency-modulated components. Thus, the user of the EMD approach should be well versed in determining when to terminate the sifting process and the suitability of the resulting IMFs, as well as in distinguishing if any corruptions by the spline fits are present.

By the same token, the users of continuous wavelet transforms must be cognizant that the result of their analysis relies heavily on the parent wavelet employed. As stated by Lewalle (1998) “Each wavelet shape is selected by the user – as is the conventional sine wave [of Fourier Analysis] -, and this limits the type of questions that can be answered.” Thus the choice of an appropriate parent wavelet will vary in each application and will greatly influence the results, though the Morlet wavelet is a natural choice for any analysis seeking to replicate local Fourier perspectives. Further, “the freedom to choose between wavelets implies the responsibility to interpret the results accordingly” (Lewalle, 1998). The poor interpretation of Morlet wavelet results in Huang et al. (1998) was largely responsible for many of the misleading statements surrounding wavelet performance. Specifically, when using the Morlet wavelet, to completely exploit the resolution capabilities, users should make careful selections of the central frequency f_o within the framework presented in Chapter 4. A lack of understanding of the durations of the dilated time and frequency windows of the analysis can yield misleading results and may have in part led to the poor results noted in the literature. Though Huang et al. (1998) did not report the exact central frequency used in their Morlet wavelet analysis, statements referring to the Morlet wavelet as “Gaussian enveloped sine and cosine wave groups with 5.5 waves” would hint at the use of a central frequency near $5/(2\pi)$, the default value in the MATLAB^{TM} Wavelet Toolbox. In this form, the undilated Morlet wavelet would have only a few cycles of oscillation in the Gaussian window, as shown in Figure 7.22a, clearly not appropriate for the wide array of signals analyzed here. In fact, the discussion of the Stokes wave highlighted the fact that a high frequency resolution wavelet analysis begins to approach the Fourier harmonic analysis and loses much of its

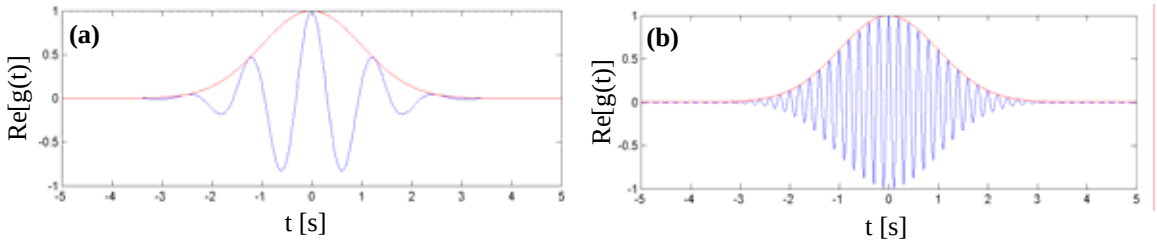

FIGURE 7.22. (a) Real component of Morlet wavelet basis function for f_o=5/(2π) Hz; (b) real component of Morlet wavelet basis function for f_o=5 Hz

temporal sensitivity, while a lower frequency analysis can uncover the nonlinear characteristic. On the other hand, as demonstrated in Example 5, for the two closely spaced waves, a higher value of central frequency was necessary to separate the two modes. These higher values of central frequency permit improved frequency resolution by packing more waves into the Gaussian window, as shown in Figure 7.22b. Therefore, it should be noted that the value of this central frequency was changed throughout this chapter and this work in order to properly tune the parent wavelet. As such discussions are not mentioned in Huang et al. (1998), it is assumed that this value was not changed for each example in that study, a fact reflected by the poor wavelet results in that work.

Further, to obtain the wavelet instantaneous frequency spectrum, users must extract the ridges of the transform. By visual inspection, one can clearly discern the highest energy in the contour map, but to obtain a skeleton plot comparable to the Hilbert spectrum, ridges must be extracted, most easily by using the local maxima of the modulus of the transform. In cases where excessive noise induces spurious local maxima, the use of more sophisticated extraction techniques is required (Carmona et al., 1998). These

approaches use the smoothness of the ridge as an additional condition in the minimization scheme and require additional experience and programming, as discussed in Chapter 4.

Finally, the examples provided in this chapter have not explored either technique's performance in the presence of noise. Huang et al. (1998, 1999) did examine several sets of measured data from earthquake, wind and wave events, which can be assumed to contain some noise, from which the HSA was able to extract IMF components and their instantaneous frequencies. However, in general, the performance of HSA in noise is dictated by approach used to accomplish the differentiation required to obtain the instantaneous frequency from the phase and the ability of the EMD process to separate noise from the signal. The differentiation scheme is particularly crucial in the accurate identification of the instantaneous frequency. A comparison of the performance of several of these differentiation approaches in the presence of noise was conduced by Boashash (1992b) and revealed that some approaches using the phase information (e.g. central difference) may have considerable difficulty in noisy situations, requiring the use of more sophisticated approaches such as Maximum Likelihood Estimators. However, all of these discussions are relevant only to the Hilbert transform itself and not the overall Hilbert Spectral Analysis. It is possible that the inclusion of EMD prior to the application of the HT may have enhanced the performance discussed by Boashash (1992b). As a result, these findings do not necessarily demonstrate a shortcoming of HSA.

On the other hand, approaches that utilized the peaks in the modulus of time-frequency distributions such as the STFT or WVD to determine the instantaneous frequency were some of the most accurate in noisy situations (Boashash, 1992b),

supporting the use of this approach for the continuous wavelet transforms in this study. This point was also made by Carmona et al. (1997), who indicated that the phase might be difficult to control in noisy situations, motivating the use of the wavelet modulus for the extraction of ridges. Delprat et al. (1992) illustrated the ability of wavelet ridges to identify a bat sonar signal embedded in noise with amplitude comparable to the signal itself. This theory of wavelet ridges was also used by Staszewski (1997, 1998) to examine the ability of wavelets to perform system identification by adding known levels of white noise to simulated structural responses and found the technique to be quite robust, even in the often problematic estimation of structural damping. The robustness of time-varying frequency system identification by wavelets in the presence of noise was also quantified by Ghanem & Romeo (2000), while the use of wavelets for cleaning noisy observations was previously advocated by Coca & Billings (1997) and Gurley & Kareem (1999).

7.7 Discussion: A Fundamental Difference

The examples presented in this chapter have highlighted a fundamental difference between the wavelet analysis and that provided by the HSA: the manner in which physically meaningful intrawave or subcyclic frequency modulations are identified. The concepts of subcyclic oscillations, denoting changes in frequency that occur within a single cycle of oscillation, and supercyclic oscillations, denoting changes in frequency that occur over the course of one or more cycles or due to rapid changes in amplitude, are introduced to help explain the performance of the continuous wavelet transform and the Hilbert spectral analysis. As exercises in nonlinear systems have indicated, the presence of intrawave modulation may be rationalized as a physical phenomenon by both

techniques. In the wavelet interpretation of these systems, the fitting of wavelets or small waves of a given scale (frequency) tends to capture local mean trends in the instantaneous frequency of the system. For systems undergoing significant amplitude fluctuations or marked supercyclic oscillations, which would induce significant frequency variations, such as in the Duffing, Lorenz and Rössler examples, the wavelet instantaneous frequency captured fundamental supercyclic frequency modulations; however the subtle characteristics of intrawave frequency variation are not held in this measure. As Priestley (1988) indicated, the instantaneous frequency is an averaged measure of the frequencies present at that instant in time. So for the Morlet wavelet, it is the frequency of the best-fit sinusoid to the data over a shortened time window. However, sinusoids at neighboring frequencies may also show some similitude with the signal over this same interval, indicating oscillations that are not perfectly sinusoidal but deviate in some way. This nonlinearity represented by subcyclic deviations must locally be treated by a summation of neighboring harmonics. The spread of these neighboring frequencies is captured by the instantaneous bandwidth measure presented in this chapter. When viewed in totality, the wavelet instantaneous frequency represents an averaged sense of the frequency of the system with time, and the bandwidth or deviation from this mean value, indicative of evolving fluctuations in signal frequency content. As demonstrated in the case of Stokian waves, these nonlinearities can be so subtle that they often only reveal themselves in the wavelet's instantaneous bandwidth. Thus the Hilbert instantaneous frequency captures both super and subcyclic oscillations simultaneously, while the wavelet separates the two classes of oscillations, with its instantaneous frequency detecting the presence of any supercyclic oscillations and the instantaneous bandwidth capturing the subcyclic features.

7.8 Conclusions

This chapter revisited many of the continuous wavelet examples used to establish the efficacy of the Hilbert Spectral Analysis, not to advocate the use of one over the other, but rather to represent both in a fair light and dispel some of the misconceptions surrounding continuous wavelets for these applications. To provide a fair comparison, a wavelet instantaneous frequency spectrum was introduced, which plots the wavelet estimates of instantaneous frequency as a function of time. This perspective produces the same skeleton plot as the Hilbert spectrum, which also must estimate instantaneous frequency. Throughout the examples provided using this representation, the judicious choice of the central frequency in the Morlet wavelet is reiterated, as improper temporal resolution of the wavelet is shown to produce results that approach a traditional Fourier analysis, while refined temporal resolutions were capable of identifying nonlinear and nonstationary signal characteristics.

While the physical meaning of the HSA result was questioned in two examples involving closely spaced cosine waves and an amplitude modulated, constant frequency oscillator, the two approaches provided comparable evidence of nonlinear behavior for a number of classical examples. However, this evidence was presented in distinctly different manners: the instantaneous frequency of Hilbert spectral analysis detects both subcyclic and supercyclic frequency modulations, while the wavelet instantaneous frequency can only detect supercyclic frequency characteristics and instead relies on the additional measure of the instantaneous bandwidth to provide subcyclic information. This finding is expected, as the continuous wavelet fits small waves over a local window in

time. The instantaneous frequency will in this case truly correspond to the scale producing the best local fit of the wavelet to the data. However, this analysis is a local summation of wavelets and therefore the number of additional wavelets at neighboring scales required to truly fit the data also provides meaningful information on the spread of frequencies about this instantaneous or best fit mean. The instantaneous bandwidth measure provides this information and the key to uncovering subcyclic phenomena. Therefore, the selection of one approach over the other is entirely dependent on the perspective desired.

CHAPTER 8

WAVELET SYSTEM IDENTIFICATION IV: FREQUENCY AND DAMPING ESTIMATION FOR CIVIL ENGINEERING STRUCTURES

8.1 Introduction

As motivated previously, the dual time-frequency character of wavelet transforms allows adaptation of both traditional time and frequency domain system identification approaches to examine non-linear and non-stationary data. The adaptations of spectral-based approaches in this research were presented in Chapters 5, 6 and 7. In particular, the coherence discussions in Chapter 6 foreshadowed some of the unique processing challenges associated with this new analysis domain. Similarly, when utilizing time-domain information from wavelet coefficients in order to conduct more precise system identification of dynamic properties, a number of the processing challenges associated with wavelets, introduced and largely addressed in Chapter 4, have increasing relevance. Although such challenges did not surface in prior applications concerned with mechanical systems, characterized by higher frequency, broader-band signals, the transition to the time-frequency domain for the analysis of Civil Engineering structures highlighted the need to understand more fully the issues chronicled in Chapter 4, especially for the popular Morlet wavelet. In particular, as these systems may possess

longer period motions and thus require finer frequency resolutions, the specific impact of end effects becomes increasingly apparent. This chapter discusses these considerations in the context of the wavelet's multi-resolution character and includes guidelines for selection of wavelet central frequencies, highlights their role in the complete modal separation measure introduced in Chapter 4, and quantifies their contributions to end effects errors and their residual impacts on estimated instantaneous frequency and more markedly, damping.

8.2 Previous Applications of Wavelets for System Identification

The Morlet wavelet and other classes of discrete and continuous wavelets have been applied to a variety of problems ranging from image and acoustic processing to fractal analysis. This study has showcased a number of these applications in the context of Civil Engineering and the adaptation of wavelet transforms to situations where Fourier transforms were traditionally used to define quantities of interest. Meanwhile, the more rigorous application of wavelets to system identification of mechanical systems is still advancing, but shows great promise thanks to the suite of parent wavelets available and flexibility inherent in the wavelet transform itself, allowing the use of many traditional time and frequency domain-based approaches.

In terms of analysis stemming from the frequency domain, the instantaneous spectrum introduced in Section 4.4 can be utilized in more traditional frameworks for system identification via wavelet-based frequency response functions (Hartin, 2001; Staszewski & Giacomin, 1997; Kyprianou & Staszewski, 1999), as well as the coherence applications in Chapter 6 and the general applications system identification in Chapters 5

and 7. A number of other researchers have also noted this dual identification potential, integrating the wavelet transform with number of system identification schemes traditionally based upon Fourier transforms, e.g. Coca & Billings (1997), Ghanem & Romeo (2000). Huang et al. (1994) used its localization and multi-resolution properties to identify the mass, stiffness, and damping matrices from measured accelerations, velocities, displacements and ground accelerations of MDOF systems to illustrate the ability of the wavelet-based approach to accurately identify stiffness and damping from short earthquake time histories, even in the presence of noise. Robertson et al. (1998a) used the discrete form of the transform to extract impulse response functions from measured system inputs and response. In comparison to traditional Fourier-based approaches, the DWT-based approach provided superior results, even with limited ensembles under various types of excitations. A second study then used this approach along with the Eigensystem Realization Method (ERA) to identify the dynamic properties and mode shapes of the system subjected to various excitations (Robertson et al., 1998b). It should be noted that in the course of these studies, various parent wavelets were employed in continuous and discrete forms of the transform.

As discussed previously, the analysis of free vibration or impulse response function (IRF) from a structure serves as one of the simplest means to identify the frequency and damping in the time domain. In the case of single degree of freedom (SDOF) structures, this identification may be easily conducted using techniques such as the logarithmic decrement, the Hilbert transform in the context of analytic signal theory, or a least squares fit of the decay curve. However, in cases where multiple degrees of freedom (MDOF) are participating, the identification becomes more involved and

necessitates the use of bandpass filtering or more advanced MDOF identification schemes. Recognizing the ability of wavelet transforms to decouple multi-component signals and their dual potential to allow analysis within the time domain, a number of researchers began applying this technique in various forms for analysis of impulse or free vibration response, e.g. Hans et al. (2000) and Lamarque et al. (2000). These concepts were overviewed in Section 3.7.4 within the broader context of a discussion on wavelet ridges and analytic signal theory in Section 3.7.

Furthermore, as the damping and natural frequency for a nonlinear mechanical system may be time-varying, piecewise linear fits to the phase and the natural log of the amplitude can be used to identify the system as it evolves with time. Variations on these concepts in Section 3.7 have been utilized by Ruzzene et al. (1997) and Staszewski (1997) to illustrate their applicability to linear system identification. Staszewski (1998) later demonstrated the applicability of the approach for non-linear systems, where the time-varying estimates of frequency and damping are truly required. Though Staszewski's work (1997, 1998) was primarily directed toward mechanical systems with fundamental frequencies larger than most found in Civil Engineering, Ruzzene et al. (1997) and Hans et al. (2000) provided examples geared specifically toward Civil Engineering, applying the techniques to full-scale data, though without any consideration of the processing concerns detailed in this chapter. When considering Civil Engineering structures of even longer period, for which the characteristics of narrowbanded response become increasingly prevalent, these previously unaddressed processing concerns highlighted in this chapter begin to surface more critically. As these systems are usually of longer period, frequency resolutions must be refined to insure modal separation. This

in turn results in an increase of end effects errors that can have a dramatic influence on the quality of wavelet amplitudes and modal properties such as damping. The occurrence of these phenomena is rationalized in this study for the popular Morlet wavelet and a framework for the analysis of ambient vibration data using wavelets and the Random Decrement Technique discussed in Chapter 2 is introduced. Demonstrations on simulated and measured full-scale data within this chapter highlight these important considerations and the manner in which the provisions in Chapter 4 are applied in wavelet-based system identification schemes for Civil Engineering applications.

8.3 Influence of End Effects in System Identification: Spectral Measures

One of the more notable signal processing concerns in the identification framework for wavelets is end effects, introduced previously in Section 4.2.2. Their impacts can be examined in both the temporal and spectral representations of wavelet transforms. While the influence of end effects in the frequency domain was clearly visualized in Figure 4.8, they may be further quantified via time-varying spectral measures. The signal under consideration, shown in Figure 8.1a, is the free vibration response of a SDOF oscillator with natural frequency f_n of 0.15 Hz and critical damping ratio ξ of 0.01. In the case of a f_o = 1 Hz wavelet analysis, the end effects have no influence on the estimate of instantaneous frequency from the ridge of the transform, but have a considerable effect on the amplitude of the wavelet skeleton for the first and last few cycles of oscillation, as shown in Figure 8.1b,e. The vertical dotted lines mark integer multiples of Δt for this analysis in the end effects measure in Equation 4.9. It is not until $3\Delta t$ that the end effects on the wavelet skeleton amplitude diminish. This is rectified by applying the padding

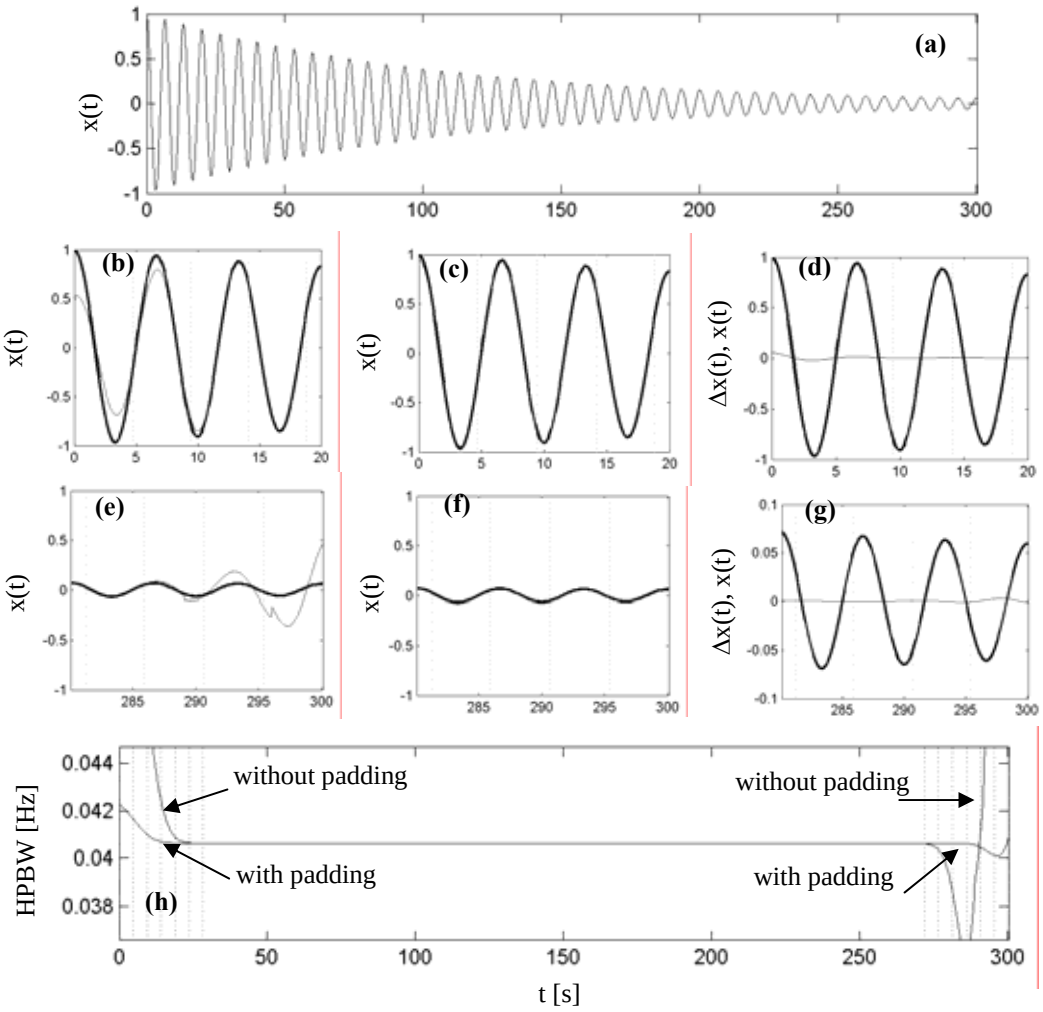

FIGURE 8.1. (a) Signal; (b) & (e) signal (dark) and wavelet skeleton (light) at ends without padding; (c) & (f) signal (dark) and wavelet skeleton (light) at ends with padding; (d) & (g) signal (dark) and difference between signal and wavelet skeleton (light) at ends with padding; (e) bandwidth estimate with & without padding

operation for $\beta = 4$, as shown in Figure 8.1c,f. After doing so, the wavelet skeleton can hardly be discerned from the actual signal, though as Figure 8.1d,g reveals, a slight deviation of the amplitude is still present at the very beginning and end of the signal, though it is small relative to the signal's amplitude at these points in time. The half-power bandwidth identified from the wavelet instantaneous spectra is constant, as expected for this linear oscillator, with the exception of the end effects region. As shown in Figure 8.1h, the bandwidth measure, being more sensitive, is significantly influenced by the end effects. When padded with $\beta = 4$, the bandwidth accuracy is vastly improved, though Figure 8.1h demonstrates that within the first $3\Delta t$, the bandwidth is still deviating, a result that cannot be fully improved with larger values of β. This is due to the fact that the remaining slight inaccuracies in the amplitude lead to a more marked inaccuracy in the sensitive bandwidth measure. Note also that the bandwidth of the resulting wavelet instantaneous spectra are larger than their Fourier equivalent, as a result of the windowing applied by the Gaussian function of the Morlet wavelet, a feature demonstrated previously Chapter 4.

8.4 Influence of End Effects in System Identification: Time Domain

Time domain system identification on the system in Figure 8.1a may proceed as discussed in Section 3.7.4. As a result of the reflective padding operation, the estimation of damping in the time domain is also enhanced, though not completely rectified. As shown in Figure 8.1e, the deviations in the amplitude with padding are slight and diminish with each cycle of oscillation, but still have marked impact for the more sensitive estimation of damping in this system. Note that the bandwidth in the previous

section and decay envelope in the previous section are both the major descriptors of damping in mechanical oscillators and are most significantly impacted by residual end effects. The error in the wavelet skeleton's amplitude is most significant at $t = 0$, though reduced from 50% to about 5% with the addition of padding. This does not affect the estimation of instantaneous frequency, which is consistently within 1%. Table 8.1 lists the identified damping from each cycle of the decay. The time span of each cycle is provided in parenthesis and less reliable values of damping are shaded in gray. As shown in column one, without padding, the damping can only be reliably estimated beyond about $5\Delta t$. Therefore, direct application of the techniques discussed in Ruzzene et al. (1997) and Staszewski (1998) for such narrowband systems should proceed using only the wavelet data beyond $5\Delta t$, though the authors make no mention of this nor account for this in their estimations. However, the padding operation introduced in this study leads to a vast improvement in the estimates from the first three cycles and produces highly accurate estimates after only $3\Delta t$, allowing more of the signal to be used in system identification.

TABLE 8.1

ESTIMATE OF DAMPING FROM WAVELET SKELETON OF SDOF SYSTEM

	$f_o = 1$ Hz, $\beta = 0$	$f_o = 1$ Hz, $\beta = 4$	$f_o = 0.5$ Hz, $\beta = 4$	$f_o = 0.25$ Hz, $\beta = 4$
Critical End Effects Region	$5\Delta t = 23.57$ s	$3\Delta t = 14.14$ s	$3\Delta t = 7.07$ s	$3\Delta t = 3.53$ s
1st Cycle (0-6.7 s)	-0.0678	0.0034	0.0054	0.0097
2nd Cycle (6.7-13.3 s)	-0.0123	0.0084	0.0099	0.0102
3rd Cycle (13.3-20.0 s)	0.0067	0.0098	0.0099	0.0101
4th Cycle (20.0-26.7 s)	0.0099	0.0099	0.0099	0.0101

Note that since the identification of this system is proceeding in the time domain, a reduced value of f_o can be used to diminish end effects, though sacrificing the frequency resolution. When doing so, it becomes possible to identify the damping within 1% accuracy using virtually the full length of padded data, as demonstrated in the last two columns of Table 8.1. While this is attractive, it is demonstrated in the following section that this may not be plausible for MDOF systems, particularly those with closely spaced modes.

8.5 System Identification from Free Vibration: MDOF Example

Additional issues associated with wavelet system identification are can be demonstrated through a MDOF example, where the issues of modal separation can be most clearly investigated. Recall that the Morlet wavelet-based analysis allows flexibility in the value of the central frequency f_o to obtain desired resolutions, as discussed previously in Chapter 4. This selection becomes critical if closely spaced modes are suspected. Staszewski (1997) discussed the use of shifted Morlet wavelets for separation of closely spaced, high frequency modes; however, in the case of low-frequency systems, the judicious selection of the central frequency of the Morlet wavelet can similarly accomplish the same operation directly. This is illustrated by the analysis of 100 seconds of data (shown in Figure 8.2), sampled at 10 Hz from the impulse response of the following system MDOF system

$$\mathbf{m}\ddot{\mathbf{x}} + \mathbf{c}\dot{\mathbf{x}} + \mathbf{k}\mathbf{x} = \boldsymbol{\delta}(t) \tag{8.1}$$

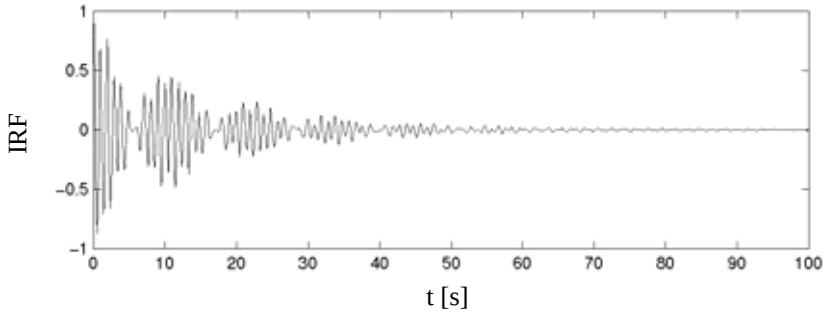

FIGURE 8.2. Impulse response function of MDOF system with closely spaced modes

where $\boldsymbol{m}$, $\boldsymbol{c}$ and $\boldsymbol{k}$ are the mass, damping and stiffness matrices, respectively, $\boldsymbol{x}$ is the vector of displacements, $\dot{\boldsymbol{x}}$ and $\ddot{\boldsymbol{x}}$ are the first and second derivatives of $\boldsymbol{x}$, and $\boldsymbol{\delta}(t)$ is the unit impulse function. In order to achieve the desired frequency characteristics, the following mass and stiffness matrices were defined

$$\mathbf{m} = m\mathbf{I} \text{ and } \mathbf{k} = k\begin{bmatrix} 4 & -1 & 0 \\ -1 & 2 & -1 \\ 0 & -1 & 4 \end{bmatrix} \qquad (8.2\text{ a,b})$$

where $\boldsymbol{I}$ is the identity matrix, m=1000 kg and k=10 kN/m. As the system is assumed to have a critical damping ratio ξ = 0.01 in each mode, a damping matrix can be defined as

$$\boldsymbol{c} = \left[\boldsymbol{m}\boldsymbol{\Phi}\boldsymbol{M}^{-1}\right]\begin{bmatrix} 2\xi\omega_1 M_1 & 0 & 0 \\ 0 & 2\xi\omega_2 M_2 & 0 \\ 0 & 0 & 2\xi\omega_3 M_3 \end{bmatrix}\left[\boldsymbol{M}^{-1}\boldsymbol{\Phi}^T\boldsymbol{m}\right] \qquad (8.3)$$

where $M_{1,2,3}$ are the modal masses of the modal mass matrix $\boldsymbol{M}$, the modal frequencies are $\omega_{1,2,3} = 2\,\pi f_{1,2,3}$, and $\boldsymbol{\Phi}$ is the matrix of mode shapes. The response at the third degree of freedom of the MDOF system as the result of a unit impulse at that location was then

generated via state-space simulation of Equation 8.1. Note that the stiffness and mass matrices in Equation 8.2a,b were selected to achieve a response with both low frequency content and closely spaced modes. The resulting frequencies are 0.567, 1.006 and 1.095 Hz, and all three modes have a critical damping ratio of 0.01. The latter two modes are within 10% of one another, requiring a refined frequency resolution, and thus providing an ideal venue in which to explore the significance of f_o for optimal modal separation.

Without a priori knowledge of the system, the selection of a central frequency for analysis should initiate from information gathered through a visual inspection of the time series, as discussed in Chapter 5. Such inspection indicates that one obvious period of oscillation is on the order of 1 s. As a general rule of thumb, a frequency resolution of one-tenth the period of oscillation is desirable, i.e. $\Delta f_{1,2}$ = 0.1 Hz. This serves as a starting point for the analysis and may be refined even further in subsequent analyses to uncover additional details. For the purposes of demonstration, varying levels of α in Equation 4.6 are used to demonstrate the influence of analysis window overlap in the adjacent frequency bands. Assuming α = 1 defaults to a direct application of Gabor's mean square duration and necessitates a minimum wavelet central frequency of 2.25 Hz. To simplify, 3 Hz is chosen for analysis. As suggested previously, α = 2 and 3 provide a more accurate means of modal separation. To demonstrate the influence of these parameters, f_o = 6 Hz and 8 Hz wavelet analyses are also performed on the same signal. Table 8.2 lists the resulting frequency and temporal resolutions as defined by Equations 4.5 and 4.8.

TABLE 8.2

WAVELET-BASED IDENTIFICATION OF MDOF SYSTEM WITH CLOSELY SPACED MODES

MODE	Resolutions		Actual		Analytic Signal ID			Ridge IF & Log Dec ID		
	Δt_i [s]	Δf_i [Hz]	f_n [Hz]	ξ	avg[f_n] [Hz]	avg[ξ]	CoV[ξ]	avg[f_n] [Hz]	avg[ξ]	CoV[ξ]
					f_o=3 Hz, β=0					
1	3.74	0.021	0.567	0.01	Incomplete Modal Separation					
2	2.11	0.038	1.006	0.01						
3	1.94	0.041	1.095	0.01						
					f_o=6 Hz, β=0					
1	7.49	0.011	0.567	0.01	0.567	0.0098	4.48%	0.566	0.0099	4.61%
2	4.21	0.019	1.006	0.01	1.006	0.0099	4.43%	1.005	0.0099	8.15%
3	3.87	0.020	1.095	0.01	1.095	0.0098	10.0%	1.094	0.0098	10.4%
					f_o=8 Hz, β=0					
1	9.98	0.008	0.567	0.01	0.567	0.0098	6.58%	0.565	0.0097	5.93%
2	5.62	0.014	1.006	0.01	1.006	0.0098	4.79%	1.008	0.0097	9.48%
3	5.17	0.015	1.095	0.01	1.095	0.0098	3.98%	1.098	0.0096	12.5%
					f_o=6 Hz, β=4					
1	7.49	0.011	0.567	0.01	0.567	0.0099	1.12%	0.566	0.0100	2.47%
2	4.21	0.019	1.006	0.01	1.006	0.0100	1.53%	1.005	0.0101	7.09%
3	3.87	0.020	1.095	0.01	1.095	0.0100	8.93%	1.095	0.0100	13%
					f_o=8Hz, β=4					
1	9.98	0.008	0.567	0.01	0.567	0.0099	1.74%	0.565	0.0099	2.91%
2	5.62	0.014	1.006	0.01	1.006	0.0100	1.13%	1.008	0.0101	8.58%
3	5.17	0.015	1.095	0.01	1.095	0.0100	0.91%	1.098	0.0098	10.4%

8.5.1 Ridge Extraction and Wavelet Instantaneous Spectra

The MDOF system identification procedure employed here is schematically represented in Figure 8.3. In this case the input to the wavelet framework comes directly from impulse response functions, following Track B in the figure. As shown in Figure 8.4a, the wavelet instantaneous frequencies identified from the ridges for f_o = 3 Hz successfully identify the first mode, but have difficulty fully separating the second and third modes, clearly indicating that the choice of central frequency did not provide adequate frequency resolution. The ridge identification using Equation 4.25 becomes very poor beyond 80 s –

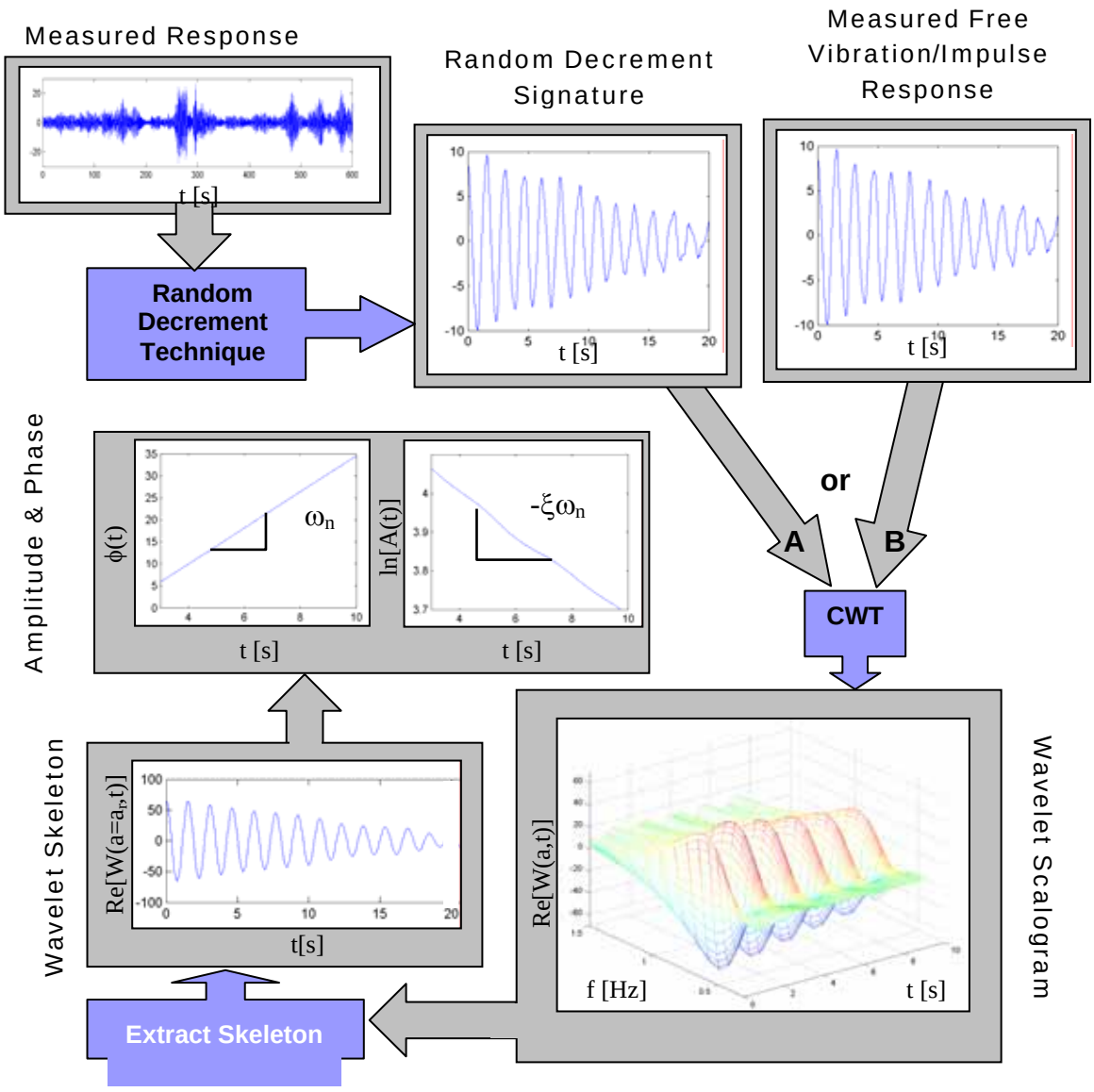

FIGURE 8.3. Wavelet system identification framework, Track A for ambient vibrations or Track B for measured free vibration or impulse response

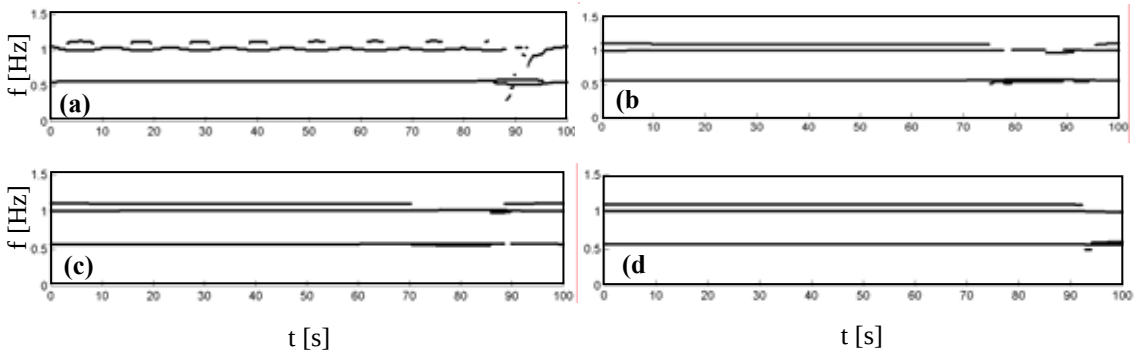

FIGURE 8.4. Instantaneous frequencies identified from ridges of wavelet transform for (a) f_o = 3 Hz, (b) f_o = 6 Hz, (c) f_o = 8 Hz and (d) f_o = 6 Hz with padding

a direct consequence of the diminished amount of signal energy at this point and demonstration of the influence of end effects. Figure 8.4b reveals that separation was possible for f_o = 6 Hz, again with some difficulty at the final seconds of the signal. The analysis for f_o = 8 Hz in Figure 8.4c merely extends the end effect region deeper into the signal. With the introduction of the padding scheme introduced in Chapter 4 to the case of f_o = 6 Hz, the slight end effects at the initiation of the signal are remedied in Figure 8.4d and diminished at the termination of the signal, although the lack of signal energy in this region makes identification of the highest mode difficult.

In general, the influence of end effects is not observed to significantly influence instantaneous frequencies, as discussed in Section 8.4. To demonstrate, the instantaneous spectra are provided in Figure 8.5, verifying the concentration of energy at the ridge frequencies. Note that Figures 8.5a and 8.5b illustrate the intermittency of modal separation evident in the first mode ridge (Figure 8.4a) for the f_o = 3 Hz analysis. Further, the progressive narrowing of the instantaneous spectral bandwidth within the frames,

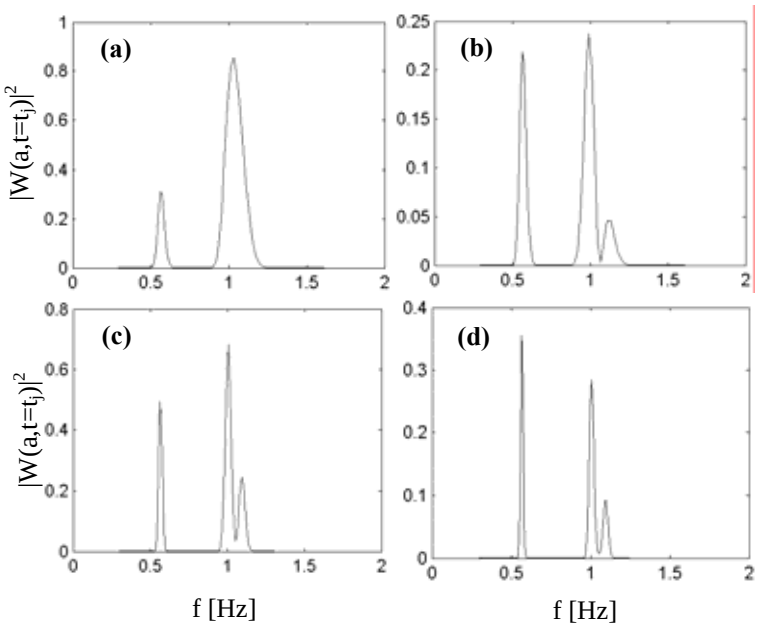

FIGURE 8.5. Instantaneous wavelet spectra for (a) f_o = 3 Hz when two modes are present, (b) f_o = 3 Hz when three modes are present, (c) f_o = 6 Hz and (d) f_o = 8 Hz

thereby indicating more complete modal separation, illustrates the refinement of frequency resolution as central frequency is increased.

8.5.2 Wavelet Skeletons and End Effects

The wavelet skeleton introduced in Chapter 3 can be extracted from the ridges identified in Figure 8.3, with the real component being proportional to the signal itself. Figure 8.5a reiterates the inability of the f_o = 3 Hz analysis to separate the two higher modes. The analyses in Figures 8.5b and 8.5c further demonstrate that such modal separation is possible with sufficient frequency resolution. It was noted in Section 8.4 that, in general, the wavelet skeletons are not capable of accurately capturing the amplitude of the signal

for the first $3\Delta t_i$ due to the end effects phenomenon, requiring $\beta = 3$ in Equation 4.9. These critical regions are marked by the vertical dotted line in each plot. Within this region, the initiation of the impulse response function in Figure 8.6 manifests a rounded hump, very evident in the second mode in Figures 8.6b and 8.6c. In addition, at the end of the signal, a flare in amplitude also occurs in this $3\Delta t_i$ region, intensifying with time. Particularly in the case of f_o = 8 Hz, the end effects regions for the first mode can consume a significant portion of the signal. It becomes evident that for high-resolution analyses, the end effects at low frequencies leave little useable signal for reliable system identification. Note that such marked end effects were not apparent in previous work due to the smaller central frequencies employed, as a result of the attention toward higher frequency phenomenon and the lack of closely spaced modes. However, in the analysis of many Civil Engineering structures, such manifestations should be expected. In efforts to diminish the presence of end effects, the reflective padding procedure of Chapter 4 is employed in Figure 8.6d, revealing the marked improvement in the wavelet approximations of the signal, shifting the vertical bars denoting the $3\Delta t_i$ regions engulfed by end effects to $t = 0$ and $t = T = 100$ s, essentially preserving the entire signal.

8.5.3 System Identification via Wavelet Amplitude and Phase

Figure 8.7 displays the phase and amplitude curves of the wavelet-transformed data for each mode, later used to identify frequency and damping for the f_o = 6 and 8 Hz analyses, which produced meaningful wavelet skeletons. For this system with constant dynamic properties, these should be straight lines, though some minor rippling occurs in the amplitude envelopes, particularly near the end effects regions. Using the analytic signal

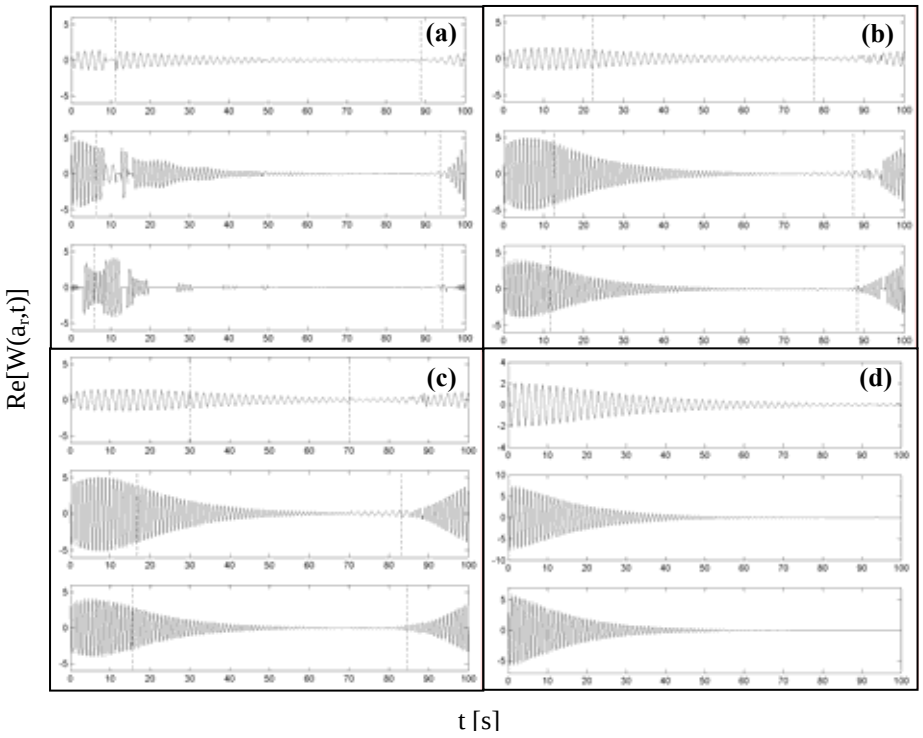

FIGURE 8.6. Real component of wavelet skeleton – each panel contains skeleton for the ridge associated with modes 1, 2 and 3, respsectivley, for (a) f_o = 3 Hz, (b) f_o = 6 Hz, (c) f_o = 8 Hz and (d) f_o = 6 Hz with padding. Dotted vertical line demarks the $3\Delta t_i$ region of end effects

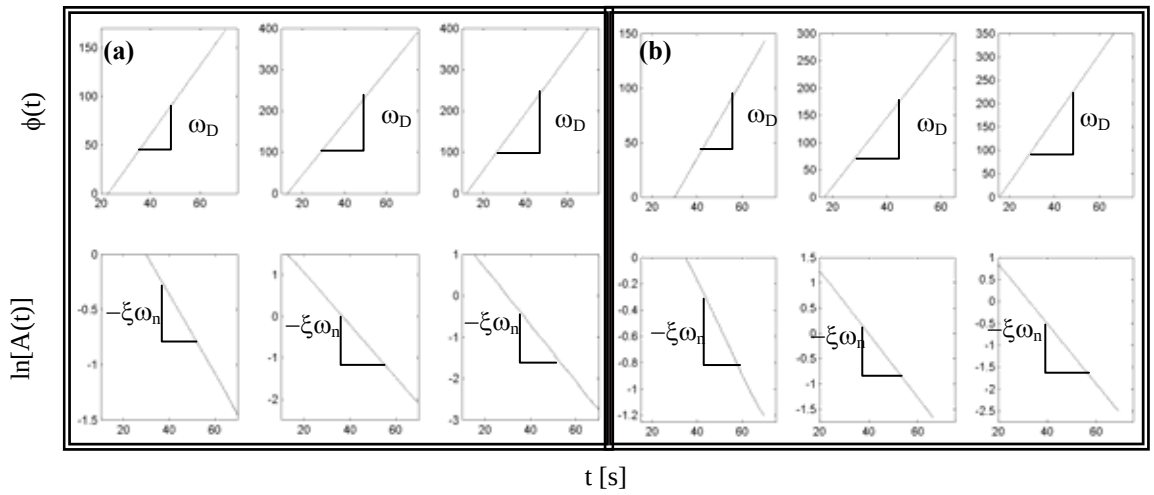

FIGURE 8.7. Wavelet phase and amplitude curves for system identification of MDOF system (solid) with linear least squares fit (dotted), for (a) f_o = 6 Hz and (b) f_o = 8 Hz. Each panel contains data for modes 1, 2 and 3 from left to right

theory discussed previously, the frequency and damping may be identified via Equations 3.35 and 3.34, through a piecewise linear fit to the phase and the natural log of the wavelet amplitude along the ridges, respectively. While the identification of frequency is generally not difficult, damping proves to be a far more elusive parameter to identify. As shown in Figure 8.8, the piecewise fits of the amplitude curves in Figure 8.7 produce damping estimates that gradually approach the actual damping of 0.01. The initial inaccuracies are the result of end effects, producing negative values of damping in Figures 8.8a and 8.8c due to the rounding of the skeleton shown in Figures 8.6b and 8.6c. As discussed in Section 8.4, without padding, damping values do not stabilize until $5\Delta t_i$, marked by the third vertical bar in each plot. By introducing the padding operation, Figures 8.8b and 8.8d, the signatures do not manifest negative damping and stabilize within $3\Delta t_i$. As discussed previously, the manifestation of end effects in the wavelet amplitudes can be minimized through the reflective padding procedure; however, slight inaccuracies in the amplitude remain, on the order of a few percent, for the first $3\Delta t_i$. For the more sensitive bandwidth measures, the presence of even slight errors in the amplitude translates into more significant deviations in parameters like damping. Still, the introduction of padding eliminates negative damping estimates and stabilizes the damping estimate sooner, though system identification for the purpose of damping estimation should not be performed on the first or last $3\Delta t_i$ of the wavelet skeleton. In light of this, the fact that many Civil Engineering structures possess very low levels of damping is actually a benefit, as the IRFs will take longer to decay, leaving adequate amounts of data for analysis despite neglecting some regions.

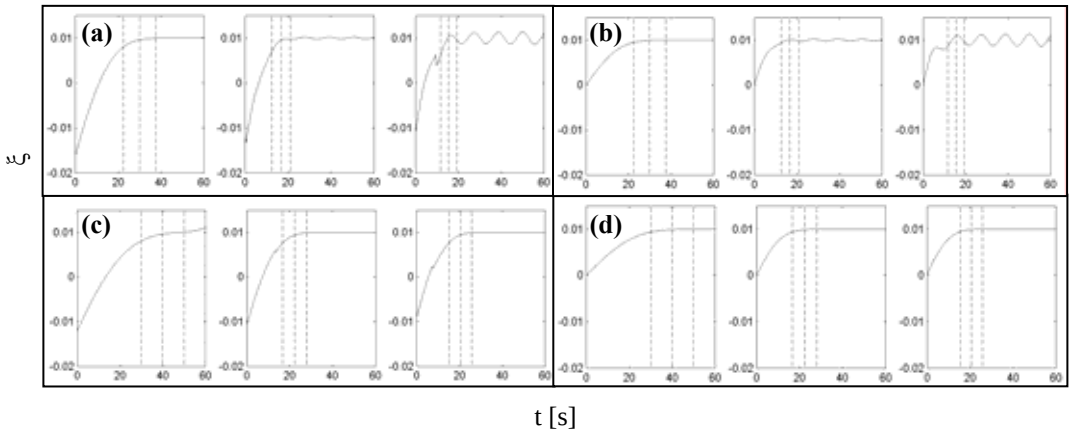

FIGURE 8.8. Identification of damping from piecewise fit to amplitude curves of MDOF system for (a) f_o = 6 Hz, (b) f_o = 6 Hz with padding, (c) f_o = 8 Hz, and (d) f_o = 8 Hz with padding. Each panel contains data for modes 1, 2 and 3 from left to right. Dotted vertical line demarks the $3\Delta t_i$, $4\Delta t_i$ and $5\Delta t_i$ end effects regions

By constraining the identification of the system to the regions beyond $3\Delta t_i$ of ends, the frequency and damping can be identified on average with considerable accuracy, as summarized in Table 8.2 provided previously in Section 8.5. The natural frequencies of the system show little fluctuation and are identified with precision and manifest little sensitivity to end effects. The damping estimates, in terms of their mean and coefficient of variation (CoV), are also quite reliable, though they temporally vary. The introduction of padding to the systems, results in a decrease in the CoV, again affirming the efficacy of this pre-processing tool. The increase in central frequency does not markedly affect the statistics of the damping estimation, though Figure 8.8 demonstrates that the behavior temporally is more reasonable. Therefore, if estimates of frequency and damping are to be obtained for a known linear system, a linear fit to the entire curve in Figure 8.7 may be performed to yield estimates similar to the averaged quantities in Table 8.2, and a value of $\alpha = 2$ should be sufficient. However, in the case of

nonlinear systems, as explored by Staszewski (1998), a piecewise analysis is necessary to capture time-varying dynamic properties. However, note the rippling of damping estimates in the f_o = 6 Hz analysis (Figures 8.8a and 8.8b). The rippling in this case is indicative of incomplete modal separation. While the frequency ridges in Figure 8.4b indicated that separation was successful, it is again the more sensitive damping measure that verifies that the bandwidths of the two systems are still slightly overlapping. This is evident when comparing Figures 8.5c and 8.5d. The increase in f_o eliminates this spurious behavior (Figures 8.8c and 8.8d), though again at the expense of temporal resolution, requiring some compromise between achieving modal separation and minimizing end effects. Unfortunately, a choice of too small a f_o may produce rippling such as that in Figure 8.8a that may be mistaken for nonlinear behavior. Therefore, if the assumption of a linear system cannot be safely made, α = 3 may be more appropriate for time-varying system identification. Clearly for low frequency Civil Engineering systems this can lead to a significant loss of data.

For comparison, the frequencies corresponding to the scales of the ridges are listed in Table 8.2 and are reasonably accurate estimates of the natural frequency. As a result, for time-frequency analysis such as that presented in Sections 8.3 and 8.4, frequencies can usually be identified solely from the amplitude of the wavelet transform for α = 1 or α = 2 if closely spaced modal components are suspected. For further comparison, an alternative means for damping estimation is provided by a logarithmic decrement approach applied to wavelet skeletons (Hans et al., 2000; Lamarque et al., 2000). Such an approach, being reliant on the peaks of the amplitude decay, is more susceptible to fluctuations, particularly in the higher modes, even when modal separation

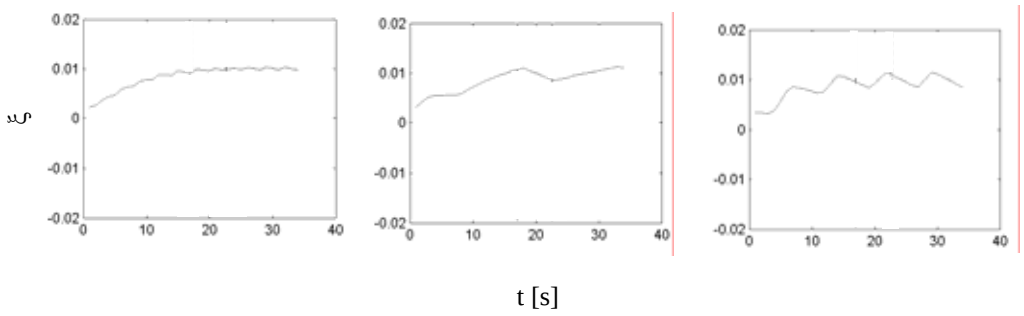

FIGURE 8.9. Identification of damping via logarithmic decrement of wavelet skeleton for f_o = 8 Hz with padding; modes 1, 2 and 3 shown from left to right

is achieved. Figure 8.9 demonstrates this for the logarithmic decrement identification of damping for f_o = 8 Hz with padding applied. Note the stabilization trend in the damping witnessed in Figure 8.8 is again apparent, though with more irregular variations. The statistics of the logarithmic decrement identification are also provided in Table 8.2 for comparison and reveal that the damping estimates are reasonable in the mean. Without padding, the CoV of the logarithmic decrement results is comparable to those obtained using the method based on analytic signal theory. However, when padding is applied and complete modal separation is assured (f_o = 8 Hz, β = 4), the CoV of the logarithmic decrement technique is significantly larger than that derived from the analytic signal identification approach presented in Figure 8.3, especially for the higher modes. This highlights that much of the variance in damping identified by the analytic signal approach is merely due to end effects and the lack of modal separation.

8.6 System Identification from Ambient Vibration: MDOF Example

Before the framework denoted as Track A in Figure 8.3 is introduced for application to actual measured data, the efficacy of the approach must be assessed. This assessment is conducted utilizing a simulated two-degree-of-freedom (2DOF) system, with frequencies of 0.2757 Hz and 0.3559 Hz and critical damping ratios of 0.01. The system is repeatedly simulated, progressively increasing the length of simulated data: Case 1 is comprised of 5 hours of data sampled at 10 Hz, Case 2 extends this to 10 hours and Case 3 to 30 hours. Intuitively, one would expect that the decrement signature more closely approximates the true impulse response or decay signature of the 2DOF system as the number of averages in the decrement increases. This generally holds true from repeated simulations of Cases 1, 2 and 3. However, it is observed that the agreement between the RDS and the signal decay diminishes in the transition zones between pockets of higher amplitude response, a consequence of the two modes beating, as shown in Figure 8.10 in the comparison of RDS obtained using the strictest RDT with local extrema trigger condition (see Chapter 2) with the actual impulse response function for the system. As a result, it can take a considerable number of averages to produce decrement signatures that more closely approximate this IRF, dependent on the random characteristics of the response within that simulation. Note in Figure 8.10 that the ability to replicate these low amplitude transitional ranges is limited. Though the periodicity is well captured, deviations in the amplitudes, even in the high amplitude peaks, are a clear sign of the difficulty in obtaining realistic envelope curves via RDT, and thereby accurate estimates of damping.

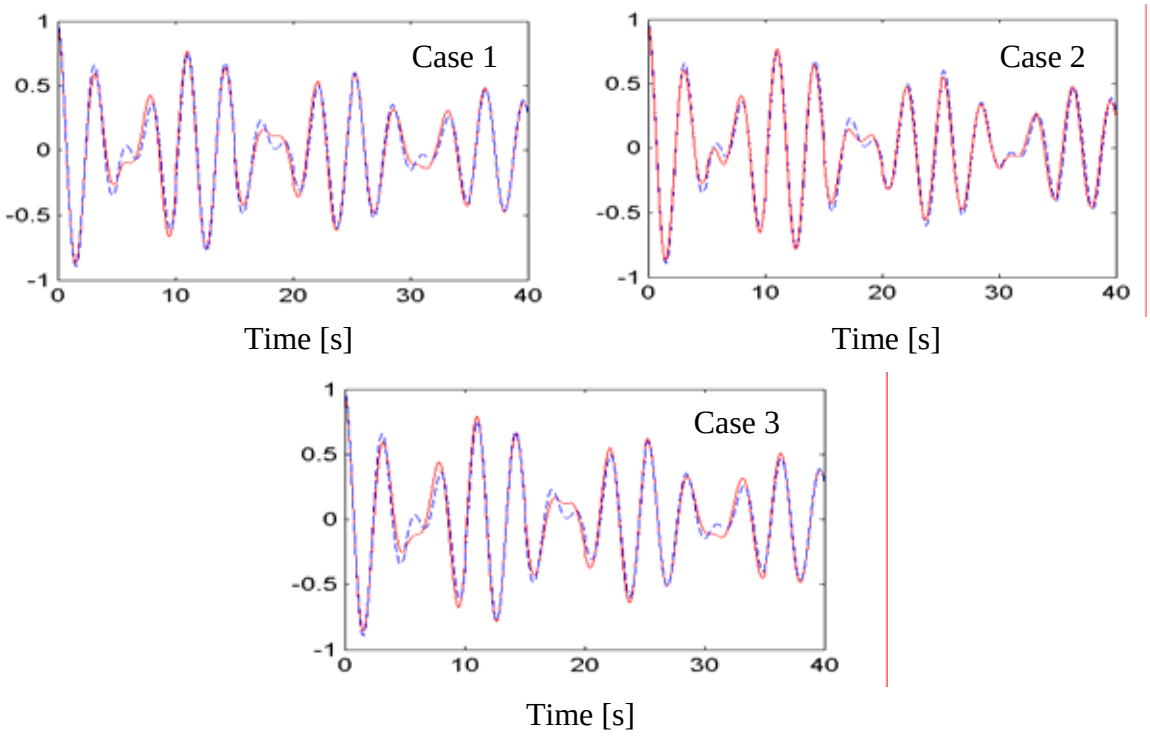

FIGURE 8.10. Random decrement signatures (solid) in comparison to actual impulse response function (dashed) for 2DOF system

The system identification methodology overviewed as Track A in Figure 8.3 is applied to the Random Decrement Signatures, with f_o = 2 Hz, β = 4 and OF = 1. In order to isolate the errors associated with inaccuracies in the Random Decrement Signature from those associated with the modal decoupling and system identification using the wavelet approximation to the analytic signal, the frequencies and dampings estimated from the RDS using this wavelet technique (Track A) are compared to those estimated from the actual system IRFs (Track B) using the same wavelet technique. The results for all three cases are chronicled in Table 8.3.

Table 8.3 demonstrates that the problem is not with the analytic signal identification technique or modal separation using wavelets, as all Track B identifications

using the IRF directly are within a few percent of the actual values. It appears instead to be tied to the RDT itself. The use of random decrement technique to obtain the decay signatures can have some uncertainty in general, as discussed in Section 2.3, and even more pronounced in the case of systems with modes that have close proximity where some beating of the envelope function occurs. In some cases the RDT may have difficulty in fully removing the random component of the response. For example, in Case 1, with only limited data, reveals good performance for Mode 1 but not for Mode 2.

TABLE 8.3

WAVELET FREQUENCY AND DAMPING ESTIMATES FROM RDS (TRACK A) AND IRF (TRACK B)

	Track A		Track B		Track A		Track B	
	f_1 [Hz]	ξ_1	f_1 [Hz]	ξ_1	f_2 [Hz]	ξ_2	f_2 [Hz]	ξ_2
Case 1	0.2764	0.0096	0.2753	0.0097	0.3561	0.0127	0.3559	0.0102
Case 2	0.2753	0.0088	0.2753	0.0097	0.3558	0.0105	0.3559	0.0102
Case 3	0.2755	0.0089	0.2757	0.0100	0.3560	0.0086	0.3559	0.0102

Doubling the amount of random data, the estimate of Mode 2 is enhanced but the estimate of Mode 1 degrades to some extent. The use of thirty hours of data in Case 3 produced underestimates of damping that are comparable if not reduced in quality compared to the data from Case 2. In fact, Case 2 gives the best overall estimate of damping in both modes, the reason for which becomes very clear when looking at how well the RDS approximates the IRF in Figure 8.10. The fact that Cases 1 and 3 produced less accurate damping estimates is clearly evident from Figure 8.10, demonstrating their inability to capture decay amplitudes and transition regions well. Thus it would seem that

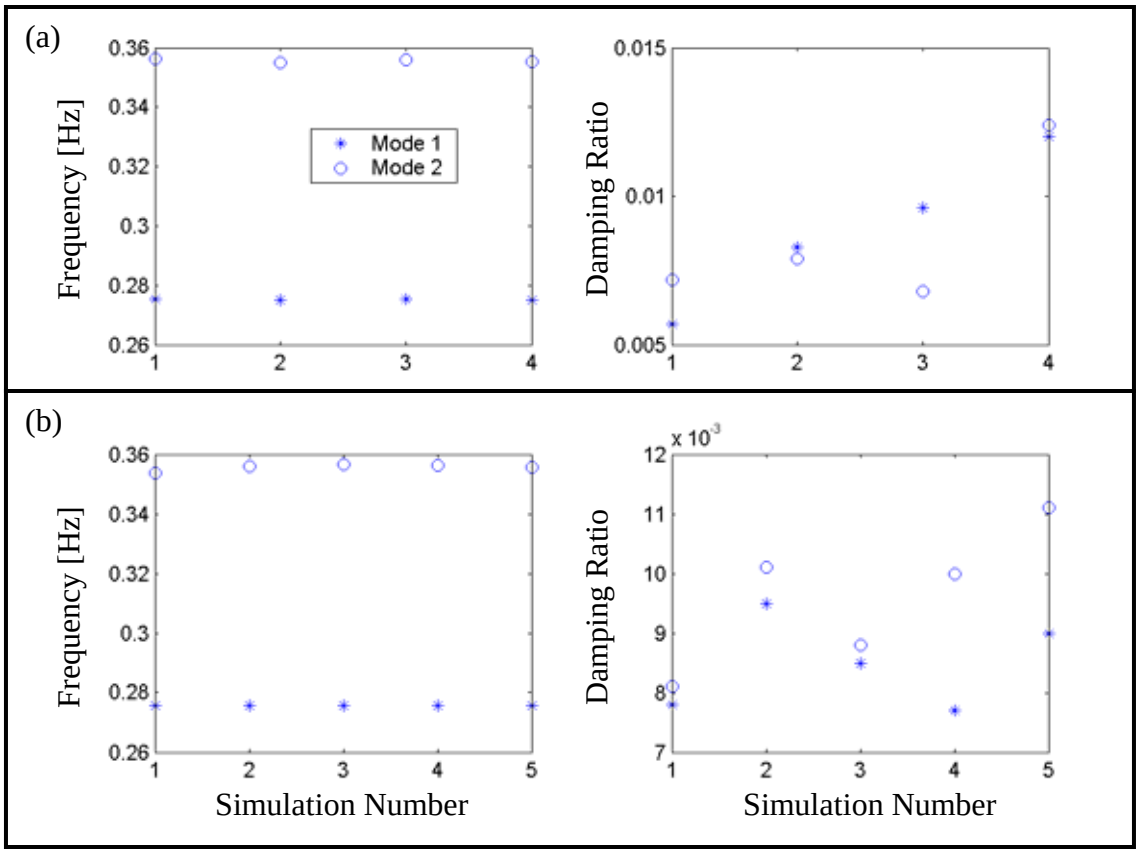

FIGURE 8.11. Frequency and damping identification by RDT and wavelet transform framework for repeated simulations of (a) Case 1 and (b) Case 2

the presence of more data does not offer clear improvement in the ability to accurately estimate damping. Moreover, this trend merely echoes the findings of Section 2.3, where the inherent randomness associated with a given simulation was found to influence the quality of the RDS and the ensuing damping identification.

To demonstrate this is again the case for this 2DOF system, Cases 1 and 2 were simulated several times and the Track B approach was applied to each time history. The results are shown in Figure 8.11. As expected, the variability in frequency estimation is limited, however, in terms of the identified damping levels, the variation between

simulations reflects the themes observed in Chapter 2. The level of variability is somewhat reduced when more data is considered, but again highlights the influence that the randomness of the process has on the performance of RDT. From the simulations of Case 2, with the aid of greater lengths of data, the average damping ratio in Mode 1 is conservatively estimated as 0.0085 and in Mode 2 as 0.0096. The good performance noted in Simulation number 2 for Case 2 (Fig. 8.11b) is the result of an RDT signature that closely approximated the actual IRF due to the random components of the response being fully cancelled in the averaging. The fact that this is not always achieved further emphasizes the need for accompanying measures such as the bootstrap approach in the Appendix of this study to evaluate the level of variance in decrement signatures.

Examples of some of the intermediate steps in this identification procedure are shown in Figure 8.12. Obviously, the breakdowns of the RDS due to increasing variance in the signature limits the amount of useable data. The progressive difficulty in ridge and skeleton extraction is evident in Figure 8.12a. Figure 8.12 demonstrates that the phase relations are about equal in the identification by both tracks and the damping in the first mode shows similar features. However, it is the higher mode damping that presents more obvious challenges, as the degree of rippling is far more pronounced in Track A again due to limitations in the RDT in recreating the proper IRF.

These examples and others within this chapter emphasize the interplay between the various parameters in the wavelet framework in Chapter 4 and the competing interests of the decrement signatures discussed in Chapter 2, particularly with respect to the end effects phenomenon, which, as shown in the beginning of this chapter, still has residual

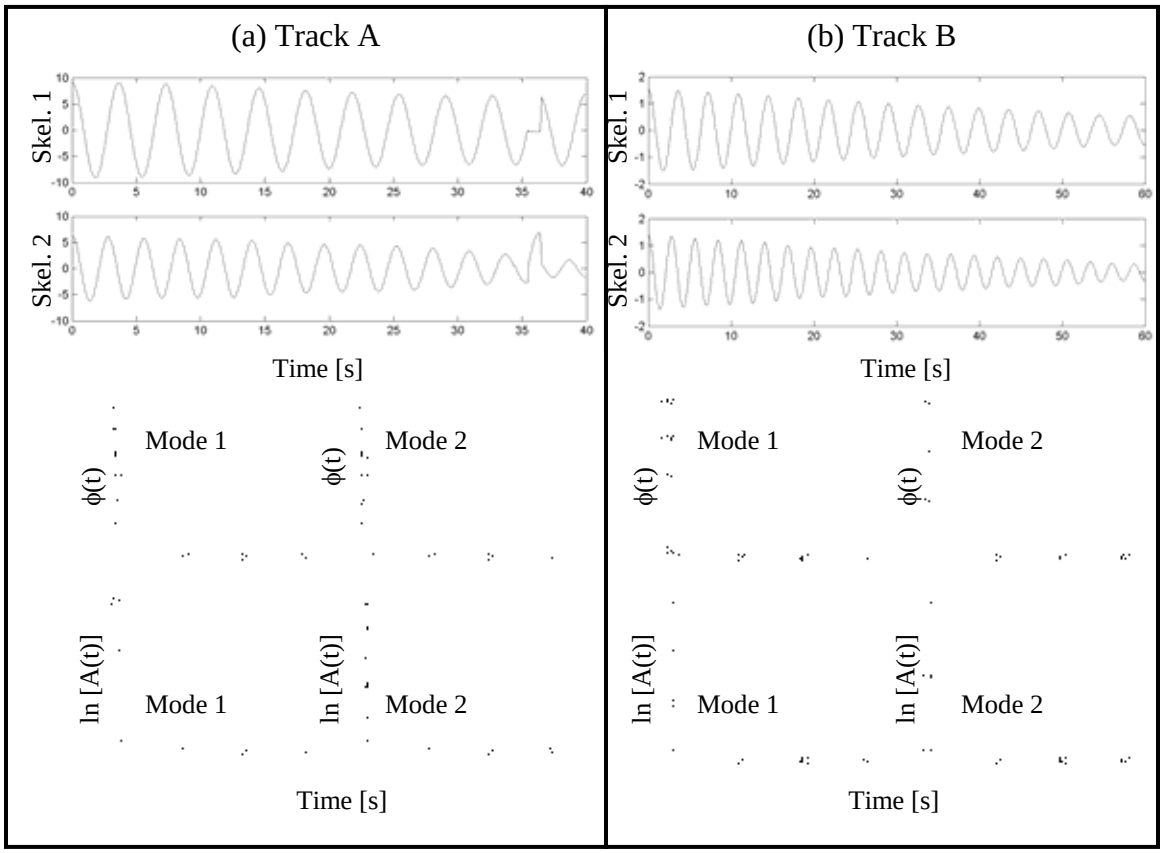

FIGURE 8.12. Wavelet-based system identification from (a) Random Decrement Signatures and (b) Impulse Response Functions

effects on damping estimation, even when reflective padding is utilized. As a result, the identification from both the IRF and RDS within this section is performed only on the useable signal components, lying beyond $3\Delta t_i$ of the padded signal. Within this region, the IRF is understandably the more consistent performer. However, to the benefit of applications to ambient vibrations, the prevalence of the first mode in the response usually permits lower values of central frequency than those required for systems such as those in Section 8.5, in which the responses are characterized by two closely spaced modes comparably participating to the response. As will be shown in the subsequent example, the dominant first mode response under wind does not typically result in

significant excitation of higher modes and thus this technique can be quite attractive for application, as the higher modes and noise make minor contributions and need only to be low pass filtered from the response, allowing lower central frequency values and thereby reduced end effects regions.

8.7 System Identification from Ambient Vibration Data: Full-Scale Example

Obtaining the IRF or free vibration curve can be difficult if not impossible for many Civil Engineering structures, as controlled testing can be costly in terms of equipment or disruptive to the daily function of the building. As a result, there is interest in developing approaches to permit the extraction of decay curves from ambient vibration data — an oftentimes challenging proposition. The Random Decrement Technique has evolved as a popular analysis tool, as discussed in greater detail in Chapter 2. Though Ruzzene et al. (1997) employed this technique to analyze full-scale bridge data, some added concerns surface when the wavelet system identification approach discussed here is merged with the RDT for low frequency systems. Chapter 2 has shown that the variance of RDS signatures increases with each cycle of oscillation as one moves further from the trigger condition, indicating that system identification should be restricted to the first few cycles of the RDS. A variance envelope on the decrement signature, developed in Chapter 2 and the Appendix of this study, illustrates, via Figure 8.13, the limited number of cycles over which identification can be reasonably made. The degradation of decrement signatures is problematic for low-frequency Civil Engineering structures, when wavelets are employed in the framework of Figure 8.13 in Track A, since the end-effect region described in

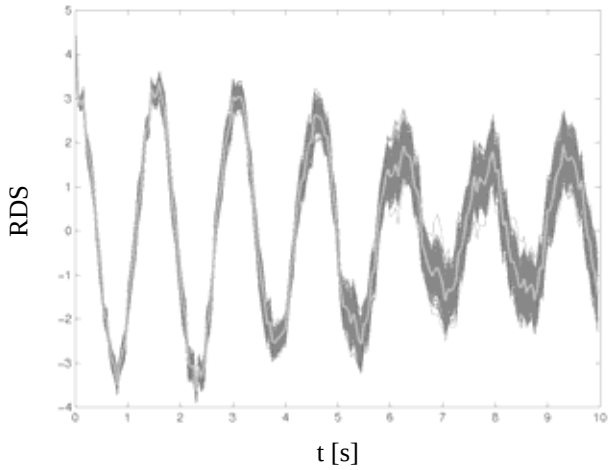

FIGURE 8.13. Example of Random Decrement Signature (gray) and variance envelope

Equation 4.9 lengthens. While padding does repair the amplitudes considerably, reliable damping identification should only proceed outside of the $3\Delta t_i$ end effects region, though frequency identification and signal amplitude reconstruction remains viable throughout. The amount of data lost can be offset to some extent by decreasing the analyzing frequency f_o of the Morlet wavelet, albeit compromising the ability to distinguish closely spaced modes. This permits the identification of damping from more reliable portions of the RDS. As motivated above, this compromise can be justified for dominant first mode responses under wind.

To illustrate, the RDT is applied to 1.5 hours of measured full-scale acceleration data, sampled at 20 Hz, a portion of which is shown in Figure 8.14. The data was measured along the y-axis of a tower in Japan during a typhoon (Tamura et al., 1993). Note that during simple free vibration tests, the tower was found to have a fundamental sway period of 1.6 seconds in both directions, with a critical damping ratio of 0.015. The

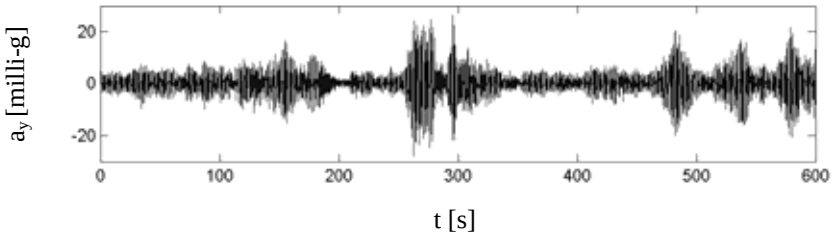

FIGURE 8.14. Ten-minute segment of the acceleration response (y-dir) of tower in typhoon

application of RDT in the strict peak trigger condition yielding 225 averaged segments, yields the signature shown in Figure 8.15a. Note the signature lacks the smooth characteristic one would anticipate from a decay of a SDOF damped oscillator, indicating the presence of higher modes or other noise in the RDS, which would normally have to be separated through some bandpass filtering. However there is no characteristic beating in the RDS, observed previously in the presence of closely spaced modes in Section 8.6, allowing the relaxation of the wavelet resolutions. Therefore, a very relaxed resolution wavelet (f_o=0.5 Hz) may be applied. The low value of central frequency then allows the maximization of the amount of usable transformed signal in light of the competing restrictions of variance in the Random Decrement Signature and the end effects of the wavelet transform, minimized to some extent with the padding operation. The real component of the wavelet coefficients, given in Figure 8.15b, identifies a single mode contributing to the response, as typically observed under wind excitation, and the decaying oscillatory character of the decrement signature. The breadth of the scalogram in the frequency domain reiterates the loss in frequency resolution, which resulted from the choice of a Morlet wavelet with superior time resolution. The skeleton extracted from

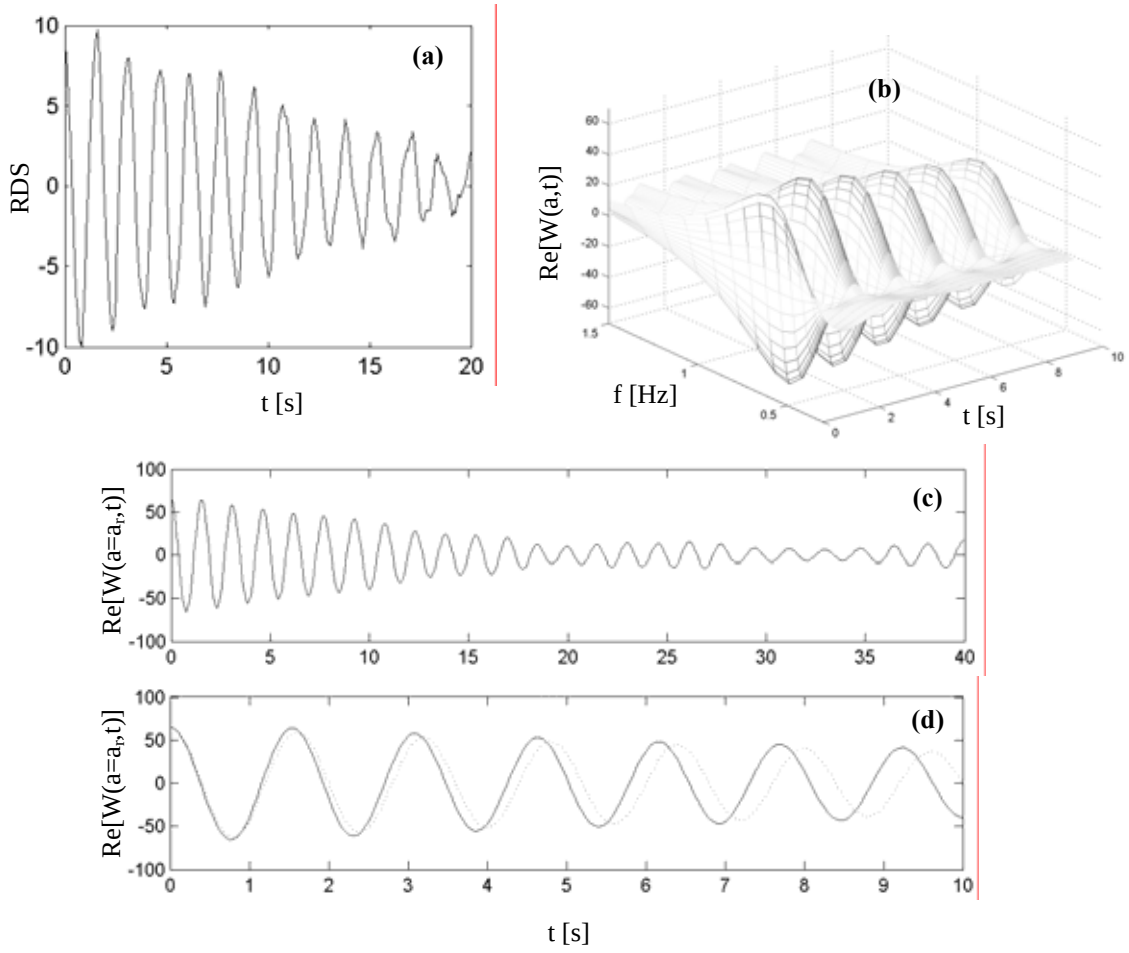

FIGURE 8.15. (a) Random decrement signature, (b) real component of wavelet-transformed Random Decrement Signature in 3D; (c) real-valued skeleton; (d) zoom of real-valued skeleton (solid) with theoretical skeleton (dotted) for f_n = 0.625 Hz and ξ = 0.015

the ridge of the wavelet is shown in Figure 8.15c and is clean and smooth, as the wavelet transform has separated the higher frequency noise in the RDS in Figure 8.15a. The RDS embodied by the skeleton appears to be relatively stable up to about 10 seconds, after which it degrades in quality as a result of the increasing variance shown in Figure 8.13. As a result, the system identification should be performed at most on the first 10 seconds of the RDS. Figure 8.15d shows a comparison between the signature in the first 10

seconds and the anticipated signature, based on the structure's known frequency and damping. Inconsistencies in amplitude and phase between the two propagate with time, as a result of RDS variance, and suggest that system identification should be performed within the first 3-4 seconds of the RDS. Though the comparison in Figure 8.15d is not available during the typical system identification process, the variance envelopes shown in Figure 8.13 allow the user to make a similar conclusion that the RDS quality is suspect beyond 4 seconds.

As discussed previously, due to minor end effects remaining in spite of padding, identification of damping should proceed beyond $3\Delta t_1$ of the initiation of the wavelet-transformed Random Decrement Signature. Thus the useable portion of the RDS may be first defined as, t_{use} = 1.66 to 10 seconds. The end effects region was minimized as a result of compromising frequency resolution, which will not significantly affect the results for this system since no closely spaced modes are present. Identification of frequency and damping by the procedure based on analytic signal theory produced estimates of frequency and damping shown in Figures 8.16a and 8.16c. Note that beyond 10 seconds, the quality of estimates rapidly degrades, due to the variance of the RDS. Zooming in on the first 10 s in Figures 8.16b and 8.16d reaffirms two previous observations: the identified frequency suffers very little as the result of end effects, and even with the padding operation, damping estimates are less reliable in the first $3\Delta t_1$ (marked by the dashed line in Figure 8.16d) though gradually approaching more stable levels. As summarized in Table 8.4, piecewise fits of the amplitude and phase of the RDS over only t_{use} produced mean frequency and damping estimates consistent with that observed from free vibration testing, though with considerable variance in the damping

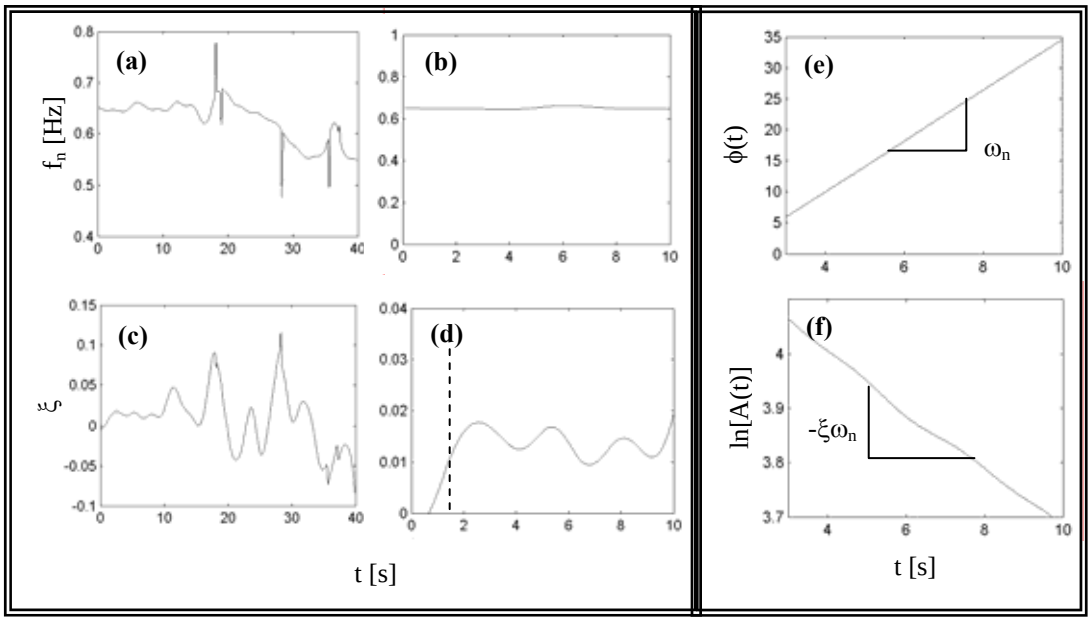

FIGURE 8.16. (a) Frequency and (c) damping identified from wavelet skeleton, zoom of (b) frequency and (d) damping estimates, (e) wavelet phase along ridge, (f) wavelet amplitude along ridge

estimate. Note that the tracking of nonlinear frequency and damping characteristics via the Random Decrement Technique, discussed by Tamura & Suganuma (1996), can be accomplished by varying the trigger condition on captured segments. The resulting decrement signature will manifest, in its first few reliable cycles, the frequency and damping referenced to the amplitude level defined by the trigger. Therefore, the RDS associated with a given trigger level can be assumed linear and any nonlinearity will be evident as the trigger level is changed and other RDS are analyzed.

In such cases where the RDS is known to represent a linear system, it is more reasonable to conduct a best fit of the entire length of t_{use} as shown in Figures 8.16e and 8.16f. Note that there is still a slight deviation in the log of the amplitude, producing a slightly smaller damping estimate than the piecewise mean. However, re-inspection of

Figure 8.15d reveals that significant deviations in phase and amplitude in the decrement signature are evident beyond the 4th second, a fact affirmed by Figure 8.16. Therefore, restricting the identification to t_{use} = 1.657 - 4 s, is more reasonable. The resulting estimates of damping (0.0151) and frequency (0.645 Hz), are both within a few percent of the values observed in free vibration test. These results are also consistent with the findings of Tamura et al. (1993) from data collected during the passage of several typhoons. The results in Table 8.4 and Figure 8.16 highlight the importance of identification in the early stages of Random Decrement Signatures. It is interesting to note that Ruzzene et al. (1997) found some discrepancy between the identified damping values and those observed previously by other techniques, possibly due to estimation of damping from the later, less-reliable cycles of the RDS. Such characteristics of the RDT make it vital that the end effects issues in wavelet transformed Random Decrement Signatures are recognized and accounted for to insure reliable system identification.

TABLE 8.4

WAVELET-BASED IDENTIFICATION FROM FULL-SCALE AMBIENTLY-EXCITED DATA

Measured in Free Vibration Test		Identified Piecewise over t_{use}			Identified from $t_{use} = 3\Delta t_1$ - 10 s		Identified from $t_{use} = 3\Delta t_1$ - 4 s	
f_n [Hz]	ξ	f_n [Hz]	avg[ξ]	CoV[ξ]	f_n [Hz]	ξ	f_n [Hz]	ξ
0.625	0.0150	0.650	0.0141	18.43%	0.651	0.0136	0.645	0.0151

8.8 Conclusions

The last several chapters have demonstrated the utility of wavelet transforms in analyzing a variety of signals in Civil Engineering, for not only time-frequency analysis but also for system identification. This popularity stems in part from its multi-resolution capabilities and the potential for direct relations to the Fourier transforms. This chapter focused on some of the processing concerns which surface in Civil Engineering applications and introduced a system identification framework applicable to measured free vibrations or ambient vibration data.

The discussions and examples in this chapter emphasized that application of the Morlet wavelet requires judicious selection of central frequency in light of the resulting time and frequency resolutions, a fact that becomes significant for Civil Engineering structures, whose dynamics are often more narrowbanded than traditional mechanical systems. For such systems, the presence of end effects can compromise the accuracy of wavelet skeletons and have even more marked effects on bandwidth measures. While the padding operation is demonstrated to improve the scalogram amplitudes thereby eliminating the appearance of negative damping, and more quickly stabilizing the behavior of damping estimates, reducing their coefficient of variation. However, the sensitivity of the damping measure still results in some inaccuracy within $3\Delta t_i$ of the ends, defining the acceptable analysis regimes of the transformed signal. Though an improvement over the results without padding, to minimize this effect, the central frequency should be kept to the smallest value possible without compromising the ability to separate closely spaced modes, an important consideration when the Random

Decrement Technique is applied for analysis of ambient vibration data. However, it was observed the when adequate modal separation was achieved and padding was applied, the coefficient of variation in the analytic signal approach is quite low, highlighting that much of the variance in damping estimates may be attributed to end effects and modal overlap and not the identification technique itself. In total, the discussions in Chapter 2 and this chapter highlight the challenges facing Civil Engineers in the identification of damping from ambient vibration. The next chapters now discuss the manner in which such ambient vibration data can be obtained.